

Detailed heat transfer distributions of narrow impingement channels for integrally cast turbine airfoils

THÈSE N° 6177 (2014)

PRÉSENTÉE LE 15 MAI 2014

À LA FACULTÉ DES SCIENCES ET TECHNIQUES DE L'INGÉNIEUR
LABORATOIRE DE THERMIQUE APPLIQUÉE ET DE TURBOMACHINES
PROGRAMME DOCTORAL EN ENERGIE

ÉCOLE POLYTECHNIQUE FÉDÉRALE DE LAUSANNE

POUR L'OBTENTION DU GRADE DE DOCTEUR ÈS SCIENCES

PAR

Alexandros TERZIS

acceptée sur proposition du jury:

Prof. J. A. Schiffmann, président du jury
Dr P. Ott, directeur de thèse
Prof. F. Gallaire, rapporteur
Dr M. Henze, rapporteur
J. Von Wolfersdorf, rapporteur



ÉCOLE POLYTECHNIQUE
FÉDÉRALE DE LAUSANNE

Suisse
2014

ACKNOWLEDGEMENTS

This study was carried out in the framework of Kraftwerk 2020 (KW2020) research project funded by the Swiss Federal Office of Energy (SFOE) and Alstom (Baden, Switzerland). The financial support as well as the permission to publish the results prior to the final thesis submission are highly appreciated.

Over the last four years, I cooperated with a number of people to only some of whom it is possible to give particular mention here. First of all, I would like to acknowledge my supervisor Dr. Peter Ott (EPFL), whose entrustment made the completion of this work possible. He kindly supported my doctoral studies giving me also the opportunity to make my own ideas happen. I would also like to thank the industrial partners of the project, Dr. Magali Cochet and Dr. Guillaume Wagner from Alstom (Baden, Switzerland) for their insightful suggestions and valuable input during the experimentation. Many thanks go also to the director of KW2020, Dr. Peter Jansohn (PSI, Switzerland), who was always interested in my work and the overall progress of the project. Thanks are also due to Prof. François Gallaire (EPFL) and Dr. Marc Henze (Alstom, Switzerland) for serving as committee members for my private thesis exam as well as to Prof. Jürg Alexander Schiffmann (EPFL) for presiding the jury of this thesis.

I am also more than grateful to my external advisors, supervisors, co-authors and valuable teachers, Prof. Bernhard Weigand and Prof. Jens von Wolfersdorf (co-referee also), from the Institute of Aerospace Thermodynamics (ITLR) of University of Stuttgart (Germany). I had the pleasure to spend a lot of time with them in our laboratory discussing various topics of convective heat transfer for applied as well as basic research. Their visiting Professorship at EPFL was definitely one of the most enjoyable periods of the year.

Of course, this work would not have been possible without technical support. Many thanks to all the staff of the workshop and especially to Jean-Pierre Rougnon, Nikolas Jaunin and Christophe Zurmühle. Special thanks go to Mr. Marc Salle, chef d'atelier, who has shown particular interest for my drawings accepting finally most of my submitted designs. During our collaboration, and due to my low competence in French language, I realised that technical drawing is just another communicative language.

I cooperated also with a number of excellent master thesis/semester project students. The exchanged students, Stefan Fechter (University of Stuttgart, Germany), Oriana Caggese (University of Florence, Italy), Santiago Lluçia (Polytechnic University of Catalunya, Spain), Dirk Ullmer (University of Stuttgart, Germany), as well as the EPFL students, Robert Wyssmann, Gabriel Gnaegi, Gwenael Hannema, Ronald Gutierrez, Sylwia Wojnarska and Baptiste Hinaux performed outstanding work, part of which contributed to several international journals.

I am also pleased that I have worked within a very friendly group of people here at EPFL. The Group of Thermal Turbomachinery (GTT), former Laboratoire de Thermique appliquée et de Turbomachines (LTT). I thank: Philip Peschke and Elia Colombo for their overall contribution in laboratory issues. Achim Zanker for showing me how to paint the liquid crystals and the big help during the movement of the laboratory. Dr. Cecile Deslot for her assistance in setting-up numerical solvers for the student projects. Magnus Jonsson for the welcome to EPFL. And the rest of the group, Sami Goecke, Virginie Chenaux, Benjamin Mergele, as well as Stina Zufferey and Margarita Jotterand-Jimenez for helping me with administrative issues. Special thanks go also to Mrs. Annick Despont, who secured my PhD request e-mail from March to June 2009.

I would also like to acknowledge my “scientific” friends, Prof. Anestis I. Kalfas (AUTH, Greece) for encouraging my research all the years of my post-graduate education giving me a lot of good advice, as well as Dr. Christos Altantzis (MIT, USA), Major Eleftherios Andreadis (Hellenic Air Force, Greece) and my best-man Dr. Georgios Michailides (École Polytechnique de Paris, France) for their suggestions on many issues that I have discussed with them. Many thanks go also to Dr. Theodoros Kyriakidis (EPFL) for his support during the setup of electronic equipment and to Dr. Serafeim Perdakis (EPFL) for his programming skills.

I also thank all my friends in Switzerland, Greece and the rest of Europe (too many to be listed here, you know who you are!) as well as to el único capitán Pablo Gabriel García (PAOK, Thessaloniki) who inspired the principles under which this thesis has been conducted by just being himself. Additionally, my “swiss family” Vagia and Simis deserve a special note for standing next by me during various times of difficulty, and of course my friends Apostolos, Giannis, Teo and Polydeukis who could easily change my mood by just looking at them. I am also more than grateful to Prêtre Alexandros Iossifidis for the very warm welcome which made my initial stay in Lausanne exceptionally pleasant.

Last but not least, my deepest gratitude goes to my parents Chrysa and Aris, my sister Athanasia and my grandmother Rachel who have always supported my choices. I would not have made it this far without them.

LAUSANNE, MARCH 24, 2014

ALEXANDROS TERZIS

ABSTRACT

Gas turbine operation at very high turbine inlet temperatures, which are usually far above the melting point of the current material technology, ensures increased thermal efficiency and useful power output. Therefore, majority of the modern gas turbines are equipped with turbine blade cooling systems in order to run safely at elevated temperatures. Turbine blade cooling is thus a leading factor of gas turbine engine design, aiming to obtain the maximum overall cooling efficiency at a minimum penalty of the engine thermodynamic cycle performance. On the other hand, the industrial tendency to push further firing temperatures, closer to fuel stoichiometric temperatures, is limited by the capabilities of the current cooling technologies (shaped film cooling holes and TBC) which approach their limits. Therefore, new concepts and more sophisticated cooling architectures have to be considered for the design of future gas turbines.

Nowadays, the capabilities of the foundry industry to produce high integrity and dimensionally accurate castings allow the production of integrally cast turbine airfoils with the so-called *double-wall* cooling technology. Cast-in turbine airfoils include a more distributed form of cooling, where the coolant can be injected in the form of impingement jets within the wall rather than the hollow of the airfoil increasing dramatically the heat exchanged capabilities. Narrow impingement cooling passages can be therefore generated close to the external hot gas flow, while the small thickness of the airfoil wall imposes significant heat transfer for all internal surfaces of the cooling cavity.

Motivated by the lack of available data in the literature, the main objectives of this thesis is the experimental evaluation and a detailed analysis of the local heat transfer distributions for all internal surfaces of narrow impingement channels. The test models consist of a single row of five impingement jets investigated over a range of engine representative Reynolds numbers. Effects of jet-to-jet spacing, channel width and height, impingement jet pattern and varying jet diameter are independently examined, composing a test matrix of 30 large-scale geometries. The effects of the various geometrical factors on the heat transfer level are correlated in an empirical model providing the first heat transfer correlation for this kind of application. For the evaluation of the heat transfer coefficients, the transient liquid crystal technique is applied providing detailed information of the local convective coefficients with great spatial resolution. Thermocouple thermal inertia on the evaluation of heat transfer coefficients are also considered.

Given that the use of different impingement geometries could play an important role on the distribution of convection coefficients, and hence, on the homogeneity of blade metal temperatures, the experimental results of this study can be used along with the external heat load for the development of thermal design models for integrally cast turbine vanes and blades.

Keywords: Turbine blade cooling, impingement cooling, convective heat transfer, liquid crystal thermography

RÉSUMÉ

L'utilisation des turbines à gaz à de très hautes températures d'entrée en turbine, permet d'obtenir de meilleurs rendements thermiques et de plus hautes puissances utiles. C'est pourquoi la majorité des turbines à gaz modernes sont équipées de systèmes de refroidissement d'aubes pour assurer le bon fonctionnement à haute température. Les systèmes de refroidissements pour aubes de turbine sont un des facteurs décisifs pour la conception de turbines à gaz et ont pour buts de maximiser la capacité de refroidissement globale des aubes tout en ayant un impact négatif minimal sur la performance du cycle thermodynamique de la turbine à gaz. D'un autre côté, la tendance industrielle d'augmenter la température de combustion, pour s'approcher de la température stoechiométrique du mélange combustible, est limitée par les technologies actuelles en matière de refroidissement d'aubes de turbine. De nouveaux concepts et des architectures plus sophistiquées de systèmes de refroidissement d'aubes doivent donc être considérés pour la conception des futures turbines à gaz.

La capacité actuelle de l'industrie de la fonderie de produire des pièces de grande qualité et précision permet la production d'aubes de turbine grâce à la technologie dite de doubles parois. Les aubes coulés permettent une meilleure distribution du refroidissement, où le fluide de refroidissement peut être injecté sous la forme de jets impactant sur la surface à refroidir plutôt que dans le corps de l'aube, augmentant drastiquement le pouvoir de refroidissement. De fins canaux de refroidissement par impacts de jets peuvent être positionnés près de l'écoulement externe, tout en ayant de très fines parois d'aubes, assurant un bon transfert de chaleur pour toutes les surfaces internes de la cavité de refroidissement.

Les données sur le refroidissement par impact de jets des aubes de turbine étant manquantes ou insuffisantes, l'objectif principal de cette thèse est l'évaluation expérimentale ainsi qu'une analyse détaillée de la distribution du transfert de chaleur local, pour toutes les surfaces internes des canaux de refroidissement par impacts de jets. Le modèle utilisé est constitué de cinq jets disposés dans une direction, qui sont investigués pour des nombres de Reynolds représentatifs de turbines à gaz réelles. Les effets de l'espacement des jets, de leur arrangement en quinconce ou en ligne, de l'épaisseur et de la hauteur des canaux, du diamètre variable des jets sont examinés indépendamment, formant une matrice de tests de 30 modèles construits à une échelle plus grande que nature. Les effets des divers facteurs géométriques sur la quantité de chaleur transférable sont corrélés dans un modèle empirique permettant d'obtenir le premier facteur de corrélation pour ce genre d'application. Pour l'évaluation des coefficients de transfert de chaleur, la technique des cristaux liquides instationnaire est utilisée, donnant une information détaillée sur les coefficients de transferts de chaleur convectifs locaux avec une grande précision spatiale. L'effet de l'inertie thermique des thermocouples utilisés dans cette technique est aussi intégré pour l'évaluation des coefficients de transfert de chaleur.

Mots-Clés : Systèmes de refroidissements pour aubes de turbine, refroidissements par jets impactants, transfert de chaleur par convection, cristaux liquides transitoire

ZUSAMMENFASSUNG

Das Bestreben, die Effektivität und Leistung von Gasturbinen immer weiter zu erhöhen, hat zu Turbineneintrittstemperaturen geführt, die weit über dem Schmelzpunkt der derzeit verfügbaren Werkstoffe liegt. Um weiterhin einen sicheren Betrieb zu gewährleisten, verfügen Schaufeln in modernen Gasturbinen daher über Kühlsysteme, welche die Materialtemperatur senken. Diese Techniken sind ein wichtiger Entwicklungsfaktor bei Designs, die darauf abzielen, die Effizienz der Kühlung zu maximieren und gleichzeitig die Einbußen im thermodynamischen Kreisprozess gering zu halten. Darüber hinaus wird die Erhöhung der Brennkammertemperatur zu Werten nahe der stöchiometrischen Temperatur durch die verfügbaren Kühltechniken begrenzt. Aus diesen Gründen ist es notwendig, neue Konzepte zur Schaufelkühlung zu untersuchen.

Fortschritte in der Gießtechnologie, insbesondere das integrale Gießen, ermöglichen heutzutage die Herstellung von doppelwandigen Turbinenschaufeln mit Kühlkanälen in der Außenwand mit integrierten Löchern zur Erzeugung von Strahlen zur internen Prallkühlung. Durch diese Strahlen kann die Kühlluft direkt auf die heiße Außenwand prallen und diese viel effektiver kühlen als es mit herkömmlichen Techniken möglich ist. Zudem wird der Wärmeaustausch durch die dünnen Wände der Kühlkanäle deutlich erhöht.

Das Ziel der vorliegenden Studie ist die experimentelle Untersuchung und Analyse der lokalen Verteilungen des Wärmeübergangskoeffizienten an internen Oberflächen in Prallkühlungskanälen, welche in der Literatur bisher nicht zu finden sind. Die Versuchsmodelle bestehen aus fünf Strahlen in einer Reihe, welche in einem Bereich der Reynoldszahl untersucht werden, wie er in realen Turbinen auftritt. Die Rolle der verschiedenen geometrischen Parameter wie des Abstandes benachbarter Kühlstrahlen, Kanalbreite und -höhe, Strahl-Durchmesser und -Anordnung und ihr Einfluß auf die Wärmeübertragung werden getrennt in 30 großmaßstäblichen Konfigurationen untersucht. Die Ergebnisse der verschiedenen Versuche werden in einem empirischen Modell korreliert und liefern so die erste Wärmeübergangskorrelation für diese Art von Anwendung. Zur Bestimmung der Wärmeübergangskoeffizienten wird die instationäre Technik mit Flüssigkristallen (transient liquid crystal technique) angewandt, wodurch der lokale Wärmeübergangskoeffizient detailliert und mit hoher räumlicher Auflösung bestimmt werden kann.

Da die verschiedenen geometrischen Konfigurationen einen Einfluss auf die Wärmeübertragung und dadurch auf die Homogenität der Schaufeltemperatur haben, können diese experimentellen Ergebnisse zusammen mit der äußeren Wärmebelastung zur Entwicklung von integral gegossenen Turbinenschaufeln genutzt werden.

Stichworte: Turbinenschaufelkühlung, Prallkühlung, konvektiver Wärmeübergang, Flüssigkristall-Thermographie

CONTENTS

Contents	xiii
List of Figures	xvii
List of Tables	xxi
1 Introduction	1
1.1 The Gas Turbine Engine	1
1.2 Historical Aspects	1
1.3 The Gas Turbine Cooling Problem	3
1.4 Turbine Blade Cooling	5
1.4.1 General discussion	5
1.4.2 Improvement of casting technologies	6
1.4.3 Wall-integrated cooling technologies	7
1.5 The Current Experimental Study	8
1.6 The Structure of the Thesis	9
2 Literature Review	11
2.1 Introduction	11
2.2 Jet Impingement Heat Transfer	11
2.2.1 Single jet	11
2.2.2 Jet arrays	14
2.3 Industrial Double-Wall Cooling Configurations	16
2.4 Narrow Impingement Channels	17
2.5 The Contribution of The Thesis	20
3 Experimental Setup	21
3.1 Introduction	21
3.2 Impingement Cooling Test Rig	22
3.2.1 Literature background	22
3.2.2 General Layout	23
3.2.3 The heater mesh	27
3.3 Test Models	30

3.4	Instrumentation	32
3.5	Concluding Remarks	35
4	Measurement Technique	37
4.1	Introduction	37
4.2	Transient Liquid Crystal Technique	38
4.2.1	The transient technique	38
4.2.2	Surface temperature measurements	38
4.2.3	Liquid crystal calibration	39
4.3	Data Reduction	40
4.3.1	Experimental procedure	40
4.3.2	Semi-infinite model	42
4.3.3	Image processing	43
4.3.4	Color Hue vs. G_{max} calibration	43
4.4	Influence of Thermocouple Thermal Inertia	43
4.4.1	Thermocouple time constant	43
4.4.2	Determination of τ_c for various conditions	45
4.4.3	Calculation of driving temperature	47
4.4.4	Effect on heat transfer coefficient	47
4.5	Experimental Uncertainties	47
4.5.1	Uncertainty analysis	48
4.5.2	Repeatability	50
4.6	Concluding Remarks	51
5	Flow Distributions	53
5.1	Flow Domain	53
5.2	Channel Pressure Drop	55
5.3	Local Discharge Coefficients	56
5.4	Crossflow and Local Massflow Distributions	57
5.5	Concluding Remarks	59
6	Heat Transfer Distributions	61
6.1	Data Presentation	61
6.1.1	Crossflow effects	61
6.1.2	Distributions of heat transfer coefficients	62
6.2	Effect of Reynolds number	64
6.3	Effect of channel height (Z/D)	65
6.3.1	Target plate	65
6.3.2	Sidewalls	67
6.3.3	Jet plate	67
6.4	Effect of channel width (Y/D)	68
6.4.1	Target plate	68
6.4.2	Sidewalls	69
6.4.3	Jet plate	70
6.5	Effect of Hole Staggering ($\Delta y/Y$)	70
6.5.1	Target plate	70

6.5.2	Sidewalls	73
6.5.3	Jet plate	74
6.6	Effect of Streamwise Jet Spacing (X/D)	74
6.6.1	Target plate	74
6.6.2	Sidewalls	75
6.6.3	Jet plate	76
6.7	Effect of Varying Jet Diameter (ΔD)	76
6.7.1	Flow distributions and discharge coefficients	77
6.7.2	Target plate	79
6.7.3	Sidewalls	80
6.7.4	Jet plate	81
6.8	Area Averaged Heat Transfer Level	82
6.8.1	Row-by-row	83
6.8.2	Full channel length	86
6.9	Thermal Performance	88
6.10	Assessment of the Results	90
7	Heat Transfer Correlation	93
7.1	Introduction	93
7.2	Regression Analysis	94
7.2.1	General	94
7.2.2	Determination of exponent m	96
7.2.3	Correlation for coefficient C	96
7.3	Concluding Remarks	99
8	Conclusions and Recommendations	101
8.1	Summary	101
8.2	Conclusions	102
8.3	Recommendations For Future Work	104
	Bibliography	105
A	Example of Technical Drawings	115
B	Digital Image Processing Tool	129
C	Thermocouple Time Constant Effects on Heat Transfer Level	133
D	Crossflow Model	135
E	Local Variation of Exponent m	137
F	Additional Heat Transfer Results	139

LIST OF FIGURES

1.1	GT-26 industrial gas turbine. Image courtesy of ALSTOM	2
1.2	Evolution of Turbine Entry Temperature (TET) for aero-engines	3
1.3	Evolution of compression Overall Pressure Ratio (OPR) for aero-engines	4
1.4	Evolution of compressor delivery temperature ($T_{coolant}$) for aero-engines	5
1.5	Schematic representation of turbine blade cooling. Adopted from Han (2013)	6
1.6	Effect of the development of casting techniques on blade cooling architectures	7
1.7	Wall-integrated narrow cooling cavities in a turbine airfoil. Left figure adopted from Lutum et al. (2002)	8
2.1	Flow regions for a single impinging free jet. After Weigand and Spring (2011)	12
2.2	Radial distribution of Nu_D for various Z/D and Re_D	13
2.3	Stagnation point $Nu_{D,s}$ as a function of Re_D and Z/D	14
2.4	Different crossflow schemes for multi-jet systems. After Obot and Trabold (1987)	15
2.5	Area averaged Nusselt number as a function of jet plate open area (A_f). Data for Inline patterns and maximum crossflow orientations. $Z/D=1-5$	16
2.6	Aero-engine turbine airfoils with double-wall cooling configurations. (a) Livsey and Hamblet (1996) , (b) Dailey et al. (2001) , (c) Moore (1997)	17
2.7	Industrial engine turbine airfoils with double-wall cooling configurations. (a) Lee and Bunker (2006) , (b) Lutum et al. (2002) , (c) Liang (2013)	17
3.1	Impingement cooling test rig	22
3.2	Inlet flare design dimensions	24
3.3	Locations and uniformity of static pressure profile on the wind tunnel ducts	26
3.4	The heater mesh configuration employed in this study	28
3.5	Temperature evolution downstream of the heater grid	29
3.6	Schematic representation of the test models	30
3.7	Narrow impingement channels painted with liquid crystals	32
3.8	Schematic representation of the pressure measurement points for determination of local jet massflow variations	33
4.1	Experimental details for the video acquisition	39
4.2	Liquid crystal calibration single jet facility	40
4.3	Liquid crystal calibration curves	40

4.4	Various frames of liquid crystal evolution with time. $T_{LC}=37.5-39.6^{\circ}C$, $\theta=0.45$, $Z/D=1$, $Re_D=40,000$	41
4.5	Influence of thermocouple time constant on temperature measurements	44
4.6	Thermocouple outputs at various temperature steps. $U_{\infty}=0.5ms^{-1}$	46
4.7	Thermocouple time constant versus (a) wire diameter and (b) plenum velocity	46
4.8	(a) Plenum temperature history extracted from thermocouple outputs and (b) DC-power supplied in the heater mesh.	47
4.9	Uncertainty level in the evaluation of heat transfer coefficient	49
4.10	Significance of scatter on repeated experiments. (a) Actual repeatability and (b) Effect of temperature step. $X/D=Y/D=5$, $Z/D=1$, $Re_D=32,400$	50
5.1	Schematic of a multi-jet system with maximum crossflow orientation and indicated jet-to-crossflow interaction. Adopted from Weigand and Spring (2011)	53
5.2	Velocity and vorticity magnitude contours (xz -plane) in the channel centerline, $y=0$, at $Re_D=32,900$. CFD results from Fechter (2011)	54
5.3	Pressure loss parameters of the impingement channels for various Re_D	55
5.4	Jet axial exit velocity profiles for the inline pattern (y -direction)	57
5.5	Local jet discharge coefficients for various Reynolds numbers	57
5.6	Local jet massflow variation and crossflow development in the channel. Comparison with the model of Florschuetz et al. (1981)	58
5.7	Local jet massflow variation and crossflow development for various channel geometries using a one-dimensional model. $Re_D=32,900$	59
6.1	Crossflow effect on the local distribution of heat transfer coefficient (h/h_{ref}) for a channel with a small cross-sectional area. $h_{ref}=188W/(m^2K)$, $Re_D=19,200$	62
6.2	Heat transfer coefficient surface contours (h/h_{ref}) for all channel interior surfaces. $h_{ref}=197W/(m^2K)$, $Re_D=19,200$	63
6.3	Spanwise averaged Nu_D distributions for all channel interior walls. $Re_D=19,200$. $X/D=Y/D=5$, $Z/D=2$, $\Delta y/D=0$	63
6.4	Reynolds number effect on the local Nu_D distribution for channel centerline ($y=0$). $X/D=Y/D=5$, $\Delta y/D=0$	64
6.5	Local $Nu_D/Pr^{1/3}$ distributions divided by the Re_D to the power of 0.7 for the channel centerline ($y=0$). $X/D=Y/D=5$, $\Delta y/Y=0$	64
6.6	Heat transfer coefficient surface contours (h/h_{ref}) for different channel heights. For the target and jet plates: $h_{ref}=330$ and $240W/(m^2K)$, respectively. $Re_D=32,400$	66
6.7	Spanwise averaged Nu_D distributions for all channel walls and different channel heights. $X/D=Y/D=5$, $\Delta y/Y=0$, $Re_D=32,400$	66
6.8	Heat transfer coefficient surface contours (h/h_{ref}) for different channel widths. h_{ref} : $302W/(m^2K)$. X/D , $Z/D=1.5$, $\Delta y/Y=0.4$, $Re_D=32,400$	69
6.9	Local and spanwise averaged Nu_D distributions on the target for different channel widths. X/D , $Z/D=1.5$, $\Delta y/Y=0.4$, $Re_D=32,400$	69
6.10	Spanwise averaged Nu_D distributions for the upper and lower sidewall for different channel widths. X/D , $Z/D=1.5$, $\Delta y/Y=0.4$, $Re_D=32,400$	70
6.11	Heat transfer coefficient surface contours (h/h_{ref}) for different jet patterns. h_{ref} : $330W/(m^2K)$. $X/D=Y/D=5$, $Re_D=32,400$	71

6.12	Heat transfer coefficient surface contours (h/h_{ref}) for the jet plate. $h_{ref}: 240W/(m^2K)$. $X/D=Y/D=5, \Delta y/Y=0.4, Re_D=32,400$	71
6.13	Local Nu_D distributions on the target plate centerline ($y=0$) for various jet patterns. $X/D=Y/D=5, Re_D=32,400$	71
6.14	Spanwise averaged Nu_D for all channel walls. $X/D=Y/D=5, Re_D=32,400$	72
6.15	Heat transfer coefficient surface contours (h/h_{ref}) for different axial jet-to-jet spacings. $h_{ref}: 294W/(m^2K)$. $Re_D=32,400, Y/D=5, Z/D=2 \Delta y/D=0.4$	75
6.16	Streamwise averaged Nu_D distributions. $Y/D=5, \Delta y/Y=0.4, Re_D=32,400$	75
6.17	Schematic representation of the varying jet diameter test cases	76
6.18	Jet axial exit velocity profiles (y -direction)	77
6.19	Local jet discharge coefficients at $Re_D=23,780$	78
6.20	Local $Re_{D,j}$ variation and crossflow development (G_{cf}/G_j)	78
6.21	Heat transfer coefficient surface contours (h/h_{ref}) for the target plate and the sidewalls for various jet size patterns. $Re_D=23,780, X/D=Y/D=5$	80
6.22	Local Nu_D distributions in the centerline of the target plate for various jet size patterns. $Re_D=23,780, X/D=Y/D=5, h_{ref}=182W/(m^2K)$	80
6.23	Spanwise averaged Nu_D for the target plate and the sidewalls for various jet size patterns. $X/D=Y/D=5, Re_D=23,780$	81
6.24	Heat transfer coefficient surface contours (h/h_{ref}) for the jet plate for various jet size patterns. $Re_D=23,780, X/D=Y/D=5$	82
6.25	Spanwise averaged Nu_D for the jet plate. $X/D=Y/D=5, Re_D=32,400$	82
6.26	Row-by-row area averaged Nu_D . $Re_D=32,400, X/D=5, \Delta y/Y=0$	83
6.27	Row-by-row area averaged Nu_D for various configurations at $Re_D=32,400$	85
6.28	(a) Complete channel area averaged Nu_D as a function of channel flow area and (b) Sidewall vs target plate Nu_D for various Reynolds numbers. $\Delta y/Y=0.4$	86
6.29	Full channel area averaged Nu_D as a function of Re_D . $X/D=5$	87
6.30	Full channel area averaged Nu_D as a function of Re_D . $X/D=Y/D=5$	87
6.31	Thermal performance comparison of different impingement cooling scenarios	89
7.1	Experimental data compared with the empirical model of Florschuetz et al. (1981)	94
7.2	Schematic representation of the correlation flow domain	97
7.3	Evaluation of heat transfer correlation for the target plate	98
A.1	The impingement cooling test rig of EPFL-GTT, photo taken by <i>Sounas</i>	115
A.2	Isometric view of the heater grid consisting of four individual mesh layers	116
A.3	A single heater mesh layer	117
A.4	Necuron 700 flange	118
A.5	1 st copper bar electrode for electrical power supply	119
A.6	2 nd copper bar electrode for electrical power supply	120
A.7	Aluminium bars used to sandwich the heater along the complete flow path	121
A.8	Isometric view of the narrow impingement channel at $X/D=Y/D=5, Z/D=1.5$	122
A.9	Narrow impingement channel at $X/D=Y/D=5, Z/D=1.5$	123
A.10	Impingement plate for $X/D=Y/D=5, \Delta y/Y=0$	124
A.11	Target plate for $X/D=Y/D=5, \Delta y/Y=0$	125
A.12	Sidewall in the streamwise direction for $X/D=5, Z/D=1.5$	126

A.13	Sidewall in the spanwise direction for $Y/D=5$, $Z/D=1.5$	127
B.1	Subtraction operation for one image of the video and green colour determination . .	129
B.2	Hue and green intensity evolution for a given pixel during the transient experiment .	130
B.3	Detection time of liquid crystal at a pixel size level. $X/D=Y/D=5$, $Z/D=1.5$	130
B.4	Comparison between the hue and the maximum green intensity method for the evaluation of local heat transfer coefficients. $X/D=Y/D=5$, $Z/D=1$, $Re_D=32,900$	131
C.1	Heat transfer coefficient surface contours (h/h_{ref}). $X/D=Y/D=5$, $Z/D=1$	133
C.2	Thermocouple time constant effect on the spanwise averaged Nu_D distributions. $X/D=Y/D=5$, $Z/D=1.5$	134
D.1	Continuous injection (left) and discrete hole injection (right) models. Figure adopted from Florschuetz et al. (1981)	135
E.1	Local variation of exponent m for various impingement channel geometries	137
F.1	Surface contours of h/h_{ref} at $Re_D=10,900$. $h_{ref}=139W/(m^2K)$	140
F.2	Spanwise averaged $Nu_D/(Re_D^{0.7}Pr^{1/3})$ distributions at $Re_D=10,900$	140
F.3	Surface contours of h/h_{ref} at $Re_D=19,200$. $h_{ref}=207W/(m^2K)$	141
F.4	Spanwise averaged $Nu_D/(Re_D^{0.7}Pr^{1/3})$ distributions at $Re_D=19,200$	141
F.5	Surface contours of h/h_{ref} at $Re_D=32,400$. $h_{ref}=395W/(m^2K)$	142
F.6	Spanwise averaged $Nu_D/(Re_D^{0.7}Pr^{1/3})$ distributions at $Re_D=32,400$	142
F.7	Surface contours of h/h_{ref} at $Re_D=45,850$. $h_{ref}=100W/(m^2K)$	143
F.8	Spanwise averaged $Nu_D/(Re_D^{0.7}Pr^{1/3})$ distributions at $Re_D=45,850$	143
F.9	Surface contours of h/h_{ref} at $Re_D=63,850$. $h_{ref}=477W/(m^2K)$	144
F.10	Spanwise averaged $Nu_D/(Re_D^{0.7}Pr^{1/3})$ distributions at $Re_D=63,850$	144
F.11	Surface contours of h/h_{ref} at $Re_D=85,900$. $h_{ref}=616W/(m^2K)$	145
F.12	Spanwise averaged $Nu_D/(Re_D^{0.7}Pr^{1/3})$ distributions at $Re_D=85,900$	145
F.13	Surface contours of h/h_{ref} various Reynolds numbers. $h_{ref}=132, 197$ and $386W/(m^2K)$ for $Re_D=10,900, 32,400$ and $45,850$ respectively.	146
F.14	Spanwise averaged $Nu_D/(Re_D^{0.7}Pr^{1/3})$ distributions	146

LIST OF TABLES

2.1	Summary of relevant previous studies	19
3.1	Summary of investigated narrow impingement channel geometries	31
4.1	K-type thermocouple thermal properties and dimensions	45
4.2	Experimental uncertainties	50
6.1	Geometrical characteristics of the investigated varying jet diameter cases	77
7.1	Summary of investigated narrow impingement channel geometries	95
7.2	Exponent m and coefficient C statistics	96
7.3	Exponent m values reported in the literature	96
7.4	Basic correlation coefficients	98
7.5	Hole offset position coefficients	98

NOMENCLATURE

Roman Symbols

Symbol and description	Units
\dot{m} massflow rate, $\rho U A$	kg/s
\dot{q} heat flux	W/m^2
A_f open area, $\frac{\pi}{4}(D/X)(D/Y)$	–
C_D discharge coefficient	–
c_p specific heat	$J/(kgK)$
D jet diameter	m
G mass velocity, ρU	$kg/(m^2s)$
h heat transfer coefficient	$W/(m^2K)$
I electrical current	A
k thermal conductivity	$W/(mK)$
L length of impingement hole	m
m exponent of Reynolds number	–
n number of impingement holes	–
Nu Nusselt number	–
P uncertainty level	%
p static pressure	Pa
Pr Prandtl number	–
R electrical resistance	Ωhm
r radial distance from stagnation point	m

Nomenclature

Nomenclature

Re	Reynolds number, Ux/ν	–
T	temperature	K
t	time	s
TP	thermal performance	–
U	velocity	m/s
X	axial jet-to-jet spacing	m
x,y,z	coordinate system	–
Y	channel width	m
Z	separation distance (channel height)	m

Greek Symbols

Symbol and description	Units
α thermal diffusivity, $k/(\rho c_P)$	m^2/s
β parameter used in Florschuetz's model	–
Δy jet offset position	m
ϵ overall cooling effectiveness, $(T_g - T_m)/(T_g - T_c)$	–
μ dynamic viscosity	$kg/(ms)$
ρ density	kg/m^3
τ_c thermocouple time constant	s
θ non-dimensional temperature, $(T - T_o)/(T_g - T_o)$	–
ν kinematic viscosity	m^2/s

Subscripts

Symbol and description
∞ freestream conditions
cf crossflow
g hot gas conditions
G_{max} green hue/intensity
j local jet position

<i>jct</i>	thermocouple junction
<i>LC</i>	liquid crystals
<i>m</i>	heater mesh
<i>o</i>	initial conditions
<i>ref</i>	reference case
<i>s</i>	stagnation point
<i>w</i>	thermocouple wire

Acronyms and Abbreviations

Description

<i>CFD</i>	Computational Fluid Dynamics
<i>OPR</i>	Overall Pressure Ratio
<i>RSS</i>	Root Sum Square
<i>SFC</i>	Specific Fuel Consumption
<i>TET</i>	Turbine Entry/Inlet Temperature
<i>TLC</i>	Thermochromic Liquid Crystals

INTRODUCTION

An introduction about gas turbine engines and the associated cooling technologies is given in this chapter. The evolution of gas turbine operating conditions over the last 60 years is presented describing also the turbine blade cooling problem. Particular emphasis is given in the modern trends of gas turbine cooling technology research introducing double-wall cooling configurations and narrow impingement cooling channels.

1.1 The Gas Turbine Engine

The gas turbine is an internal combustion engine that is extensively used for aircraft or marine propulsion, land-based power generation and other industrial applications, due to the capability of producing very large amounts of useful power depending on its size and weight. Additionally, the possibility of firing with multiple fuels such as natural gas, kerosine, diesel fuel, bio-fuels, methane and other fuels, ensures flexibility to the demands of the potential fuel market establishing the gas turbine engine as a very attractive energy conversion device.

Gas turbine operation is based on *Brayton* thermodynamic cycle where ambient air is compressed (ideally isentropic process) and then runs through a mixing chamber where fuel is added (ideally isobaric process). The pressurised heated air and fuel mixture is then ignited in an expansion cylinder and energy is released, causing the heated air and combustion products to expand in a turbine (ideally isentropic process). The turbine exhaust gases can be then either used to drive a power free turbine (i.e. electricity production) or accelerated in a nozzle producing thrust (i.e. aircraft propulsion). An example of a gas turbine with sequential combustion technology (Alstom GT26) and the corresponding thermodynamic cycle are shown in Figure 1.1. In this industrial gas turbine, additional fuel is injected downstream of the high pressure turbine stage increasing further the performance and the efficiency of the engine.

1.2 Historical Aspects

The gas turbine engine is undoubtedly one of the most important inventions of the 20th century. However, the claim to the invention is a highly controversial issue that has to date never been resolved. The meaning of the word *turbine*, traces its history in ancient years where Hero of

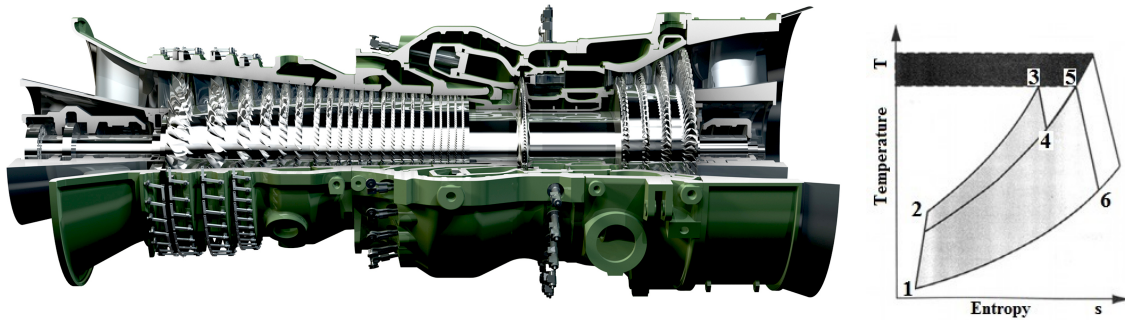


Figure 1.1: GT-26 industrial gas turbine. Image courtesy of ALSTOM

Alexandria (10-70AD) developed a device named *Aeolipile*. Although the machine was not able to produce useful work, it demonstrated the result of accelerating steam jets through nozzles causing a bronze sphere in a rotational movement. The idea of a thermodynamic cycle similar to the modern gas turbines was proposed by John Barber (UK) in 1791, who patented a design that contained the basic components of a modern gas turbine engine. Of course, history has recored a substantial number of designs, trials and attempts of producing gas turbines, as for example Rene Armengaud and Charles Lemale (France) in 1903 and Franz Stolze (Germany) in 1904 who successfully tested experimental gas turbines with centrifugal and axial flow turbomachines, respectively. However, the history of gas turbine as a viable energy conversion device started in 1928, where Frank Whittle (UK) received an award for his patent on jet engine propulsion. He reported that the exhaust gases from the gas turbine could be used, instead of propellers, in order to propel the aircraft, envisaging flying speeds in the order of 500mph at a time where typical airplanes could not reach 200mph (Pugh, 2001). This potential was a direct consequence of the very large amount of useful power that a gas turbine could produce compared to any reciprocating engine of that period. The first successful static test of Whittle's engine performed in April 1937 providing a thrust of 4.44kN and an efficiency of 14%. At the same period, Hans von Ohain, a German engineer acting independently from Whittle's team in UK, designed and successfully produced the first all jet engine (Heinkel HeS 1), which powered the first jet aircraft in history (Heinkel He 178) in August 1939. The same year, Brown Boveri Company introduced the first industrial gas turbine in history which installed for electricity production in a public power station in Neuchâtel, Switzerland (1939). This included a 4MW power system where the turbine provided power of 15.4MW , of which 11.4MW was absorbed by the compressor. The operating conditions included a turbine inlet temperature of 538°C , a pressure ratio of 4.2 and an overall thermal efficiency of 17.4% (Hunt, 2011).

Apparently, very early in the 20th century, the concept of the gas turbine engine became world-widely known to many engineers and it was quickly recognised that this technological concept had a huge potential being limited only by the state of art of the associated technologies and the materials available at that period. These prospects were based on raising turbine inlet temperatures of the Neuchâtel gas turbine from 538°C , which was absolutely safe for the uncooled turbine blades made of the available heat resisting steel, to 650°C improving the cycle efficiency by 28% (from 18% to 23%). Additionally many engineers at that period could foresee the prospect of turbine inlet temperature being increased to above 800°C taking advantage of the improvements in material science coming in the near future or the cooling of the hot section components, i.e. turbine blades, where the first concepts of cooling architectures have been patented in early '40s (!), e.g. Mayer (1941).

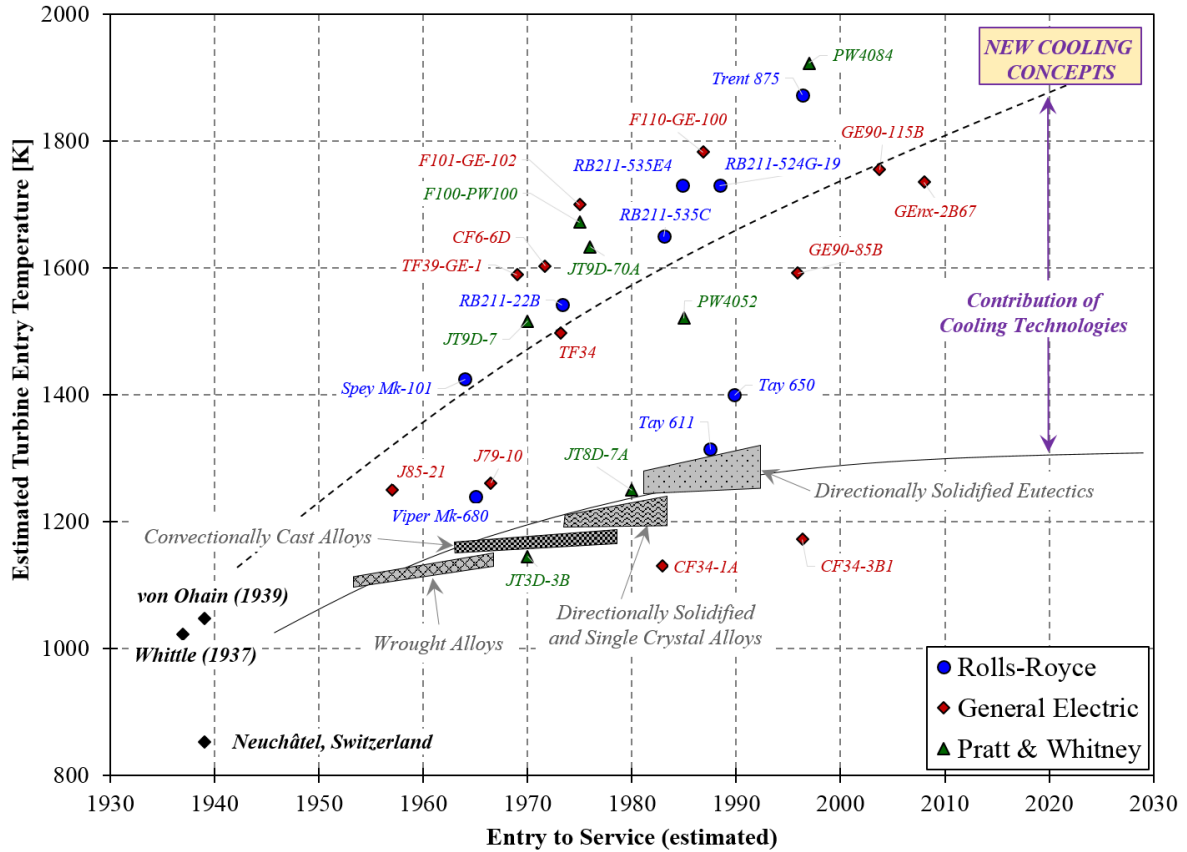


Figure 1.2: Evolution of Turbine Entry Temperature (TET) for aero-engines

1.3 The Gas Turbine Cooling Problem

Over the last 50 years, the gas turbine engine has been established as the most important means of high speed aircraft propulsion and power generation. Therefore, gas turbine engine manufacturers, in order to survive in the highly competitive world of engine market, are making great efforts to reduce the engine operating costs. For this reason, the fuel efficiency of the engine is of vital importance and all major companies are involved in extensive research into ways of improving this quantity. It is also well established, since the development of the first gas turbines, that the overall engine performance, meaning increased power output and reduced specific fuel consumption (SFC) and emissions (NO_x), is primarily affected and increased by increasing the combustion firing temperature, which affects the turbine entry temperature (TET), and the overall engine pressure ratio (OPR), which in turn affects the compressor delivery temperature (combustion chamber inlet temperature). The evolution of these key design parameters over the last 60 years are presented in Figures 1.2, 1.3 and 1.4, for three worldwide known aero-engine manufacturers. The data have been collected from various sources, including technical specification websites ([here](#)), aero-engine catalogs ([here](#)), company newsletters and calculations made by the author of this thesis. However, it should be noticed that TET is a highly confidential number being repressed by engine manufacturers and the values indicated are estimated.

Figure 1.2 shows that improvements in material technology, from simple wrought alloys and conventionally castings, to directionally solidified and single crystal superalloys, have allowed an increase of the maximum allowable blade metal temperature by only 350K over the last 60 years. The importance of this increase, however, can be appreciated by noting that a small increase of

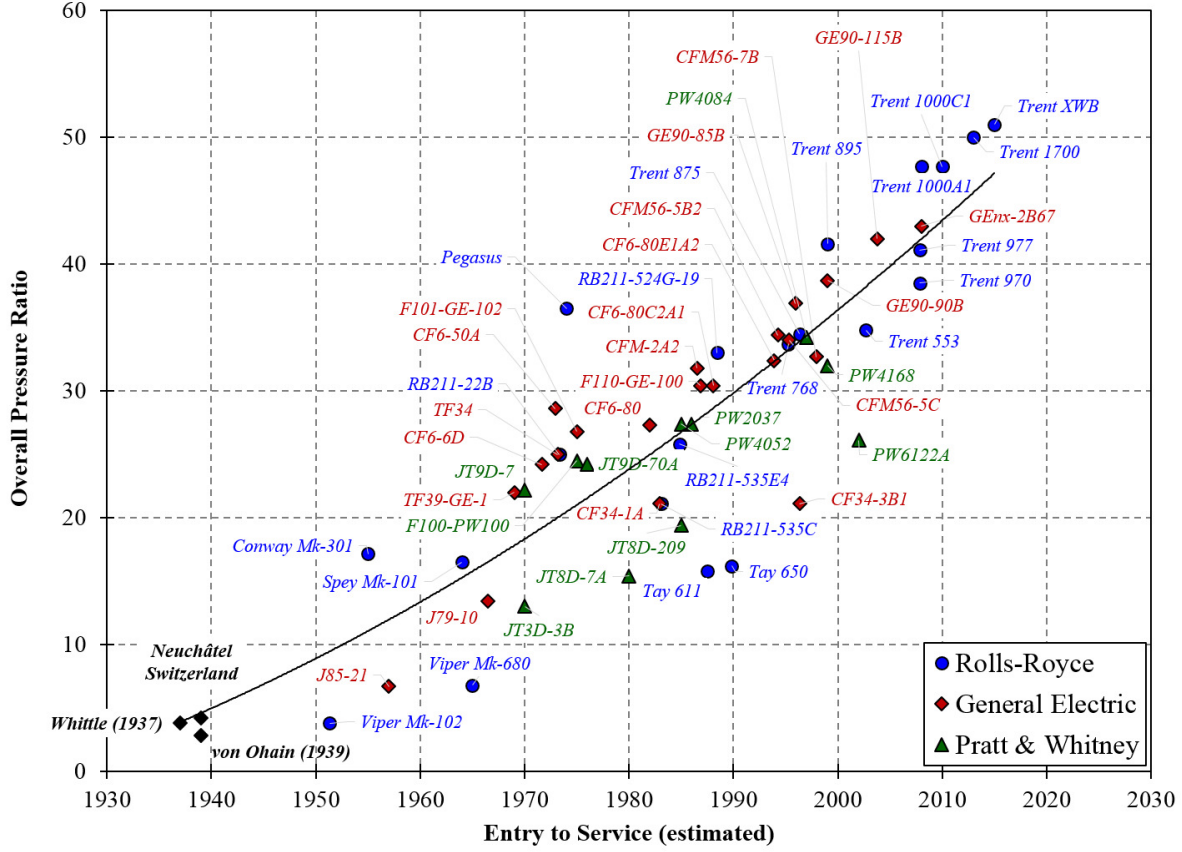


Figure 1.3: Evolution of compression Overall Pressure Ratio (OPR) for aero-engines

50K in turbine firing temperature can provide a corresponding increase of 8-9% in power output and 2-4% improvement in cycle efficiency. On the other hand, the evolution of turbine entry temperatures, shows that TET values are far above the acceptable material limit, and hence the melting point of the current material technology, and it will approach values of 2000K in the near future. Therefore, the majority of the existent gas turbines are equipped with turbine cooling systems in order to run safely at elevated temperatures, increasing also the operating life of the hot section components. As a result, the difference between the overall trend of turbine inlet temperature and the trendline of the maximum allowable blade metal temperature, it is actually the contribution of cooling technologies, which as shown in Figure 1.2, is continuously increased due to the development of more advanced cooling architectures.

The cooling air is usually taken from the compressor exit, so that the air has adequate pressure in order to make the cooling process possible, and it is directed to the turbine vanes and blades. The overall efficiency of the cooling system can be expressed in terms of a cooling effectiveness given by:

$$\epsilon = \frac{T_{gas} - T_{blade}}{T_{gas} - T_{coolant}} \quad (1.1)$$

which actually means that the compressor delivery temperature ($T_{coolant}$) plays an important role in the efficiency of a cooling system. This parameter is a measure of how well the coolant temperature potential is used to reduce the wall temperature in respect to the hot gas mainstream. Meanwhile, in order to increase engine performance, the compressor pressure ratio has been increased from about 10 to above 50, as shown by Figure 1.3. Considering also a polytropic efficiency for the compression of about 0.75 and 0.9 for 1960 and 2010, respectively, an increase

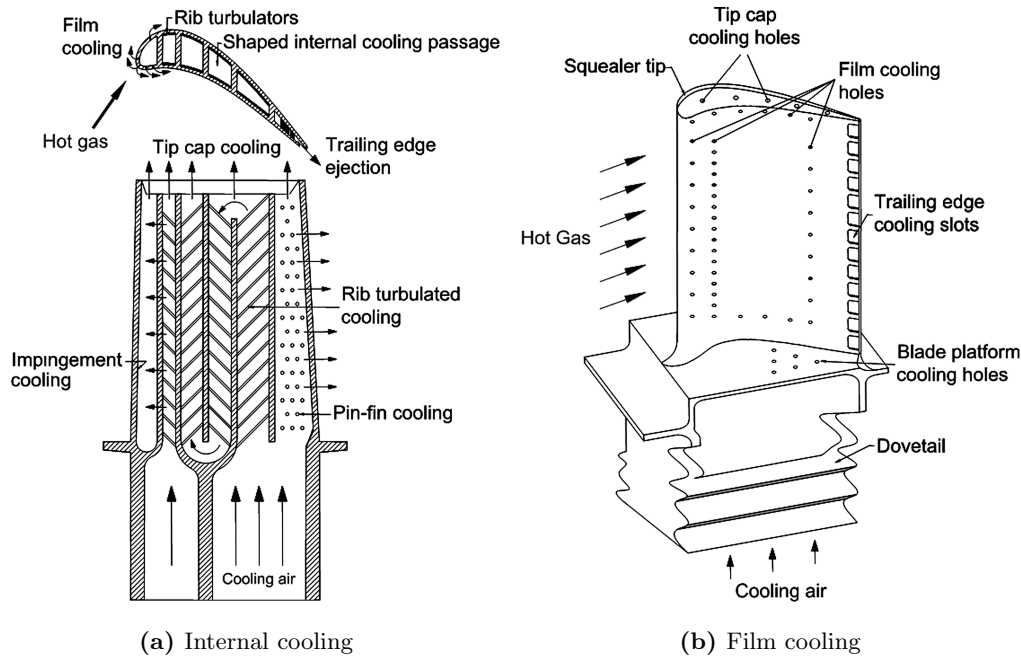


Figure 1.5: Schematic representation of turbine blade cooling. Adopted from Han (2013)

gases. Within the passages, enhanced internal convection coefficients can be achieved using rib-roughened cooling ducts or pin-fin array configurations as shown in Figure 1.5(a). Impingement cooling is also applicable at critical regions where high heat transfer rates are required, as for example the leading edge of nozzle guide vanes. A review for heat transfer augmentation technologies for internal cooling can be found in Ligrani (2013). In turbine blade external cooling, also called as *film cooling*, relatively cold air is injected from the inside of the blade to the outside blade metal surface forming a protective thin film cooling layer between the metal and the hot gas mainstream. Film cooling is very efficient allowing higher turbine inlet temperatures, however, at the expense of aerodynamic penalties due to the interaction between the injected air with the main flow. Of course, an efficient cooling system is achieved by combining internal and external cooling, and in many cases depends on the customer's needs, i.e. civil or military applications.

1.4.2 Improvement of casting technologies

At this point, one can clearly appreciate the improvement of turbine cooling technologies, since their introduction in service at late 1950s, by a quick calculation of the overall cooling effectiveness from Eq. 1.1. Considering values from the data presented in Figures 1.2 and 1.4, it can be easily obtained that ϵ has been increased from about 0.35 in 1960, aiming to values above 0.65 in the near future indicating the tremendous improvement of cooling architectures, mainly thanks to the development of the casting technologies.

It is widely accepted that the capabilities of the foundry industry to produce high integrity and dimensionally accurate castings is very largely due to the demands of the gas turbine engine. Castings are extensively used in gas turbines for economic as well as design purposes since investment casting is the only feasible way of producing the intricate cooling passages inside the turbine vanes and blades with high integrity and dimensional control. For example, the thickness of thin sections such as trailing edge airfoils can be produced with an accuracy up to $\pm 0.05\text{mm}$ while film or impingement cooling holes of less than 0.8mm diameter have been produced nowadays

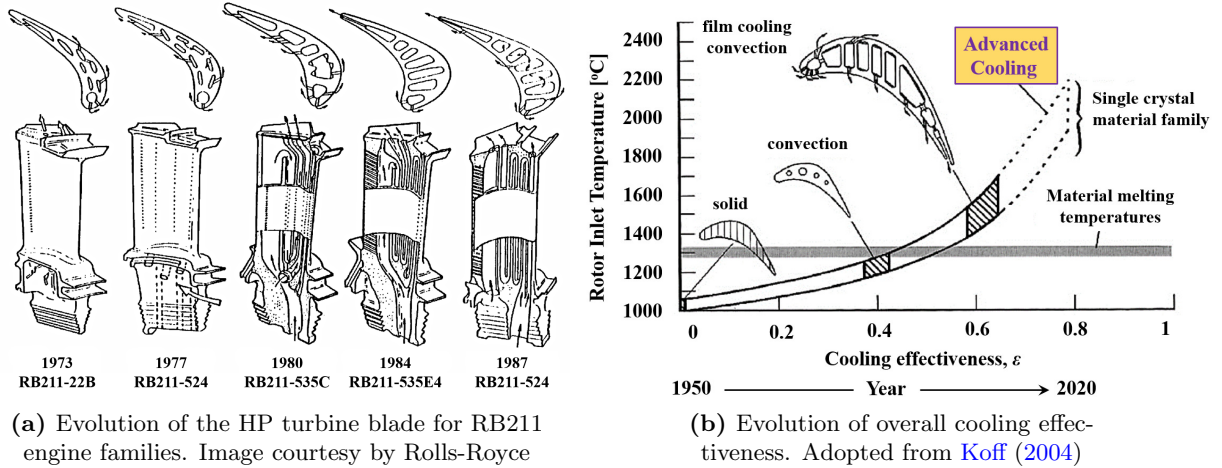


Figure 1.6: Effect of the development of casting techniques on blade cooling architectures

(Meetham, 1981). Moreover, the possibility of producing multi-element superalloys, increasing further the strength and oxidation resistance over the encountered temperature range, is also a great advantage of casting processes.

An example of the improvement of casting techniques is illustrated in Figure 1.6(a) which shows the evolution of the high pressure rotor blade for the RB-211 (Rolls-Royce) engine families. It is clearly observed that the shape of the blade becomes more complex, and hence, more advanced cooling architectures have been applied given their manufacturing feasibility, improving the overall capabilities of the cooling systems. The evolution of the overall cooling effectiveness is indicated in Figure 1.6(b). As the turbine blade cooling systems continue to develop, higher engine firing temperatures are continuously applied. Therefore, the development of more sophisticated turbine blade cooling architectures are of prime importance for the design of future gas turbines.

1.4.3 Wall-integrated cooling technologies

Nowadays, further increase of turbine inlet temperatures is limited by the capabilities of the current cooling technologies (shaped film cooling holes and thermal barrier coatings) which approach their limits as discussed in the review study of Bunker (2007). On the other hand, internal cooling becomes increasingly important since the performance losses caused by film cooling injection (Hartsel losses), described in Hartsel (1972), dictates limited usage of external cooling in future turbine systems. Therefore, new concepts and more advanced internal cooling techniques have to be considered.

Recent developments in soluble core and composite casting have allowed very intricate internal passages to be manufactured. Composite casting refers to a large number of processes in which molten metal is cast on to a solid metal component, so that the two subsequently form one integral unit. This double-wall configuration is composed of an outer airfoil skin and an inner support wall that are metallurgically bonded to one another. The space between the double walls forms a passage for coolant flowing closely adjacent to the airfoil skin. This has opened up the possibility of casting small cooling cavities of relatively low aspect ratio inside the external wall of turbine airfoils. The production of integrally cast turbine airfoils is therefore manufacturing feasible resulting in a *double-wall* configuration, as shown in the patent of Alstom in Figure 1.7.

Integrally cast turbine airfoils include a more distributed form of cooling, where the coolant

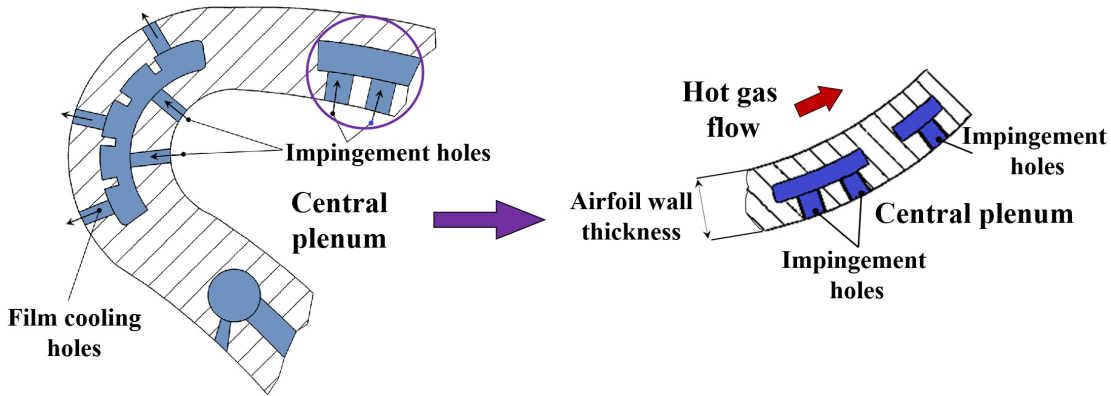


Figure 1.7: Wall-integrated narrow cooling cavities in a turbine airfoil. Left figure adopted from [Lutum et al. \(2002\)](#)

flows in narrow cavities within the wall rather than the hollow of the airfoil, and thus increasing the wetted heat transfer area. [Chyu and Alvin \(2010\)](#) evaluated numerically, under realistic engine conditions, that at a given cooling flow rate double-wall cooling technologies significantly reduce blade metal temperatures (up to $100K$) while the reduction is highly dependent on the level of internal heat transfer coefficients. Inside of such narrow cavities, heat transfer coefficients can be substantially increased using various area enhancers ([Bunker et al., 2004](#); [Ligrani, 2013](#)), small pre-film impingement chambers ([Gillespie et al., 1998](#)), high crossflow impingement passages ([Chambers et al., 2005](#)) or even small impingement configurations ([Terzis et al., 2014](#)). Regarding the latter case, narrow impingement channels with relatively low crossflow can be produced consisting of single or doubled rows of impingement holes as shown in the right side of Figure 1.7. A turbine airfoil can include a plurality of such impingement channels in the spanwise direction ensuring homogenous distribution of the material temperature.

Such wall-integrated designs offer several practical advantages:

- The reduced external wall-thickness of the airfoil results in increased heat conduction capabilities between the internal coolant flow and the external hot gas flow.
- Additional heat transfer surface is provided which is in good thermal contact with the heated sections as the cooling airflow is restricted only to the hot walls.
- There is an obvious improvement in the thermal coupling between external and internal impingement surfaces, all of which now contribute to the external cooling (target plate, sidewalls and impingement plate).
- The jet issuing plate is cast into the structure of the airfoil, and hence, it is not subjected to vibrational problems. This allows deployment of such impingement channels in rotating components, i.e. turbine blades, due to the improved structural integrity.

1.5 The Current Experimental Study

Within a turbine vane or blade, the coolant flow through the narrow impingement passage is relatively complex, and hence, it is very difficult to predict accurately using numerical tools, the distributions of local heat transfer coefficients. On the other hand, precise thermal models require detailed knowledge of the convective boundary conditions in all heat transfer surfaces of

the blading in order to ensure reliable blade metal temperature predictions. As a result, turbine airfoil designers base their blade cooling modelling calculations on experimental results and empirical correlations obtained in laboratories at engine representative flow conditions.

Contrary to multi-array impingement configurations, a detailed review can be found in the study of [Weigand and Spring \(2011\)](#), very few studies focused on the experimental evaluation of narrow impingement channels, with limited information for the sidewalls and the jet issuing plate which significantly confines the overall geometry. Therefore, the main objective of this thesis is the:

Experimental evaluation and detailed analyses of the local heat transfer distributions for all internal surfaces of narrow impingement channels consisting of a single row of five holes, investigating effects of various channel geometrical factors and correlating the data in an empirical model valid over a wide range of engine representative Reynolds numbers.

The present experimental study has used relatively large scale models of an idealised narrow impingement passage to provide an understanding of the convection heat transfer coefficients in a real part of a turbine blade. All the heat transfer experiments were performed at engine representative Reynolds numbers so that the resulted Nusselt numbers are directly applicable to the engine cooling channels. Given the use of large scale models, the influence of Mach number at the required flow conditions was assumed negligible, as shown by [Park et al. \(2007\)](#), and therefore, no attempt was made to simulate this dimensionless group for compressibility effects. Spatially resolved heat transfer coefficient distributions were obtained using the transient liquid crystal technique, which finds great applicability in turbomachinery applications over the last 20 years.

Due to the lack of available data in the literature for this kind of application, the results of this thesis significantly contribute to the development of integrally cast turbine blade thermal design models since they contain detailed information for all the internal impingement surfaces. The experimentally obtained heat transfer coefficients can be then used along with the external heat load to predict blade metal temperatures. Effects of various geometrical factors, such as axial jet-to-jet spacing, passage width and height, and hole offset position from the channel centerline or the use of varying jet diameters could play an important role on the distribution of convection coefficients, and hence, on the homogeneity of blade metal temperatures. Of course, another contribution of this work is that validation of computational analysis tools, i.e. CFD, can be carried out based on high resolved experimental data obtained in this thesis.

1.6 The Structure of the Thesis

The literature survey carried out in the course of this study is presented in Chapter 2, which summarises the heat transfer characteristics of single and multi-jet impingement configurations containing also industrial examples for in-wall cooling technologies. In Chapter 3 the experimental arrangement including the specifications and the manufacturing procedures applied to construct the impingement cooling test rig are being described in detail. Chapter 4 addresses the experimental methods used for the evaluation of local convection coefficients. The transient liquid crystal technique, which considers also thermocouple thermal inertia effects, is presented including also an uncertainty analysis for the heat transfer results. The flow distributions, supported by some numerical results, are described in Chapter 5. This chapter contains also pressure

probe traversing measurements carried out to evaluate local jet massflow distributions and local jet discharge coefficients. The experimental heat transfer distributions inside the narrow impingement channels are analysed by various post-processing procedures in Chapter 6 and correlated in Chapter 7. The thesis is concluded with Chapter 8 where an overall discussion of the results is given. This chapter contains the conclusions of the study concerning the heat transfer capabilities of the narrow impingement channels as well as recommendations for further research activities.

LITERATURE REVIEW

This chapter presents a large part of the literature review employed in the course of this study. First, an introduction about single and multi-jet impingement heat transfer is presented. Then, double-wall cooling configurations are demonstrated with real turbine airfoil profiles and several studies focused on narrow impingement channels are reviewed. The chapter concludes with the main contributions of this thesis in the current state of literature.

2.1 Introduction

Among many convection transport processes, jet impingement is a particularly attractive cooling mechanism due to the very high local heat transfer rates that can be achieved in the stagnation zones. Impingement jets are used over a wide range of engineering applications for reasons of thermal management, as for example in the cooling of turbine blades and vanes, drying technologies and temperature control of electronic equipment. For gas turbine engines, apart from the very high convection coefficients, another advantage of impingement cooling is the relatively low manufacturing cost compared with other cooling technologies, i.e. film cooling. Nevertheless, it should be noticed that the construction of this flow arrangement weakens the material strength, and therefore, impingement cooling was mainly used in static components and critical regions where thermal loads are excessively high, i.e. nozzle guide vanes (NGVs). However, the integral casting of holed impingement surfaces, which is now possible through advanced manufacturing technologies, increases the structural integrity of investment castings, extending also their usage in rotating components.

2.2 Jet Impingement Heat Transfer

2.2.1 Single jet

Jet impingement provides high local heat transfer coefficients due to the very small thickness of the developed boundary layer around the stagnation zone and at a certain radial distance from the stagnation point. Therefore, the heat exchange between the fluid and the wall is enhanced considering that the hydrodynamic and the thermal boundary layers are dynamically similar.

The main flow and heat transfer characteristics of a baseline geometry with a single jet

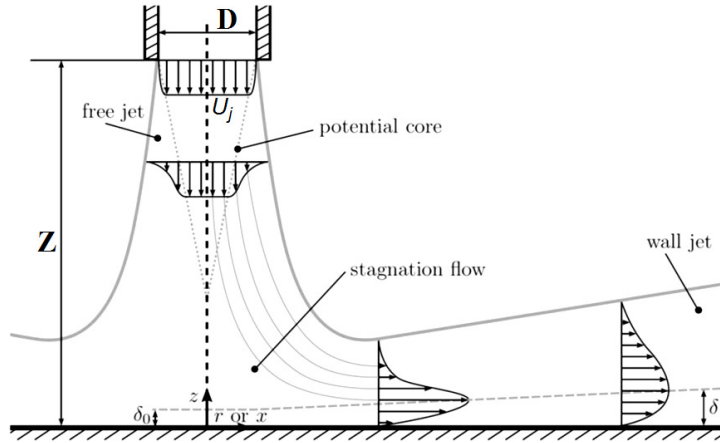


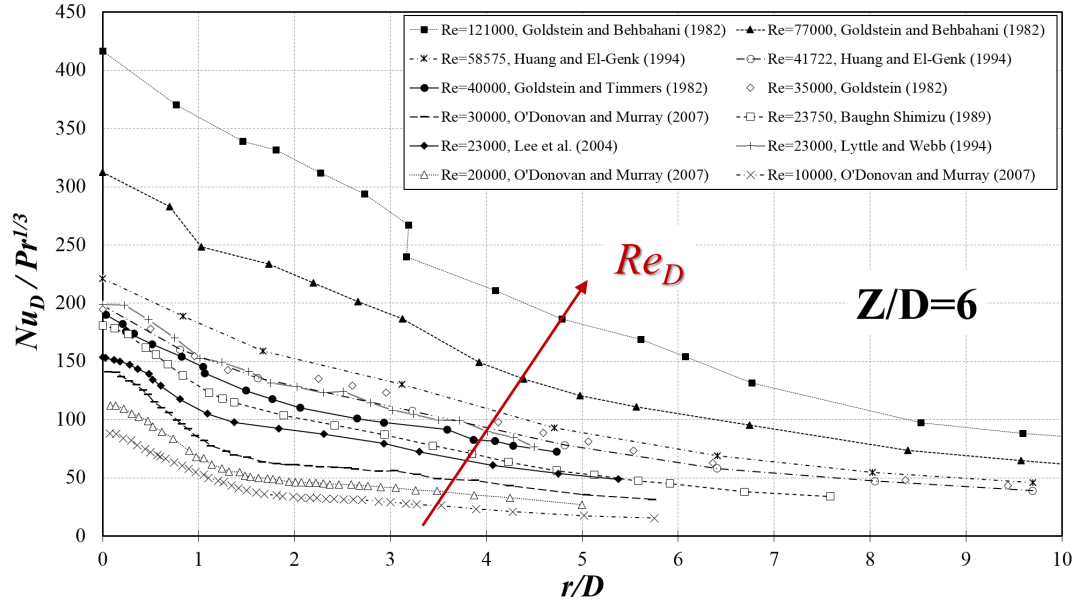
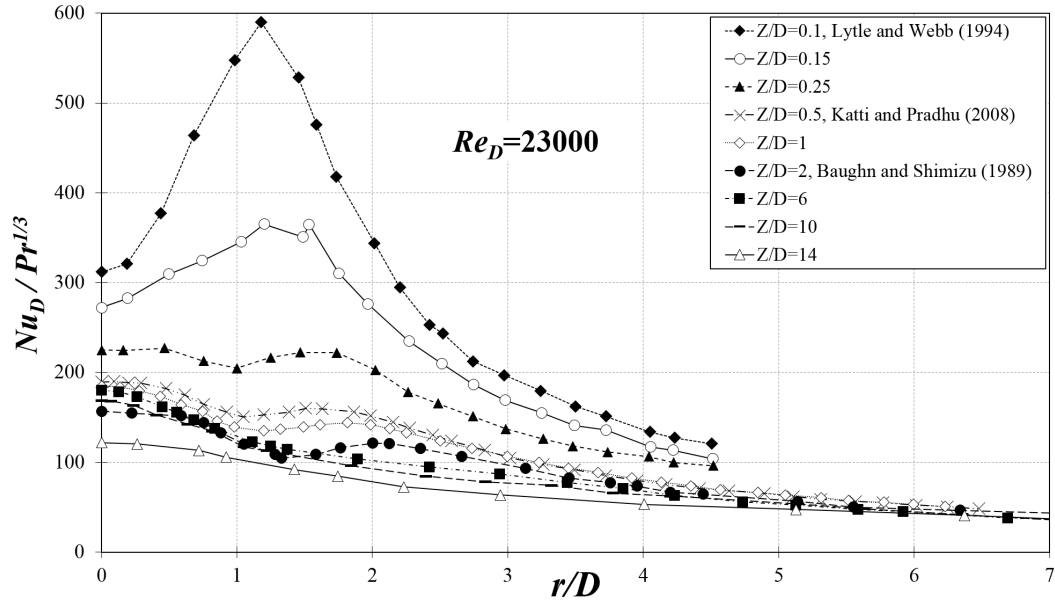
Figure 2.1: Flow regions for a single impinging free jet. After Weigand and Spring (2011)

impinging onto a flat surface is very well documented in the literature in a variety of configurations, and review studies can be found in Martin (1977), Jambunathan et al. (1992) and Viskanta (1993). Therefore, there is no particular need to be repeated here and only an introduction about some fundamental aerodynamic concepts and terminology will be given for future reference. A schematic representation of the flow characteristics of a single impinging jet is illustrated in Figure 2.1, which shows that the free jet creates a stagnation region under the nozzle exit and retains the nozzle exit velocity magnitude in its potential core. Generally, potential core is extended about $5D$ to $7D$ as the free jet is developed depending on the design shape of the nozzle. After impingement with the opposite wall, commonly known as target plate, the jet is accelerated in the radial direction reaching a maximum velocity at about $1D$ from the stagnation point. In this region, a very thin laminar boundary layer starts to develop which turns to turbulent in the wall jet region starting at about $2D$ from the stagnation point. The strong aerodynamic and thermal interaction that exists between the jet and the target plate greatly affects the local heat transfer distributions over the exposed surface.

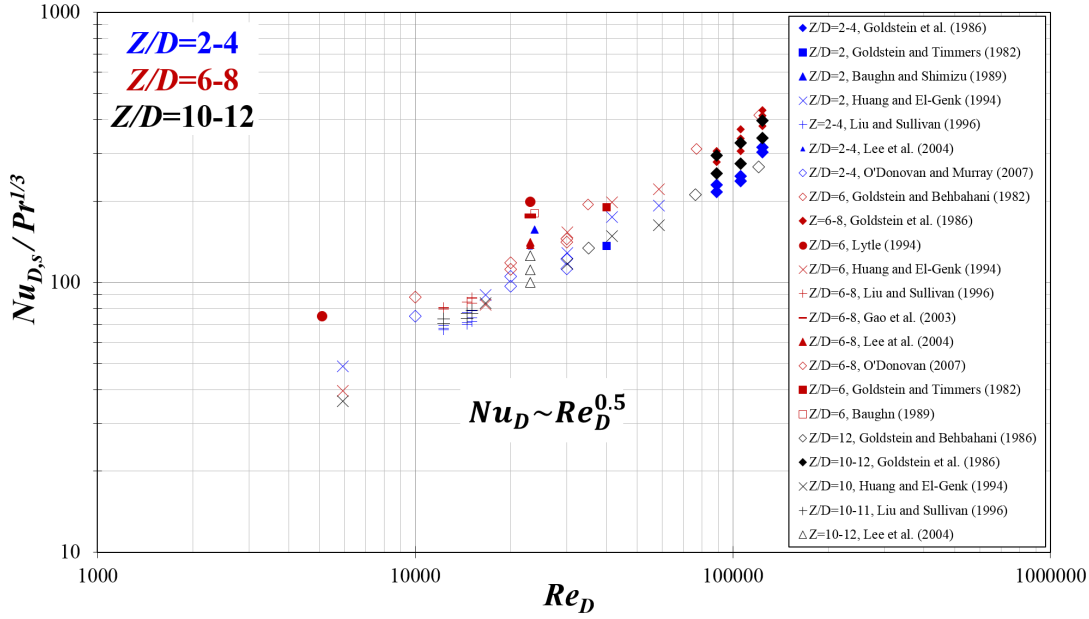
The results of jet impingement heat transfer research concluded a power-law relating heat transfer levels and flow conditions ($Nu \sim Re^m$), i.e. Goldstein et al. (1986), where typical values of exponent m are varied between 0.5 for laminar-stagnation point regions and 0.8 for turbulent-jet wake regions (Zhou and Ma, 2006). Additionally, a considerable effect of jet-to-target plate distances (Z/D) on the level and distribution of convection coefficients is also observed, especially for free impinging jets, i.e. Baughn and Shimizu (1989). Stagnation point heat transfer is maximised when the target surface is placed at the end of jet potential core ($Z/D \sim 5-7$) and secondary peaks of heat transfer appear at a certain radial distance ($r/D \sim 2$), when $Z/D \leq 2$. Obviously, the local heat transfer distribution is a direct consequence of the resulting flow field, which is characterised by a spectrum of vortical structures and strong recirculation zones, as shown by smoke flow visualisation experiments (Popiel and Trass, 1991).

The above discussed trends are presented in detail in Figures 2.2 and 2.3. These figures include experimental data collected from a vast number of literature sources, e.g. Goldstein and Behbahani (1982); Kataoka (1985); Goldstein et al. (1986); Baughn and Shimizu (1989); Van Der Meer (1991); Liu et al. (1993); Mohanty and Tawfek (1993); Lytle and Webb (1994); Huang and El-Genk (1994); Angioletti et al. (2003); Gao et al. (2003); Lee et al. (2004); O'Donovan and Murray (2007); Katti and Prabhu (2008b).

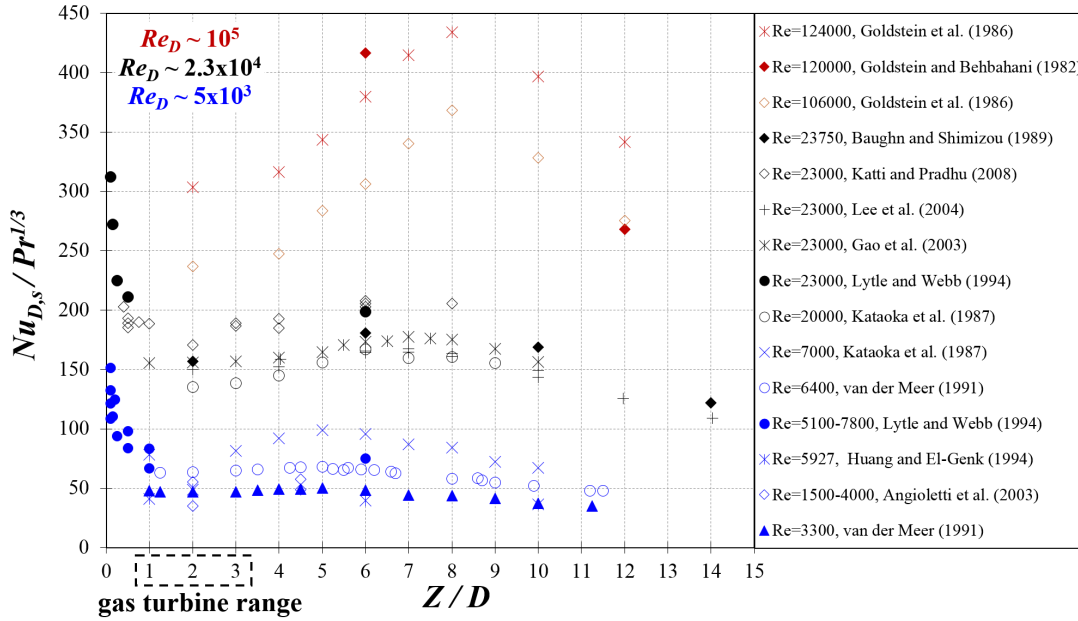
Figure 2.2(a) shows the local Nusselt number distribution at $Z/D=6$ over a wide range of

(a) Effect of Reynolds number, Re_D (b) Effect of separation distance, Z/D **Figure 2.2:** Radial distribution of Nu_D for various Z/D and Re_D

Reynolds numbers. A local heat transfer maximum is achieved at the stagnation point and a sharp reduction of $Nu_D / Pr^{1/3}$ is observed as r/D , and hence the thickness of the boundary layer, is increased. However, for low jet-to-target plate distances, a secondary peak of heat transfer appears at about $r/D \sim 1.5$. Note that the intensity of the secondary peak is increased with reducing Z/D and may exceed the stagnation point heat transfer if $Z/D \leq 0.5$. The stagnation point $Nu_{D,s}$ as a function of Re_D is illustrated Figure 2.3(a), which clearly shows the power law dependence where the exponent of Reynolds number is 0.5 following correlations for laminar flows. The effect of Z/D , shown in 2.3(b), indicates that stagnation point Nusselt number is maximised at the end of the jet potential core, at about $Z/D=6$ for $Z/D \geq 1$. On the other hand, if $Z/D \leq 1$, a sharp increase of $Nu_{D,s}$ is observed. Similar trends are noticed over a range of Re_D varied from about 5,000 to 100,000. Note also that the typical range of separation distances



(a) Effect of Reynolds number, Re_D



(b) Effect of separation distance, Z/D

Figure 2.3: Stagnation point $Nu_{D,s}$ as a function of Re_D and Z/D

for real gas turbine airfoils varies between $Z/D=1$ and 3, especially for the double-wall cooling configurations presented in Section 2.3, where the small external wall thickness of the airfoil dictates narrow and relatively short cooling cavities. Within this range, as shown by Figure 2.3(b), stagnation point heat transfer remains approximately at the same as there is no space in order to allow the development of the jet potential core.

2.2.2 Jet arrays

The main difference between a single jet and a multi-jet configuration impinging onto a flat surface is the interaction between the adjacent jets for the latter case. The strength of this interaction depends on the geometrical characteristics of the jet array, i.e. jet-to-jet streamwise

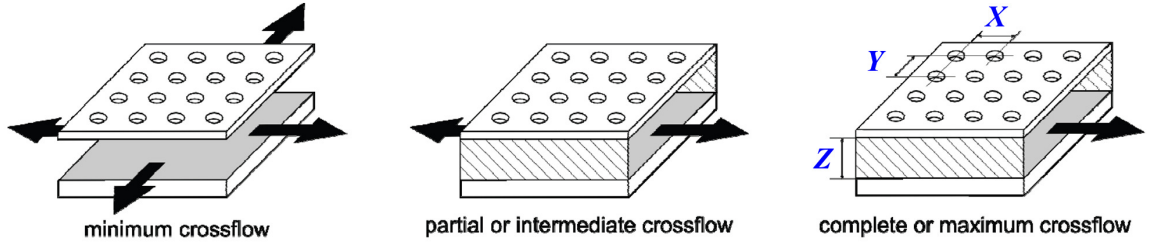


Figure 2.4: Different crossflow schemes for multi-jet systems. After [Obot and Trabold \(1987\)](#)

(X) and spanwise (Y) spacings, the separation distance (Z) and the influence of the crossflow generated by the spent air of the upstream jets.

The strength of the crossflow within the impingement array is determined by the design of the outflow and the associated routing of the spent air. One typically differs between minimum, intermediate, and maximum crossflow, as displayed in [Figure 2.4](#). In gas turbine blade cooling applications, due to the orientation of the coolant flow, maximum crossflow configurations are more practicable, and thus mainly applied. Therefore, for the prediction of heat transfer coefficients, local flow effects need to be taken into account. The achievable Nusselt number over a well-defined heat transfer area is then given by empirical correlations of the form:

$$\overline{Nu} \propto f \left[Re_j, Pr, \left(\frac{G_{cf}}{G_j} \right), \left(\frac{X}{D} \right), \left(\frac{Y}{D} \right), \left(\frac{Z}{D} \right) \right] \quad (2.1)$$

where G_{cf}/G_j is the ratio of the mass velocity of the generated crossflow to the local jet mass velocity. Such correlations developed by [Florschuetz et al. \(1981\)](#) and confirmed later by [Bailey and Bunker \(2002\)](#). The applicability of these correlations on narrow impingement channels is discussed in detail in [Chapter 7](#). Regarding the achievable heat transfer rate, the same trends with the single jet impingement are generally observed for flow velocity effects. Nusselt numbers increase with Reynolds number, following a power law ($Nu \sim Re^m$), where local values of m are in agreement with single jet literature. Typical values for the area averaged exponent m vary between 0.66 and 0.72 accounting for both stagnation and wall-jet regions ([Huang et al., 1998](#); [Florschuetz et al., 1981](#); [Bailey and Bunker, 2002](#); [Van Treuren et al., 1994](#)).

Another important design factor of impingement cooling systems is the jet density of the system which describes actually the porosity of the jet perforated plate. The dimensionless open area A_f has been established as a characteristic parameter describing this quantity. For inline jet arrays, it is defined as the ratio of jet hole area to the opposite heat transfer surface:

$$A_f = \frac{\pi}{4} \left(\frac{D}{X} \right) \left(\frac{D}{Y} \right) \quad (2.2)$$

Since the open area is defined as the ratio of jet hole area to opposing heat transfer surface area, one can expect an increase in heat transfer with increasing A_f . A variation of the open area for two different jet average Reynolds numbers is shown in [Figure 2.5](#). The figure contains data obtained from [Kercher and Tabakoff \(1970\)](#); [Hollworth and Berry \(1978\)](#); [Chance \(1974\)](#); [Metzger et al. \(1979\)](#); [Andrews et al. \(1987\)](#); [El-Gabry and Kaminski \(2005\)](#); [Florschuetz et al. \(1981\)](#). For very small values of A_f , i.e. between 0.1% and 1%, the jets are spaced far apart from each other. Consequently, the overall heat transfer is relatively small because the stagnation regions with the corresponding high-intensity heat transfer values are distant from one to

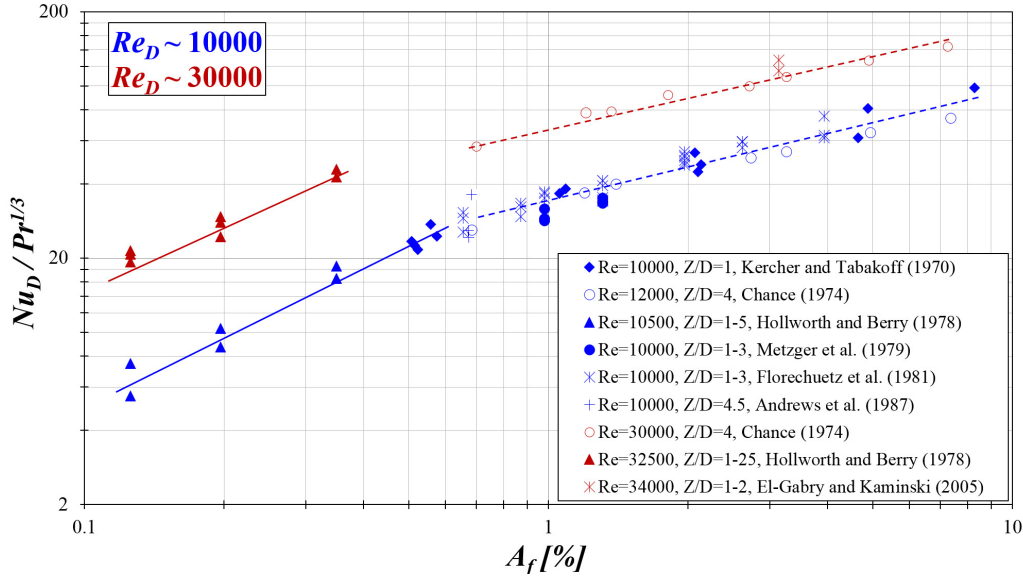


Figure 2.5: Area averaged Nusselt number as a function of jet plate open area (A_f). Data for Inline patterns and maximum crossflow orientations. $Z/D=1-5$

another. As the open area is increased, i.e. the percentage of perforation rises, a greater portion of the total target plate surface is covered by the stagnation regions and the achievable heat transfer rate is sharply increased. However, further increase of A_f beyond a critical limit results in an overlapping of the stagnation point regions of heat transfer which effectively limits the heat transfer growth. This point can be observed at about 1% of open area. From this point, area average heat transfer coefficients scale to the open area with a power law but the rate of increase is considerably smaller. This behaviour has been reported by many researchers, e.g. Kercher and Tabakoff (1970); Chance (1974); Hollworth and Berry (1978); Huber and Viskanta (1994). From the above observations, optimum values for the open area were suggested to be around 1% to 3%. It has also been reported, that crossflow interference is typically more significant for configurations with larger open areas (Bailey and Bunker, 2002). Note also that, increasing the open area also increases the sensitivity of Nu_D to the separation distance Z/D , that is why the scatter in Figure 2.5 is higher for bigger values of A_f .

2.3 Industrial Double-Wall Cooling Configurations

The capabilities of the foundry industry to produce high integrity and dimensionally accurate castings allow the production of integrally cast turbine airfoils with the so called *double-wall* cooling technology presented briefly in Section 1.4.3. Figures 2.6 and 2.7 demonstrate some industrial examples based on patents from various gas turbine engine manufacturers.

In all the examples, the turbine airfoil comprises a central cooling cavity extending in the spanwise direction and relatively narrow cooling cavities situated within the wall of the airfoil bounding the central cavity. The narrow cooling cavities provide local cooled surface areas much closer to the pressure and suction surface of the blade increasing the cooling capabilities due to the thinner external wall of the airfoil. A further increase of the convective heat transfer in the interior of the blade is achieved if the cooling air is supplied in the cavity by impingement cooling holes. Therefore, the fluid enters the wall-integrated cooling passages in the form of impingement jets. In many cases, the spent air of impingement can be used directly for film

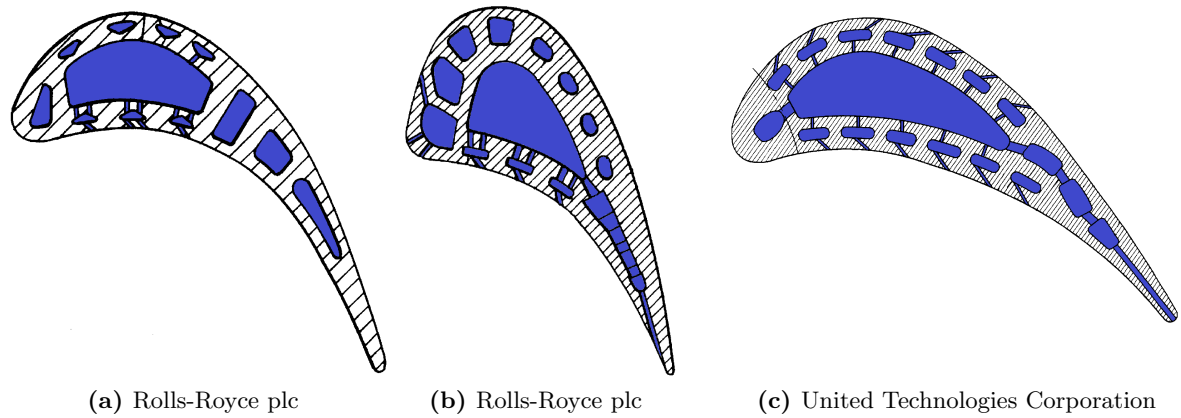


Figure 2.6: Aero-engine turbine airfoils with double-wall cooling configurations. (a) [Livsey and Hamblet \(1996\)](#), (b) [Dailey et al. \(2001\)](#), (c) [Moore \(1997\)](#)

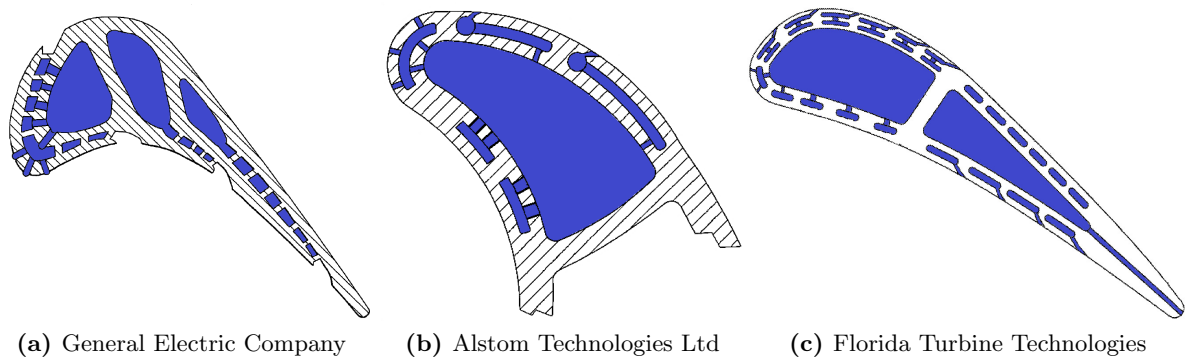


Figure 2.7: Industrial engine turbine airfoils with double-wall cooling configurations. (a) [Lee and Bunker \(2006\)](#), (b) [Lutum et al. \(2002\)](#), (c) [Liang \(2013\)](#)

cooling extraction combining impingement and film cooling, as for example in [Figure 2.6](#), or restricted to narrow configurations consisting of single or double rows of impingement jets, as indicated by the patents in [Figure 2.7](#). Regarding the latter case, a plurality of cooling cavities can be included in the spanwise direction ensuring homogenous distribution of the material temperature.

Apparently, the geometrical characteristics of the narrow impingement channel play an important role in the turbine blade thermal design, since the channel height and width, the jet-to-jet spacing, the hole offset position from the channel centerline and other geometrical factors may vary the (1) local heat transfer distributions, and thus the blade metal temperatures, (2) the channel pressure drop which in turn affects the required pumping power to move the coolant flow along the cavity and (3) the number of cooling activities per blade surface which directly affects the cooling air consumption.

2.4 Narrow Impingement Channels

Most of the aspects of multi-array impingement cooling systems are described in detail in the review of [Weigand and Spring \(2011\)](#). One of the most important design factors is the so-called generated crossflow, especially for gas turbine blades and vanes where the large applicability of maximum crossflow orientations (single channel exit designs), reduces the heat transfer capabilities of the downstream regions of the jet array, as shown by [Obot and Trabold \(1987\)](#).

Crossflow effects are also of great importance in narrow impingement channels where the spent air of the jets interferes with the other walls of the channel (sidewalls and jet plate) providing complex structures which can be very different compared to single jet-crossflow interactions. In the literature, there are several studies related to narrow impingement channels. However, contrary to multi-jet arrays, a detailed physical assessment of their heat transfer performance is not adequately known. Additionally, limited information has been presented for sidewalls and jet-plate heat transfer which is of great significance for double-wall cooling designs. This section discusses the current state of literature of narrow impingement configurations. The geometrical details of the cited investigations are summarised in Table 2.1.

Gillespie et al. (1998) investigated the local heat transfer distribution for all the surfaces of an integrally cast impingement cooling geometry. The overall configuration consisted of seven impingement holes in a staggered arrangement where the spent air of the jets was vented through five inline film cooling holes. They observed that the heat transfer rate was comparable to that of multi-array configurations in the range of $Re_D=21,000-40,000$, however, low crossflow was developed due to the film cooling extraction. The additional surfaces around the impingement holes were seen to be important regions contributing to heat transfer from the coolant to the wall in turbine blades. Chambers et al. (2005) carried out experiments in order to investigate the effect of initial crossflow in a high aspect ratio cooling channel consisting of nineteen impingement holes in a staggered arrangement. The experiments were conducted for both target and jet issuing plate in the range of $Re_D=10,000-35,000$. The authors observed the classic impingement patterns on the target plate for low mass-flux ratios. However, no impingement enhancement was observed at high crossflow momentum due to the incapability of the jets to traverse the channel height. For the jet plate, high effectiveness values were observed at the wake of the jets. Some improvements on the achievable heat transfer of the target plate on the same geometry were reported later by Chambers et al. (2010) using shaped elliptical impingement holes in order to provide better penetration capabilities of the downstream jets. At the same cooling flow rate, they observed a heat transfer enhancement between 28% and 77% for at early channel positions and about 16% for the high crossflow dominated region. Ricklick et al. (2010) and Ricklick and Kapat (2011) investigated the effects of channel height and sidewalls on an inline row of fifteen impingement holes in the range of $Re_D=10,000-35,000$. The results showed a low dependance on the separation distance and significant heat transfer on the lateral sidewalls of the channel due to the narrow passage width. Sidewalls of low separation distances found to perform better in terms of area averaged heat transfer. Jet plate heat transfer was not measured. Al-Agal (2003) determined experimentally the local heat transfer distributions on the target and the jet issuing plate of high crossflow impingement channels at $Re_D=14,000-30,000$ and over a range of channel geometrical factors. The results indicated that area averaged heat transfer coefficients are slightly lower compared to conventionally multi-array arrangements, i.e. Florschuetz et al. (1981), due to the more intense crossflow produced in the confined channel. Terzis et al. (2012c, 2014) investigated in detail the effect of hole offset position from the channel centerline in a single row of five impingement jets in the range of $Re_D=10,900-86,100$. They reported a reduction of the overall cooling performance as the hole offset position is increased similar to multi-jet configurations. The reduction of heat transfer was found to be more intense at lower channel heights where higher crossflow velocities occur. For the sidewalls of the channel, they reported that full staggered configurations might be beneficial for the achievable heat transfer rate since the jets are placed very close to the lateral walls. No results for the jet plate were reported. Uysal

Table 2.1: Summary of relevant previous studies

Authors	Rows	Holes	L/D	X/D	Y/D	Z/D	$\Delta y/D$	$Re_D (\times 10^4)$	Sidewalls	Jet plate
Gillespie et al. (1998)	1	7	1.25	4	7.5	1.25	1.9	2.1-4.2	No	Yes
Chambers et al. (2005)	1	19	1.25	4.36	3.03	1.54	1.8	1-3.5	No	Yes
Uysal et al. (2006)	1	6	~8.5	7.5	6.8	0.8,1.6,2.4	0	1.4-4	No	Yes
Ricklick et al. (2010)	1	15	1	5	4	1,3,5	0	1.7-4.5	Yes	No
Lamont et al. (2012)	1	9	1	8	8	1,2,3	0	~0.9	No	No
Al-Agal (2003)	1,2,3,	6,12,18	1.5	6.5	4	1.33-8	0	1.4-3	No	Yes
Miller et al. (2013)	1	5	2	4	4	2,4	0	5-8	No	No
Stoakes and Ekkad (2011)	2	5	2.5	2,4,5	2,4,5	1,2	0	0.5-1.5	No	No
Terzis et al. (2014)	1	5	1	5	5	1,2,3	0,2,3,8	1-8.6	Yes	No
Fechter (2011)	1	5	1	5	5	1,3	0,2	1-4.5	Yes	Yes
THIS STUDY	1	5	1	5,8	3,4,5,6	1,1.5,2,3	0,1.2,2,3,8	1-8.6	Yes	Yes

et al. (2006) studied the effect of varying jet diameter in a narrow channel consisting of six inline holes in the range of $Re_D=14,000-40,000$. They observed that the heat transfer coefficient with constant jet diameter is spatially more uniform than that with non-uniform diameters. The authors examined also heat transfer on the jet plate where for the averaged results heat transfer coefficients were about 50% to 60% lower compared to the target plate. No results for the sidewalls were reported. Effects of varying jet diameter on a rib-roughened target plate were experimentally investigated by Miller et al. (2013) in a narrow channel of five inline impingement jets. Three different rib orientations were used on the target plate including: horizontal, chevron and X-shape ribs. X-shape ribs provided the best heat transfer performance. Lamont et al. (2012) investigated rotation effects in a narrow channel consisting of nine inline impingement holes. The stationary results indicated similarities with previous investigations concerning the impingement patterns. However, the inlet flow run parallel to the jet faces resulting in a reduction of the local Reynolds number in the streamwise direction. Consequently the stagnation point heat transfer of the downstream jets was slightly reduced. Stoakes and Ekkad (2011) performed a comprehensive conjugate-CFD study in a narrow channel consisting of two rows of inline impingement holes balancing heat transfer and channel pressure drop. They concluded that designs with fewer holes per row provide comparable heat transfer with less cooling flow consumption and lower pressure drop. These above discussed trends were also confirmed numerically by Fechter et al. (2013) in the range of $Re_D=15,000-45,000$. The authors presented also results for the jet plate where the area averaged heat transfer level was about 50% lower compared to the target plate.

2.5 The Contribution of The Thesis

The present study differs from preceding research since a vast number of different narrow impingement channel geometries are experimentally evaluated in terms of their thermal performance over a wide range of engine representative Reynolds numbers (10,900-86,500). The geometrical characteristics of the 30 impingement channel models tested are presented in Section 3.3. The contributions of the work reported in this thesis are set out below:

- The design and development of a completely new test facility for impingement cooling heat transfer research using relatively large air heaters.
- A new method for transient liquid crystal experiments which considers also thermocouple thermal inertia effects for the evaluation of heat transfer coefficients.
- Local heat transfer coefficients are evaluated and analysed with great spatial resolution for all internal surfaces of the narrow impingement channel providing information over the complete wetted heat transfer area, all of which contributes to the cooling process.
- Effects of various geometrical factors, such as jet-to-jet axial spacing, channel height and width, cooling hole offset position from the channel centerline, cooling jet size variation as well as crossflow effects, are in detail investigated providing a parametric study of different channel geometries.
- The effects of channel geometrical factors on the streamwise area averaged heat transfer values are correlated in an empirical equation using a regression analysis model. This is the first heat transfer correlation for narrow impingement channels reported in the open literature.

EXPERIMENTAL SETUP

This chapter presents the main characteristics and specifications of the impingement cooling test rig of GTT. The overall arrangement comprises an open circuit wind tunnel operated in suction mode. Initial tests were carried out in order to verify the functionality and operability of the test rig within the required flow conditions. The large scale impingement models are also presented. Additionally, the accuracy of the measurement equipment is discussed.

3.1 Introduction

The experimental investigation involved in this study required a test rig capable of delivering the necessary flow conditions, providing also the means for accurate measurements. The design of the impingement cooling test rig has been the subject of an extensive literature survey since a variety of similar configurations have been used by previous researchers. The test facility has been designed and manufactured with certain objectives:

- to be capable of generating constant, uniform and two-dimensional flow over the full length of the wind tunnel in the range of incompressible flow
- to provide the necessary temperature step in the flow
- to accommodate the narrow impingement channels test models allowing a parametric study of different geometries using identical measurement equipment
- to allow easy access to the measurement surfaces and the heater grids
- to be flexible from the design and simple from the manufacturing point of view

The general arrangement comprises a small-scale wind tunnel operated in suction mode and equipped with the necessary electronics and other instrumentation. The overall test facility consists of an inlet flare, a short section of square ducting that contains an air heater, the narrow impingement channel test models, the exhaust pipe with a laminar flow element and a vacuum pump. An overall schematic representation of the test facility is illustrated in Figure 3.1. The design and the assembly of this small wind tunnel were carried out with such flexibility so that any further modification can be easily performed.

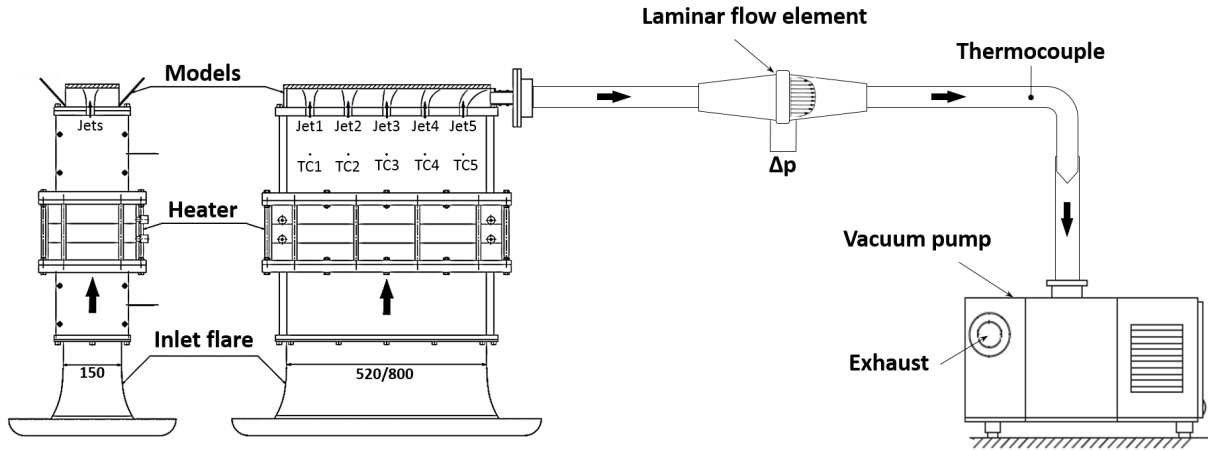


Figure 3.1: Impingement cooling test rig

3.2 Impingement Cooling Test Rig

3.2.1 Literature background

A large variety of test facilities and measurement techniques have been used by previous investigators for heat transfer experiments on multi-array impingement configurations. In relatively early studies, i.e. Kercher and Tabakoff (1970); Chance (1974); Hollworth and Berry (1978) and Andrews et al. (1987), open circuit wind tunnels operated in blowing mode were mainly used. Ambient air was supplied in a plenum chamber before flowing through a perforated jet plate and impinging over an iso-flux surface formed by various insulated and electrically heated copper blocks. Knowing the supplied power, the authors used a steady state heat transfer approach to determine convection coefficients using a number of embedded thermocouples at various streamwise and spanwise positions. However, due to the fixed plenum size, open area effects were evaluated by varying the number and the diameter of the holes on the perforated jet plate resulting to different values of generated crossflow and Mach number at the same flow conditions. A more sophisticated design with interchangeable plenum chambers of different streamwise lengths was proposed by Metzger et al. (1979). A relatively long electrically heated target surface was exposed to an array of impinging jets where the total number of rows in the streamwise direction was fixed to ten. The different length requirements for the various jet-to-jet spacings were satisfied by replacing the jet plate and the upstream plenum with a fitted one while the overall span of the jet array extended beyond the end of the heated target surface minimising flow pattern edge effects on the heat transfer distributions. Therefore, using the test rig described above, Florschuetz et al. (1980) were able to quantitatively evaluate crossflow effects generated by the spent air of the jets under the same potential flow characteristics. Some experiments were also performed with initial crossflow (Florschuetz et al., 1984; Florschuetz and Su, 1987) supplied from a different plenum chamber. The main drawback of the aforementioned test facilities is the relatively poor heat transfer resolution that can be obtained on the examined surfaces, as a direct consequence of the limited amount of embedded thermocouples. As a result, the main conclusions were restricted to area averaged heat transfer coefficients and over a well defined exposed surface, which concluded however, very useful and precise correlations for real turbine blade thermal designs, i.e. Florschuetz et al. (1981). In more recent years, an infrared thermal imaging technique has been applied (Park et al., 2007; Goodro et al., 2008), increasing

the resolution of steady state heat transfer experiments. However, this technique requires also a test section made of a special material which is transparent to infrared radiation while infrared images taken under laboratory conditions also have an inherent noise problem coming from the image sensor which is a charge coupled device.

Apart from steady state experiments, there are also a number of test rigs reported capable for transient techniques of measuring heat transfer coefficients, as for example the setups of [Van Treuren et al. \(1994\)](#) and [Huang et al. \(1998\)](#). The principle of a transient technique is to observe the time response of the surface temperature to a known step change of the driving gas temperature. Compressed air was first supplied in an electric heater and then to an introductory plenum where valves were used in order to isolate the main flow from the plenum chamber of the test rig. Once the conditions were stabilised, the temperature step was achieved by switching properly valves and bypass flow so that hot air from the introductory plenum was introduced inside the jet array forcing the colour response of a liquid crystal surface coating. Heat transfer coefficients were therefore evaluated with great spatial resolution by post-processing of the recorded video. On the other hand, the disadvantage of fast acting valves is the complexity of the design and that the mainstream temperature cannot be represented as real step. Other approaches include rapidly inserting a model into a wind tunnel of a constant mainstream temperature which is higher than the initial model temperature, i.e. [Falcoz et al. \(2006\)](#) and [Wagner et al. \(2007\)](#). However, the performance of any mechanical injection system depends on the size and the inertia of the model. As a result, the large scale impingement models employed in this study were assumed not suitable for pneumatic insertion mechanisms.

The mechanical complexities of fast acting valves or model positioning activators can be avoided using an air heater, originally described by [Gillespie et al. \(1995\)](#). The heater mesh can be used in order to increase the temperature of the air passing through it, taking advantage of the *Joule heating*. According to [Esposito et al. \(2009\)](#), the change of the mainstream temperature can be achieved within $33ms$ which can be assumed acceptable for a transient experiment. Several test rigs that are presented in the literature involve heater mesh configurations, i.e. [Son et al. \(2001\)](#); [Spring et al. \(2010\)](#) and [Xing et al. \(2011\)](#). In these studies, ambient air, passing through the heater mesh and the plenum chamber, was injected in the impingement array at the required flow conditions. Electric power was then suddenly supplied on the heater mesh changing the mainstream temperature to the required level while the evolution of the wall temperature response on the examined surfaces was optically monitored using liquid crystals.

A careful analysis of the design principles used in all of the aforementioned experimental arrangements facilitated the development of the test rig used in the course of this thesis.

3.2.2 General Layout

The wind tunnel is of open circuit design and consists of an inlet flare, a rectangular section of square ducting that contains an air heater, the large-scale test models, the exhaust piping system and the driving pump. The various wind tunnel components are discussed in brief as follows:

The inlet flare

The objective of the inlet flare in open circuit wind tunnels is to accelerate the flow from ambient conditions to the flow conditions required in the working section. During this acceleration, smooth and attached flow should be maintained, all the way from the inlet to the throat

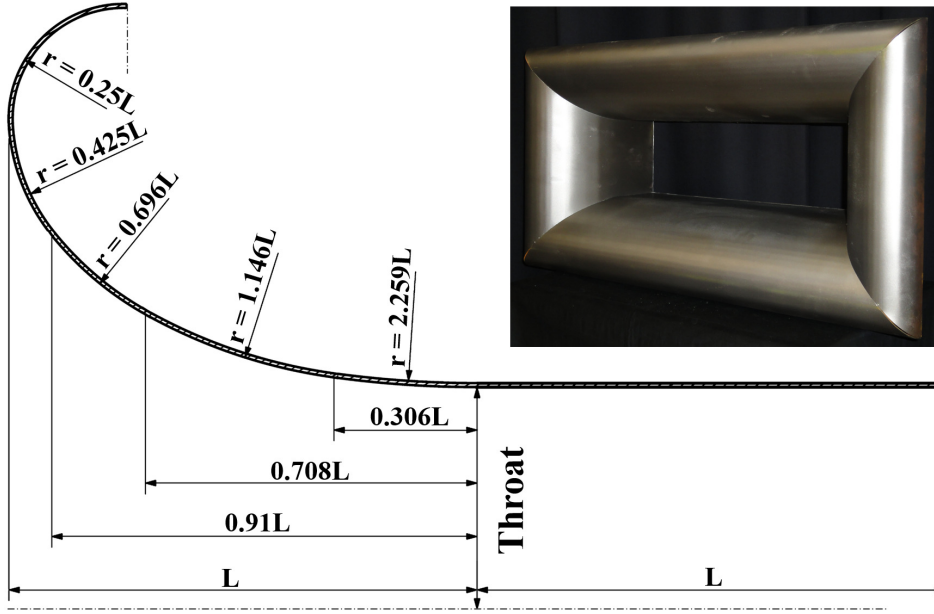


Figure 3.2: Inlet flare design dimensions

of the flare. In a general design concept, steeper wall curvature can be used at the lips of the bellmouth intake since the relatively low velocities in this region force the flow to withstand strong acceleration without separating. However, as the acceleration process progresses, adverse pressure gradients appear reaching the limits of flow separation. In this region, the flare's profile curvature is decreased in order to avoid the risk of recirculation and thick boundary layers.

The boundary layer thickness in a bellmouth inlet depends on the severity of the adverse pressure gradient on the flare in the region of the throat, and subsequently, the curvature of the inlet flare has an important effect on the boundary layer thickness on the tunnel walls (Bell and Mehta, 1989). The aerodynamic design of the inlet flare was based on an early work focused on flares for annular intakes for aero-engine ground tests described by McKenzie (1966), as well as the design principles presented by Bell and Mehta (1988). Since the heater grid configuration has a rectangular cross-section, the original design, based on circular ducts, has been transformed in order to match the overall dimensions of the tunnel. The similarity parameter used in this study is the following geometrical ratio:

$$\frac{2A_{throat}}{P_{throat}l} \quad (3.1)$$

where l is the distance from the lips to the throat of the inlet flare and, A and P are the area and the perimeter of the throat, respectively. According to McKenzie (1966), for an adequate inlet flare design the above geometrical ratio, which describes the dimensions of the inlet flare, should not exceed a critical value of $2/3$, and thus, the required length of the flare is given by:

$$l = \frac{3}{2} \frac{\alpha\beta}{\alpha + \beta} \quad (3.2)$$

where α and β are the throat dimensions. From these dimensions a satisfactory inlet flare can be designed knowing only the dimensions of the cross-section at the throat.

The basic drawing of the inlet flare is shown in Figure 3.2 where the shape of the flare has been approximated by a series of circular arcs similar to McKenzie (1966). The radius and the

axial length of the curvatures are given as factors of l . The distance between the throat of the flare and the standard measurement plane (heater mesh) should be at least l . The inlet flare was manufactured by assembling four bended Stainless Steel plates of $2mm$ thickness bought from BR-TEC Roschli AG and welded in-house by the Atelier de l'Institut de génie Mécanique.

The contraction ratio obtained by the particular inlet flare design has been defined as the area ratio of the inlet to the surface of the throat and it was determined as:

$$CR = \frac{A_{inlet}}{A_{throat}} \approx 4.5$$

The resultant contraction ratio can be considered adequate for the purposes of this study. A higher contraction ratio would cause the background turbulence level and the boundary layer thickness on the tunnel walls to reduce. However, the installation of the heater grid configuration, consisted of several low porosity mesh layers, eliminates the distortions of the developed flow achieved at the position of the thermocouples. Therefore, it was assumed that any further effort to increase the contraction ratio of the flare would have a minimal effect on the final result. At the throat of the flare a ventilation air filter has been installed in order to protect the heater mesh and the wind tunnel instrumentation from possible dust injection.

Wind tunnel ducting

Ideally, the working section of a subsonic wind tunnel should have a cross-section area as large as possible. However, in this particular case there is no need to insert a test model in the mainstream since the test models are already part of the wind tunnel ducting. The objective is therefore to provide a uniform temperature step in the flow and the necessary flow rates inside the narrow impingement channels.

The main wind tunnel ducting located downstream of the inlet flare consists of two identical parts of rectangle cross-section ($520 \times 150mm^2$), installed directly upstream and downstream of the heater grid assembly. The length and the wall thickness of the two square ducts are $285mm$ and $20mm$, respectively. These two transition pieces are manufactured by wood of low thermal conductivity, tending to minimise possible heat losses downstream of the heater and upstream of the jet plate. A rendering image of the wooden transition piece is illustrated in Figure 3.3(a). Two honeycombs were also mounted at the throat of the bellmouth and upstream of the heater grids in order to make velocity profiles more uniform and remove possible swirl. The selection of the honeycombs was based on the design principles outlined by Mehta and Bradshaw (1979). The two Aluminium honeycombs are of hexagonal cell design with a regular side of $2mm$ and a cell length about 15 times bigger. Between the two wooden square ducts four heater mesh layers were installed. More details about the heater grid can be found in Section 3.2.3.

Within the range of massflows examined in this study, the plenum velocity upstream of the jet plate was around $0.5m/s$ or even less. At this velocity magnitude, pressure acquisition measurements are difficult to be obtained in order to determine the uniformity of the plenum velocity profiles. The uniformity of the flow was therefore evaluated with a number of static pressure taps installed around the whole flow path as shown in Figure 3.3(b). The average values of 1000 pressure signals acquired at a rate of $25Hz$ are indicated in Figure 3.3(d) for upstream and downstream positions of the heater. The static pressure uniformity was evaluated over a wide range of jet average Reynolds numbers varying between 20,000 and 160,000 testing also the stability and operability of the test rig at low speed compressible flows ($Ma_{jet}=0.35$).

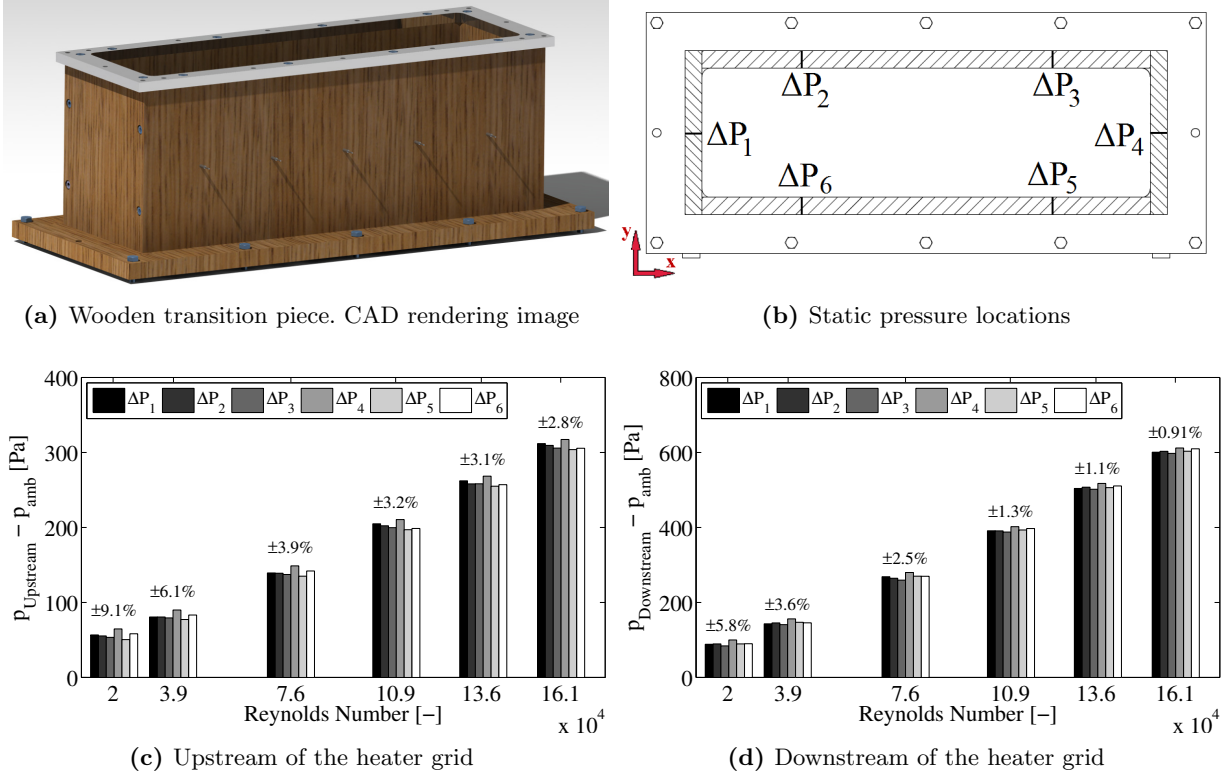


Figure 3.3: Locations and uniformity of static pressure profile on the wind tunnel ducts

The standard deviation of static pressure profiles at each measurement plane is less than 5% indicating the excellent functionality of the inlet flare. Note that the difference between the values of Figures 3.3(a) and (b) provides the pressure drop through the air heater.

At the top of the working section, the experimental test models have been manufactured in order to be completely detachable from the tunnel, and thus, facilitating the investigation of different channel geometries. This gives flexibility and freedom to the researcher to test the desirable model keeping the main wind tunnel measurement equipment unchanged. More details about the experimental test models can be found in Section 3.3.

The driving pump

The air source used for the current test facility is a single stage, oil sealed rotary vane pump (SOGEVAC SV1200) which was selected in order to satisfy the requirements of the experiments. The pump is driven by a foot mounted motor (CEI Standard) via four V-belts and operates at constant volume flow conditions. The specifications of the pump can be summarised as follows:

Nominal pumping speed [m^3/h]	: 1100
Motor power [kW]	: 22
Motor rotational speed [rpm]	: 1800
Noise level [dB]	: 75
Total mass (with tubing) [kg]	: 1600
Flange connections	: DN125PN10(ASA 150–6")

The power output from the pump depends on the overall aerodynamic load of the tunnel generated by the intake filter, the honeycombs, the heater grid configuration, the jet perforated

plate and other loss generating items located in the tunnel according to the needs of experiments. The massflow rate is regulated by an inlet vane placed at the suction port of the pump and controlled with a laminar flow element. This configuration provides the flexibility of very fine regulation of the mainstream velocity inside the wind tunnel. More details about the laminar flow element can be found in Section 3.4.

3.2.3 The heater mesh

General overview

In this study, the transient liquid crystal technique was used for the determination of local convection coefficients on the examined surfaces. In a typical transient heat transfer experiment, the flow initial temperature is subjected to a sudden temperature change and the evolution of a liquid crystal isotherm is optically monitored. In the present study, the required temperature step in the flow was obtained using an air heater.

The heater grid is made of metallic material through which electrical current passes in order to increase the temperature of a fluid using *Joule* heating. In order to maintain dimensional stability, the metallic mesh is of woven construction and manufactured of intersecting wires of relatively small diameter (in the order of μm) defining apertures where the fluid to be heated passes. The heater mesh generally spans along the whole flow path of the duct and it is attached to electrodes to which an electrical power source is connected to supply current to the mesh. Gillespie et al. (1995), characterised the performance of heater meshes through a combination of theory and experiments, and reported that the smaller is the wire diameter, the higher is the efficiency of the heat exchange given by the following equation:

$$\eta = \frac{T_2 - T_1}{T_m - T_1} \quad (3.3)$$

where T_1 and T_2 are the fluid temperatures upstream and downstream of the heater, and T_m is the temperature of the mesh wire. Typical efficiency values vary between 0.5 and 0.65 for wire diameters of $200\mu m$ and $25\mu m$, respectively, when the velocity of the fluid to be heated is around $1m/s$. This means that for typical temperature steps used in transient liquid crystal experiments, i.e. $\Delta T=60K$, problems associated with overheat wires in the tunnel are avoided. Additionally, most of the electrical power supplied in the mesh is transferred to the flow allowing also a quick estimation of the temperature step through the energy balance:

$$T_2 - T_1 = \frac{I^2 R}{\dot{m}c_p} \quad (3.4)$$

where I is the supplied current, R is the overall resistance of the heater mesh and $\dot{m}c_p$ is the heat capacity rate of the flow.

Description and technical details

Careful manufacturing of the heater ensures that a uniform flow temperature is achieved downstream of the mesh. The heater mesh configuration employed in this study consists of an assembly of four individual layers pressurised together by steel bars in order to increase the uniformity of heating, similar to ITLR arrangements (University of Stuttgart). Figure 3.4(a) shows the overall assembly where the distance between the individual mesh layers is $50mm$ resulting in a total heat exchanger length of $150mm$.

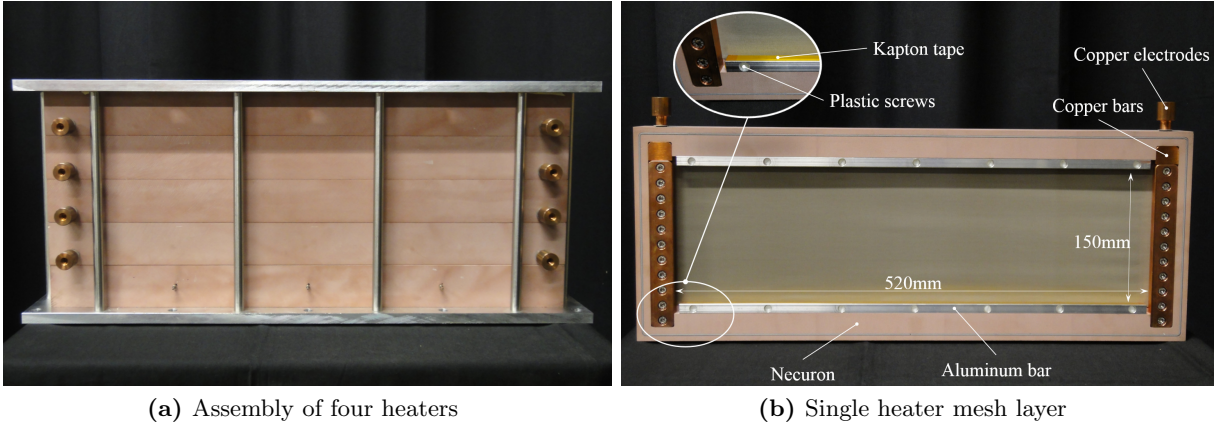


Figure 3.4: The heater mesh configuration employed in this study

Detailed characteristics of a single mesh layer are illustrated in Figure 3.4(b). The main flange of the heater is manufactured by Necuron 700, a plastic material capable to operate at elevated temperatures ($\sim 170^\circ C$). The St. Steel 1.4401 mesh spans over the whole flow path of the wind tunnel composing an effective heating area of $520 \times 150 (mm)^2$. The wire diameter and the mesh aperture are both $25 \mu m$ resulting in an open area (mesh porosity) of $A_o = 25\%$. The small wire diameter allows the heater mesh to run at a lower temperature than for thicker meshes due to the higher mesh efficiency ensuring also that any turbulence produced by the mesh is dissipated within a very short distance. On the small sides, the heater is pressurised between two copper bars where the electrical current is supplied (electrodes). Note that the electrodes are sufficiently large so that the resistance does not cause excessive heating. On the large sides of the cross-section, the heater is pressurised between the Necuron flange and an aluminium bar which is electrically isolated from the metallic mesh using a single layer of high thermal resistant Kapton tape. The aluminium bar is mounted over the Necuron flange with plastic bolts eliminating the risk of short circuits. The overall duration of a transient experiment was in the order of 90s, which was found absolutely safe for the Necuron flange causing absolutely no damage.

One of the main concerns for safe and proper functionality of large mesh heaters is the elongation due to thermal expansion. In this study, sagging and bending of the metallic grids are avoided since the mesh is sandwiched over the whole flow path. Therefore, the maximum elongation bending equals the bending of the small side ($150mm$). A rough calculation of the mesh elongation for the small side of the mesh, considering an extreme case of $T_m = 250^\circ C$ and a thermal expansion coefficient of $15.9 \times 10^{-6} K^{-1}$ gives approximately:

$$\Delta l = \alpha l \Delta T \approx 0.65mm$$

This elongation results in a maximum bending of $8mm$ which was absolutely safe for the four adjacent mesh layers used in this study (difference of $50mm$).

Achievable temperature step

Ireland et al. (1999) reported that a temperature uniformity less than $\pm 1.3^\circ C$ can be obtained downstream of the heater when the flow temperature is increased by $20^\circ C$. However, what matters at the end is the uniformity between the temperature levels of the impingement jet holes and the accurate determination of the gas temperature which drives the transient experiment. Subsequently, a number of preliminary tests have been carried out in order to test

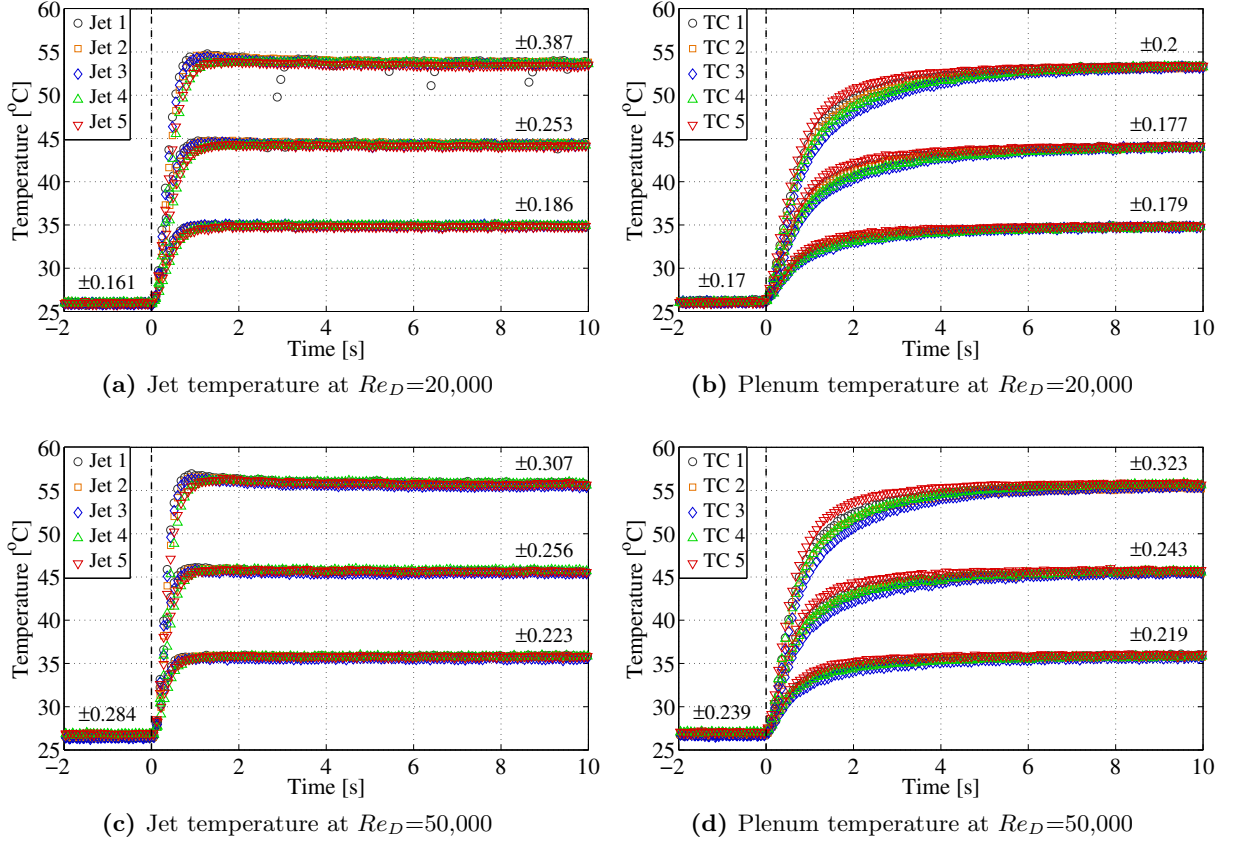


Figure 3.5: Temperature evolution downstream of the heater grid

the operability and functionality of the heater using a single mesh layer.

Five thermocouples were embedded directly upstream of the inlet of each impingement hole in order to acquire the temperature step for each individual jet. The gas temperature was also acquired by five additional thermocouples equally distributed in the plenum upstream of the jet plate. The Reynolds number, based on the jet diameter, was varied from 10,000 to 70,000 while temperature steps of approximately 10°C , 20°C and 30°C were performed at each individual Reynolds number.

Figure 3.5 indicates the evolution of the jet and plenum temperature for two different Reynolds numbers as acquired by K -type thermocouples with exposed junction ($d_w = 0.13\text{mm}$). First of all, the simultaneous response of the five plenum and jet thermocouples implies a uniformly obtained heating downstream of the mesh and similar velocity magnitudes which means that the average Reynolds number calculated from the measured massflow in the laminar flow element is adequate to describe the flow conditions inside the narrow impingement channel. Note also the jet thermocouples for both $Re_D = 20,000$ and $50,000$, respond faster compared to the plenum thermocouples, due the higher local velocities, and hence smaller values of thermocouple time constants. More details about thermocouple thermal inertia effects can be found in Section 4.4. For both jet and plenum thermocouples and over the full range of investigated flow conditions, the initial temperature (T_o) can be always determined with an uncertainty of $\pm 0.3^\circ\text{C}$, with a tendency of increasing accuracy at higher Re_D . For the hot conditions, the uncertainty in the determination of the driving gas temperature (T_g) is increased at higher temperature steps and Reynolds numbers. Similar to the initial temperature, the accuracy is almost identical for jet and plenum thermocouples indicating that in case of an ideal step assumption, T_g can

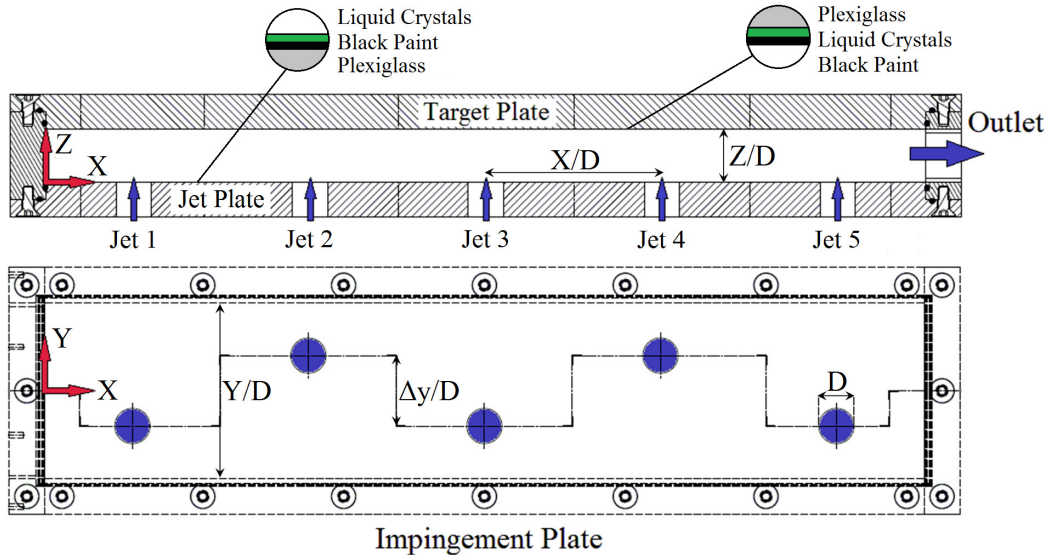


Figure 3.6: Schematic representation of the test models

be measured adequately accurate on both locations. Chambers et al. (2005) and Ieronymidis et al. (2010) reported a standard error of $\pm 0.5^\circ C$ and $\pm 0.3^\circ C$ on both initial and jet temperature while the hot gas deviation in the study of Schueren et al. (2013) was around $\pm 0.4^\circ C$. In this study, temperature uniformity downstream of the heater was always less than $\pm 0.4^\circ C$ for both plenum and jet location measurements. As a result, due to the relatively low uncertainty, the initial temperature (cold) and the gas temperature (hot) can be accurately determined by temperature measurements either at the jet inlet or in the plenum.

3.3 Test Models

The experimental test models are a large scale representation of an ideal impingement cooling channel as it can be cast-in in modern turbine airfoils. This configuration consists of a narrow passage where several jets impinge over a flat target plate while a single exit design is used resulting in a maximum crossflow orientation.

A schematic representation of the test models is illustrated in Figure 3.6. First of all, for the purposes of this work, a coordinate system has to be assigned to the test models in order to assure consistency in the references to the various measurement locations in the narrow impingement channel. The coordinate system used is indicated in Figure 3.6 as well. The length of the passage is described by the axial direction where the streamwise coordinate (x) is measured in the centerline of the channel beginning from the closed side. Passage width, and therefore different spanwise locations are described by the crosswise coordinate (y), measured vertically to the axial direction, while the coordinate (z) which describes the height of the impingement passage is measured normally to the impingement plate of the tunnel in the direction of the target plate.

The narrow channels consist of a single row of five impingement holes of equal length-to-diameter ratio ($L/D = 1$). The diameter of the impingement hole was selected in order to keep the maximum jet Mach number below 0.22 neglecting also compressibility effects according to Park et al. (2007). All impingement jets are supplied from the same plenum, and therefore, they have the same total pressure. A single exit mode was applied for the spent air of the jets

Table 3.1: Summary of investigated narrow impingement channel geometries

Test No.	X/D	Y/D	Z/D	$\Delta y/D$	$\Delta y/Y$	ΔD	Re_D
1	5	3	1.5	1.2	0.40	Uniform	10,900–45,850
2	5	4	1.5	1.6	0.40	Uniform	10,900–45,850
3	5	5	1.0	0.0	0.00	Uniform	10,900–85,900
4	5	5	1.0	2.0	0.40	Uniform	10,900–85,900
5	5	5	1.0	3.8	0.76	Uniform	10,900–85,900
6	5	5	1.5	0.0	0.00	Uniform	10,900–85,900
7	5	5	1.5	2.0	0.40	Uniform	10,900–85,900
8	5	5	1.5	3.8	0.76	Uniform	10,900–85,900
9	5	5	2.0	0.0	0.00	Uniform	10,900–85,900
10	5	5	2.0	2.0	0.40	Uniform	10,900–85,900
11	5	5	2.0	3.8	0.76	Uniform	10,900–85,900
12	5	5	3.0	0.0	0.00	Uniform	10,900–85,900
13	5	5	3.0	2.0	0.40	Uniform	10,900–85,900
14	5	5	3.0	3.8	0.76	Uniform	10,900–85,900
15	5	6	1.5	2.4	0.40	Uniform	10,900–45,850
16	8	3	1.5	1.2	0.40	Uniform	10,900–45,850
17	8	4	1.5	1.6	0.40	Uniform	10,900–45,850
18	8	5	1.0	2.0	0.40	Uniform	10,900–45,850
19	8	5	1.5	2.0	0.40	Uniform	10,900–45,850
20	8	5	2.0	2.0	0.40	Uniform	10,900–45,850
21	8	5	3.0	2.0	0.40	Uniform	10,900–45,850
22	8	6	1.5	2.4	0.40	Uniform	10,900–45,850
23	5	5	1.5	0	0	5% Increasing	10,900–45,850
24	5	5	1.5	0	0	5% Decreasing	10,900–45,850
25	5	5	1.5	0	0	10% Increasing	10,900–45,850
26	5	5	1.5	0	0	10% Decreasing	10,900–45,850
27	5	5	3	0	0	5% Increasing	10,900–45,850
28	5	5	3	0	0	5% Decreasing	10,900–45,850
29	5	5	3	0	0	10% Increasing	10,900–45,850
30	5	5	3	0	0	10% Decreasing	10,900–45,850

representing a maximum crossflow orientation. Effects of a number of geometrical factors were investigated composing a test matrix of 30 different channel geometries summarised in Table 3.1. Axial jet-to-jet spacing (X/D) was set to 5 and 8, channel width (Y/D) was varied between 3 and 6, and channel height (Z/D) from 1 to 3. Three different impingement hole patterns were studied: an inline ($\Delta y/Y=0$), a low-stagger ($\Delta y/Y=0.4$) and a full-stagger configuration ($\Delta y/Y=0.76$) where the jets are placed very close to the sidewalls. Additionally, varying jet diameters, increasing or decreasing constantly towards the channel exit were investigated in an attempt to regulate the generated crossflow. Figure 3.7 shows typical narrow impingement channels painted with thermochromic liquid crystals. The liquid crystal signal on the side walls was monitored by mirrors placed at an angle of $45deg$ as shown in Figure 3.1. Several Reynolds numbers were examined between 10,900 and 85,900. The test models are manufactured of transparent acrylic material (Plexiglas) so that the observation of liquid crystals can be performed from the back of the test rig plate for both target and jet plates. The Plexiglas roughness (R_z) was measured $0.4\mu m$. Furthermore, the mechanical properties of the model allow the assumption of a semi-infinite body while the lateral conduction during the transient experiment can be

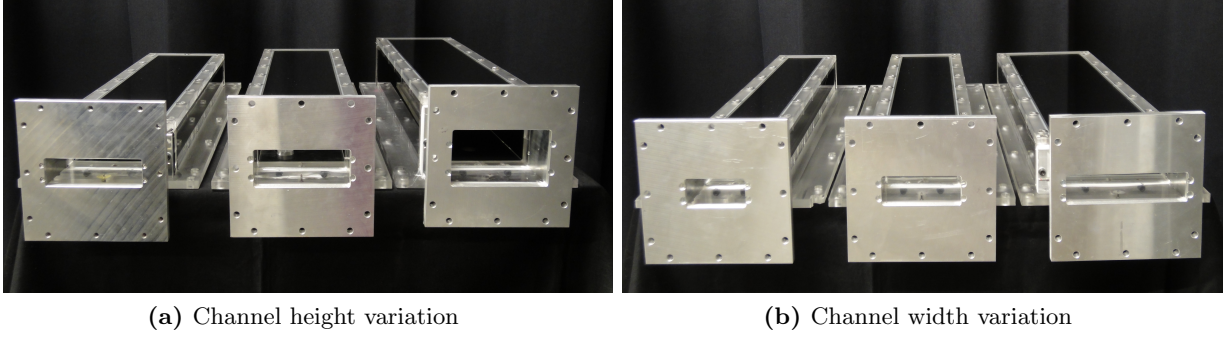


Figure 3.7: Narrow impingement channels painted with liquid crystals

considered negligible. The mechanical properties of the material provided by the supplier are summarised as follows:

Density, ρ [kg/m^3]	: 1190
Thermal conductivity, k [$W/(mK)$]	: 0.19
Specific heat, c_p [$J/(kgK)$]	: 1140
Melting point [$^{\circ}C$]	: 150–160
Thermal diffusivity, α [m^2/s]	: 1.08×10^{-7}
Tensile strength at $20^{\circ}C$ [MPa]	: 72
Tensile strength at $73^{\circ}C$ [MPa]	: 35
Flexural strength at $20^{\circ}C$ [MPa]	: 110

The large scale turbine impingement cooling passages have been manufactured in-house by ATME and they are completely detachable from the wind tunnel in order to allow easy access to the heater grids facilitating also the quick investigation of different channel geometries by a simple replacement.

3.4 Instrumentation

The various experimental tasks undertaken in the course of this study have used a variety of measurement techniques involving various instruments. Both time averaged and instantaneous measurements have been made possible using the electronic equipment and data acquisition system of the tunnel. The operational function of all the instrumentation used in the experimental arrangement is discussed in brief. The following paragraphs contain a short description of the specifications of the main instruments in the experimental assembly.

Static pressure tappings

Many parts used for the construction of this small wind tunnel are fitted with a number of static pressure tappings. Aluminium tubes ($2mm$ O.D. and $1.15mm$ I.D.) specified for fluidic connection and bought from LEMO connectors, were embedded into the walls of the tunnel at different positions in order to carry the pressure levels to the pressure scanner device. The wind tunnel ducting is equipped with fourteen static pressure taps. Eight of them are installed directly upstream of the heater mesh and the remaining six are located $150mm$ downstream of the heater mesh. They are embedded around the whole flow path in order to verify the uniformity and the average pressure level at these particular measurement locations (see Figure 3.3). Additionally,

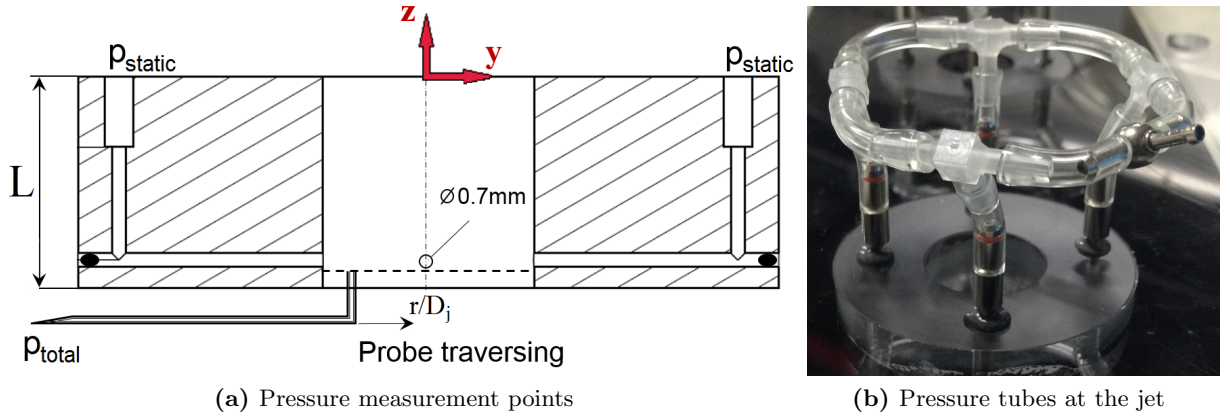


Figure 3.8: Schematic representation of the pressure measurement points for determination of local jet massflow variations

four static pressure tapings were drilled at the exit of the test models evaluating the pressure drop of the narrow impingement channels.

The determination of flow distribution among each individual jet was accomplished by static pressure tapings and Pitot probes inserted from the sidewall of the channel evaluating the velocity profiles in the spanwise direction. The measurement points, indicated in Figure 3.8, were carried out a few millimetres upstream of the nozzle exit eliminating deflection effects of the downstream jets. Four static pressure taps, diameter of 0.7mm and equally distributed around the perimeter of each jet provided the level of static pressure. Total pressure distributions were measured by a traverse of a Pitot tube of 0.6mm (I.D.) and 1mm (O.D.). Local jet discharge coefficients were therefore evaluated for each individual jet over a range of Reynolds numbers similar to the heat transfer tests.

Massflow determination

The air exhausts at the exit of the narrow impingement channel to the driving vacuum pump. The total massflow through the wind tunnel is controlled via a throttle valve and evaluated using a laminar flow element mounted upstream of the vacuum pump. The jet average Reynolds number, based on jet the diameter (D), is calculated from the total massflow rate as follows:

$$Re_D = \frac{4\dot{m}}{nD\mu} \quad (3.5)$$

where n is the total number of impingement holes, and μ is the dynamic viscosity calculated at hot conditions (heater mesh in operation). The laminar flow element is from TetraTec Instruments, model type LFE 50MC02-06 with an operational nominal flow range until $29,000\text{l}/\text{min}$. The pressure drop in the laminar flow element is transferred as a current signal in a PC where the evaluation of massflow is made possible via LabVIEW considering also the calibration parameters of the device. The temperature of the flow in the LFE is measured with a J -type thermocouple inside the exhaust pipe for more accurate determination of air properties. However, the absolute pressure in the laminar flow element is calculated (with the current measurements) with a standard error of $\pm 1000\text{Pa}$, and thus, the air density is evaluated with an accuracy of $\pm 0.0012\text{kg}/\text{m}^3$ at 20°C . As a result, the massflow, and therefore the jet averaged Reynolds number can be only determined with a certain accuracy. The standard error in the calculation of Re_D was parabolically reduced at higher flow speeds. Typical uncertainties in the determination

of Reynolds number are in the order of 6%, 3% and 1% for Re_D of 10,000, 30,000 and 75,000, respectively, indicating that the overall mass flow rate is accurately determined.

DC–Power Supply

The heating of the flow is achieved by supplying current in the metallic heater meshes using a power supply equipped with advanced DC rectifiers of PSP family. The complete system consists of a single cabinet designed for air cooling. This compact DC rectification system is based on modular technology built into sturdy steel cabinet with front doors and removable side panels offering accessibility, flexibility and reliability. The maximum power output of the DC unit is $30kW$ ($60V-500A$), while the specifications of the device are summarised as follows:

Main voltage [-]	: $3 \times 400V / 50Hz$
Input current [A]	: 84
Main power [kVA]	: 58
DC Power Output [kW]	: 30 ($60V/500A$)
residual ripple	: less than 3% over full range
Adjustment	: constant current and voltage control
Control accuracy	: less than 1%
Cooling	: air cooling
Ambient temperature and altitude	: up to $35^\circ C$ and 1000m
Dimensions per cabinet	: W/D/H=1000/800/2000mm(+100mm base)

The maximum output power is obtained when the resistance of the object where the electrodes are connected equals the resistance calculated from the specifications of the device. This means that in order to achieve full power output the total resistance of the heater grid configuration should be around $R_{DC}=0.12\Omega hm$. The resistance of a single mesh layer was $0.375\Omega hm$ and only slightly increased at higher flow rates due to the higher mesh temperature. Therefore, the usage of two parallel mesh layers will give a final heater mesh configuration resistance of approximately $R_m=0.125\Omega hm$ which is very close to the requirements of the DC-Power supply.

Temperature acquisition

The overall instrumentation is equipped with a DAQ chassis (NI-CompactDAQ USB) on which various acquisition modules can be installed. For the purposes of temperature acquisition, a 16-Channel thermocouple input module (NI-9213) is installed on the CompactDAQ system. Any type of thermocouple can be connected to the module which is programmable with LabVIEW. In this study, K -type thermocouples are used for the determination of the gas temperature which drives the transient experiment. K -type thermocouples are relatively inexpensive and consist of Chromel (90% Ni and 10% Cr) and Alumel (95% Ni, 2% Mn, 2% Al and 1% Silicon). Their temperature range is between $-300^\circ C$ and $1350^\circ C$ and their sensitivity is approximately $41\mu V/^\circ C$. Although, the production process of thermocouples is well defined by the manufacturers, the response of a particular thermocouple depends on the exact composition of the metals used to manufacture it, resulting in a slightly different response when thermocouples of the same K -type are exposed to the same measurement conditions. Subsequently, thermocouples need to be calibrated in order to deliver interpretable measurement information.

The calibration curve for a thermocouple is obtained by comparing the thermocouple output to precise thermometer data. For the calibration purposes of this study, the sixteen thermocouples were placed into a liquid bath (LAUDA RK 20 KS) together with a high precision

thermometer, OMEGA DP251, which was used as reference temperature ($\pm 0.005^\circ C$). The temperature of the bath was gradually increased from $5^\circ C$ to $95^\circ C$ and then decreased from $100^\circ C$ to $10^\circ C$, with $10^\circ C$ steps on both cases, in order to consider also hysteresis phenomena during the calibration. The reference temperature has been compared with the average value of 1000 samples of the individual thermocouples acquired at $100 Hz$. The standard deviation of the individual thermocouples inside the water bath was always below $\pm 0.07^\circ C$. Typical error between the average values of the calibrated sixteen thermocouples inside the bath was below $\pm 0.06^\circ C$. During the preliminary experiments, made in order to test the functionality of the heater mesh, ten thermocouples were installed. Five of them were installed in the plenum and the rest five were placed directly upstream of each impingement hole in order to acquire the temperature step for each individual jet. Additionally, a *J*-type industrial thermocouple was used to measure the temperature upstream of the laminar flow element allowing the determination of air properties, and therefore, for the evaluation of the mass flow rate.

Camera settings and resolution

The evolution of the liquid crystals was recorded with a high definition RGB camera, model AVT Pike-310C, connected with a frame grabber of $800 Mbit/s$ to the tower of a 16GB-RAM computer. These hardware capabilities allowed real time image saving, and thus, images with great spatial resolution of approximately 6 pixels/ $(mm)^2$ to be acquired. The typical spatial resolution is translated to approximately 1735 pixels per impingement hole area while the recorded video data were digitised at a frame rate of $20 Hz$. Uniform and strong illumination throughout the length of the test rig was provided by two fluorescent lights (colour temperature, $6000 K$) mounted on both sides of the test rig in order to avoid shadows and reflections. The external surfaces of the models were cleaned with alcohol before the execution of each experiment ensuring dust removal and clear optical access.

3.5 Concluding Remarks

The experimental requirements and the final configuration of the experimental facility have been described as well as the specifications of the test models involved in the present experimental investigation. The specifications of the heater mesh configuration have been also presented. The initial tests undertaken to verify the operability of the wind tunnel within the required mass flow range and temperature steps, as well as the accuracy of the measurement equipment of the tunnel have been also described.

The initial tests indicated that the narrow impingement passage test rig is equipped with all the necessary electronics and other instrumentation for accurate measurements. The accuracy during the operation of various critical wind tunnel components, such as the heater grid configuration and the laminar flow element, did allow high quality transient liquid crystal measurements to be carried out.

MEASUREMENT TECHNIQUE

This chapter presents the transient liquid crystal measurement technique which was used for the experiments carried out in the course of this study. The measurement technique considers also thermocouple thermal inertia effects caused by the relatively low velocities at the measurement points. Thermocouple time constants effects on the calculation of the impingement heat transfer coefficient are also discussed. The chapter concludes with the experimental uncertainties.

4.1 Introduction

Convection transport processes are very difficult to be evaluated analytically or numerically and the need for a better understanding of various heat transfer mechanisms led to the development of heat transfer coefficient measurement techniques. Significant improvements were achieved for the complicated turbomachinery flows, which are characterised by three-dimensional turbulent flows, and thus include relatively complex spatial heat transfer coefficient distributions.

For convective heat transfer experiments, accurate wall temperatures are essential since the heat transfer coefficient is determined by the *Newton's law of cooling* as:

$$h = \frac{\dot{q}}{T_s - T_\infty} \left[\frac{W}{m^2K} \right]$$

where, \dot{q} is the rate of wall heat flux at the interface between the fluid and the solid boundary and the temperatures T_s and T_∞ are the wall (or surface) and fluid temperature, respectively. In general, a variety of measurement techniques may be applied in order to evaluate convection coefficients within a model of a turbine cooling passage. Steady state, transient or hybrid techniques, using infrared cameras, thermocouples, heat flux sensors as well as temperature or even pressure sensitive paints can be used and combined providing local or area averaged results. Note that in an ideal experimental procedure with the identical flow conditions, the different measurement techniques will provide very similar results given that the heat transfer coefficient is a property of flow and not of the fluid. However, the objective of this thesis is a comparison of the heat transfer characteristics of different narrow impingement cooling channel geometries, and therefore, the transient liquid crystal technique which is well documented in the literature over the last 20 years, was selected.

4.2 Transient Liquid Crystal Technique

4.2.1 The transient technique

The principle of a transient technique is to observe the time response of the surface temperature to a known step change of the driving temperature. Knowing the initial temperature of the surface and the material thermal properties of the model, local heat transfer coefficients on the model surface can be determined by analysing the surface temperature evolution during the transient test. Contrary to the steady state method, the transient technique is of short duration so that lateral conduction inside the test model remains small compared to surface heat transfer, and can thus be neglected. Under specific model thermal properties, the thermal conduction into the model is assumed one-dimensional and no correction needs to be applied accounting for lateral effects. Different techniques have been used to generate the step change in the driving temperature including fast acting valves, model positioning activators or heater mesh configurations. More details can be found in Section 3.2.1.

4.2.2 Surface temperature measurements

The surface temperature distributions were determined using Thermochromic Liquid Crystals (*TLC*) which, as their name says, respond to a local temperature change by a local colour change. The main advantage of liquid crystals is the direct temperature determination of the complete model surface, which means high spatial resolution, and the minimum intrusiveness of the flow.

Thermochromic liquid crystals are organic compounds derived from esters of cholesterol which have two distinct melting points. At the first melting point, the solid turns to a cloudy liquid and at the second the liquid becomes clear. This cloudy phase, known also as mesomorphic phase, is a condition intermediate between a true solid crystal and an isotropic liquid. In this phase the molecules are movable but still organised in the form of a helical pattern. Mechanically this substance acts like a liquid, but it still has many of the optical properties of crystals. A typical liquid crystal substance reflects lights of different wavelengths more or less strongly due to a re-orientation (rotation) of the liquid crystal's helical lattice depending on the temperature (Kleine, 1968). The selective light reflection usually gives rise to a spectrum of colours on the heat transfer model surface. Detailed description of thermochromic liquid crystals regarding their physical and chemical properties as well as other characteristics can be found in Kasagi et al. (1989), the review study of Parsley (1991) or various operation handbooks (i.e. Hallcrest). Therefore, no additional information will be given here.

For the purposes of this thesis, liquid crystals are practically temperature indicators that modify incident white light and display colour whose wavelength is proportional to temperature. Therefore, a specific correspondence between the hue/intensity of the colour and the indication temperature can be obtained by proper calibration. Liquid crystals are usually painted over the whole surface of interest for temperature visualisation purposes providing the spatial distribution of the wall temperature. The phenomenon is reversible, repeatable, and therefore, the painted model can be used for heat transfer experiments over a considerable period of time. Due to their slightly milky appearance a black background is required ensuring that all light transmitted through the liquid zone is absorbed. As a result, reflections which compete with the resulting image are avoided providing brilliant colours. Therefore, a sprayable black paint was applied above the liquid crystal coating allowing observation of the colours from the back of the target plate, as shown in Figure 4.1. The total thickness of the coating was measured with a surface

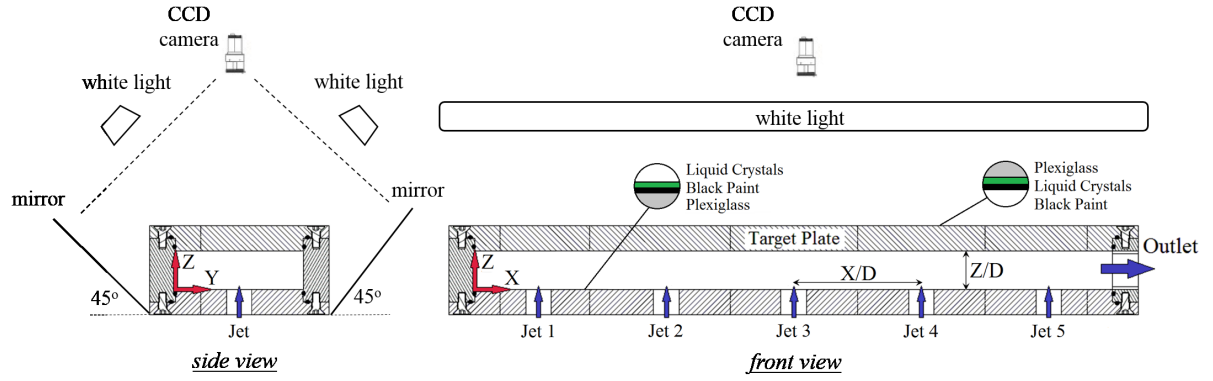


Figure 4.1: Experimental details for the video acquisition

roughness tester between $40\mu m$ and $50\mu m$, and therefore, the time response of the painting was assumed negligible ($\sim 20msec$) according to Ireland and Jones (2000). Note that for the jet plate experimentation the target plate was replaced by a transparent one and the coatings were painted in the opposite order. Monitoring the signal of liquid crystals on the sidewalls was achieved by mirrors installed at an angle of 45° degrees as illustrated in Figure 4.1.

Uniform and strong illumination through the whole length of the test rig was achieved by a pair of two white fluorescent lights (colour temperature- $6000K$) mounted on both sides of the test rig in order to avoid shadows and reflections. The test model surface was cleaned with alcohol after the execution of each experiment in order to ensure clean optical access on the examined surfaces.

4.2.3 Liquid crystal calibration

Using liquid crystals, the temperature is indirectly measured and an exact relationship between the surface temperature and a distinct indication event of the TLC has to be obtained. Liquid crystals progressively exhibit all colours of the visible spectrum as they are heated within a certain temperature range. In this study, liquid crystals with $1^\circ C$ bandwidth (red start to blue start) were used in order to reduce the overall uncertainty in the determination of the specific hue/intensity values. The sprayable liquid crystals were bought from Hallcrest Ltd, type R38C1W.

The calibration of liquid crystals was carried out in a single jet test facility under the same conditions as the main experimentation resulting in a kind of an *in-situ* calibration. Figure 4.2 shows a schematic representation of the single impinging jet calibration test rig and a picture taken from the CCD camera position. The test model used for the calibration is made of a thick acrylic plate ($40mm$) painted with liquid crystals and black paint. A K -type thermocouple was mounted on the exposed surface of the plate acquiring the stagnation wall temperature. The calibration procedure was quite straightforward. The temperature of the jet was increased to the colour play temperature of liquid crystals at around $37.5^\circ C$. After a considerable amount of time which allowed the assumption of steady state conditions, the temperature of the impinging jet was gradually increased with small temperature steps of about $0.06^\circ C$, and the recorded images were chromatically analysed around the surface thermocouple.

Primarily, two different methods are commonly used for calibration. Hue methods, based on the visual colour perception derived from the HSL colour model, and maximum intensity methods, based on RGB camera channels. The calibration curves for the hue value and the

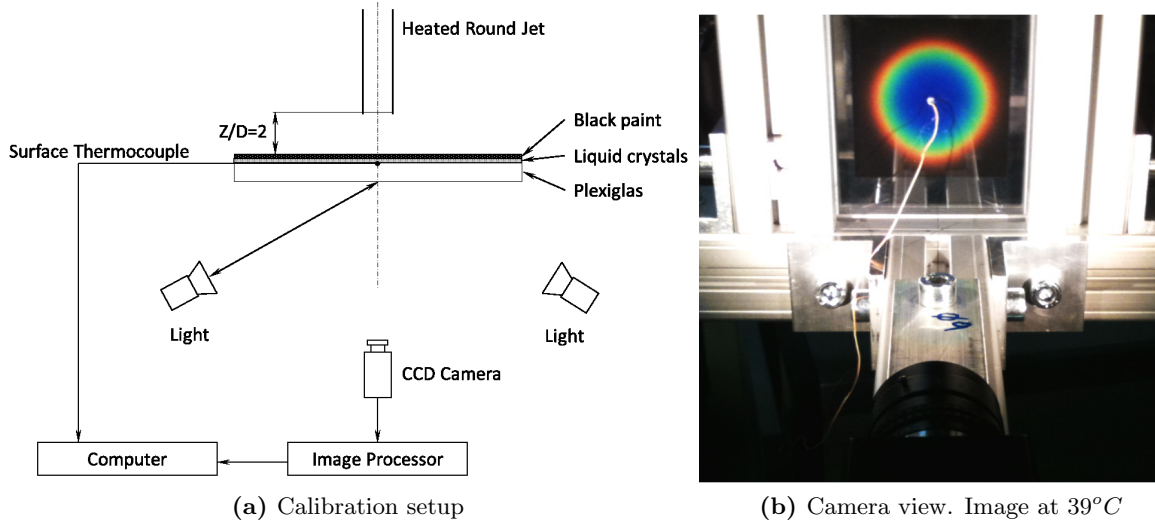


Figure 4.2: Liquid crystal calibration single jet facility

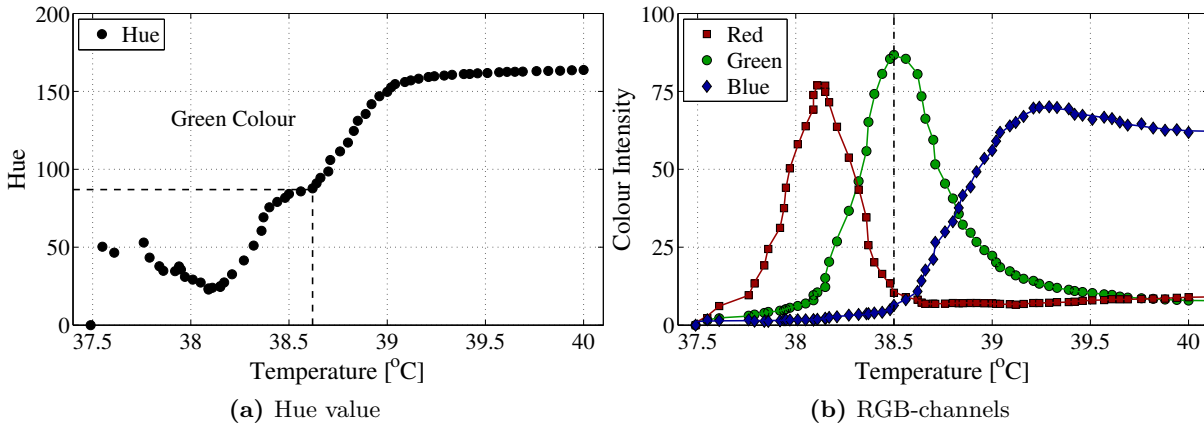


Figure 4.3: Liquid crystal calibration curves

RGB channels are both illustrated in Figure 4.3. As expected, the hue value of the liquid crystals is increased with temperature with higher slope around the green region (80°). This means that the hue value which corresponds to the green colour can be determined with lower uncertainty compared to other colours, and hence, $T_G = 38.6 \pm 0.15^{\circ}\text{C}$. On the other hand, the RGB component of interest for the heat transfer experiments is the green channel which provides a maximum intensity at a specific temperature, which is $T_{G_{max}} = 38.5 \pm 0.1^{\circ}\text{C}$. As both methods offer advantages and disadvantages, a comparison between them on the evaluation of heat transfer coefficient is presented in Section 4.3.4.

4.3 Data Reduction

4.3.1 Experimental procedure

The experiments were carried out using the transient liquid crystal technique described in detail by Baughn (1995), Ireland et al. (1999) and Stasiak and Kowalewski (2002). This technique uses the full surface temperature history derived from the colour of the liquid crystals in order to obtain full surface heat transfer coefficient distributions, which actually means great spatial resolution with minimum intrusiveness of the flow.

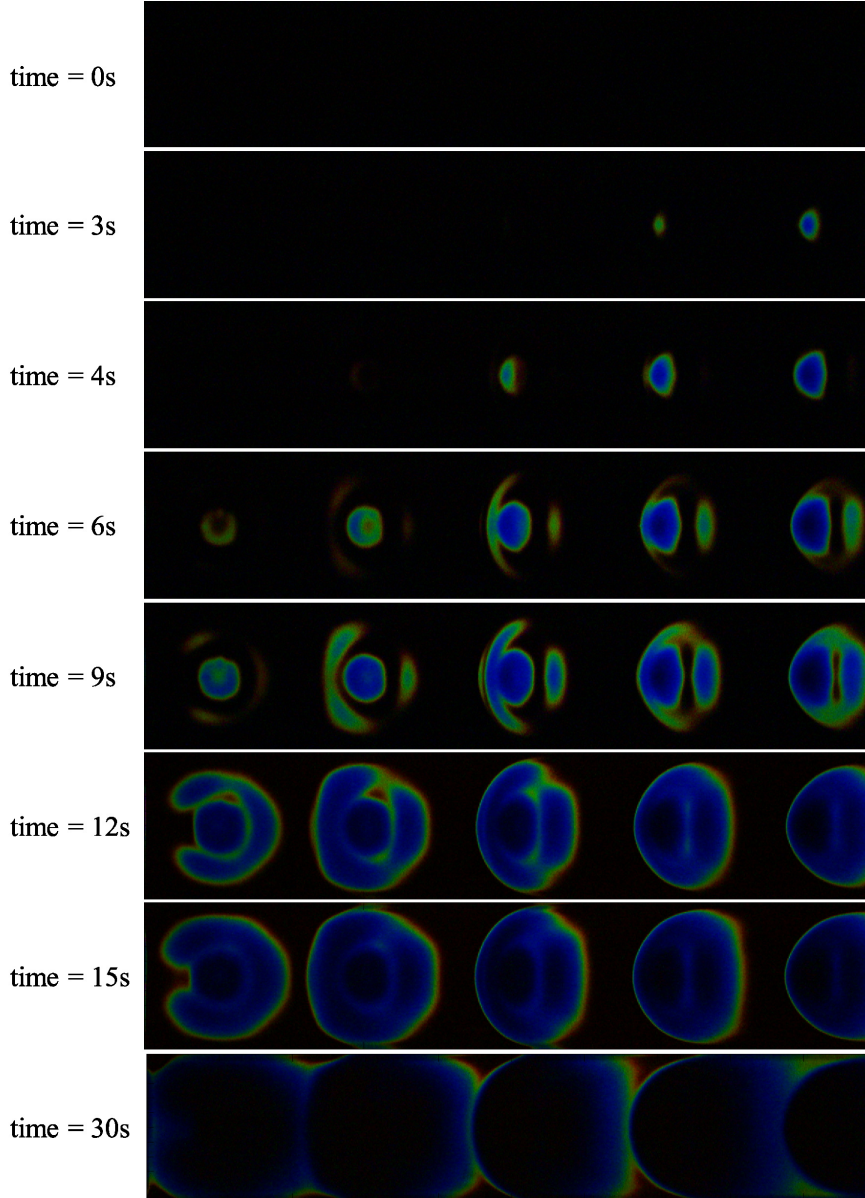


Figure 4.4: Various frames of liquid crystal evolution with time. $T_{LC}=37.5\text{--}39.6^{\circ}\text{C}$, $\theta=0.45$, $Z/D=1$, $Re_D=40,000$

In a typical transient liquid crystal experiment, the flow initial temperature (T_o) is subjected to a sudden temperature change and the evolution of a liquid crystal isotherm (T_{LC}) is optically monitored. This experimental procedure was also considered in the course of this study. First of all, the vacuum pump, which operated at constant volumetric flow conditions, was set to operate at a slightly higher pumping speed accounting also for the increase of the kinematic viscosity of air at higher temperatures during the calculation of the desirable Reynolds number, which was determined at hot conditions. For example, kinematic viscosity of air at ambient pressure and 60°C is about 20% higher compared to 20°C . Once the cold conditions were stabilised, a sudden change of the mainstream temperature was obtained by applying electrical power to the metallic heater mesh, and the evolution of the liquid crystals was recorded with a CCD camera at a frame rate of 20Hz. The video frame corresponding to the beginning of the transient test (zero point) was determined by an LED powered by the copper electrodes of the heater. The video was then cropped at the required pixel size and prepared for the post processing. Figure

4.4 shows various time frames of the liquid crystal evolution after the initiation of the heating step. Note also that some main characteristics of the generated flow domain, as for example the development of the crossflow and the formation of the horseshoe vortex around the downstream jets are visible without post-processing providing already a sense of surface flow visualisation.

4.3.2 Semi-infinite model

The key feature of the transient liquid crystal technique is the time measurement from the beginning of the transient test to the appearance of the calibrated liquid crystal colour. This creates a specific correspondence for the detection time of liquid crystals (t_{LC}) and the wall temperature (T_{LC}) at that moment. If the thermal conductivity of the model where the liquid crystals are sprayed on, is sufficiently low, the wall temperature response is limited to only a thin layer near the wall surface and the lateral conduction can be neglected. Therefore, the temperature evolution into the model is assumed to be one-dimensional, $T(z, t)$, and a semi-infinite medium approach, $T(z \rightarrow \infty, t) = T_o$, is used for the solution of Fourier's equation which yields to (Incropera et al., 2007):

$$\frac{\partial T}{\partial t} = \frac{k}{\rho c} \frac{\partial^2 T}{\partial z^2}$$

Considering the initial conditions and a surface convection boundary condition in the form of:

$$T(z, 0) = T_o, \quad -k \left. \frac{\partial T}{\partial z} \right|_{z=0} = h[T_g - T(0, t)]$$

the relation between the wall surface temperature and the heat transfer coefficient h at the interface between the fluid and the model surface ($z=0$), can be obtained as follows:

$$\theta = \frac{T_{LC} - T_o}{T_g - T_o} = 1 - \exp\left(\frac{h^2 t_{LC}}{\rho c k}\right) \operatorname{erfc}\left(\frac{h\sqrt{t_{LC}}}{\sqrt{\rho c k}}\right) \quad (4.1)$$

where θ is the non-dimensional temperature ratio and ρ , c and k are the density, specific heat and thermal conductivity of the model, respectively. Knowing the detection time of liquid crystals for each pixel, the local heat transfer coefficient can be calculated given that all other quantities are accurately known. However, in most cases it is extremely difficult or even impossible to obtain an ideal step change in the mainstream temperature. In this case, Duhamel's superposition theorem (Kwak, 2008) can be applied approximating the real gas temperature evolution by a series of ideal temperature steps as follows:

$$T_{LC} - T_o = \sum_{i=1}^N \left[\Delta T_{g,(i,i-1)} \times \left[1 - \exp\left(h\sqrt{\frac{t_{LC} - t_i}{\rho c k}}\right) \exp\left(h^2 \frac{t_{LC} - t_i}{\rho c k}\right) \right] \right] \quad (4.2)$$

where ΔT_g and t_i are the gas temperature and time changes obtained from the plenum temperature history. Note that $T_g(t)$ was corrected for thermocouple thermal inertia. More details can be found in Section 4.4.

The colour response of liquid crystals to temperature is very fast and the response time is the order of a few milliseconds. Ireland and Jones (2000) reported values varying between $3ms$ and $10ms$ for liquid crystal coatings of $10-30\mu m$. Additionally, as shown by Vogel and Weigand (2001), for a flat plate with typical Biot numbers ($Bi \leq 1$), the error in the determined heat transfer coefficient is small and the semi-infinite body assumption can be considered valid as

long as the non-dimensional experiment time is less than a critical value:

$$\frac{\alpha t}{\delta^2} \leq \frac{1}{4} \quad (4.3)$$

where, δ is the penetration depth, t is the duration of the experiment and α is the thermal diffusivity of the model. The thickness of the plates has been chosen to be $20mm$ in order to ensure semi-infinite conditions resulting in a theoretical allowable measurement time up to $3min$.

4.3.3 Image processing

The digital image processing system used for the transient liquid crystal experiments is described in detail in Appendix B.

4.3.4 Color Hue vs. G_{max} calibration

The heat transfer coefficients were evaluated using the maximum green intensity method which is less sensitive to illumination and view angles (Poser et al., 2007; Rao and Xu, 2012). A comparison between the two liquid crystal calibration methods on the evaluation of the heat transfer level is also presented in Appendix B.

4.4 Influence of Thermocouple Thermal Inertia

In small impingement configurations with a few number of holes fed from the same plenum chamber, i.e. see Figure 4.5(a), the area ratio of the total flow areas of the jets to the flow path of the plenum feeding the jets is very small leading to very low plenum velocities. For typical engine Reynolds numbers and laboratory size test models, where jet diameters are normally varied between 5 and $25mm$, this might lead to plenum velocities in the order of $1m/s$ or even less. In such cases, it is extremely difficult to determine accurately the evolution of the plenum temperature which drives the transient experiment using commercial thermocouples due to their thermal inertia, even if their sensing junction is exposed to the flow. Furthermore, application of Duhamel's superposition theorem on the thermocouple outputs would lead to significantly over-estimated heat transfer coefficients (Terzis et al., 2012b). On the other hand, recent temperature probe developments consisting of platinum thin films painted onto quartz and cordierite hemisphere cylinders (Mansour et al., 2008) may eliminate thermal inertia effects. However, these probes are relatively costly, fragile and developed with complex manufacturing procedures. Therefore, a mathematical correction for thermocouple time constant was applied.

4.4.1 Thermocouple time constant

A fine-wire thermocouple immersed in a gas flow can be considered as a lumped capacitance body due to the small size of its junction and the metallic material. Therefore, its time response characteristics can be expressed by a first-order lag system:

$$T_g(t) = T(t) + \tau_c \frac{dT}{dt} \quad (4.4)$$

where T_g is the fluid temperature to be measured, T is the temperature corresponding to the thermocouple output and τ_c is the time constant of the thermocouple junction. The thermocouple output indicates the temperature of the surrounding fluid if τ_c is equal to zero, however, as τ_c gets larger the thermocouple output will begin to lag compared to the fluid flow temperature,

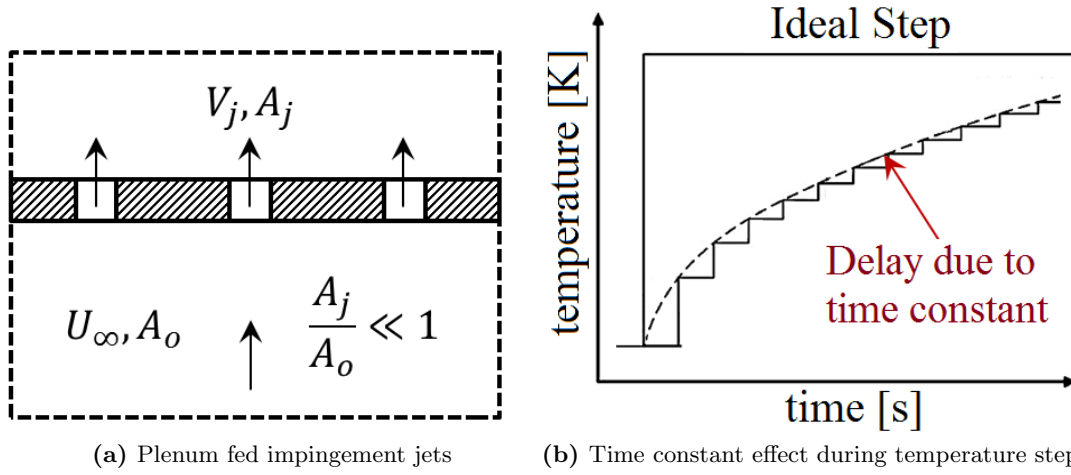


Figure 4.5: Influence of thermocouple time constant on temperature measurements


as shown in Figure 4.5(b). If the time constant is known in advance, the fluid temperature can be easily obtained from Equation 4.2 and Duhamel's superposition theorem can be intrepidly applied. However, even if τ_c is given by the manufacturer's specifications, in reality, it is practically unknown and unavailable due to the large dependence on the flow conditions and/or the physical properties of the surrounding fluid.

In the literature, there are many studies focused on the experimental determination of thermocouple time constants. These include *Internal Heating Techniques* (IHT) where heating of the thermocouple junction and wires is obtained by applying electrical pulses. The observation of the decay in junction temperature after the removal of the heating current allows the determination of the time constant under constant flow and surrounding temperature conditions (Ballantyne and Moss, 1977; Park and Ro, 1996). However, IHT methods are not satisfactory if the thermocouple is operating near its limit of survivability, while time constant determination under heating conditions is practically not allowed. Additionally, *Peltier* effects may introduce non-homogeneous heating of the wire causing additional error sources (Petit et al., 2000). Another method, known as *External Heating Techniques* (EHT), examines thermocouple response characteristics under known changes in the surrounding fluid temperature. The fluid can be either gas, as for example in the studies of Miles and Gouldin (1993) and Farahmand and Kaufman (2001), or liquid, e.g. Murdock et al. (1963). The main advantage of this method is the capability of determining time constants under both heating ($T_g \geq T_{jct}$) and cooling ($T_g \leq T_{jct}$) conditions. A separate category of EHT is the dual-probe technique in which thermocouple time constants are deduced by comparing the responses of two different thermocouples with unequal time constants subjected to identical external temperature fluctuations (Strahle and Muthukrishnan, 1976; Tagawa et al., 1998; Kobayashi et al., 2008; Tagawa et al., 2011). Other approaches include infrared radiation (Melvin, 2002) or heating with a laser (Beckman et al., 1993).

Physically, the time constant represents the time it takes for a system step response to reach 63.2% of its final asymptotic value. In this study, τ_c was determined by a step response method. Thermocouples of different wire diameter were installed in the plenum chamber of the test rig experiencing airflows of constant velocity magnitude. The flow was then subjected to a sudden temperature change (heating or cooling) by activating the heater mesh. The time constant of a given thermocouple was determined by measuring the time after the initiation of the thermal step and it was defined as the time required to reach 63.2% of the steady-state

Table 4.1: K-type thermocouple thermal properties and dimensions

Parameter	Units	Chromel	Alumel	TC junction
ρ	kgm^{-3}	8730	8600	8665
c_p	$J(kgK)^{-1}$	448	523	486
k	$W(mK)^{-1}$	19	30	25

d (mm)	d_{jct} (mm)	d_{jct}/d	TC junction
0.08	0.21	2.63	
0.13	0.31	2.38	
0.25	0.54	2.16	
0.51	1.04	2.05	
0.81	1.52	1.88	

conditions. Conduction and radiation errors were neglected because they principally affect the average temperature indication rather than the dynamic response.

4.4.2 Determination of τ_c for various conditions

In this work, K-type thermocouples with exposed junction consisting of *chromel-alumel* wires were used due to the fact that the physical properties of the wires, shown in Table 4.1, are not greatly different, and therefore, the junction material can be considered as an equivalent mixture of the two wire pairs. Each thermocouple had a different wire diameter varying between 0.08 and 0.81mm according to manufacturer's specifications (OMEGA Engineering). For the measuring junction, close pictures indicated that a spherical profile better approximates the shape of the welded connection. The bead-to-wire diameter ratio was found to be dependent on the wire size, as shown also in Table 4.1, with values not very far from the widely accepted ratio of 2.5. However, it should be noted that the material and the real shape of the junction are practically unknown due to the great dependence on the welding procedure.

Figure 4.6 indicates thermocouple outputs at various temperature steps and wire diameters on both heating and cooling conditions. The plenum velocity was 0.5m/s. As expected, the smaller the wire diameter is, and hence the measuring junction, the quicker is the response of the thermocouple at a given temperature step change, no matter whether the sensor experiences a heating or a cooling process. Steady-state conditions are reached after approximately 10s when a fine wire thermocouple is used ($d=0.08mm$), while the indication temperature of a relatively thick thermocouple ($d=0.81mm$) never reaches the asymptotic value even if the time after the initiation of the thermal step is 60s. Additionally, the non-dimensional temperature is independent of the heating/cooling step suggesting a negligible effect of temperature level on the response time. The typical duration of a transient heat transfer experiment can be varied between 20 and 100s depending on the thickness and the thermal conductivity of the model. Therefore, a fine wire thermocouple is required in the plenum of the current test rig in order to provide a good representation of the average asymptotic value in the case of an ideal temperature step assumption. However, application of Duhamel's superposition theorem, which requires good knowledge of the driving gas temperature history, requires a correction based on the thermocouple thermal inertia. Given the step response method applied in this study, the time constant of a particular thermocouple is defined as the time required to reach 63.2% of the steady-state gas temperature after the initiation of the heating or cooling step. It should be

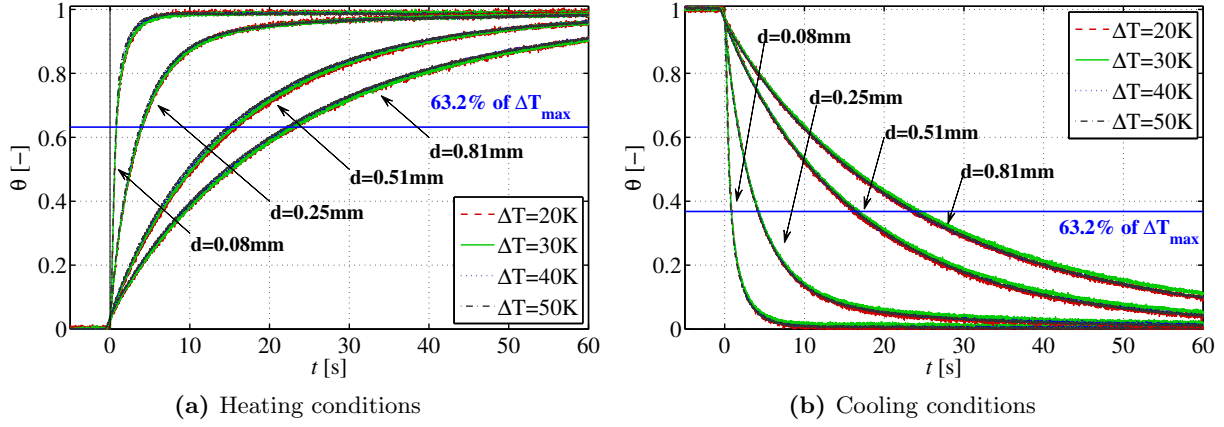


Figure 4.6: Thermocouple outputs at various temperature steps. $U_\infty = 0.5 \text{ m/s}$

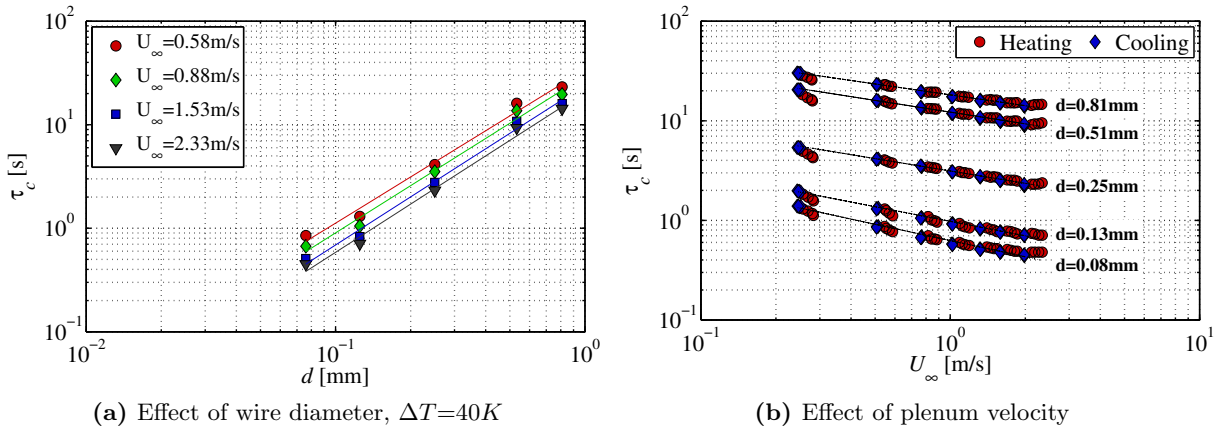


Figure 4.7: Thermocouple time constant versus (a) wire diameter and (b) plenum velocity

noted, however, that the τ_c calculated by this method is only an averaged representative value.

Figure 4.7(a) shows that the time constant strongly depends on the wire diameter for fixed flow conditions. The time constant can be reduced by a factor of 25 if the wire diameter of the thermocouple is reduced from 0.81 to 0.08 mm. The inclination of the lines remains constant as the airflow velocity increases, and thus τ_c is proportional to $d^{1.52}$, which is close to the exponent value of $5/3$ suggested by Park and Ro (1996). The small fluctuations from the estimated line can be attributed to measurement uncertainties during the determination of thermocouple wire diameter. Figure 4.7(b) shows the effect of plenum velocity, U_∞ . Note that the results of all the thermal steps are included on the chart given the negligible effect of temperature level observed in Figure 4.6. The higher the plenum velocity, the faster is the response of the thermocouple. Time constants are reduced however only by 50% as U_∞ increases from 0.24 to 2.3 m/s. No difference between heating and cooling was observed approximating the data in a single correlation line. Additionally, a reduction of the slope of the trendline is observed as the wire diameter, and hence the measuring junction size is increased. This is attributed to the lower convective heat transfer coefficients around the measuring junction that makes the effect of airflow velocity less intense. The experimental data were successfully correlated by the following empirical equation:

$$\tau_c = 27.3d^{1.52}U_\infty^{-n}; \text{ where, } n = 0.35d^{-0.16} \quad (4.5)$$

where d is the wire diameter in mm, U_∞ is the airflow velocity in m/s and n is a function of

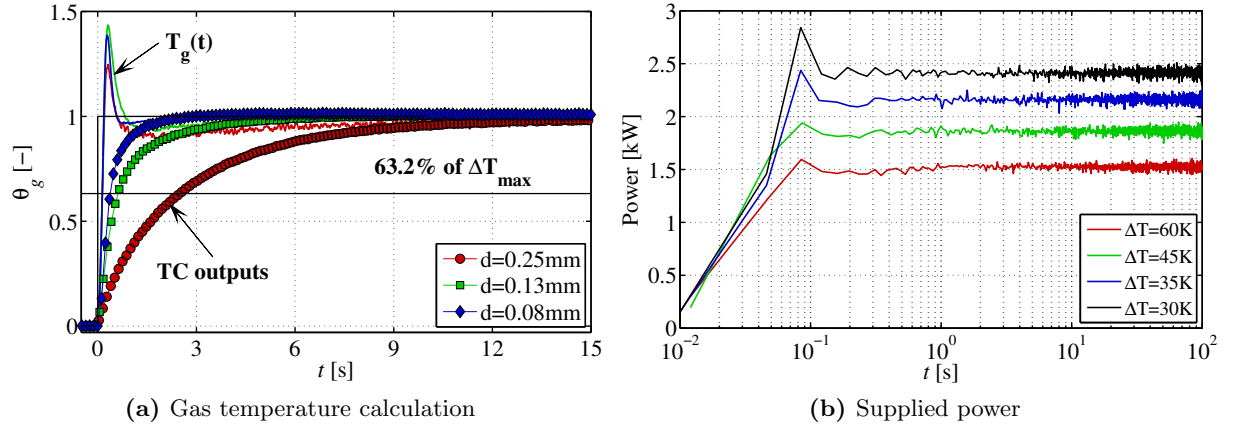


Figure 4.8: (a) Plenum temperature history extracted from thermocouple outputs and (b) DC-power supplied in the heater mesh.

the thermocouple size typically varied between 0.3 and 0.7 as noted by [Kee et al. \(1998\)](#). In this study, exponent n was varied between 0.34 and 0.54. τ_c can be calculated in seconds within an accuracy of 7.5% in the range of $d=0.08\text{--}0.81\text{mm}$ and $U_\infty=0.25\text{--}2.3\text{m/s}$. The main advantage of calculating time constants through the wire diameter is that the dimensions and the shape of thermocouple can be directly taken into account. A heat transfer correlation for flow over K -type thermocouples with exposed junction can be found in [Terzis et al. \(2012b\)](#).

4.4.3 Calculation of driving temperature

Figure 4.8 indicates the hot gas temperature and the temperature history in the plenum as acquired from three different thermocouples. $T_g(t)$ was calculated using equation 4.4 and the experimentally obtained thermocouple time constant. It is observed that the hot gas temperature is independent of the thermocouple size, which means that all the thermocouples in the plenum experience the same flow temperature history. Additionally, an overshooting of the plenum temperature is observed directly after the initiation of the heating step. This is attributed to the transient response of the DC-power supply and a short duration power overshoot occurring during the adjustment of the desirable electrical energy according to the heater mesh resistance. This transient response of the device was measured less than 50ms by [Terzis et al. \(2012a\)](#); however, it unavoidably affects the temperature of the heater mesh, which is the only resistance source in the circuit, and a short thermal overshoot is generated in the plenum.

4.4.4 Effect on heat transfer coefficient

As discussed above, the outputs of various thermocouples of different wire diameter, provide the same plenum temperature history calculated from Equation 4.4. This gave confidence in order to consider the extracted hot gas temperature evolution for the evaluation of the heat transfer coefficients. The effect of thermocouple thermal inertia on the level of evaluated heat transfer is described in detail by [Terzis et al. \(2012b\)](#) and summarised in Appendix C.

4.5 Experimental Uncertainties

The first step in defining the uncertainty of the experimental testing is to identify the sources that could introduce and propagate an error in the final results, no matter whether the error is

systematic or random. These factors can be categorised in those affecting the determination of the massflow rate, which is the pressure drop and the temperature in the laminar flow element, and to those affecting the calculation of the heat transfer coefficient. Given that the specific uncertainty in the determination of massflow rate, and hence, the Reynolds number depends on the accuracy of the measurement equipment, this section presents an uncertainty analysis for the heat transfer results of the thesis.

4.5.1 Uncertainty analysis

The uncertainties estimation of the heat transfer results was based on the method of small perturbations outlined by Moffat (1988) and applied in transient liquid crystal experiments by Yan and Owen (2002) and Owen et al. (2003). This approach uses the Root-Sum-Square (RSS) method combining the individual uncertainty terms of the independent variables of Equation 4.1, in the calculation of the dependent variable, which is the heat transfer coefficient h . The independent variables which affect the calculation of h are the plenum temperature history, $T_g(t)$, the detection time of liquid crystals t_{LC} , the liquid crystal temperature (T_{LC}) and the model material thermal properties (ρck).

Using non-dimensional parameters, the solution of one-dimensional transient heat conduction equation (Equation 4.1) for the semi-infinite plate can be written as follows:

$$\theta = 1 - e^{\alpha^2} \operatorname{erfc}(\alpha) \quad (4.6)$$

with,

$$\theta = \frac{T_{LC} - T_o}{T_g - T_o} \quad \alpha = h \sqrt{\frac{t_{LC}}{b}} \quad (4.7)$$

Assuming that the random uncertainties of the measured temperature, time event and model thermal properties are independent of each other, the following expressions can be obtained:

$$P_\alpha^2 = \left(\frac{d\alpha}{d\theta} P_\theta \right)^2 \quad (4.8a)$$

$$P_h^2 = \left(\frac{dh}{d\alpha} P_\alpha \right)^2 + \left(\frac{dh}{db} P_b \right)^2 + \left(\frac{dh}{dt_{LC}} P_{t_{LC}} \right)^2 \quad (4.8b)$$

$$P_\theta^2 = \left(\frac{d\theta}{dT_{LC}} P_{T_{LC}} \right)^2 + \left(\frac{d\theta}{dT_o} P_{T_o} \right)^2 + \left(\frac{d\theta}{dT_g} P_{T_g} \right)^2 \quad (4.8c)$$

where the uncertainty P is the product of the standard deviation (σ) and the Student's factor taken equal to 2 due to the large number of samples. Therefore, P represents the 95% confidence range for a given measurement ($\pm 2\sigma$) assuming that the data display Gaussian distribution.

The uncertainty in the calculation of heat transfer coefficient (h) at a given measurement point can be calculated by substituting Equations 4.7, 4.8(a) and 4.8(c) to Equation 4.8(b):

$$P_h^2 = \left(\frac{dh}{d\theta} \right)^2 \left[\left(\frac{d\theta}{dT_{LC}} P_{T_{LC}} \right)^2 + \left(\frac{d\theta}{dT_o} P_{T_o} \right)^2 + \left(\frac{d\theta}{dT_g} P_{T_g} \right)^2 \right] + h^2 \left[\left(\frac{P_b}{2b} \right)^2 + \left(\frac{P_{t_{LC}}}{2t_{LC}} \right)^2 \right] \quad (4.9)$$

The total uncertainty can be therefore evaluated in a pixel size level indicating the spatial error distribution on the model surface. Obviously, the error propagation analysis is independent

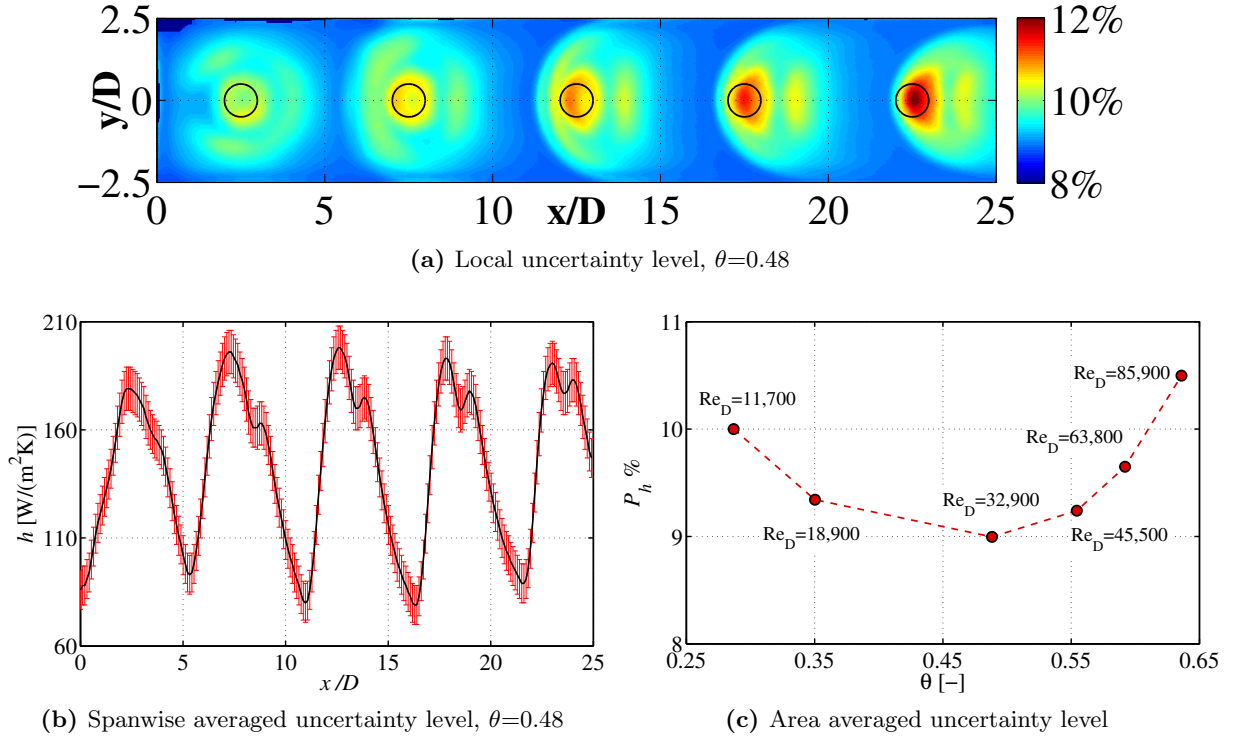


Figure 4.9: Uncertainty level in the evaluation of heat transfer coefficient

of the channel geometry, and hence, only the results for the target plate of the inline pattern of $Z/D=1$ are presented.

Figure 4.9(a) shows the target plate uncertainty level, as caused by the individual measured parameters. The overall uncertainty is spatially varied and increases in the stagnation point regions where the detection time of liquid crystals is relatively short. This means that higher heat transfer coefficients are evaluated with higher uncertainty. A detailed example is shown in Table 4.2 which indicates the uncertainty level of the measured parameters and their individual error propagation in the final result for three different cases: a typical low- $65W/(m^2K)$, medium- $125W/(m^2K)$ and high- $300W/(m^2K)$ heat transfer coefficient. For the temperature acquisition typical standard deviations were $\pm 0.08K$ for the initial temperature (T_o) and higher for the hot gas temperature (T_g), similar to the results of Hoefler et al. (2012) and Schueren et al. (2013). T_g uncertainty was varied due to the lower temperature step applied at higher Reynolds numbers in order to maintain an approximately constant liquid crystal appearance time. Therefore, typical values of hot gas temperature standard deviations were varied between $\pm 0.15K$ and $\pm 0.3K$ for the highest and lowest Reynolds number. For the present example, P_{T_g} was ± 0.43 ($\pm 2\sigma$). For the wall temperature, the uncertainty was $\pm 0.1K$ obtained from the liquid crystal calibration curve (see Figure 4.3). These uncertainties, P_{T_o} , $P_{T_{LC}}$ and P_{T_g} , correspond to about 1%, 1.3% and 2.95% uncertainty level in the calculation of the heat transfer coefficient and they are independent of the level of heat transfer. The contribution of model thermal properties on the total uncertainty remains also constant at 5%. Another important factor for the overall uncertainty is the magnitude and determination of the liquid crystal detection time which was $t_{LC} \pm 0.1$. Combining all the above error propagation factors the overall uncertainty level in the calculation of h was about 8.6%, 9.2% and 11.8% for $65W/(m^2K)$, $125W/(m^2K)$ and $300W/(m^2K)$, respectively.

Figure 4.9(b) shows the spanwise averaged uncertainty level which was generally in the order

Table 4.2: Experimental uncertainties

Parameter	Units	Value	Error	low- h	medium- h	high- h
h	$W/(m^2K)$	-	-	65	125	325
T_o	$^{\circ}C$	22.3	± 0.16	1.03	1.03	1.03
T_g	$^{\circ}C$	56.4	± 0.43	1.19	1.19	1.19
T_{LC}	$^{\circ}C$	38.7	± 0.12	1.22	1.22	1.22
ρck	$W\sqrt{s}/(m^2K)$	576	± 29	5.00	5.00	5.00
t_{LC}	s	34.4	± 0.1	0.14	-	-
		6.8	± 0.1	-	0.75	-
		1.5	± 0.1	-	-	3.3
	Overall uncertainty level			8.58%	9.19%	11.74%
	Repeatability			3.58%	4.19%	6.74%

of 10% for the stagnation regions (peaks) and about 8.5% for the wall jet regions (valleys). As discussed briefly above, in order to obtain an approximately constant liquid crystal appearance time of about 2s, the temperature step was decreased at higher Reynolds numbers, increasing the non-dimensional temperature θ . The area averaged uncertainty level as a function of θ , and hence the flow speed, is indicated in Figure 4.9(b). \bar{P}_h was generally varied between 8.5 and 11% over the full range of flow conditions examined in this study, while a minimum value is observed when θ is about 0.48 which is very close to the optimum value of 0.52 reported by Yan and Owen (2002). Obviously, heat transfer coefficients for all channel geometries were evaluated with similar uncertainty level as in the above example.

4.5.2 Repeatability

The experimental uncertainties, shown in Table 4.2, indicate the range in which the real heat transfer coefficient values are situated. This include also the uncertainty of the material properties, which is a systematic error since the real thermal properties are not adequately known, and thus do not change on repeated experiments. For relative comparisons, however, a lower uncertainty level should be considered excluding the material properties. This results in repeatability values between 3% and 7% over the full range of the achievable heat transfer coefficients and it actually means that the difference in the heat transfer level between different geometries should be generally above 5% in order to allow reliable comparisons of different channels and regions.

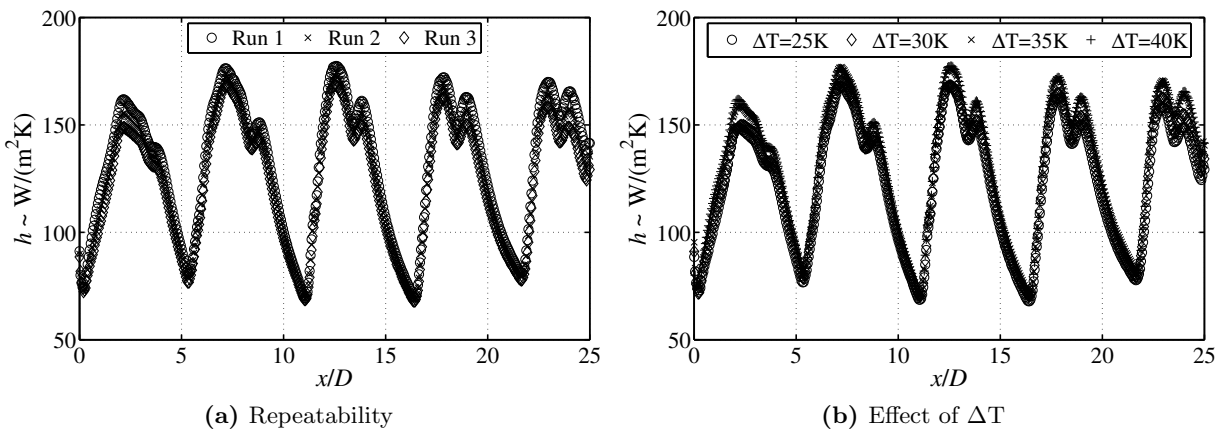


Figure 4.10: Significance of scatter on repeated experiments. (a) Actual repeatability and (b) Effect of temperature step. $X/D=Y/D=5$, $Z/D=1$, $Re_D=32,400$

Figure 4.10(a) shows three different runs of the same geometry at the same flow and temperature step conditions where the very good agreement between the spanwise averaged heat transfer coefficient shows the accuracy of the measurements. Additionally, experiments were carried out at different temperature steps and they have been proven independent of the temperature level within the experimental uncertainties, as shown in Figure 4.10(b).

4.6 Concluding Remarks

The measurement technique used for the evaluation of heat transfer coefficients has been presented in detail. This contains a new procedure which combines different transient heat transfer methods. The transient liquid crystal technique, used for evaluation of heat transfer coefficients, and the lumped capacitance method, used for the extraction of the real temperature history which drives the transient liquid crystal experiment. Therefore, thermal inertia characteristics of thermocouples with exposed junction were investigated over a range of temperature steps and flow conditions, and their time constants were directly applied in the calculation of heat transfer coefficients. Finally, an uncertainty analysis indicated that the experiments can be accurately repeated with an overall uncertainty in the calculation of heat transfer coefficient varying between 3% and 7% depending on the liquid crystal detection time.

FLOW DISTRIBUTIONS

This chapter describes the main flow structures and characteristics inside the narrow impingement channels. The discussion is also supported by some numerical results (CFD) of the current geometries (Fechter, 2011). In addition, local jet discharge coefficients were experimentally evaluated using static pressure tapings and probe traversing measurements at the exit of each individual jet. The experimentally measured local massflow distributions are also compared with the one-dimensional model given by Florschuetz et al. (1981).

5.1 Flow Domain

Local heat transfer coefficients are generally a property of the flow, and therefore, the fluid flow aspects of impinging jets are of vital importance for a better understanding of convection transport processes, as these cannot be separated from heat transfer aspects (and vice versa). The flow domain of an impingement jet is well documented in the open literature, i.e. Martin (1977), and it is characterised by a spectrum of vortical structures and strong recirculation zones which are enhanced at low separation distances and confined configurations, as shown by the smoke flow visualisation studies of Popiel and Trass (1991) and Baydar and Ozmen (2006).

In a multi-jet arrangement with a maximum crossflow orientation, where the spent air of the jets is forced to exit the channel from a single side, as shown in Figure 5.1, the flow domain is more complicated due to the interaction between the generated crossflow and the downstream jet(s). Generally, there are two types of interactions which do not occur in a single impinging

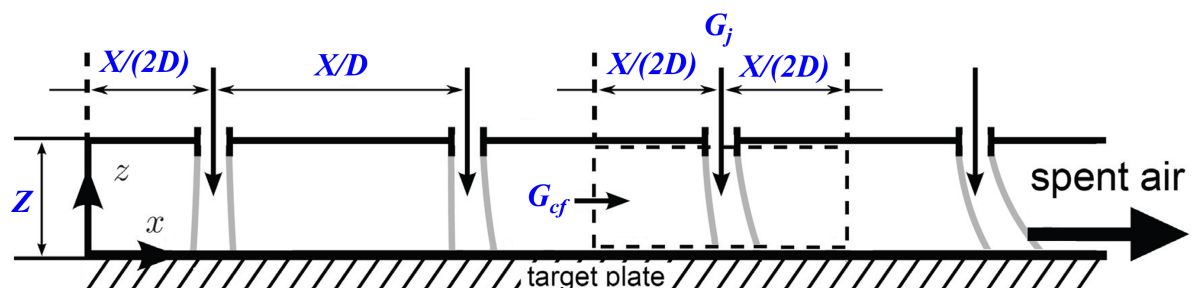


Figure 5.1: Schematic of a multi-jet system with maximum crossflow orientation and indicated jet-to-crossflow interaction. Adopted from Weigand and Spring (2011)

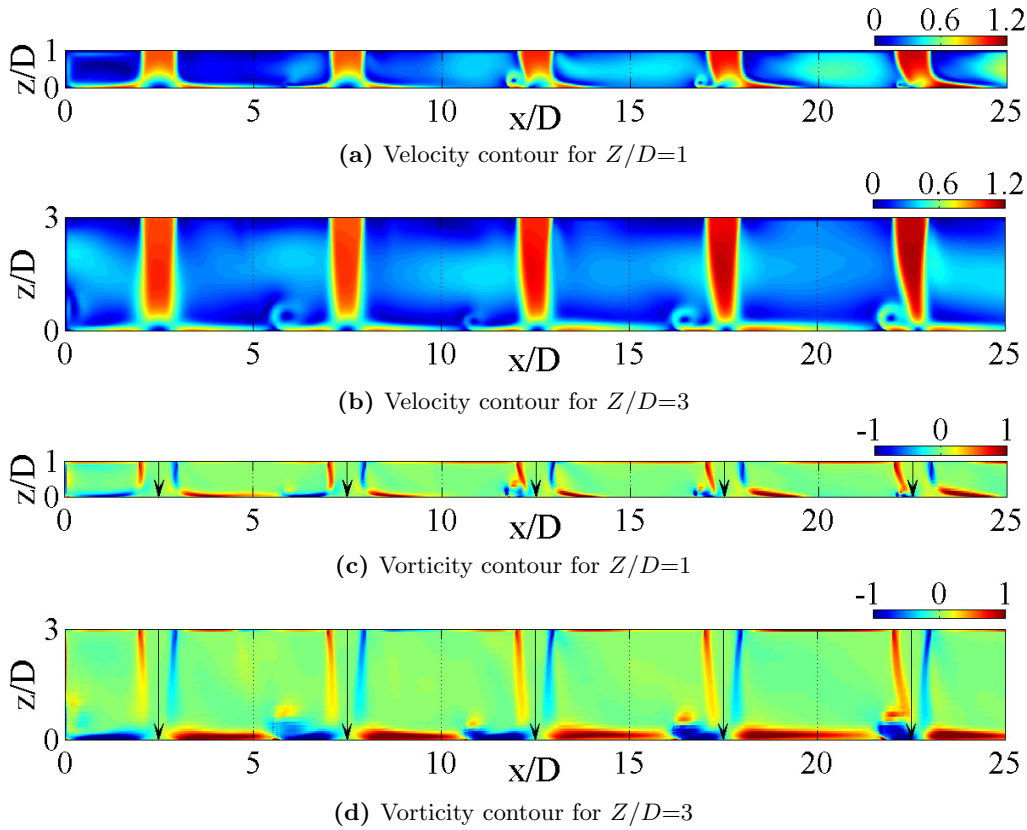


Figure 5.2: Velocity and vorticity magnitude contours (xz -plane) in the channel centerline, $y=0$, at $Re_D=32,900$. CFD results from [Fechter \(2011\)](#)

jet. The first is the possible jet-to-jet interaction between pairs of adjacent jets prior to their impingement onto the target plate. This type of interference, which is due to shear layer expansion, is of importance for arrays with closely spaced jets and large separation distances between the jet orifices and the impingement target surface. The second is the interaction due to the collision of surface flows from adjacent jets, also referred to as secondary stagnation zones. These regions are characterised by boundary layer separation and eddying of the flow. The disturbances predominantly occur for arrays with small interjet spacing, small separation distances, and large jet velocities. Depending on the strength of this interaction, upwash flows can develop between pairs of adjacent jets and form recirculating vortices. The above effects can be accentuated further by an additional interaction with the crossflow formed by the spent air of the jets (schematically shown in Figure 5.1). The strength of the crossflow within the impingement array is influenced, apart from the design of the outflow and the associated routing of the spent air, by the geometrical characteristics of the jet array, as for example, the channel height (Z) and the open area ratio (A_f). Obviously, crossflow effects are enhanced as Z is decreased and A_f is increased.

Crossflow effects are of great importance also in narrow impingement channels where the spent air of the jets interferes with the other walls of the channel (sidewalls and jet plate) providing complex flow structures that can be very different compared to single jet-to-crossflow interactions or periodic multi-jet arrangements. For this kind of applications there are some aspects of the flow physics that are difficult to be captured without the use of some numerical techniques. For this purpose, some CFD results of [Fechter \(2011\)](#) will be presented. This numerical analysis, merely intended as support for the experimental data, will allow a better description of the heat transfer results that are found experimentally.

Figures 5.2(a) and (b) show the velocity magnitude contours for the mid-plane of the inline jet pattern for $Z/D=1$ and 3. Since the CFD results are only presented as a mean for further understanding of flow physics, the data are normalised by the average jet bulk velocity. It is observed that the crossflow velocities are continuously increased towards the channel exit as required also by the mass conservation. This increase of crossflow momentum forces a deflection of the the potential core of the downstream jets. This deflection is larger at $Z/D=1$ as a direct consequence of the lower channel height, and hence higher crossflow momentum. Additionally, the intensity of the colour for the velocity contour shows slightly higher velocity magnitudes of the downstream jets. This indicates a non-uniform massflow distribution through the impingement holes despite their geometrical similarity. This distribution is typical in maximum crossflow orientations when the jets are fed by a common plenum chamber due to the decreasing channel static pressure, and hence higher local Reynolds numbers of the downstream jets. Figures 5.2(c) and (d) show that the vorticity is maximised very close to the stagnation point region where the velocity gradients are relatively high due to the flow acceleration in the wall jet region as well as on both sides of the potential core due to the shearing with the surroundings. Furthermore, the total size of the vortex structures is similar for both channel heights indicating that the resulting flow structures are more pronounced at $Z/D=1$.

5.2 Channel Pressure Drop

A fair judgement of a cooling scheme should not only be based on the heat transfer coefficients, but also on the overall pressure drop through the impingement geometry.

In this study, the overall pressure drop of each impingement geometry was evaluated from the plenum to channel exit. Figure 5.3(a) shows the pressure ratio for various channel heights using a low-staggered pattern ($\Delta y/Y=0.4$) at $X/D=5$ and 8, and as a function of Reynolds number. For all geometries, the pressure ratio is increased with increasing Reynolds number following a power law. Furthermore, the pressure ratio for $Z/D=1$, is about 8-9% higher compared to $Z/D=3$, indicating reduced channel pressure drop as Z/D is increased. This is attributed to the lower crossflow momentum which results at lower pressure drop at a given channel length. Comparing the results of $X/D=5$ and 8, similar trends are observed, however, at a given channel cross-sectional area, the overall pressure ratio for $X/D=8$ is about 6-7% higher compared to $X/D=5$ due to the larger channel length.

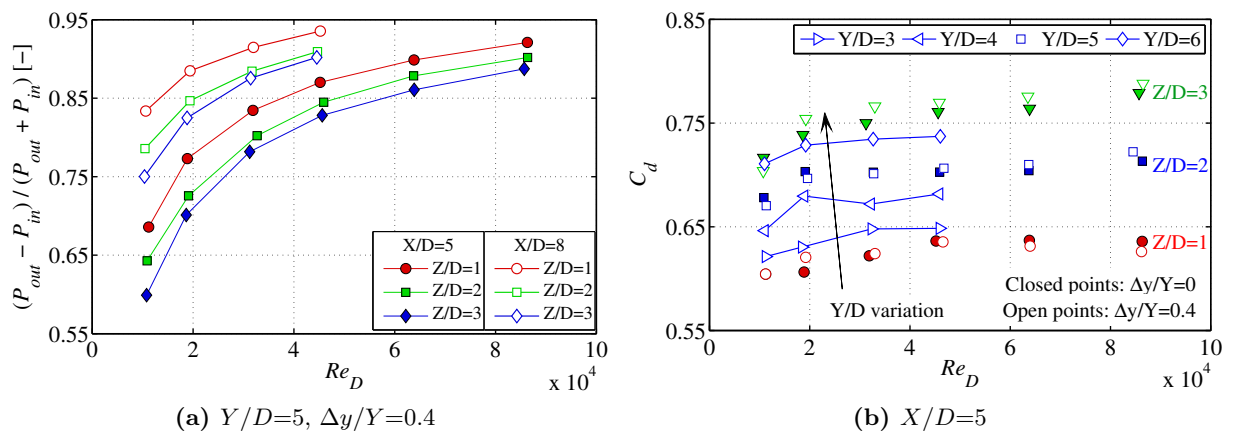


Figure 5.3: Pressure loss parameters of the impingement channels for various Re_D

Another indication of the pressure loss through the impingement geometry is the complete channel discharge coefficient. It should be noticed, however, that this is separated from the impingement plate or the individual jet discharge coefficients, which are discussed in Section 5.3, but the discharge of a specific geometry including all channel walls. The channel discharge coefficient can be calculated for incompressible flows by:

$$C_D = \frac{\dot{m}}{n\rho\pi\frac{D^2}{4}} \sqrt{\frac{\rho}{2\Delta p_{ch}}} \quad (5.1)$$

where \dot{m} is the overall massflow, n is the number of impingement holes and Δp_{ch} is the channel pressure drop. Figure 5.3(b) indicates actually the channel pressure drop at a given coolant massflow. The channel discharge coefficients are almost independent from Reynolds number although a slight increase can be observed at low Re_D . Additionally, as expected there is a tendency of increasing C_D with increasing the channel cross-sectional area. In particular, C_D at $Z/D=1$ and 2 are about 18% and 4% lower than $Z/D=3$, respectively. Note also that the impingement jet patterns are shown to have minimum effect on the overall channel discharge capabilities.

5.3 Local Discharge Coefficients

Local jet discharge coefficients ($C_{D,j}$) were experimentally evaluated for each individual hole over a range of Reynolds numbers similar to the heat transfer tests. Discharge coefficients were defined as the ratio of the actual jet massflow to the theoretical massflow through the geometric area of the jet assuming incompressible flows conditions. Calculation of discharge coefficient assuming compressible isentropic perfect gas flows resulted in differences less than 1%.

The determination of flow distribution among each individual jet was accomplished by static pressure tapings and traversing of Pitot probes inserted from the sidewall of the channel. Details about the measurement points and the experimental procedure can be found in Section 3.4. The jet axial velocity profiles were therefore evaluated in the spanwise direction. The velocity profiles, normalised by the velocity in the center of the jet are shown in Figure 5.4. All jets experience a top-hat exit velocity profile where the flat part of the distribution is about 80-85% of the jet diameter. Note that local velocities are slightly higher closer to the edges of the impingement hole at around $r/D_j=0.38$ similar to Lee and Lee (2000). As a result, the thickness of the boundary layer is around $0.1D_j$ for the majority of the cases. Due to the uniformity of the jet size pattern the velocity profiles are almost identical for all jets for both channel heights indicating that Z/D does not affect the velocity distribution at the exit of the impingement hole. Figure 5.4 shows that the velocity profiles are very similar for $Re_D=20,000$ and 60,000, indicating no dependence with Re_D over the full range of flow conditions.

The length-to-diameter ratio (L/D) of the jets was equal to one (short orifice) and hence, the total conditions in their *vena-contracta* were measured similar to the upstream plenum conditions and the discharge static pressure was assumed similar to the downstream pressure. Local discharge coefficients were therefore evaluated by the actual local massflows variations calculated by:

$$\dot{m}_j = \rho \frac{\pi D^2}{4} \bar{U}_j \quad (5.2)$$

where D is the jet diameter and \bar{U}_j is the bulk velocity obtained from the preceding velocity

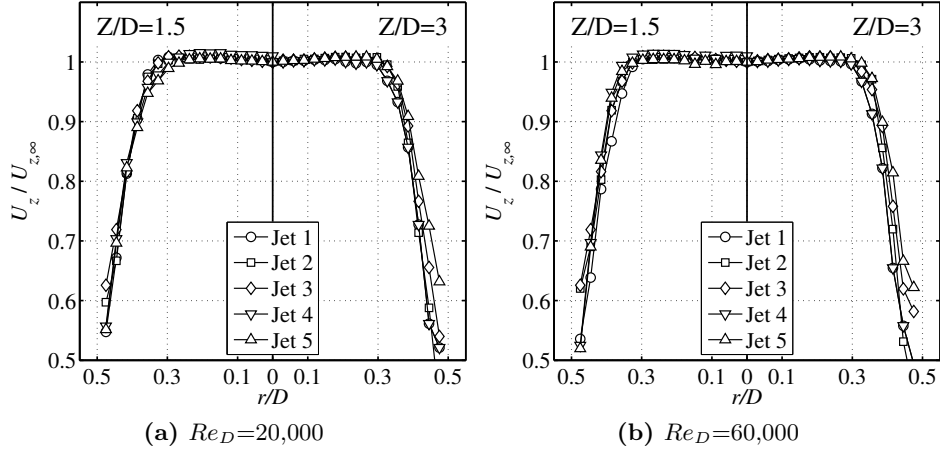


Figure 5.4: Jet axial exit velocity profiles for the inline pattern (y -direction)

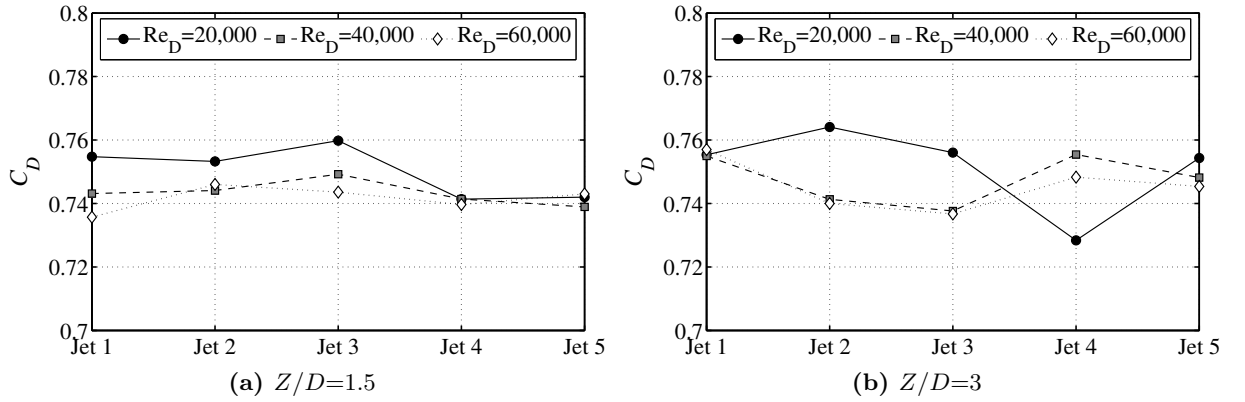


Figure 5.5: Local jet discharge coefficients for various Reynolds numbers

profiles assuming axisymmetric distribution. It should be noticed, however, that this is an approximation, especially for the streamwise direction where the deflection of the jets may result in a non-symmetric distribution. Note that the measurement plane was defined a few millimetres upstream of the jet exit eliminating jet potential core deflection effects for the downstream regions. Balancing the massflow over the five jets and the laminar flow element resulted in differences less than 9% and 3% for the lowest and highest Reynolds number.

Figure 5.5 shows the local C_D of each individual jet for different Reynolds numbers based on the average jet massflow. For both $Z/D=1$ and 3, C_D remains essentially constant around 0.75, from jet 1 to jet 5 indicating that crossflow effects do not affect the local jet discharge as shown also by Florschuetz and Isoda (1983) who observed constant values of C_D when crossflow-to-jet mass velocity ratio is below unity. Additionally, the local discharge coefficients are independent of Reynolds number in the range of investigated flow conditions similar to Lichtarowicz et al. (1963) who reported constant C_D values of around 0.78 for $L/D=1$, between $Re_D=10,000$ and 40,000. Therefore, for the jet plate, an overall average discharge coefficient value of 0.75 ± 0.1 was assumed for all channel geometries and over the complete range of Re_D .

5.4 Crossflow and Local Massflow Distributions

As discussed briefly earlier, for relatively low channel heights, with maximum crossflow orientations and when the jets are fed by a common plenum chamber, the jet massflow distribution

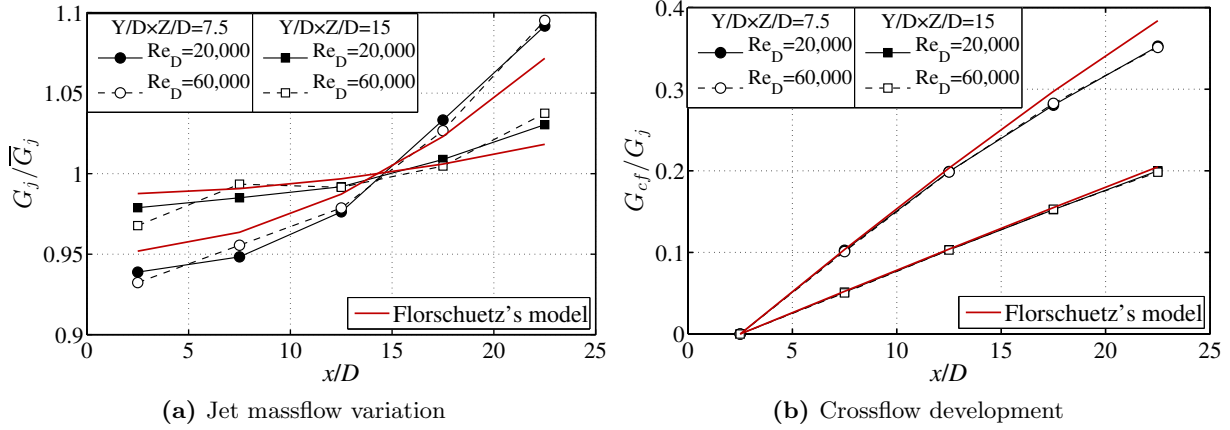


Figure 5.6: Local jet massflow variation and crossflow development in the channel. Comparison with the model of Florschuetz et al. (1981)

increases towards the channel exit due to the decreasing static pressure and hence, higher local discharge pressure differences. Florschuetz et al. (1981) had the good approach to homogenise this effect for constant discharge coefficients using a transpiration flow approach where the discrete hole is replaced by a surface over which the flow injection is continuously distributed. Therefore, an analytical solution can be obtained for the local jet massflow distributions and crossflow development given by:

$$\frac{G_j}{\bar{G}_j} = \frac{\beta n \cosh(\beta(x/x_j))}{\sinh(\beta n)} \quad (5.3)$$

and

$$\frac{G_c}{G_j} = \frac{1}{\sqrt{2}C_D} \frac{\sinh(\beta(x/x_j - 1/2))}{\cosh(\beta(x/x_n))} \quad (5.4)$$

where $\beta = C_D \sqrt{2}(\pi/4)/[(Y/D)(Z/D)]$ and $x = x_j(i-1/2)$, $i=1,2,3 \dots n$. More details about this one-dimensional model can be found in Appendix D. The model leads to the result that the flow distribution is independent of the streamwise hole spacing and impingement hole pattern, depending, for a given discharge coefficient and number of rows, only on the channel flow area.

Figure 5.6 illustrates the streamwise jet mass velocity variation and the crossflow development for two particular cases. The channel width is constant at $Y/D=5$ and the channel height is varied from $Z/D=1.5$ to 3. The experimentally obtained jet massflow distributions and crossflow development are compared also with the model of Florschuetz et al. (1981) considering an overall average impingement plate discharge coefficient of 0.75 obtained from Figure 5.5. As expected, larger G_j variations are observed for $Z/D=1.5$ due to the higher pressure drop in the channel. In particular, G_j/\bar{G}_j increases from about 0.93 for jet 1 to 1.09 for jet 5. On the other hand, very low variation is observed for $Z/D=3$ since G_j/\bar{G}_j is increased by only 5% from jet 1 to 5. The local jet mass velocity distributions agree relatively well with the one-dimensional model. For both channel heights, jet mass velocities from the probe measurements are slightly under-determined for jets 1,2 and 3 and over-determined for jets 4 and 5. In particular, for $Z/D=1.5$ and upstream jets, the under-determination is in the order of 4% while for the crossflow dominated region the differences are in the order of 6%. For $Z/D=3$, the jet mass velocity distribution is better captured by the pressure probes and the overall differences are less than 2%.

The right part of Figure 5.6 shows the streamwise distribution of the generated crossflow-

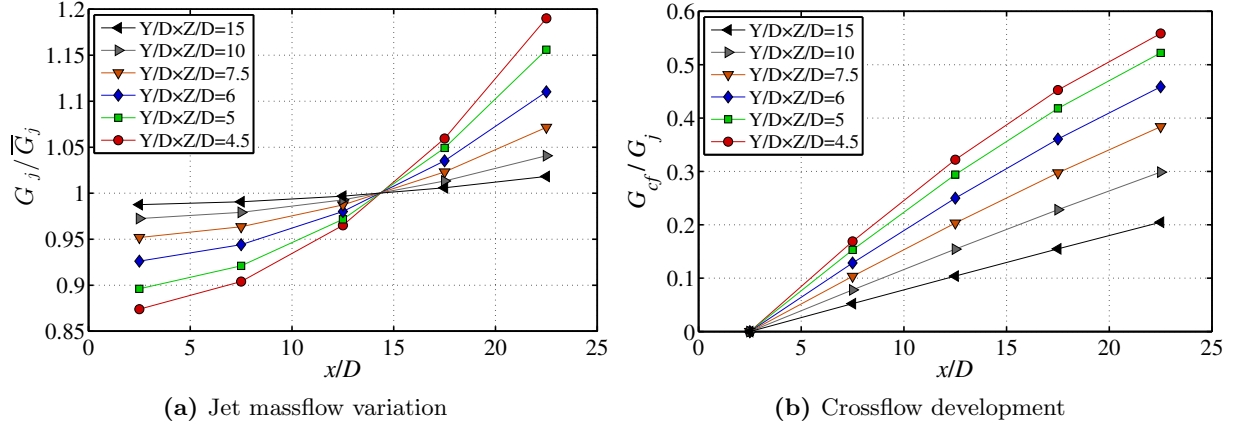


Figure 5.7: Local jet massflow variation and crossflow development for various channel geometries using a one-dimensional model. $Re_D=32,900$

to-local jet mass velocity ratio (G_{cf}/G_j). As expected, crossflow increases towards the channel exit and the development is obviously more pronounced at smaller channel cross-sections ($Y/D \times Z/D$). G_{cf}/G_j reaches the value of 0.35 and 0.2 at the last jet for $Z/D=1.5$ and 3, respectively. For both channel heights the agreement with the model of [Florschuetz et al. \(1981\)](#) is excellent over the full channel length. However, for jets 4 and 5 at $Y/D \times Z/D=7.5$, the amount of crossflow is under-determined about 5% and 9% as a direct consequence of the local jet mass velocity under-determination of the upstream jets presented in [Figure 5.6\(a\)](#).

The overall agreement between the local jet massflow distributions obtained through the pressure probe traverses for each individual hole and the model of [Florschuetz et al. \(1981\)](#) is very satisfactory and confirms the applicability of an one-dimensional model for discrete hole arrays. [Figure 5.7](#) shows the model determined jet mass velocity variations (G_j/\bar{G}_j) and crossflow development (G_{cf}/G_j) for various channel geometries where the above discussed trends are explicitly illustrated.

5.5 Concluding Remarks

In this chapter, structures and characteristics of the flow domain developed inside the narrow impingement channels were presented. The overall discussion was supported by some numerical results allowing to understand the flow physics, and hence the convection transport mechanisms. Additionally, local jet massflow variations were experimentally evaluated with pressure probe traverses at the exit of each individual jet. Local jet discharge coefficients were therefore evaluated and they have been proven independent of the generated crossflow, Re_D and Z/D . In this study, the discharge coefficient of the jets, and hence of the jet plate, was determined to be 0.75 ± 0.1 . The results indicated also that local jet massflow variations and crossflow development are enhanced with reducing channel cross-sectional area. The experimentally measured massflow distributions showed excellent agreement with the model of [Florschuetz et al. \(1981\)](#) indicating that an one-dimensional transpiration model can be safely applied for discrete hole arrays as well.

HEAT TRANSFER DISTRIBUTIONS

This chapter presents the determined heat transfer data. Crossflow effects and heat transfer coefficient distributions for all interior surfaces of the narrow impingement channels are discussed in detail as well as the impact of channel height (Z/D) and width (Y/D), jet-to-jet axial spacing (X/D), impingement jet offset position ($\Delta y/Y$) and varying jet diameter (ΔD). The results are analysed by various post-processing procedures aiming to quantify and clarify the difference between the heat transfer performance of different geometries over a wide range of engine representative Reynolds numbers (11,900-86,000).

6.1 Data Presentation

In this section, an overview about the distribution of convection coefficients inside the impingement channels will be given considering also the main structures of the flow domain connecting heat transfer and fluid flow aspects. The discussion is focused on two main parts: Crossflow effects, generated by the spent air of the upstream jets and a comparison of the heat transfer coefficient distributions for all channel walls (target plate, sidewalls, jet plate).

6.1.1 Crossflow effects

Figure 6.1 shows the heat transfer coefficient surface contour (h/h_{ref}) for a channel with $Y/D \times Z/D = 6$ and a low jet staggered arrangement. The results are normalised with the maximum value occurring which was $188 W/(m^2 K)$ for the target plate at $Re_D = 19,200$.

For the upstream channel positions, and due to the relatively low channel height ($Z/D = 1.5$), heat transfer coefficients are maximised in the stagnation point regions and a secondary peak appears for the first jet (no crossflow) in agreement with single impingement jet literature (see Section 2.2.1). As the flow accelerates towards the exit of the channel, the effect of crossflow generated by the spent air of the upstream jet(s) becomes visible and the pattern of the heat transfer coefficient is converted from a circular (jet 1) to a horseshoe vortex (jet 3) shape distribution, although an interaction between the jets and the sidewalls can be observed. Note that, at further downstream positions, the momentum of the crossflow is high enough preventing jets 4 and 5 to traverse vertically the channel height. Therefore, their peak stagnation point heat transfer is significantly shifted in the direction of the flow, similar to a jet in crossflow situation, e.g. Metzger and Korstad (1972) and Bouchez and Goldstein (1975).

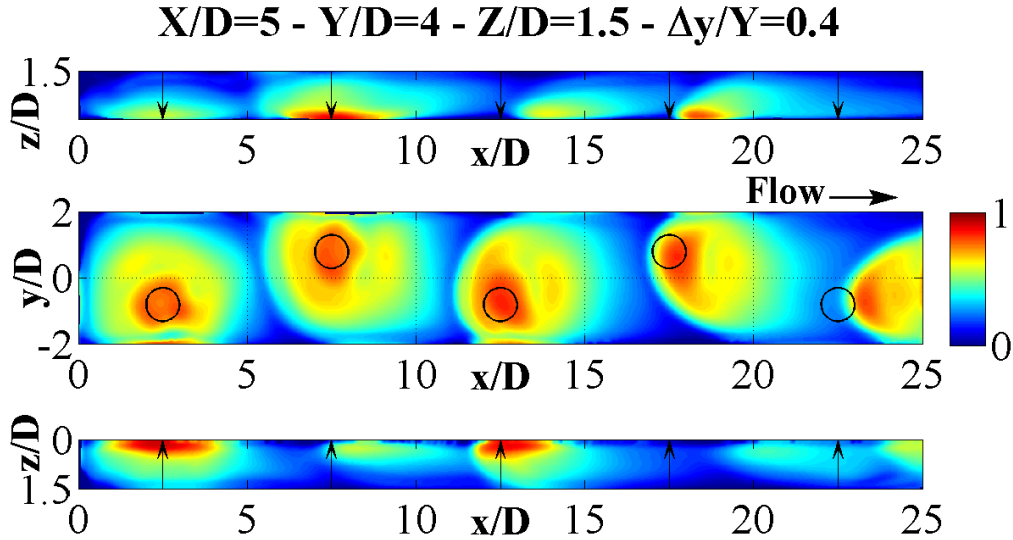


Figure 6.1: Crossflow effect on the local distribution of heat transfer coefficient (h/h_{ref}) for a channel with a small cross-sectional area. $h_{ref}=188W/(m^2K)$, $Re_D=19,200$

For the sidewalls of the channels, higher heat transfer is observed closer to the target plate ($z=0$) as the wall jet flow impinges out the sidewalls. Peak heat transfer appears at approximately the same axial position with the corresponding stagnation points on the target plate, especially at the low crossflow dominated region (jets 1, 2 and 3). At downstream positions, the peak heat transfer is reduced and the wall jet traces of jets 4 and 5 are also deflected in the direction of the flow similar to the target plate stagnation points. This means that the amount of crossflow is high enough to prevent the direct impact of the impinged flow with the lateral walls. However, this results in a more homogeneous distribution of cooling in z -direction.

6.1.2 Distributions of heat transfer coefficients

Figure 6.2 shows a qualitative comparison of the heat transfer coefficient surface contours (h/h_{ref}) for all channel walls at $Z/D=2$ and $\Delta y/Y=0$. Given the overall geometrical symmetry, only half of the target and the jet plate are visualised on the same image. The surface contour shows clearly the differences in the distributions of heat transfer between channel interior walls. Heat transfer coefficients on the jet plate are highly affected as the channel sidewalls interfere with the wall-jet flow causing a post-impingement flow on the impingement plate. The up-lift moving of the flow causes high local heat transfer rates close to the sidewalls of the channel. Furthermore, at the wake of the downstream jets a continuously increased region of high heat transfer is observed since the jets act as pedestals enhancing downstream heat transfer. Note that the achievable heat transfer in the vicinity of jet 1 is relatively low indicating a small interaction between the jet plate and the post-impingement flow. For the target plate and the sidewalls, similar trends with Figure 6.1 are observed, however, the stagnation point regions of the downstream jets are more pronounced due to the larger channel flow area which attenuates crossflow effects.

Figure 6.3 shows the distributions of spanwise averaged Nu_D allowing a quantitative comparison between the channel interior walls. As expected, $Nu_D/(Re_D^{0.7}Pr^{1/3})$ levels are higher on the target plate which experiences the stagnation point regions. Furthermore, the level of Nu_D is slightly increased towards the channel exit which could be attributed to the decreasing static pressure, and thus, higher local $Re_{D,j}$ of the downstream jets (see Figure 5.7). The spanwise

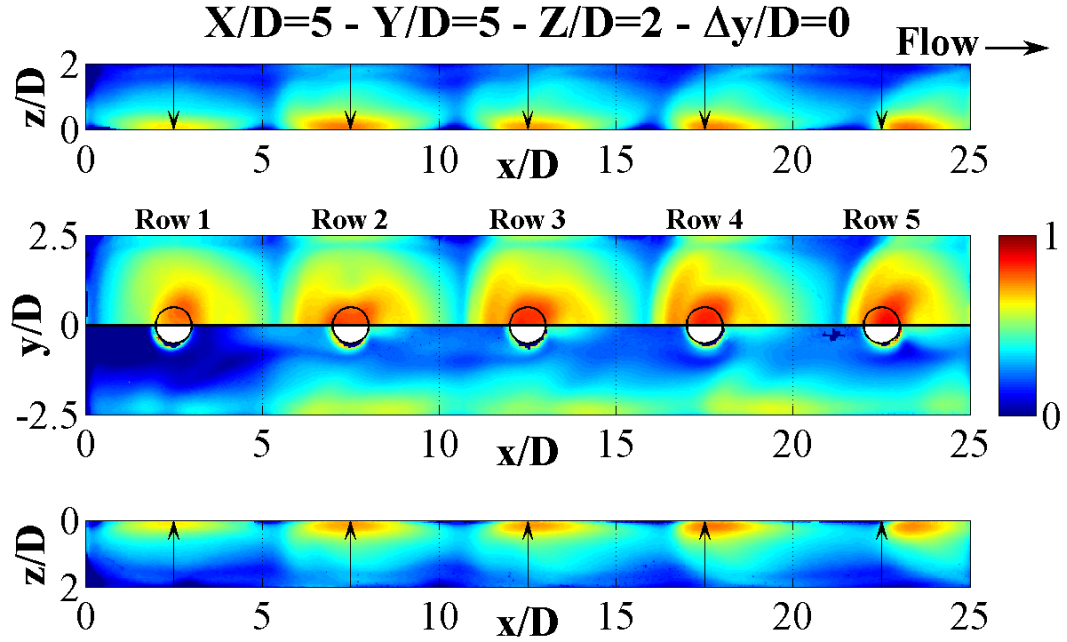


Figure 6.2: Heat transfer coefficient surface contours (h/h_{ref}) for all channel interior surfaces. $h_{ref}=197W/(m^2K)$, $Re_D=19,200$

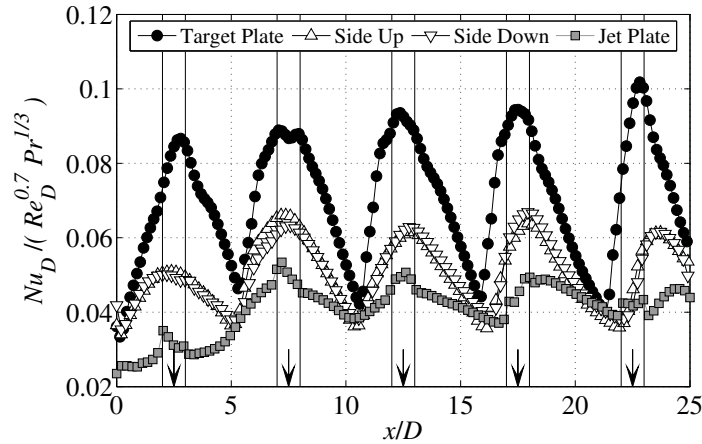


Figure 6.3: Spanwise averaged Nu_D distributions for all channel interior walls. $Re_D=19,200$. $X/D=Y/D=5$, $Z/D=2$ $\Delta y/D=0$

averaged Nu_D distributions on the sidewalls show similar trends as the target plate. Peaks of heat transfer appear at the regions where the wall jet impinges the sidewalls, however, the differences between peak and valleys are considerably smaller compared to the target plate. The level of Nu_D is around 35-40% lower compared to the target plate indicating less cooling of the sidewalls. Note also that the distributions of the upper and the lower sidewall are the same, as a direct consequence of the overall geometrical symmetry ($\Delta y/Y=0$). The jet plate data indicate a more distributed form of cooling with no peaks observed but with much lower heat transfer capabilities compared to the other walls. The reduced Nu_D level is about 55% and 30% lower compared to the target plate and the sidewalls, respectively. Note also that there is a tendency of increasing Nu_D towards the channel exit which actually means that crossflow can be beneficial for the cooling of the jet plate. Finally, it can be observed that spanwise averaged Nu_D for all channel walls are similar in level in the region between the jets where the collision of the wall jet regions of two adjacent jets takes place.

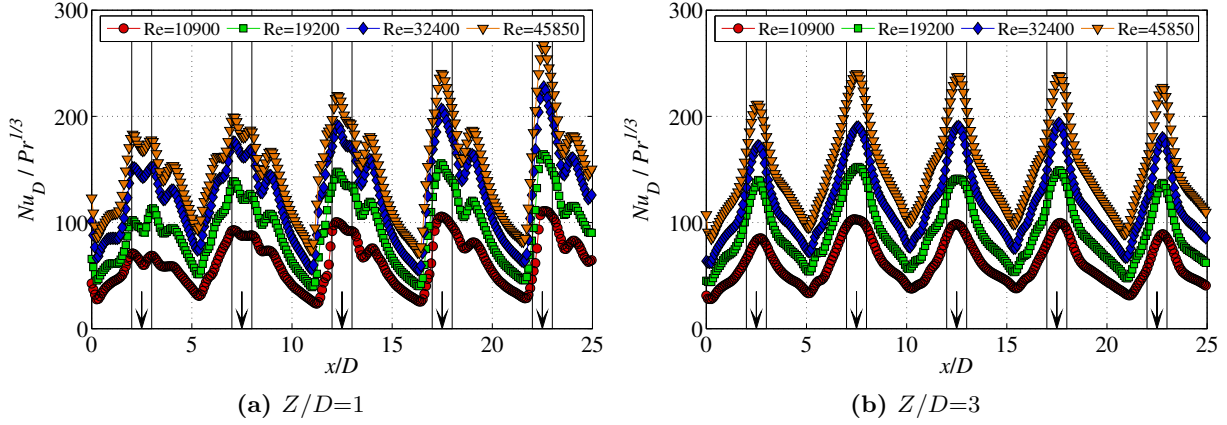


Figure 6.4: Reynolds number effect on the local Nu_D distribution for channel centerline ($y=0$). $X/D=Y/D=5$, $\Delta y/D=0$

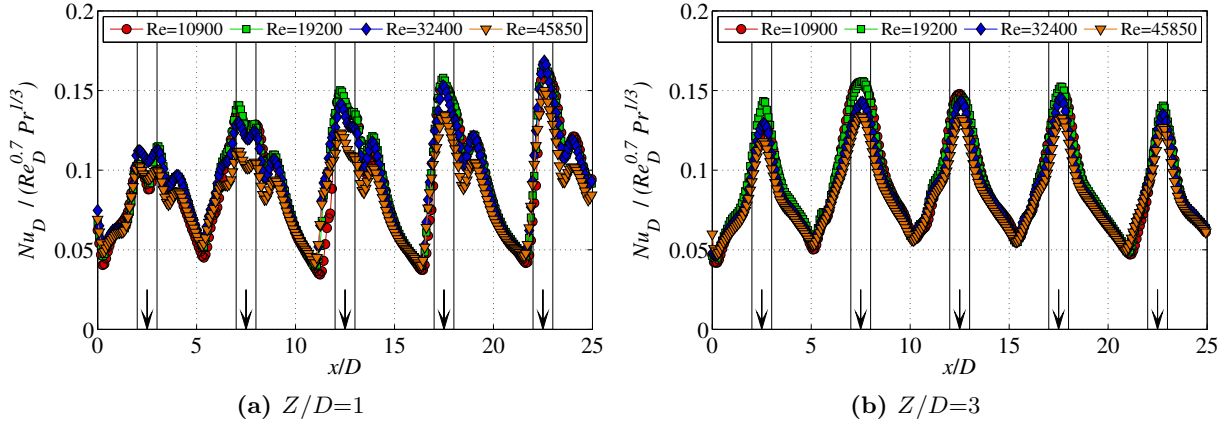


Figure 6.5: Local $Nu_D/Pr^{1/3}$ distributions divided by the Re_D to the power of 0.7 for the channel centerline ($y=0$). $X/D=Y/D=5$, $\Delta y/Y=0$

6.2 Effect of Reynolds number

Figure 6.4 shows the effect of jet average Reynolds number on the local Nusselt number of the channel centerline ($y=0$), for the inline pattern of $Z/D=1$ and 3. As expected Nu_D is increased with increasing Reynolds number. For both channel heights, Nu_D is increased by a factor of about 2.5 as the Re_D is quadrupled from 10,900 to 45,850. It is also well established from convective heat transfer research, i.e. Kays et al. (2004), that Nusselt number increases with Reynolds number following a power-law where an exponent m is usually introduced in order to describe and correlate the heat transfer level in the form of: $Nu \sim Re^m$. Exponent m is a function of Z/D and r/D (Jambunathan et al., 1992), while typical values vary between 0.5 (laminar) and 0.8 (turbulent), for the stagnation point and far wall jet regions.

For the present data, the local $Nu_D/(Pr^{1/3}Re_D^m)$ ratios are almost identical when the exponents 0.68 and 0.73 are used for $Z/D=1$ and 3, respectively. Therefore a common value of 0.7 has been selected to plot the data in Figure 6.5. The differences observed, especially in the stagnation point regions for both Z/D are attributed to the laminar state of the boundary layer, where the appropriate exponent value is 0.5. However, very good agreement is observed between the jets in the collision of the wall jet regions where the flow domain is relatively complex resulting in turbulent structures. More details about the local exponent distribution can

be found in Appendix E. Figure 6.5 shows also that the overall distribution of heat transfer coefficient remains constant with the Reynolds number, which means that the flow topological structures are similar for the lowest and the highest Reynolds number. Therefore, only the results of $Re_D=32,400$ will be presented for the later discussion. More results for the rest of the Reynolds numbers can be found in Appendix F.

6.3 Effect of channel height (Z/D)

This section investigates the effect of channel height (Z/D) on the cooling performance of narrow impingement channels. Four different separation distances have been considered varying between $Z/D=1$ and 3, however, only these two margin values will be discussed. The streamwise jet-to-jet spacing and channel width were constant, $X/D=Y/D=5$. Given the independency of the heat transfer distribution with Reynolds number, only the results of $Re_D=32,400$ will be presented. Figure 6.6 shows the surface contours of heat transfer coefficient where the results are normalised with the maximum value appeared on the data, approximately $330W/(m^2K)$ and $240W/(m^2K)$ for the target plate/sidewalls and jet plate, respectively. A quantitative comparison between the two separation distances is made in Figure 6.7 which shows the spanwise averaged $Nu_D/(Re_D^{0.7}Pr^{1/3})$ distribution for the different Z/D .

6.3.1 Target plate

For the target plate, as expected higher heat transfer coefficients are obtained in the stagnation point regions. As the flow accelerates towards the exit of the channel, the pattern of the heat transfer coefficient is progressively converted from a circular (jet 1) to a horseshoe vortex shape distribution for both Z/D . However, the overall evolution of the heat transfer coefficient to the exit of the channel, as for example the curvature of the horseshoe vortex pattern, is less pronounced at $Z/D=3$. This is attributed to the higher Z/D which decreases the momentum of the generated crossflow at a given Re_D , and hence the interaction with the downstream jets, which results in an overall decay of the flow phenomena observed at $Z/D=1$.

For $Z/D=1$, secondary peaks appear around the stagnation regions of the very upstream jets. At the positions of jets 2 and 3, the formation of the horseshoe vortex destroys the circular pattern of the secondary peak ring which is however always visible at the wake region downstream of each jet since it is protected somehow from the fluid of the jet. At the last hole (jet 5), the momentum ratio between the jet and the crossflow is still high enough and jet 5 is well able to traverse the channel height. Therefore, a similarity with a flow over cylinder pattern can be observed and a small deflection of the stagnation point region can also be noticed. Note also that the stagnation point heat transfer increases towards the channel exit due to the decreasing static pressure, and hence, higher local Reynolds numbers (see Figure 5.7). This is also visible in the local Nu_D distributions of Figure 6.5(a), where the the stagnation point region differs from jets 1 and 2 to jets 3, 4 and 5. At the first two jets, a donut shape distribution is observed and secondary peaks appear on both sides of the stagnation point. However, as the crossflow generated from the spent air of jets 1 and 2 is developed, the distribution of Nu_D is rearranged and shifted in the direction of the flow with increased levels of heat transfer. Similar behaviour has been observed also by Chambers et al. (2005) and Son et al. (2001) and it is typical for low channel heights when the jets are fed by a common plenum. For $Z/D=3$, on the other hand, no secondary peak ring at jet 1 can be observed and the heat transfer coefficient is continuously

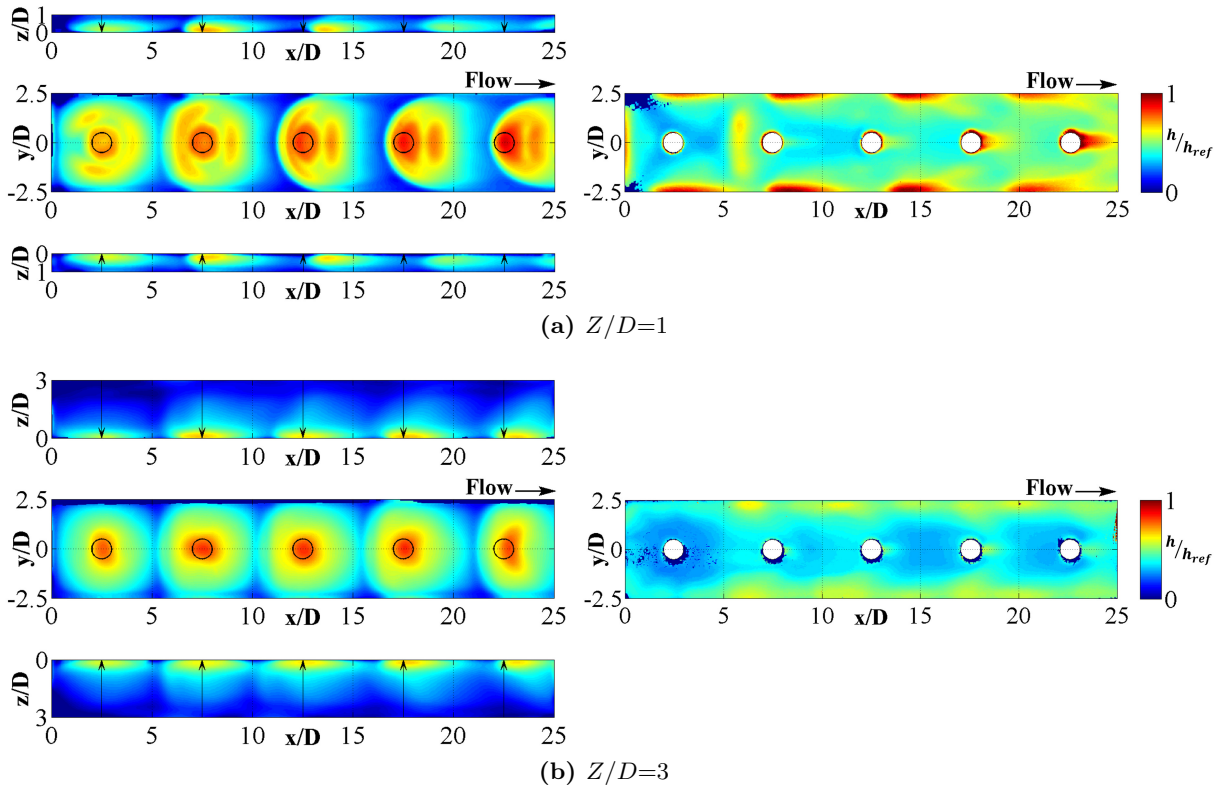


Figure 6.6: Heat transfer coefficient surface contours (h/h_{ref}) for different channel heights. For the target and jet plates: $h_{ref}=330$ and $240W/(m^2K)$, respectively. $Re_D=32,400$

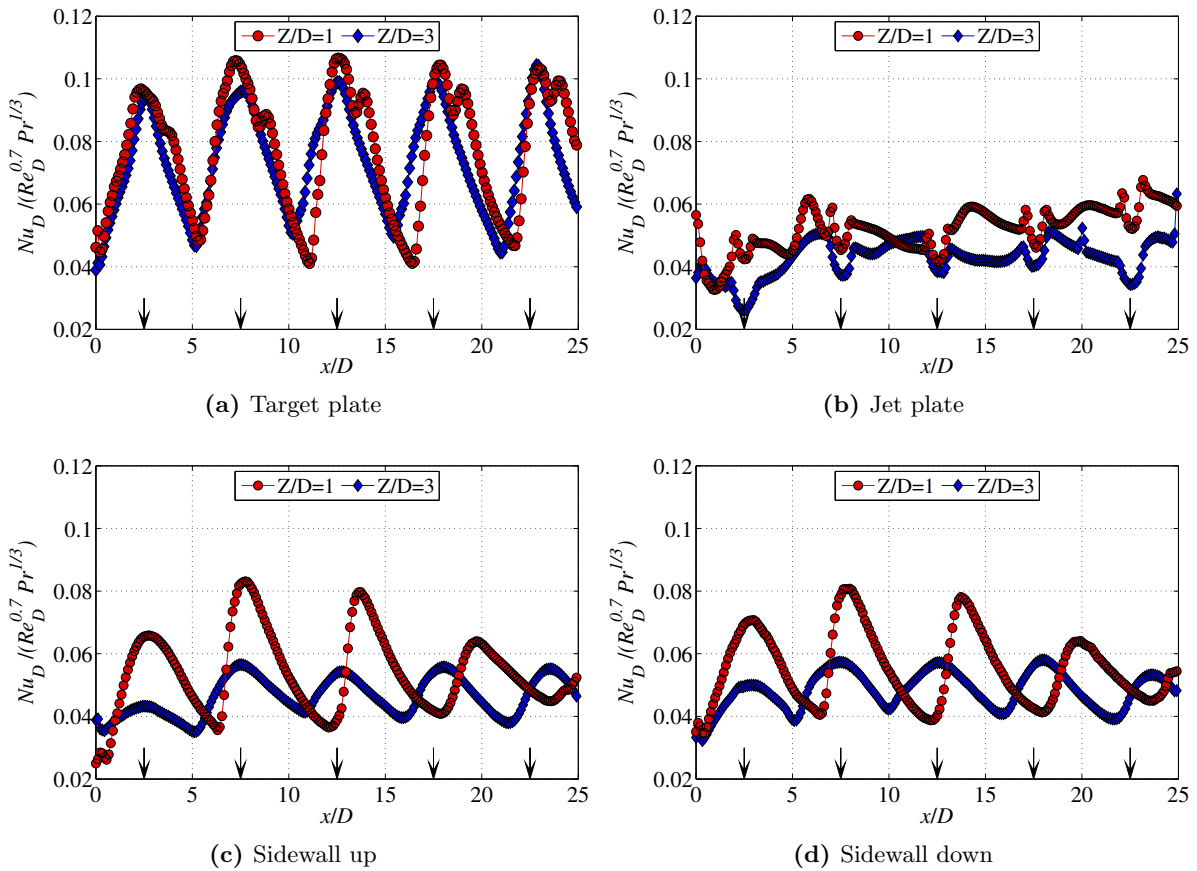


Figure 6.7: Spanwise averaged Nu_D distributions for all channel walls and different channel heights. $X/D=Y/D=5$, $\Delta y/Y=0$, $Re_D=32,400$

reduced from the stagnation to the wall jet region. Contrary to $Z/D=1$, the heat transfer patterns of jet 2 to 5 are quite circular indicating the much lower impact of the crossflow as Z/D increases. Additionally, the stagnation point heat transfer, as shown in Figure 6.5(b), is fairly constant, due to the similar local Reynolds numbers presented in Figure 5.7(a).

Figure 6.7(a) indicates the spanwise averaged Nu_D on the target plate. Spanwise averaged Nu_D has a slightly different distribution for the two separation distances. $Z/D=1$ has secondary peaks for all the jets and shows a bigger difference between peaks and valleys. However, the Nu_D level is very similar indicating a small effect of Z/D on the spanwise averaged results. The increase of stagnation heat transfer from jet 1 to jet 5 observed in Figure 6.5(a) for $Z/D=1$, is somewhat smoothed out here. The peaks are only slightly increased until jet 3 and they are about constant from jet 3 to 5. The lower stagnation heat transfer of the first jets is therefore compensated by a better lateral coverage of the wall jet region due to lower interaction with the crossflow which results in similar spanwise averaged Nu_D with the downstream positions. For jets 4 and 5, the displacements of the peak heat transfer are also visible in Figure 6.7.

6.3.2 Sidewalls

Given the overall geometrical symmetry, the level and distribution of heat transfer coefficients on the sidewalls of the channels are the same for the upper and the lower wall. For both $Z/D=1$ and 3, as discussed briefly earlier, higher heat transfer is observed closer to the target plate ($z=0$) as the wall jet flow impinges the sidewall causing a kind of a stagnation point region. The level and size of this enhanced heat transfer region is similar for both Z/D , as a direct consequence of the same jet diameter which causes a similar development of the boundary layer on the target plate, and hence, a similar thickness of the wall jet flow. This results in unnoticeable differences on the level and the spreading of the heat transfer pattern between $Z/D=1$ and 3. Therefore, the main effect of increasing Z/D is the addition of a region with low interaction with the wall jet flow resulting in an area with low heat transfer, as well as the smaller deflections of the peak heat transfer due to the lower crossflow momentum. This is clearly observed on the spanwise averaged Nu_D distributions in Figures 6.7(c) and (d), where for the upstream channel positions (jets 1, 2 and 3), the peak Nu_D is about 40% higher for $Z/D=1$. However, the generated crossflow attenuates the peak heat transfer at $Z/D=1$ while the results of $Z/D=3$ show a slightly increased heat transfer level towards the channel exit resulting in similar Nu_D levels with $Z/D=1$. Furthermore, similarly to the deflection of the primary peaks on the target plate, the wall jet regions are also deflected in the downstream direction and the peak heat transfer coefficients do not appear at the same axial position with the stagnation points on the target plate. The deflections are enhanced at $Z/D=1$ due to the more intense crossflow effects.

6.3.3 Jet plate

The convective transport processes on the impingement plate are highly affected as the channel sidewalls interfere with the wall jet flow causing a post-impingement flow on the jet plate. Therefore, the distance between the target and the jet plate plays an important role on the level and distribution of heat transfer coefficients. For both Z/D , the up-lift moving of the flow causes high local heat transfer coefficients close to the sidewalls of the channel, however, the heat transfer traces are better distinguishable for $Z/D=1$, as shown in Figure 6.6. This is attributed to the higher intensity of the post-impingement flow as the channel height is reduced. Similar to the target plate and the sidewalls, the post-impingement flow is also shifted in the direction

of the crossflow. Note that for $Z/D=1$, the peak heat transfer caused by the post-impingement flow of jet 5 is not observed within the length of the channel due to the overall deflection of its potential core. Furthermore, at the wake of the downstream jets a continuously increased region of heat transfer is observed since the jets act as pedestals enhancing downstream heat transfer. The heat transfer increase towards the channel exit could be attributed to the lower penetration of the jets (higher potential core deflection) due to the increased crossflow momentum similar to film cooling scenarios. The upstream jets do not produce wake heat transfer regions since their momentum is much higher compared to the momentum of the generated crossflow. For $Z/D=3$ the level of heat transfer and the overall phenomena described above are significantly less pronounced which is a direct consequence of the higher channel height and hence a lower interaction with the post-impingement flow. For both Z/D , a region of low heat transfer in the vicinity of jet 1, which forms a triangular shape distribution for $Z/D=1$ similar to the results obtained by Caggese et al. (2013) for a fully confined single jet configuration under the same geometrical characteristics and flow conditions.

A quantitative comparison between $Z/D=1$ and 3 is indicated by the spanwise averaged Nu_D in Figure 6.7(b). Generally, the impingement plate spanwise averaged $Nu_D/(Re_D^{0.7}Pr^{1/3})$ is about 30% and 50% lower compared to the sidewalls and the target plate, respectively. Contrary to the other walls, the distribution is more uniform with no peaks and valleys for both separation distances. Additionally, for both Z/D there is a tendency of increasing Nu_D towards the channel exit which actually means that crossflow can be beneficial for the cooling of the jet plate. However, spanwise averaged Nu_D for $Z/D=1$ is about 15% and 35% higher, compared to $Z/D=3$, at the low and high crossflow dominated regions, respectively.

6.4 Effect of channel width (Y/D)

Effects of channel width were investigated using a low staggered jet pattern. Three different channel widths have been considered varying between $Y/D=3$ and 5. The X/D and Z/D were constant at 5 and 1.5, respectively. Similar to Section 6.3, only the results of $Re_D=32,400$ are presented. Figure 6.8 shows the surface contours of heat transfer coefficient (h/h_{ref}) for $Y/D=3$ and 5, normalised with the maximum value on the target plate of $Y/D=5$, approximately $302W/(m^2K)$. A quantitative comparison of different channel widths is made in Figures 6.9 and 6.10 which show local and spanwise averaged $Nu_D/(Re_D^{0.7}Pr^{1/3})$ distributions for the target plate and the sidewalls, including the results of $Y/D=4$ presented in Figure 6.1.

6.4.1 Target plate

Figure 6.8 shows a similar distribution of heat transfer coefficients as Figure 6.1, where the overall pattern is progressively converted from a circular to a horseshoe vortex shape distribution towards the channel exit. Therefore, the variation of Y/D mainly affects the downstream channel positions, and particularly, the stagnation point heat transfer of jets 4 and 5. At $Y/D=5$, the downstream jets impinge the target plate generating a local peak of heat transfer which is slightly shifted in the flow direction. At $Y/D=3$, on the other hand, the momentum of jets 4 and 5 is not able to compensate the generated crossflow, and hence, they are not able to traverse the channel height. This results in a destruction of the peak stagnation point heat transfer and a significant bending of the jet potential core. This can be clearly noticed in Figure 6.9(a) by observing the variation of the local Nu_D of the last jet. For the low crossflow dominated region,

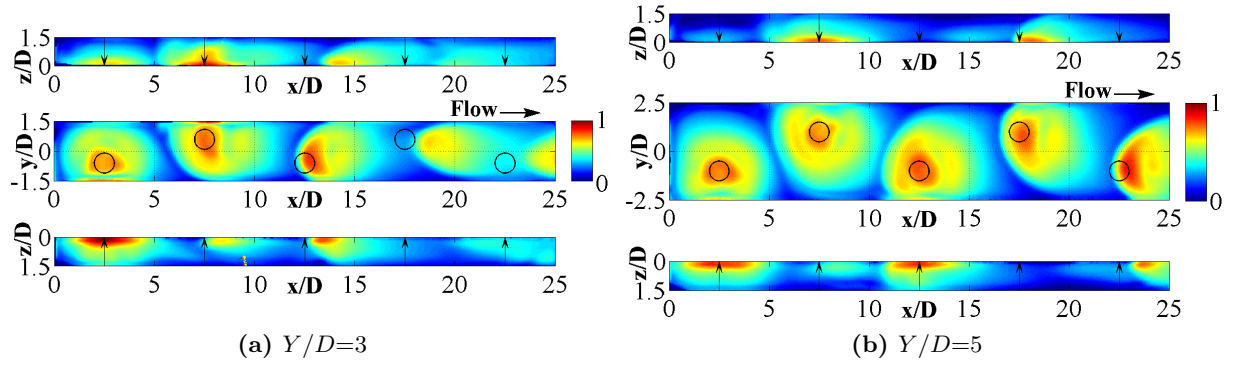


Figure 6.8: Heat transfer coefficient surface contours (h/h_{ref}) for different channel widths. h_{ref} : $302W/(m^2K)$. X/D , $Z/D=1.5$, $\Delta y/Y=0.4$, $Re_D=32,400$

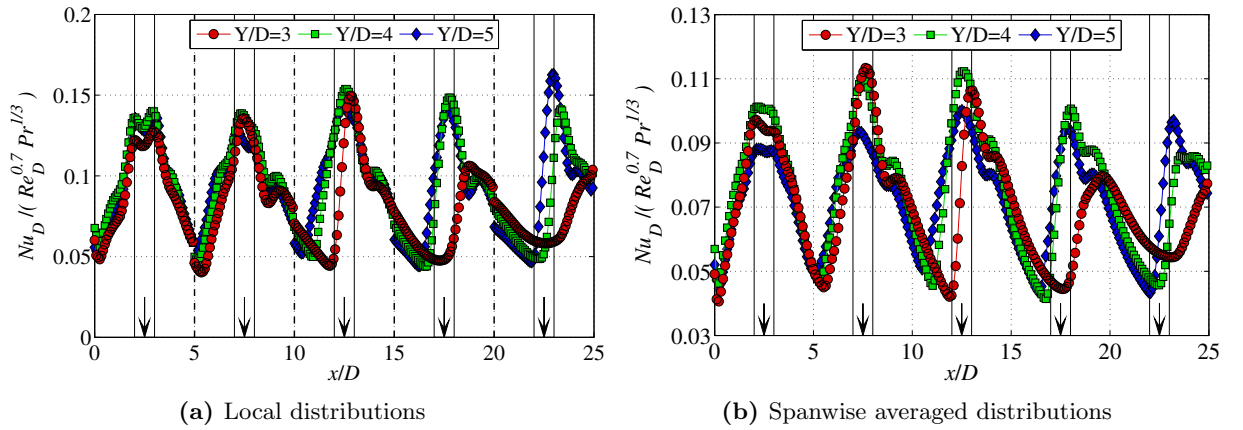


Figure 6.9: Local and spanwise averaged Nu_D distributions on the target for different channel widths. X/D , $Z/D=1.5$, $\Delta y/Y=0.4$, $Re_D=32,400$

the level of stagnation point heat transfer is fairly similar as observed in Figure 6.9(a), where the donut shape distribution of Nu_D for jet 1 is almost identical in level and distribution for $Y/D=3$, 4, and 5. Therefore, the main difference of varying Y/D at upstream channel positions is the increase of the wall jet region which reduces the jet plate open area by adding a low heat transfer region. This is better observed in the spanwise averaged Nu_D distributions of Figure 6.9(b). These data indicate higher heat transfer coefficients of the upstream channel positions using low passage widths, i.e. $Y/D=3$, while the downstream channel positions are better cooled using wider channels, which in turn means lower crossflow rates. Note that for $Y/D=3$, the stagnation point heat transfer of the fifth jet is also not visible in the spanwise averaged results. For all cases, the heat transfer coefficients in the wall jet region are less affected by Y/D since the local and the spanwise averaged Nu_D of different channel widths have about the same level.

6.4.2 Sidewalls

For the sidewalls of the channel, the surface contours in Figure 6.8 indicate higher local heat transfer coefficients at $Y/D=3$, due to the fact that the jets are placed closer to the sidewalls resulting in more direct interaction. As the passage width increases, i.e. $Y/D=5$, the local heat transfer is reduced, especially in the intermediate region between two jets of the same row. A quantitative comparison between the different channel widths for both sidewalls is illustrated by the spanwise averaged results in Figure 6.10. On both sidewalls, upstream channel positions are

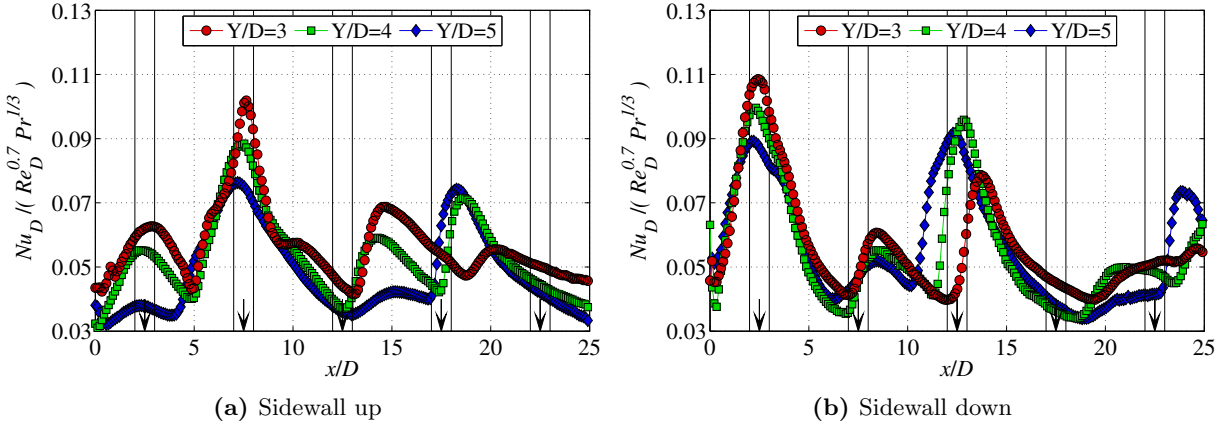


Figure 6.10: Spanwise averaged Nu_D distributions for the upper and lower sidewall for different channel widths. X/D , $Z/D=1.5$, $\Delta y/Y=0.4$, $Re_D=32,400$

better cooled with low width channels, as clearly illustrated in the peak heat transfer coefficients of jets 1 and 2. At the axial position of jet 3, where the crossflow has been formed by a notably amount, $Y/D=3$ provides better heat transfer capabilities for the upper sidewall and, $Y/D=4$ and 5 for the lower wall. It is worth to be noticed also the difference in the deflection of the heat transfer peak of jet 3 (sidewall down) which is enhanced as Y/D is reduced. For the high crossflow dominated regions (jets 4 and 5), the developed crossflow results in a more distributed form of cooling by preventing the generation of peak heat transfer coefficients with a simultaneous decrease of the achievable heat transfer rate.

6.4.3 Jet plate

The jet plate local heat transfer coefficient distributions for various channel widths were not evaluated in the course of this study.

6.5 Effect of Hole Staggering ($\Delta y/Y$)

This section investigates the effect of hole offset position from the channel centerline which has been in depth investigated by Terzis et al. (2014). Three different impingement jet patterns were considered according to the notation of Figure 3.6: an inline pattern ($\Delta y/Y=0$), a low-staggered ($\Delta y/Y=0.4$) and a full-staggered ($\Delta y/Y=0.76$) arrangement. The Z/D was varied between 1 and 3 investigating the impact of impingement jet offset position at different channel heights. The streamwise jet spacing and channel width were constant, $X/D=Y/D=5$. Similar to the preceding sections, only the results of $Re_D=32,400$ will be presented. Figures 6.11 and 6.12 show the normalised surface contours of heat transfer coefficient for the staggered arrangements where h_{ref} is the same with Figure 6.6 allowing a direct comparison with the case $\Delta y/y=0$. A quantitative comparison between different jet patterns is made in Figure 6.13, which shows local Nu_D distributions on the channel centerline ($y=0$) for the target plate and Figure 6.14, which presents the spanwise averaged $Nu_D/(Re_D^{0.7} Pr^{1/3})$ for all channel walls.

6.5.1 Target plate

For the target plate, it can be easily observed that the overall pattern of the heat transfer coefficient is no longer symmetrical to the channel centerline and the peak heat transfer levels

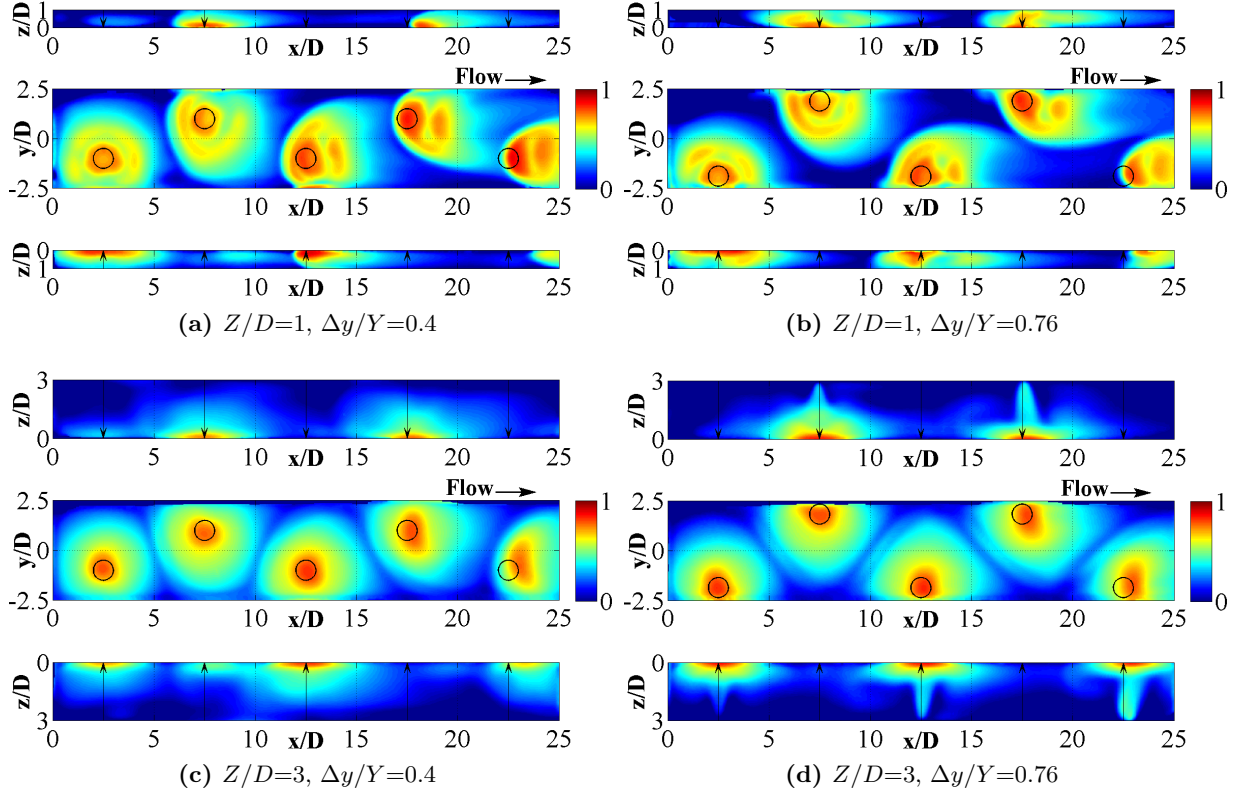


Figure 6.11: Heat transfer coefficient surface contours (h/h_{ref}) for different jet patterns. h_{ref} : $330\text{W}/(\text{m}^2\text{K})$. $X/D=Y/D=5$, $Re_D=32,400$

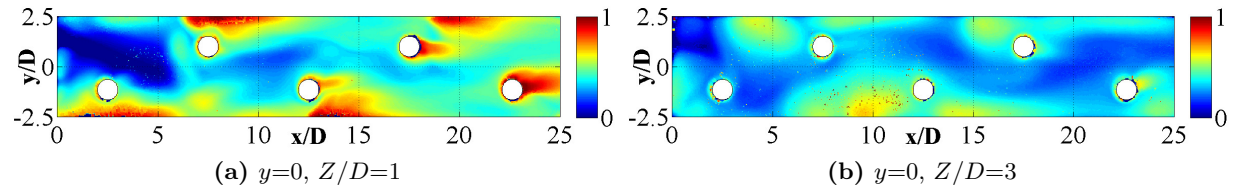


Figure 6.12: Heat transfer coefficient surface contours (h/h_{ref}) for the jet plate. h_{ref} : $240\text{W}/(\text{m}^2\text{K})$. $X/D=Y/D=5$, $\Delta y/Y=0.4$, $Re_D=32,400$

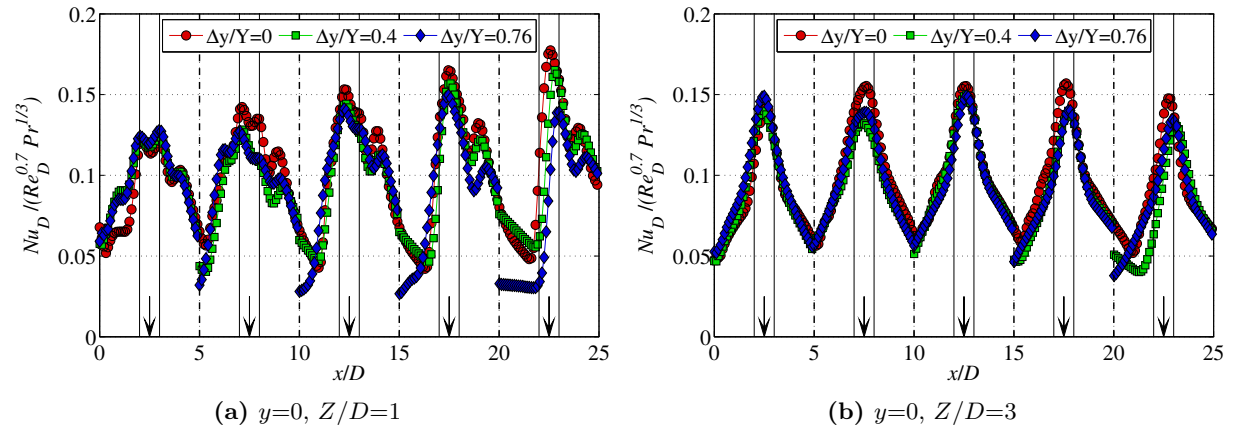
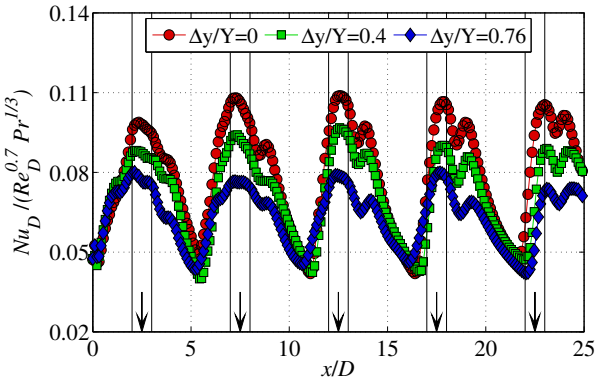
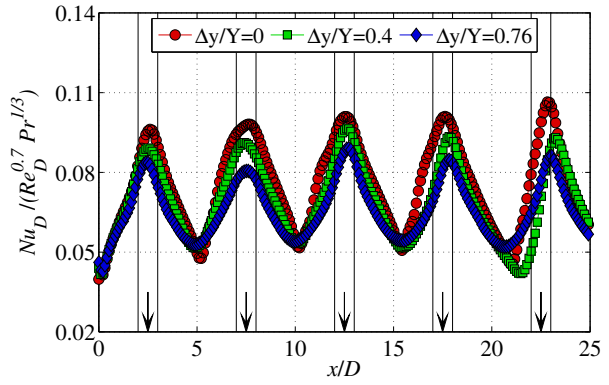


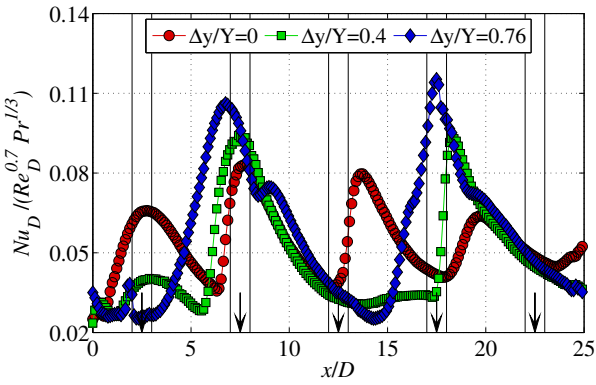
Figure 6.13: Local Nu_D distributions on the target plate centerline ($y=0$) for various jet patterns. $X/D=Y/D=5$, $Re_D=32,400$



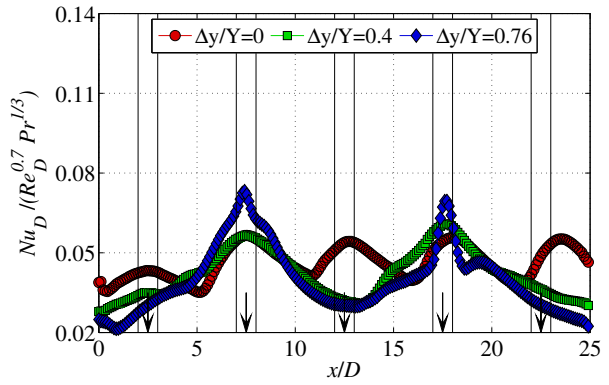
(a) Target plate, $Z/D=1$



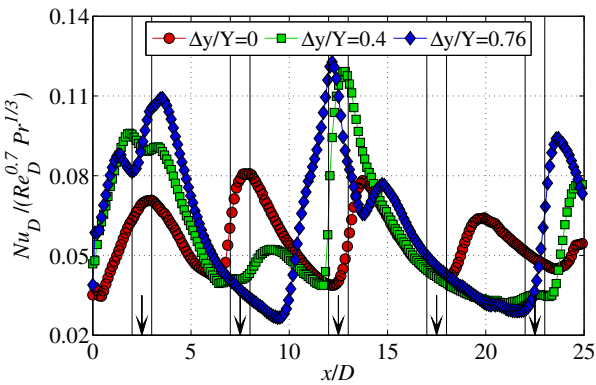
(b) Target plate, $Z/D=3$



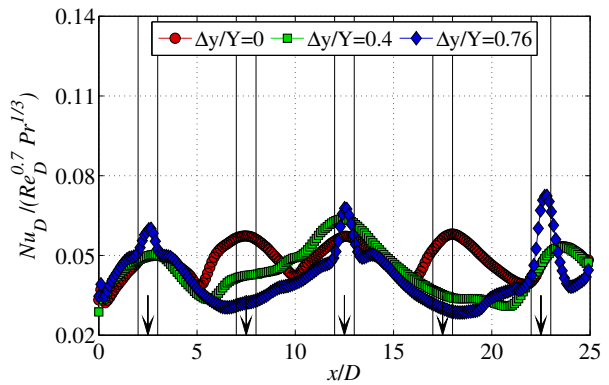
(c) Sidewall up, $Z/D=1$



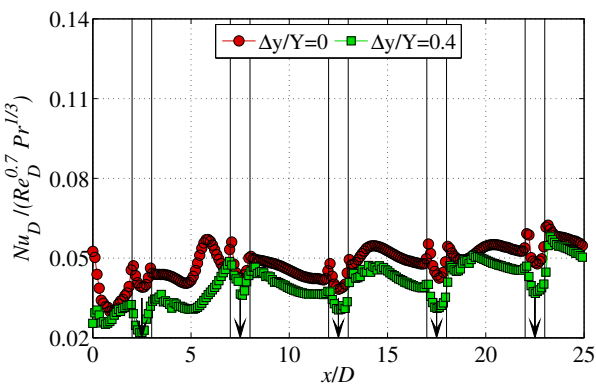
(d) Sidewall up, $Z/D=3$



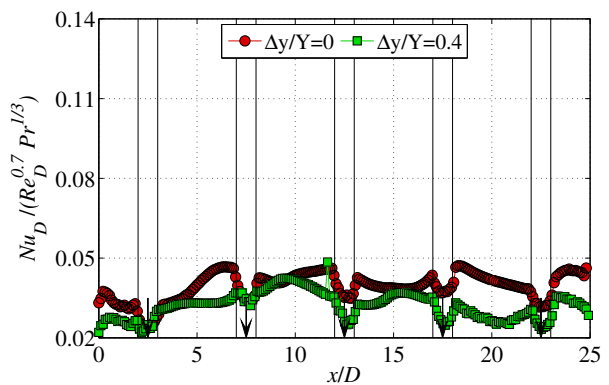
(e) Sidewall down, $Z/D=1$



(f) Sidewall down, $Z/D=3$



(g) Jet plate, $Z/D=1$



(h) Jet plate, $Z/D=3$

Figure 6.14: Spanwise averaged Nu_D for all channel walls. $X/D=Y/D=5$, $Re_D=32,400$

are shifted according to the new jet positions. At $Z/D=1$, the interaction between the jets and the sidewalls can be clearly observed since only a part of the secondary peak ring (jets 1 and 2) and the horseshoe vortices (jets 3, 4 and 5) is noticeable. Note also that, for $Z/D=1$ and $\Delta y/Y=0.76$, Figure 6.11(b), a region of liquid crystal inactivity (no colour change) is observed on the top left corner indicating a region with very low heat transfer coefficients. Furthermore, the heat transfer levels are slightly lower compared to the inline cases, presented in Figure 6.6, indicating an overall reduction of the convective heat transfer when a staggered jet pattern is used. This is better observed in Figure 6.13 which shows that stagnation point heat transfer is gradually reduced and more deflected towards the channel exit. This is because of the direct influence of the generated crossflow which is higher compared to the inline case where the jets are somehow protected from the incoming flow by the upstream jets. The impact of jet pattern at $Z/D=3$ is similar to $Z/D=1$, however, the overall effect is less pronounced.

The spanwise averaged $Nu_D/(Re_D^{0.7}Pr^{1/3})$ distributions, shown in Figures 6.14(a) and (b), indicate that the heat transfer level is reduced compared to the inline case with the reduction being higher as the jet staggering position is increased. This is because the lateral spread of the staggered jets on the target surface does not cover the whole width of the channel resulting in a bigger low heat transfer region as shown also by the surface contours in Figure 6.11. However, the overall Nu_D distribution remains the same for the inline and staggered arrangements. The reduction of spanwise averaged results with increasing $\Delta y/Y$ is higher at $Z/D=1$ where the overall impact of crossflow is more pronounced. The lowest heat transfer coefficient is always located at the first jet due to the lower local Re_D . The crossflow generated by the spent air of the upstream jets has thus a beneficial effect up to the fifth jet and this holds also for the lowest Z/D configuration. A very similar trend was found by [Son et al. \(2001\)](#) for staggered arrays in multi-jet configurations with Z/D between 1.9 and 3.

6.5.2 Sidewalls

On the sidewalls of the channels, the surface contours in Figure 6.11, show that the heat transfer coefficient is locally increased compared to the inline case since the jets are placed closer to the sidewalls resulting in direct interaction. Subsequently, the peak heat transfer coefficients are not shifted in the downstream direction and appear in the same axial position with the stagnation points on the target plate. The local increase of heat transfer level is obviously enhanced with increasing $\Delta y/Y$. Note also the jet traces at $Z/D=3$ and $\Delta y/Y=0.76$ which start from the jet plate and wipe out close to the target plate ($z=0$). Additionally, the wall jet region of jets 3 and 5 is unobservable on the upper sidewall and vice-versa for jets 2 and 4. This indicates that the amount of crossflow is sufficiently high in order to prevent the wall jets from reaching the sidewall of the opposite side of the channel resulting in low heat transfer areas.

Hole staggering effects on the sidewalls are quantitatively compared by the spanwise averaged results in Figures 6.14(c) to (f). For all the cases, the heat transfer coefficient is locally increased with increasing the hole offset position and placing the jets closer to the sidewall. Particularly, this holds for jets 2 and 4 in the upper wall and jets 1, 3 and 5 for the lower sidewall. In addition, the spanwise averaged results for $Z/D=1$ show bigger differences between peak and valleys compared to the target plate distributions. Between the peaks of heat transfer on the same sidewall, however, an opposite behaviour is observed with the spanwise averaged Nu_D numbers being highest and lowest when $\Delta y/Y=0$ and 0.76, respectively. This is attributed to the fact that an increase of jet offset position results actually in a negative jet staggering for this

region with a corresponding remotion of the local jet to the other sidewall. Between the jets, the spanwise averaged heat transfer level is very similar indicating a small effect of $\Delta y/Y$. Similar trends are observed for $Z/D=3$, however, the overall level of Nu_D numbers is considerably lower.

6.5.3 Jet plate

As expected, the heat transfer distribution on the jet plate is rearranged according to the new jet positions similar to the target plate. For $Z/D=1$, the peak heat transfer caused by the post-impingement flow is maintained and enhanced in magnitude at the side of the jet which is closer to the sidewall but completely disappeared on the other side which is closer to the channel centerline. This suggests that the peak heat transfer is protected by the sidewall and the jet itself on one side and it is directly exposed to the crossflow on the other side. Additionally, the jet wake region of high heat transfer at the position of the downstream jets is increased and this could be attributed to the increased influence of the crossflow since the jets on the inline pattern are somehow protected from the upstream jet. This higher jet and crossflow interaction results in a larger deflection of the jet potential core which is apparently beneficial for the local heat of the downstream positions. Nevertheless, the level of heat transfer coefficients is observed to be reduced with increasing hole offset position similar to the target plate. This can be easily noticed by comparing the intensity of the colour of the surface contours in Figures 6.6 and 6.12.

Figures 6.14(g) and (h) show the spanwise averaged Nu_D distributions, and hence, a quantitative comparison of the effect of $\Delta y/Y$ for $Z/D=1$ and 3, respectively. Note that experiments using a full staggered arrangement ($\Delta y/Y=0.76$) were not performed for the jet plate. For $Z/D=1$, the distribution of spanwise averaged Nu_D with $\Delta y/Y=0.4$ is very similar to the inline pattern. The only noticeable difference is detected upstream of jet 2, where the peak heat transfer observed at the inline pattern is disappeared for $\Delta y/Y=0.4$. For $Z/D=3$, similar trends are observed, however, the heat transfer coefficients are relatively smaller compared to $Z/D=1$. Similar to the target plate, hole staggering effects are more pronounced at high crossflow momentum (low Z/D) while the heat transfer coefficients for $Z/D=3$ are clearly smaller compared to $Z/D=1$ for both inline and staggered jet patterns.

6.6 Effect of Streamwise Jet Spacing (X/D)

This section investigates the effect of streamwise jet-to-jet spacing (X/D) which is well documented in the literature for multi-jet arrangements i.e. [Hollworth and Berry \(1978\)](#) and [Andrews et al. \(1987\)](#). Figure 6.15 indicates the heat transfer coefficient surface contours for $X/D=5$ and 8, for $Re_D=32,400$, where the $h_{ref}=294W/m^2K$ is the maximum value of $X/D=5$. Contrary to the preceding sections, the streamwise averaged $Nu_D/(Re_D^{0.7}Pr^{1/3})$ distributions will be presented in Figure 6.16 considering the heat transfer variations in the axial direction.

6.6.1 Target plate

Contrary to the channel width variation presented in Section 6.4, the momentum of the crossflow is unaffected when X/D is varied, since the channel cross-sectional area remains the same. Therefore, the main effect of increasing X/D , and hence reducing the open area (A_f), it is to substantially increase wall jet regions introducing lower heat transfer coefficients. This means that for higher values of X/D the overall heat transfer is reduced due to an inadequate coverage of the exposed surface. This is clearly observed in the surface contours of Figure 6.15, where the

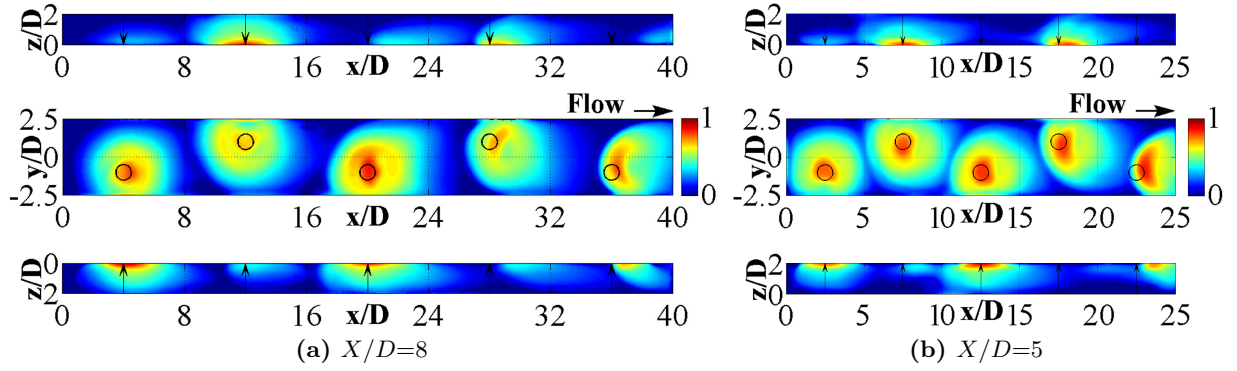


Figure 6.15: Heat transfer coefficient surface contours (h/h_{ref}) for different axial jet-to-jet spacings. h_{ref} : $294W/(m^2K)$. $Re_D=32,400$, $Y/D=5$, $Z/D=2$, $\Delta y/D=0.4$

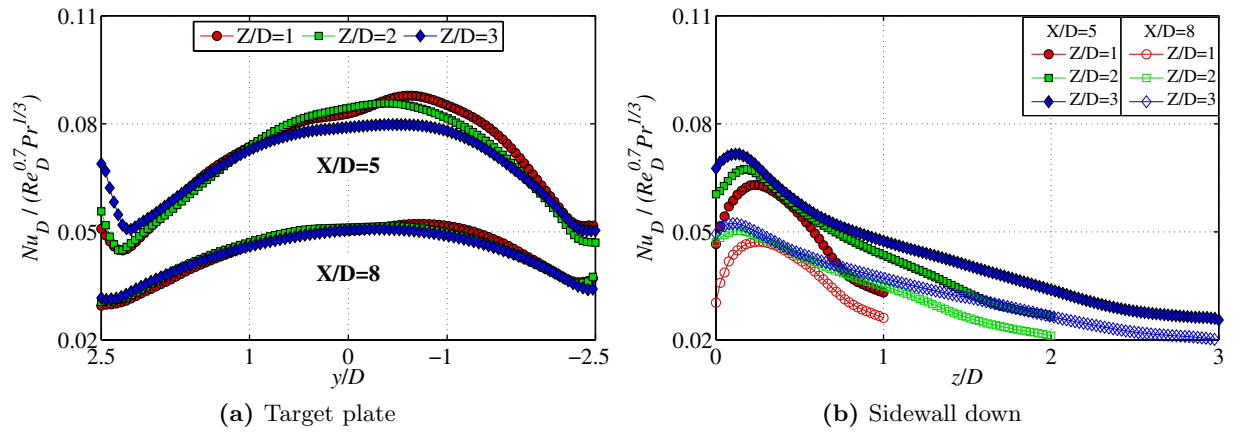


Figure 6.16: Streamwise averaged Nu_D distributions. $Y/D=5$, $\Delta y/Y=0.4$, $Re_D=32,400$

target plate areas between the jets experience considerably lower convection coefficients when X/D equals to 8 since the jets, and hence their stagnation point regions, are farther between them.

The quantitative comparison in Figure 6.16(a) indicates that the streamwise averaged Nu_D is about 35-40% lower for $X/D=8$ over the full channel width. A similar reduction was observed by other authors by doubling X/D for multi-array arrangements, i.e. Kercher and Tabakoff (1970) and Chance (1974). Additionally, it is worth to be noticed that increasing the open area ratio by varying X/D from $8D$ to $5D$, increases also the sensitivity of Nu_D to other geometrical factors, such as Z/D . This means, the streamwise averaged Nu_D numbers for the various channels heights are closer for $X/D=8$. Note also that the overall heat transfer distribution is slightly inclined towards the right sidewall due to the asymmetry of the low stagger configuration with three jets on the lower part (see Figure 6.15). Furthermore, closer to the side walls of the channels, and especially for $X/D=5$, the heat transfer coefficients are slightly increased, probably due to the interaction with the wall and the attempt of the crossflow to overcome the downstream jet(s) which results in higher local velocities and increased turbulence levels. It should be also noted that similar effects of Y/D and Z/D variation were also observed for $X/D=8$.

6.6.2 Sidewalls

For the sidewalls of the channel, the effect of X/D is similar with the target plate since the distance between the jets is increased. This is quantitatively illustrated in 6.16(b), which shows

the vertically averaged Nu_D distributions on the lower sidewall. The results indicate that the Nu_D level at $X/D=8$ is about 30% and 15% lower close to the target plate ($z=0$) and the jet plate ($z=Z$), respectively. It is also noticeable that the heat transfer is increased close to the target plate with a local maximum of the vertically averaged heat transfer coefficient at about $Z/D=0.25$, 0.16 and 0.11 for $Z/D=1$, 2 and 3, respectively. The movement of this local maximum closer to the target plate ($z=0$) at higher Z/D values is attributed to the secondary peak ring appeared on the target plate at low Z/D values. This results in a bigger thickness of the wall jet region, and hence, broader interaction of the impinged flow with the sidewalls.

6.6.3 Jet plate

The jet plate local heat transfer coefficient distributions for various streamwise jet-to-jet spacings (X/D) were not evaluated in the course of this study.

6.7 Effect of Varying Jet Diameter (ΔD)

Considering the preceding sections of the chapter, it can be easily understood that the developed crossflow plays an important role on the level and distribution of heat transfer. Crossflow is one of the most important design factors, especially for gas turbine blades and vanes where the large applicability of maximum crossflow orientations (single channel exit designs), reduces the heat transfer capabilities of the downstream regions of the jet array, as shown by [Obot and Trabold \(1987\)](#). Therefore, this section investigates the impact of varying jet diameters, increasing or decreasing constantly towards the channel exit in an attempt to regulate the generated crossflow.

The examined channels consist of a single row of five inline cooling holes tested at $Z/D=1.5$ and 3. Three cases for the varying jet diameter will be discussed, as shown in Figure 6.17. A uniform one, a 10%-decreasing and a 10%-increasing jet pattern. The geometrical characteristics of the models are summarised in Table 6.1. Note that the magnitude of local Z/D_j varies by a factor of 1.5 at the same geometry. The center of the jets is always located at the same axial position resulting in a slightly different streamwise spacing. The local X/D_j based on the upstream jet, Y/D_j , as well as the variation of local open area ($A_{f,j}$), are also listed in Table 6.1. Compressibility effects were neglected since the maximum Mach number of the smallest jet was always below 0.15 over full range of flow conditions tested in this series of experiments.

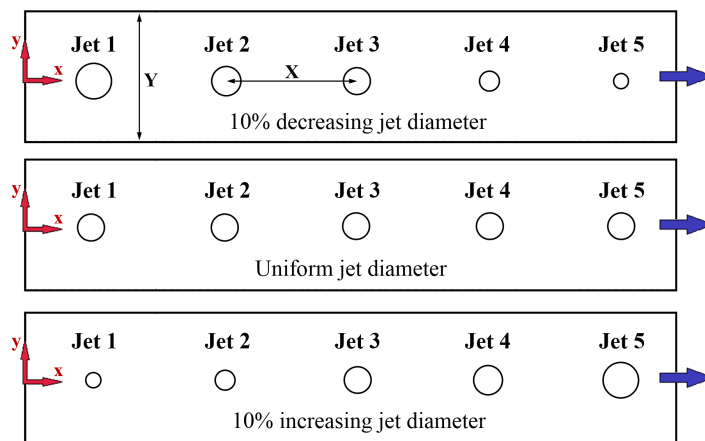
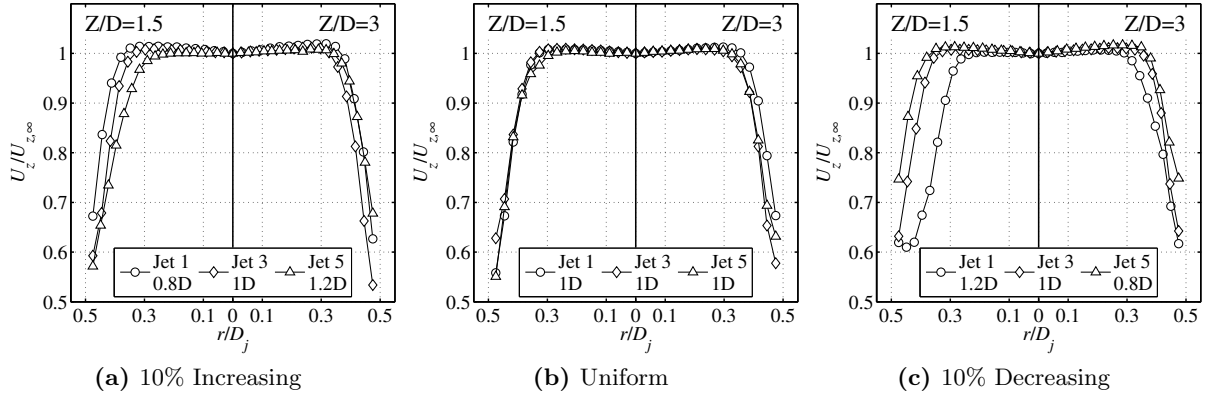


Figure 6.17: Schematic representation of the varying jet diameter test cases

Table 6.1: Geometrical characteristics of the investigated varying jet diameter cases

DECREASING		-10%	$X/D=5$	$Y/D=5$	$A_f=3.2\%$	$Z/D=1.5$	$Z/D=3$
Jet	Diameter	Size	X/D_j	Y/D_j	$A_{f,j}$	Z/D_j	Z/D_j
1	$1.2D$	24mm	-	4.16	4.52	1.25	2.5
2	$1.1D$	22mm	4.16	4.54	3.8	1.36	2.72
3	$1.0D$	20mm	4.54	5	3.14	1.5	3
4	$0.9D$	18mm	5	5.55	2.54	1.66	3.33
5	$0.8D$	16mm	5.55	6.25	2.01	1.875	3.75

INCREASING		+10%	$X/D=5$	$Y/D=5$	$A_f=3.2\%$	$Z/D=1.5$	$Z/D=3$
Jet	Diameter	Size	X/D_j	Y/D_j	$A_{f,j}$	Z/D_j	Z/D_j
1	$0.8D$	16mm	-	6.25	2.01	1.875	3.75
2	$0.9D$	18mm	6.25	5.55	2.54	1.66	3.33
3	$1.0D$	20mm	5.55	5	3.14	1.5	3
4	$1.1D$	22mm	5	4.54	3.8	1.36	2.72
5	$1.2D$	24mm	4.54	4.16	4.52	1.25	2.5

**Figure 6.18:** Jet axial exit velocity profiles (y -direction)

6.7.1 Flow distributions and discharge coefficients

The amount of crossflow of each configuration was determined by probe traversing measurements for each individual jet as described in Section 3.4. The pressure traverses revealed the jet axial velocity distribution at the exit of the hole (y -direction). The velocity profiles, normalised by the velocity in the center of the jet, are shown in Figure 6.18. For clarity purposes, only the jets 1, 3 and 5 are included in the figure providing nevertheless a sense of the evolution of the velocity profiles towards the channel exit. All jets experience a top-hat velocity profile, where generally, the flat part of the distribution is about 75-85% the jet diameter. Note that local velocities are slightly higher closer to the edges of the impingement hole similar to Lee and Lee (2000). For the uniform jet size pattern, shown in Figure 6.18(b), the velocity profile is almost identical for all jets for $Z/D=1.5$ and 3 as a direct consequence of the overall geometrical similarity between the jets (see also Figure 5.4). However, for the 10%-increasing and 10%-decreasing jet size patterns, shown in Figure 6.18(a) and (c), respectively, there is a tendency for higher velocity gradients as the local L/D_j is increased (reduced D_j) due to the different local discharge coefficients. Note also that for jet 1 of the decreasing jet size pattern, the flow separation is highly distorted close to the edges of the hole at $Z/D=1.5$.

The local discharge coefficients were therefore determined by Equation 5.2. Figure 6.19 shows

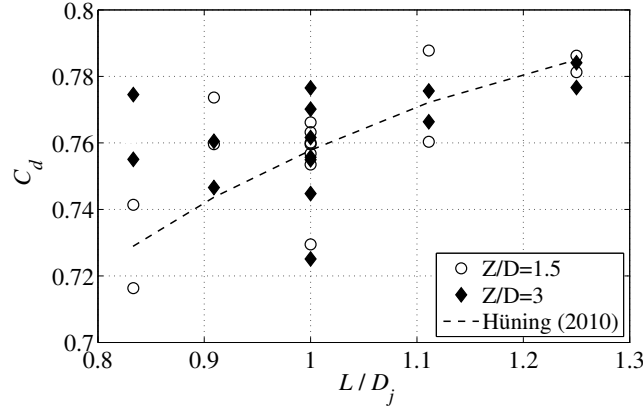


Figure 6.19: Local jet discharge coefficients at $Re_D=23,780$

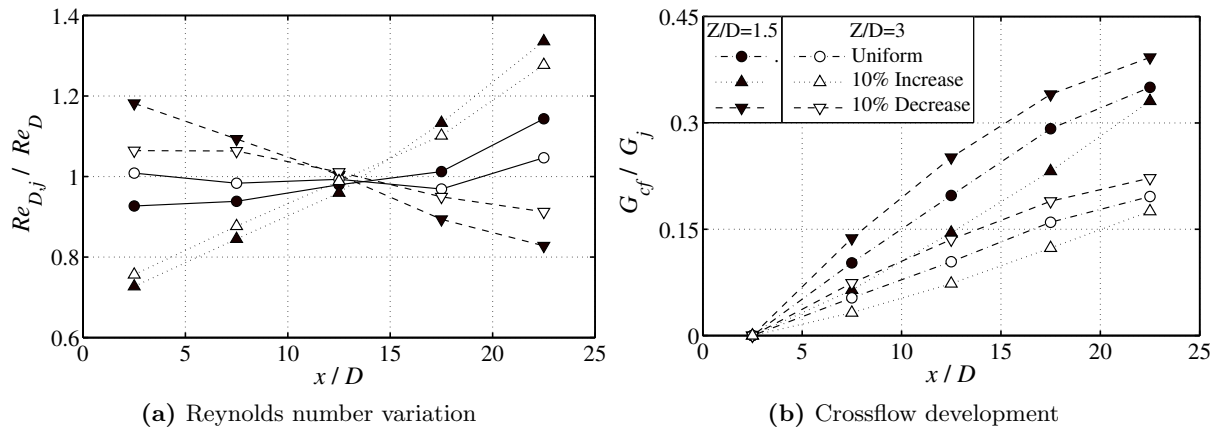


Figure 6.20: Local $Re_{D,j}$ variation and crossflow development (G_{cf}/G_j)

local C_D values as a function of L/D_j for the two channel heights at $Re_D=23,780$. Local discharge coefficients increase from about 0.73 to 0.78 as the jet diameter is reduced from $1.2D$ to $0.8D$, and hence L/D_j is increased from 0.83 to 1.25. The local discharge coefficients are also in agreement, in terms of level and trend, with the correlation given by Hünig (2010) for short orifice plates. No dependence with Z/D was observed as a direct consequence of the similarity of the velocity profiles for both channel heights (see Figure 5.4). Additionally, no particular trend was observed with the axial jet position indicating that local L/D_j effects on C_D are more important than the crossflow effect in this flow range, in agreement with Florschuetz and Isoda (1983). Additionally, discharge coefficients were independent of the Reynolds number in the range of investigated flow conditions ($Re_{D,j}=14,470-75,500$) similar to Lichtarowicz et al. (1963). The overall uncertainty is in the order of 7% and 4% for the lowest and for the highest L/D .

Figure 6.20 illustrates the streamwise Reynolds number variation based on the local jet diameter and the bulk velocity of each impingement hole. As expected, larger $Re_{D,j}$ variations are observed for $Z/D=1.5$ due to the higher pressure drop in the channel. In particular, for the uniform jet pattern, $Re_{D,j}/Re_D$ increases from 0.92 for jet 1 to 1.17 for jet 5. On the other hand, very low variation is observed for $Z/D=3$ since $Re_{D,j}$ is increased by only 5% from jet 1 to 5. However, when the jet diameter is increased by 10%, the overall increase of $Re_{D,j}$ is more pronounced with reduced values for the upstream jets and increased for the downstream ones. This is attributed to the continuously increased jet diameter from $0.8D$ to $1.2D$ which in turn increases the local $Re_{D,j}/Re_D$ from 0.76 to 1.38. On the other hand, $Re_{D,j}$ is axially decreased

with reducing jet diameters. The right part of Figure 6.20 shows the streamwise distribution of the generated crossflow-to-local jet mass velocity ratio (G_{cf}/G_j). As expected, crossflow increases towards the channel exit as a direct consequence of the single channel exhaust, and the development is more pronounced at $Z/D=1.5$. G_{cf}/G_j reaches the value of 0.35 and 0.2 at the last jet for $Z/D=1.5$ and 3, respectively. For both channel heights, a lower amount of crossflow is generated when a 10%-increasing jet pattern is used which is attributed to the reduced values of local jet mass velocities in these regions. On the other hand, crossflow is abruptly increased when a decreasing jet pattern is considered. For example, the amount of crossflow generated at jet 3 for the decreasing jet pattern of $Z/D=3$ equals the amount of crossflow generated for the increasing jet pattern of $Z/D=1.5$, which means that jet size variations in this region are able to compensate the reduced channel cross-sectional area.

6.7.2 Target plate

If the jet diameter is axially varied, either increasing or decreasing, the resulting range of local Z/D_j affects moderately the level of stagnation point heat transfer, as shown also by single jet experiments, i.e. Katti and Prabhu (2008a); Lee et al. (2004). Therefore, the main effect of varying jet diameter is the variation of the local open area ($A_{f,j}$) which results in a different width of the stagnation region, as well as the influence of the generated crossflow.

For jet 1, in the absence of crossflow, the smallest jet diameter in Figure 6.21(a), increases the local values of Y/D_j for both $Z/D=1.5$ and 3, resulting in a region of very low heat transfer on the upstream corners of the channel. Contrary, if the diameter of jet 1 is increased from $0.8D$ to $1.2D$, the reduced values of Y/D_j increase the stagnation point region, and hence the overall heat transfer level. As the crossflow in the channel is developed, the distribution of heat transfer is very similar for the three different jet patterns given the similar diameters of jets 2, 3 and 4. However, as the jet pattern is varied from an increasing to a decreasing jet diameter, the stagnation points are more deflected downstream due to the larger generated crossflow, shown also in Figure 6.20(b). Note that similar trends are observed for both $Z/D=1.5$ and 3, although the tendencies are clearly more significant for the lower channel height. The influence of the generated crossflow at the different jet size patterns is more evident in the stagnation point region of jet 5. For the decreasing jet size pattern, the peak heat transfer is more deflected in the streamwise direction while the size of the horseshoe vortex is smaller and more bended due to the influence of the larger crossflow momentum. These trends are more evident in the local $Nu_D/(Re_D^{0.7}Pr^{1/3})$ distributions illustrated in Figure 6.22. The decreasing jet pattern slightly increases the local stagnation point heat transfer of the downstream jets and it is more shifted in the direction of the main flow. For the increasing jet size pattern, on the other hand, the local Nu_D numbers are lower, and the deflection of the jet is less affected. The uniform jet pattern lies in between. For $Z/D=3$, the effect of varying jet size is weak and only the jet 5 is affected mainly using a decreasing jet size pattern.

The target plate spanwise averaged $Nu_D/(Re_D^{0.7}Pr^{1/3})$ distributions are illustrated in Figures 6.25(a) and (b), for $Z/D=1.5$ and 3, respectively. By using varying jet diameters, the heat transfer rate is mainly affected on the low and the high crossflow dominated regions, while in the middle of the channel the results are very similar for both channel heights. For $Z/D=1.5$ and around jet 1 region, spanwise averaged Nu_D are about 15% lower using an increasing jet size pattern since the local Y/D_j is 20% and 50% higher compared to the uniform and the decreasing jet size patterns, accordingly. For $Z/D=3$, the trends are the same, however, the

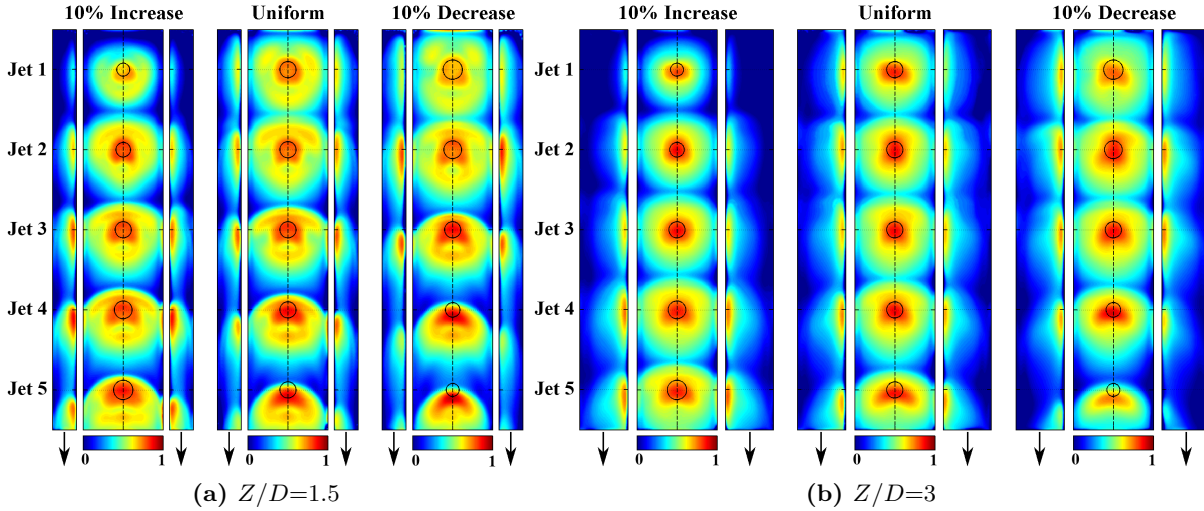


Figure 6.21: Heat transfer coefficient surface contours (h/h_{ref}) for the target plate and the sidewalls for various jet size patterns. $Re_D=23,780$, $X/D=Y/D=5$

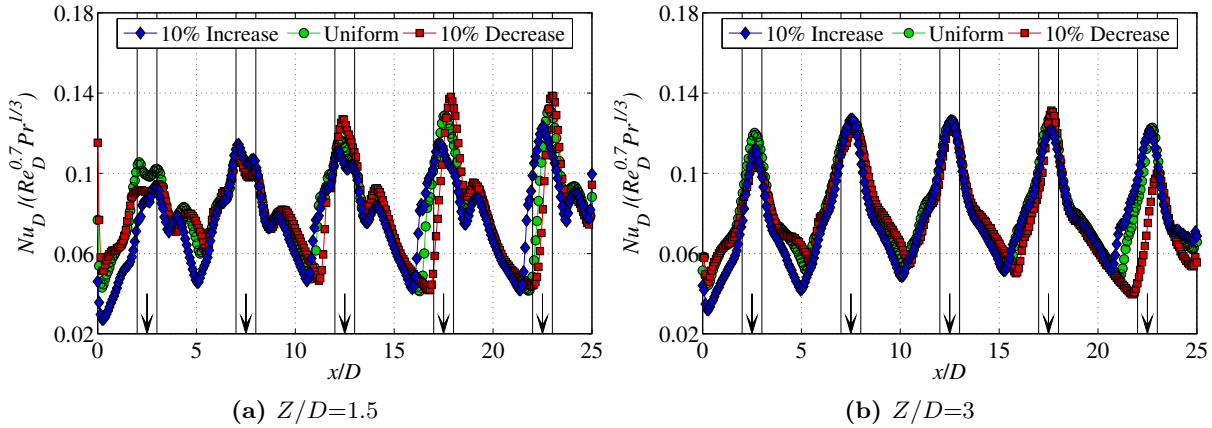


Figure 6.22: Local Nu_D distributions in the centerline of the target plate for various jet size patterns. $Re_D=23,780$, $X/D=Y/D=5$, $h_{ref}=182W/(m^2K)$

overall reduction could be attributed also to the increased values of local channel height, which is $Z/D_j=3.75$, and hence it has an unfavourable effect on the stagnation point heat transfer, as shown also by [Kataoka \(1985\)](#). For the high crossflow dominated region, it is important to reduce the upcoming crossflow and this is achieved by utilising an increasing jet size diameter pattern. This is clearly observed for jet 5 for both $Z/D=1.5$ and 3 where the lowest heat transfer maxima and the largest jet deflection are obtained for the decreasing jet pattern. Nevertheless, the effect of varying jet diameter is less significant for $Z/D=3$.

6.7.3 Sidewalls

Contrary to the target plate, the effect of varying jet diameter has a noticeable effect on the sidewall heat transfer, as shown in [Figure 6.21](#). Upstream channel positions experience higher heat transfer coefficients with decreasing jet size patterns, and hence lower local Z/D_j , while downstream channel positions with increasing jet size patterns so that the local Z/D_j is also reduced. The effect a different jet size pattern is clearly observed on the traces of jet 5 at $Z/D=1.5$. The two counter-rotating vortices of the horseshoe vortex impinge on the sidewall enhancing the local heat transfer in case of an increasing jet size pattern ($G_{cf}/G_j=0.32$). On the other hand,

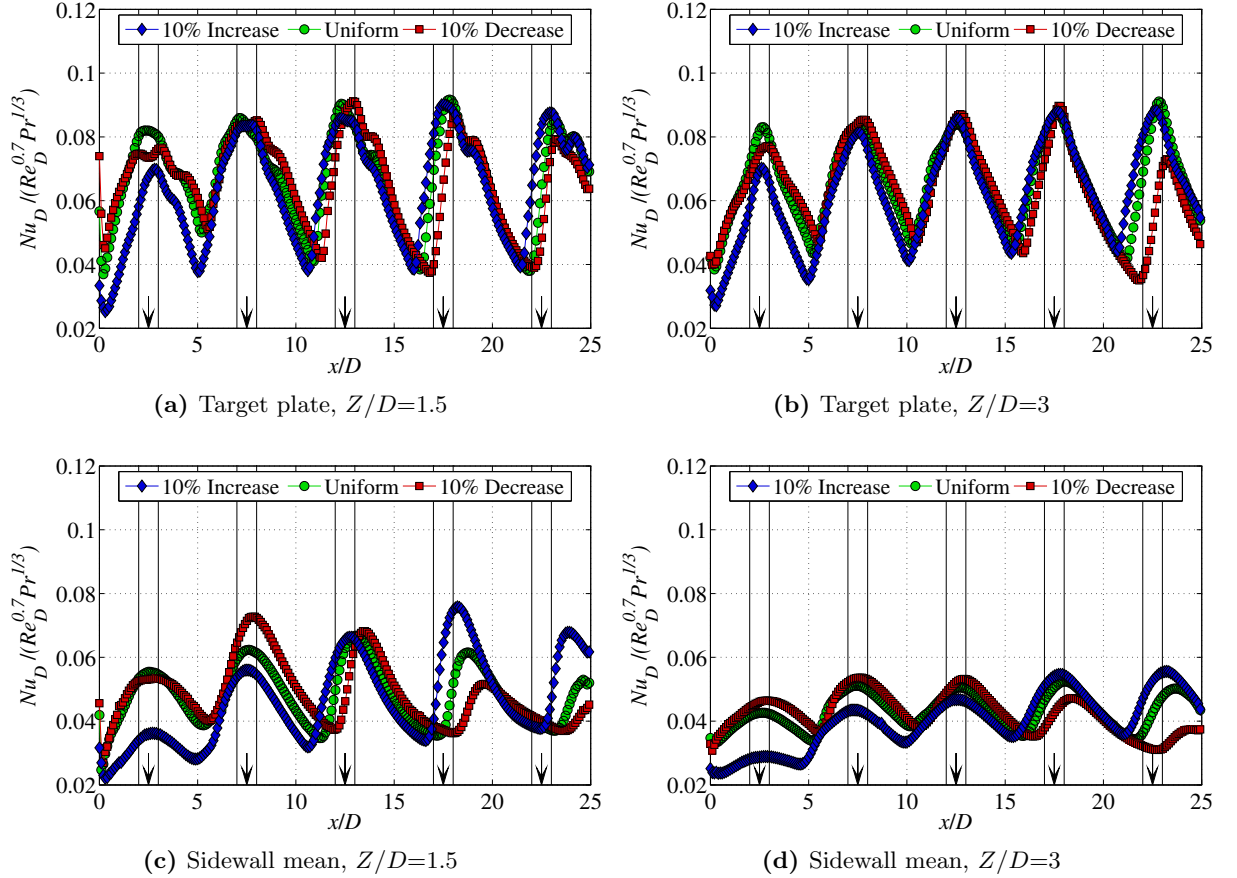


Figure 6.23: Spanwise averaged Nu_D for the target plate and the sidewalls for various jet size patterns. $X/D=Y/D=5$, $Re_D=23,780$

the higher crossflow momentum obtained using a decreasing hole size ($G_{cf}/G_j=0.43$), attenuates the strength of the horseshoe vortex which is no longer able to impinge the sidewalls, and therefore, the traces of jet 5 are hardly seen on the contour. Similar trends are observed for $Z/D=3$, however, the deflection of the peak heat transfer is less pronounced, indicating again that the overall effects of the generated crossflow are less important at higher values of Z/D .

At $Z/D=1.5$, the spanwise averaged $Nu_D/(Re_D^{0.7}Pr^{1/3})$, shown in Figures 6.25(c) and (d), are continuously increased toward the channel exit with a 10%-increasing jet diameter pattern. This is attributed to the reduced local values of Z/D_j and Y/D_j which results in a thicker wall jet flow, as well as to the reduced amount of the upcoming crossflow since less massflow is added in the channel. Contrary, the use of a 10%-decreasing jet size pattern reduces the spanwise averaged Nu_D through the length of the channel for the opposite reasons. Note that the peak heat transfer of jet 5 is almost destroyed by the generated crossflow, especially for $Z/D=1.5$. The effect of varying jet diameter for $Z/D=3$ is less pronounced due to the higher values of local Z/D_j which induce regions of relatively low heat transfer values close to the jet plate.

6.7.4 Jet plate

Figure 6.24 shows the heat transfer coefficient surface contours for the jet plate, normalised by the maximum value, which was $120W/(m^2K)$ for the decreasing jet size pattern of $Z/D=1.5$. Similar to the target plate, in the absence of crossflow (jet 1), the heat transfer increases with increasing jet diameters due to the increased values of open area, and hence, greater stagnation

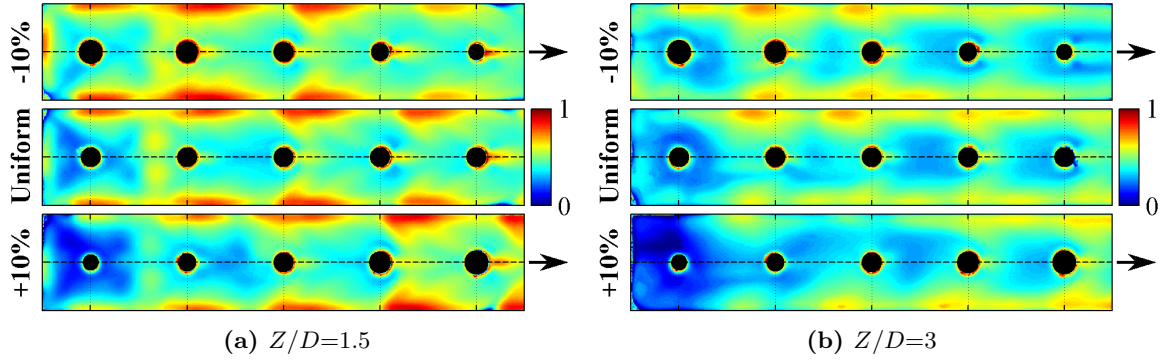


Figure 6.24: Heat transfer coefficient surface contours (h/h_{ref}) for the jet plate for various jet size patterns. $Re_D=23,780$, $X/D=Y/D=5$

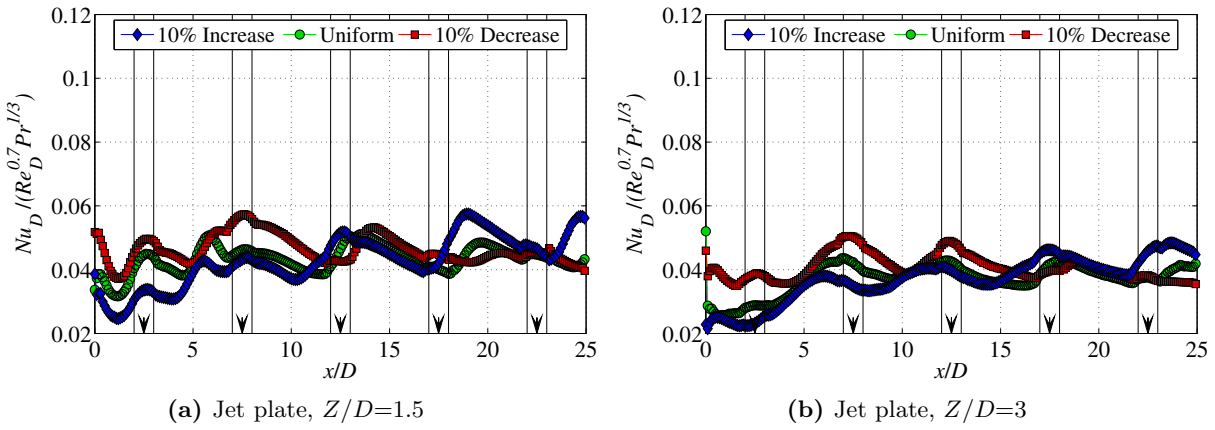


Figure 6.25: Spanwise averaged Nu_D for the jet plate. $X/D=Y/D=5$, $Re_D=32,400$

point regions. On the other hand, for both Z/D , there is a region of very low heat transfer around jet 1 for the case of an increasing jet size pattern. As the crossflow is developed, the heat transfer levels are increased, and the rate of increase is higher as the jet size pattern is converted to an increasing one. This is more evident at downstream positions as the jet diameter and the massflow added to the channel increase. Therefore, increased jet diameters towards the channel exit can be beneficial for the high crossflow dominated regions and vice versa.

The spanwise averaged distributions, shown in Figure 6.25, indicate an overall increase of the Nu_D numbers towards the channel exit for all examined cases. The lowest Nu_D is always obtained around jet 1 region where no crossflow is developed. As the crossflow is generated, Nu_D increases indicating that crossflow has a beneficial effect for the impingement plate heat transfer until jet 3. From this point, a large increase of Nu_D is observed for the increasing jet size pattern for both Z/D . This is attributed to higher values of local $A_{f,j}$ which increases the size of the stagnation point region on the target plate, and consequently, the amount of post-impingement flow on the jet plate. On the other hand, the use of a 10%-decreasing jet size pattern reduces the Nu_D of the very downstream regions.

6.8 Area Averaged Heat Transfer Level

In the majority of experiments, over 95% of the exposed heat transfer area could be recorded with a liquid crystal signal, and therefore, the data are assumed adequate for a good represen-

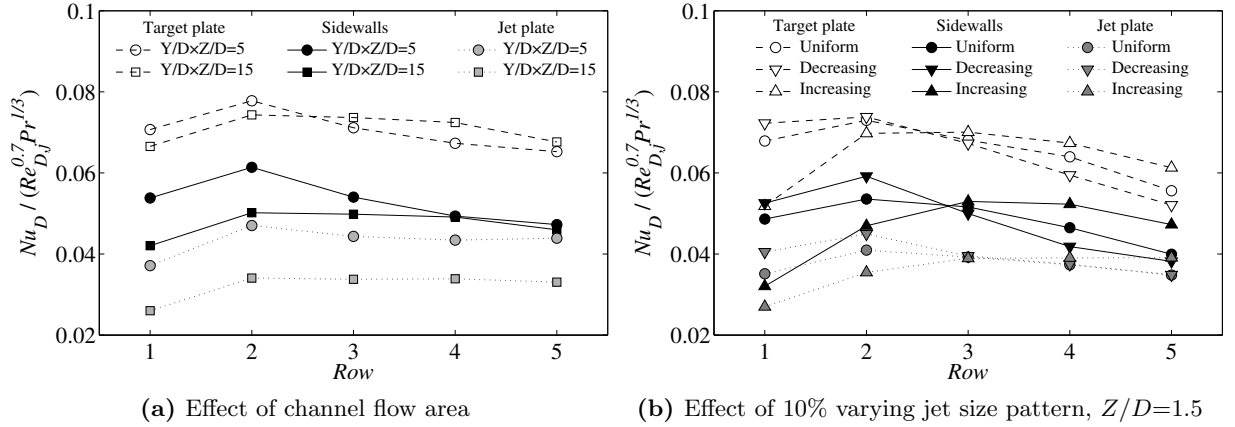


Figure 6.26: Row-by-row area averaged Nu_D . $Re_D=32,400$, $X/D=5$, $\Delta y/Y=0$

tation of the area averaged heat transfer level. This section discusses the effect of the various geometrical factors presented in the preceding sections of the chapter, on the row-by-row and full channel length area averaged Nu_D .

6.8.1 Row-by-row

Figure 6.26(a) shows the effect of channel cross-sectional area on the row-by-row area averaged $Nu_D / (Re_D^{0.7} Pr^{1/3})$ for all channel interior surfaces. Note that the Nu_D level is divided by the local $Re_{D,j}$, and therefore, the y -axis values allow a direct evaluation of the achievable heat transfer.

For the target plate, which experiences the stagnation point heat transfer, small effects of channel flow area are generally observed with a heat transfer degradation towards the channel exit caused by the development of the crossflow. At the low crossflow dominated region (jets 1 and 2), higher heat transfer is obtained at $Y/D \times Z/D=5$ which indicates that in the absence of crossflow narrower channels provide better cooling performances. However, crossflow effects are more intense for low values of channel area resulting in a deeper heat transfer degradation for the downstream jets. This indicates that wider channels are more desirable for downstream channel positions by reducing crossflow momentum.

The sidewalls of the channel show a reduction of Nu_D in the order of 30-35% compared to the target plate. Generally, similar trends are observed, however, the overall effect of $Y/D \times Z/D$ at upstream channel positions is more pronounced. At the high crossflow dominated region, negligible effect of channel area is observed since the developed crossflow attenuates the achievable Nu_D of the narrower channel by deflecting the wall jet regions of the downstream jets.

Contrary to the other walls, the jet-plate area averaged Nu_D remains constant in the stream-wise direction, however, the level of Nu_D is about 50-60% lower compared to the target plate, with the reduction being higher at wider channels. The stability of the streamwise area averaged Nu_D indicates that at a given configuration, the developed crossflow and the flow phenomena occurring at the bottom of the channel cause negligible changes on the top jet plate. Additionally, higher heat transfer is achieved for narrower channels over the full passage.

The effect of varying jet diameter is indicated in Figure 6.26(b). Similar to Figure 6.26(a), the heat transfer is decreased towards the channel exit due to the developed crossflow. The main effect of using varying jet size patterns can be noticed for the low (jets 1 and 2) and high (jets 4 and 5) crossflow dominated regions. For all channel walls, at upstream channel walls, the

area averaged Nu_D is maximised when a decreasing jet size pattern is used due to the increased local open areas, and hence, broader stagnation zones. In particular, for the target plate only, the Nu_D using a 10%-decreasing jet size pattern is about 8% and 28% higher compared to the uniform and the 10%-decreasing jet size pattern, respectively. On the other hand, at jets 4 and 5, Nu_D is maximised when a 10%-increasing jet size pattern is used. This is attributed for two reasons. Firstly, the use of increasing the jet size results in higher Reynolds numbers of the downstream regions, and secondly, the developed crossflow is smaller resulting in lower heat transfer degradation compared to the uniform and the decreasing jet size pattern. Note that for the middle of the channel, the heat transfer level is very similar which is attributed to the same jet diameter of jet 3, although Nu_D is slightly lower for the decreasing jet size pattern due to slightly the increased crossflow momentum generated from jets 1 and 2. For the sidewalls of the channel similar trends are generally observed, however, the achievable Nu_D is about 30% lower compared to the target plate while the effect of varying jet size is more pronounced especially for the low crossflow dominated region, i.e. jet 2. The jet plate heat transfer is somehow stabilised after jet 3 and the effect of varying jet diameter shows negligible effect on the level of Nu_D . However, for jet 1, Nu_D is decreased with reducing jet diameter due to the smaller interaction with the post-impingement flow.

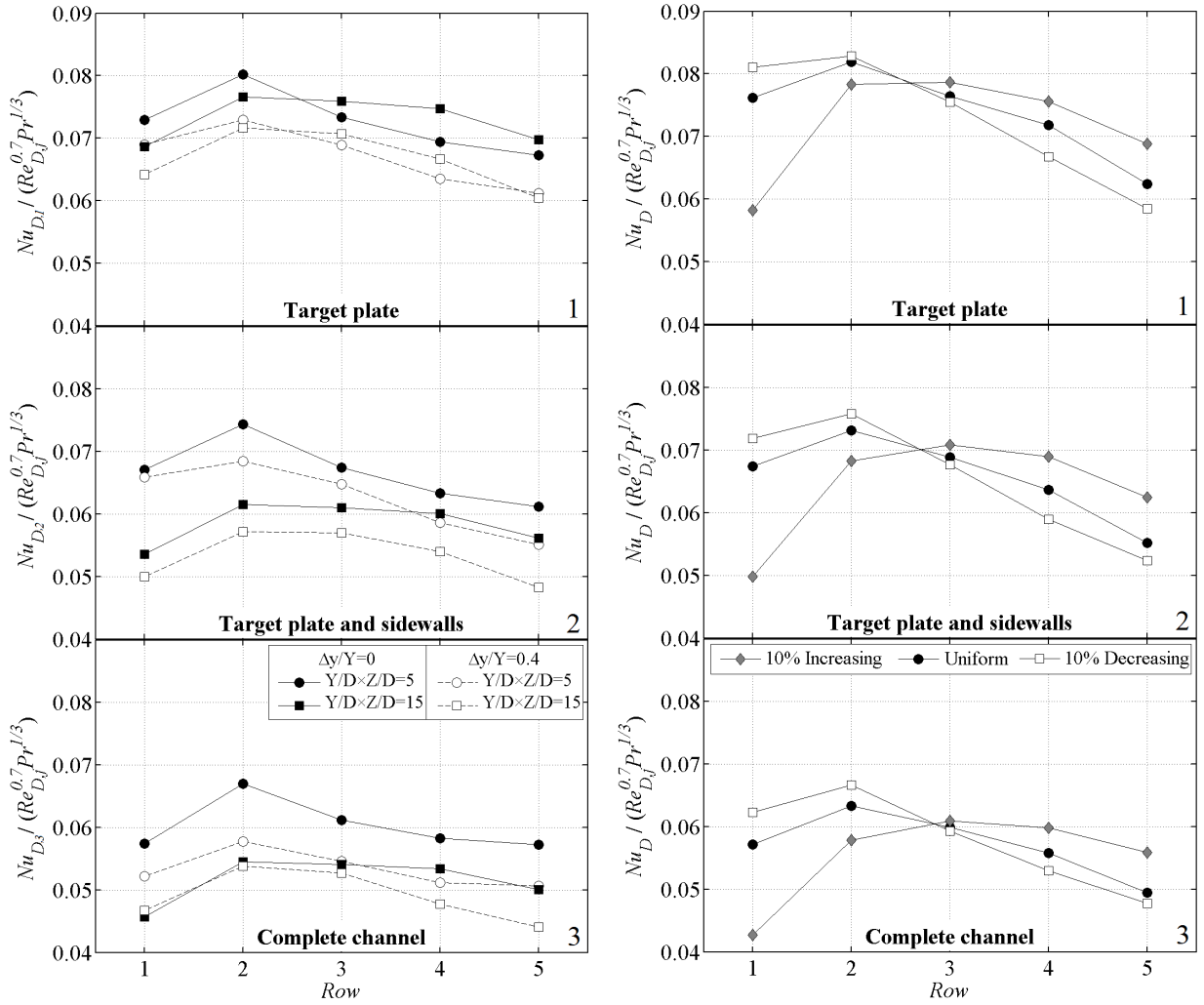
In many applications what matters at the end is the cooling potential of the complete impingement channel considering all interior walls. Therefore, apart from the target plate itself, all interior surfaces have been combined by taking a weighted average value depending on the exposed heat transfer area. For the calculation of the combined Nu_D the following equations were used:

$$Nu_{D,2} = \frac{\frac{Y}{D} Nu_{D,target} + \frac{Z}{D} (Nu_{D,side,up} + Nu_{D,side,down})}{\frac{Y}{D} + 2\frac{Z}{D}} \quad (6.1a)$$

$$Nu_{D,3} = \frac{\frac{Y}{D} (Nu_{D,target} + Nu_{D,imp}) + \frac{Z}{D} (Nu_{D,side,up} + Nu_{D,side,down})}{2\left(\frac{Y}{D} + \frac{Z}{D}\right)} \quad (6.1b)$$

Figure 6.27(a) shows the effect of channel cross-sectional area and impingement hole pattern considering the target plate (1-top figure), the target plate and the sidewalls (2-middle figure), and the complete channel area including the jet plate (3-bottom figure). For all the combinations, the heat transfer degradation towards the channel exit is still observed as caused by the development of the generated crossflow. For the target plate, by using a low staggered jet pattern ($\Delta y/Y=0.4$) the achievable heat transfer level is about 10-15% lower compared to the inline jet pattern over the full length of the channel.

Considering also the sidewalls, Nu_D is decreased by about 15-25% depending on the axial row position. Generally, similar trends with the pure target plate data are observed, however, the effect of $Y/D \times Z/D$ is more pronounced. This is attributed to the fact that, channels with smaller cross-sectional area are more compact and their sidewalls contribute more to the overall cooling process as discussed in the preceding sections. Therefore, the local area averaged Nu_D for $Y/D \times Z/D=5$ is clearly higher compared to $Y/D \times Z/D=15$ over the full channel length. The maximum and minimum differences are about 20% and 10% for jets 1 and 5, respectively. The use of a jet offset position from the channel centerline, has a minimal effect on the distribution of heat transfer and the main effect is the reduction of Nu_D by about 15% compared to the inline jet pattern. As a result, the lowest Nu_D is observed for $\Delta y/Y=0.4$ of the highest channel



(a) Effect of channel flow area and hole offset position

(b) Effect of varying jet diameter, $Z/D=1.5$ **Figure 6.27:** Row-by-row area averaged Nu_D for various configurations at $Re_D=32,400$

cross-sectional area.

Regarding the complete channel internal area (apart from the back wall which blocks the narrow channel from one side), the bottom plot in Figure 6.27(a) shows similar trends with the middle figure, however, the rate of the heat transfer degradation towards the channel exit is somehow reduced, especially for $Y/D \times Z/D=5$. This is attributed to the addition of the jet plate Nu_D which is relatively constant behind jet 3, as shown in Figure 6.26(a). However, the level of heat transfer coefficients is considerably lower compared to the other walls and hence, the main effect of jet plate heat transfer is to slightly reduce the local area averaged Nu_D . Note also that the effect of channel flow area is even more pronounced especially for jets 3, 4 and 5 where Nu_D for $Y/D \times Z/D=15$ is about 15% lower compared to $Y/D \times Z/D=5$.

Figure 6.27(b) indicates the the row-by-row area averaged Nu_D when a varying jet diameter pattern is used. The main difference of considering additional walls to the local area averaged Nu_D is a general heat transfer reduction for all the rows while the overall trends and pattern remain the same. For example, Nu_D in the middle jet considering only the target plate is about 12% and 25% higher compared to the target plate/sidewalls and the complete channel area.

Note also that for all the combinations and configurations presented in Figures 6.27 and 6.26, the Nu_D level around jet 1 region is relatively low indicating a local minimum value. [Fechter](#)

(2011) reported difficulties in predicting the heat transfer of the first jet using two-equation turbulence models, while the velocity magnitude measurements indicated a highly distorted flow at jet 1 compared to the downstream jets. These might indicate a region of high flow unsteadiness which was not possible to be captured with the measurement technique employed in this study.

6.8.2 Full channel length

Figure 6.28(a) indicates the area averaged Nu_D over the full channel length as a function of channel cross-sectional area for various jet average Reynolds numbers and a low jet staggered configuration ($\Delta y/Y=0.4$). Nu_D was calculated considering both target plate and sidewalls due to their significance in double-wall cooling configurations. It can be observed that there is an optimum flow area of $6D^2$ where the cooling capabilities of the channel are maximised. Below this critical line, the high crossflow momentum developed reduces the overall cooling performances by greatly attenuating the heat transfer level of the downstream jets (deflection of jet potential core). On the other hand, increasing channel flow area results in reduced crossflow effects, and thus, better heat transfer can be achieved. However, this reduces the heat transfer capabilities of the sidewalls and the upstream positions resulting in an overall reduction of the area averaged Nu_D . Note also that the Nu_D level for $X/D=8$ is about 35-40% lower compared to $X/D=5$ while the results are also maximised at $Y/D \times Z/D=6$ indicating that crossflow effects have the same impact for both axial jet-to-jet spacings.

Figure 6.28(b) shows the ratio of the area averaged Nu_D obtained on the sidewalls over the target plate as a function of channel flow area. For small cross-sectional areas the Nu_D on the sidewalls is comparable with the target plate heat transfer since the ratio of Nusselt numbers approaches the value of 0.9 at $Y/D \times Z/D=4.5$. Low values of Z/D increase the heat transfer capabilities of the sidewalls as shown in Figure 6.7 due to the lower exposed area in z -direction. Additionally, if Y/D is decreased, the sidewalls are placed closer to the stagnation zones on the target plate and hence, experience a more aggressive wall jet flow, as shown in Figure 6.10. On the other hand, as $Y/D \times Z/D$ increases the contribution of the sidewalls on the overall cooling process is considerably reduced since the ratio of Nusselt numbers approaches the value of 0.65 at $Y/D \times Z/D=15$. Note also that for both plots in Figure 6.28 similar trends can be observed over the full range of flow conditions indicating also the incompressible character of the flow.

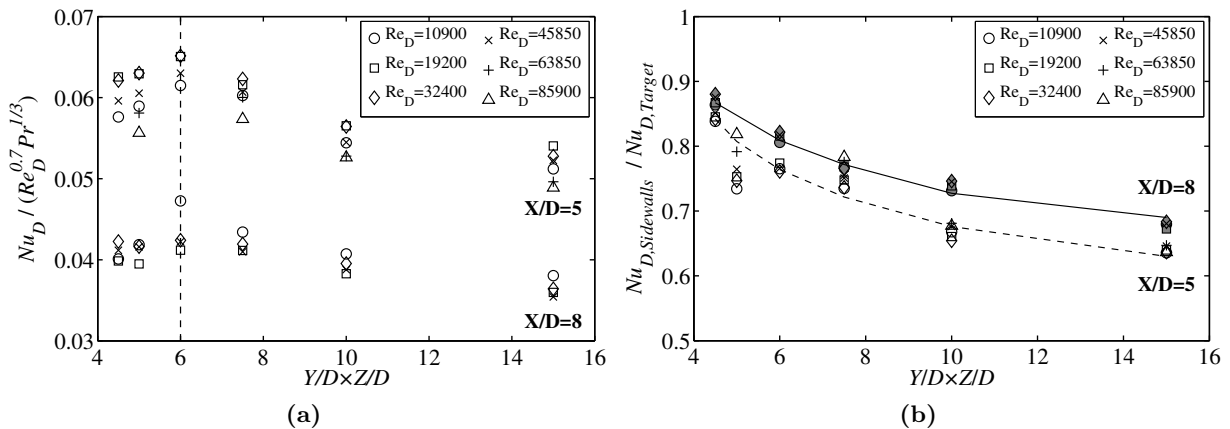


Figure 6.28: (a) Complete channel area averaged Nu_D as a function of channel flow area and (b) Sidewall vs target plate Nu_D for various Reynolds numbers. $\Delta y/Y=0.4$

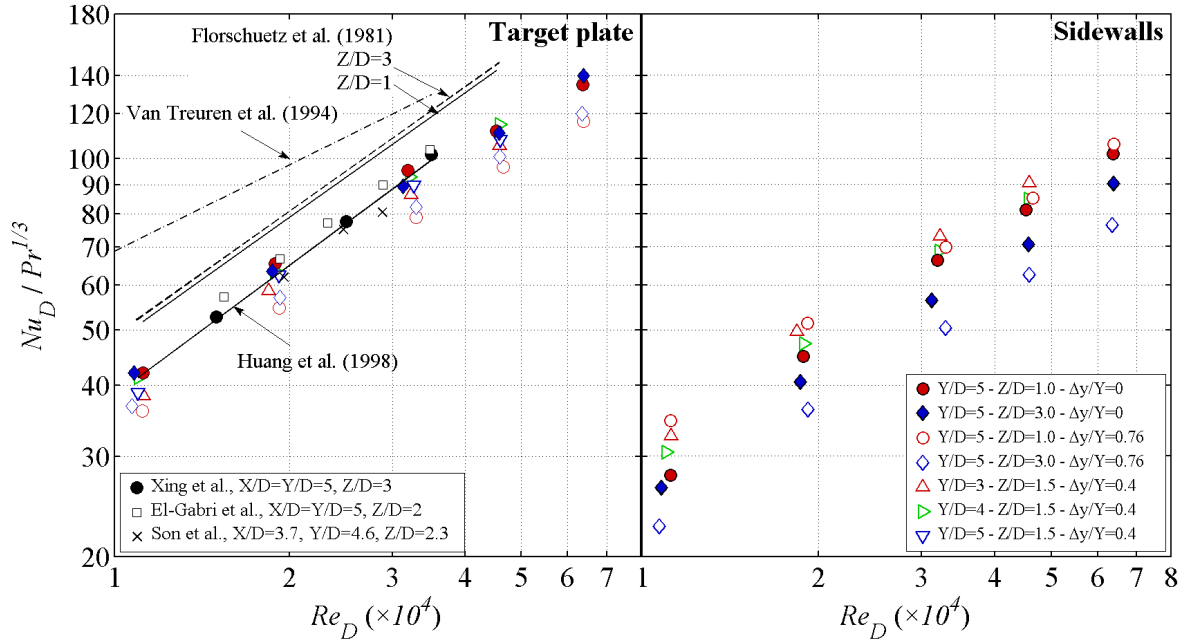


Figure 6.29: Full channel area averaged Nu_D as a function of Re_D . $X/D=5$.

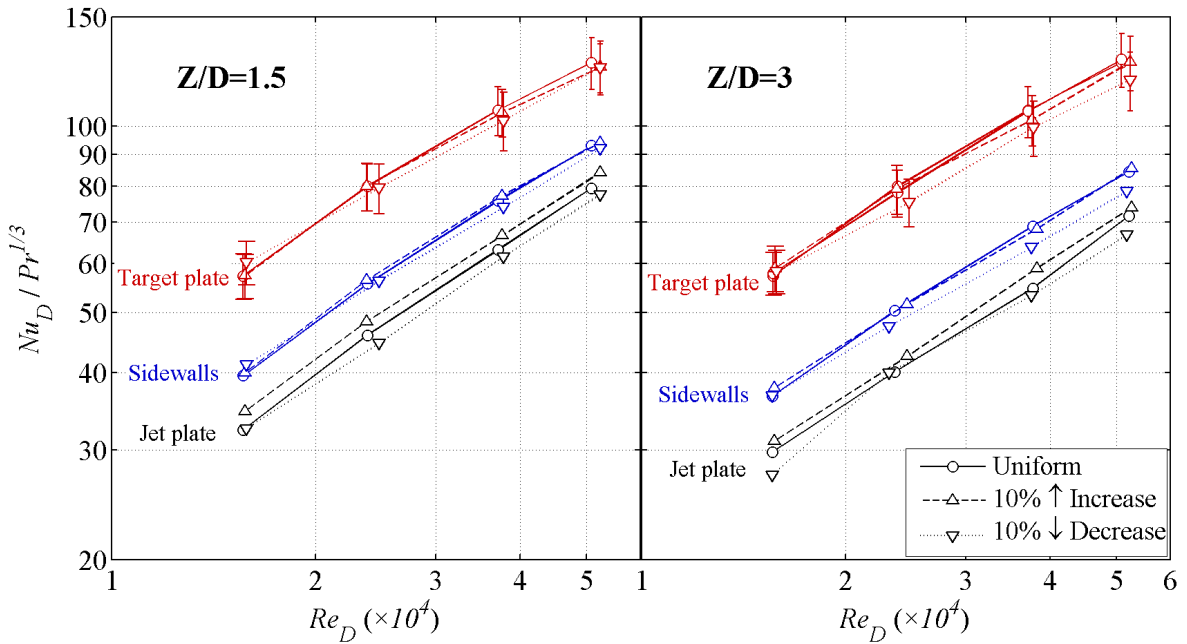


Figure 6.30: Full channel area averaged Nu_D as a function of Re_D . $X/D=Y/D=5$

The full channel length area averaged Nu_D as a function of Re_D for various geometries and surfaces is indicated in Figures 6.29 and 6.30. The experimental results of the target plate are compared with various literature data obtained from multi-jet configurations with maximum crossflow orientation and similar geometrical parameters, and hence open area, i.e. El-Gabry and Kaminski (2005); Xing et al. (2010); Son et al. (2001), as well as to existing heat transfer correlations, i.e. Van Treuren et al. (1994); Florschuetz et al. (1981); Huang et al. (1998). Figure 6.29 indicates that the area averaged Nusselt number increases with increasing Reynolds number following a power law in the form, $Nu \sim Re^m$, for both target plate and sidewalls. More details about the heat transfer correlation of the present study and the dependence of Nu_D with Re_D and other geometrical factors can be found in Chapter 7. For the target-plate, the area

averaged Nu_D of narrow impingement channels is observed to be comparable with multi-array configurations. However, the Nu_D level is about 20% lower compared to Florschuetz's correlation over the full range of flow conditions. The correlation given by Van Treuren et al. (1994) overestimates the heat transfer rate since it relates the Re_D effects on the stagnation point regions, where the appropriate value for the exponent of Reynolds number is 0.5, that is why the slope of the line is reduced. Additionally, the large scatter in the chart can be attributed to the different geometrical details of the above studies including also nozzle shapes and design, jet turbulence, region of averaging area, mass flow rate determination or even differences of the applied measurement techniques. At a given Re_D , higher heat transfer levels are achieved for the inline impingement hole pattern with very small differences between $Z/D=1$ and 3. On the other hand, the minimum is observed for $\Delta y/Y=0.76$ of $Z/D=1$ due to the direct impact of the generated crossflow. For the staggered configuration, a reduction of 5% to 20% is observed as the separation distance is decreased and the hole offset position is increased.

For the sidewalls of the channel, the averaged heat transfer rate is considerably lower compared to the target plate over the entire range of Re_D , as shown in Figure 6.29. For the inline case, Nu_D on the sidewalls is about 20-30% lower than on the target plate, depending on Z/D . On the other hand, a full staggered pattern of impingement holes ($\Delta y/Y=0.76$) can be beneficial at $Z/D=1$ compared to the inline pattern since the jets are placed very close to the wall. As expected, minimum values of Nu_D are observed for $Z/D=3$ where a full offset of the impingement jets reduces the area averaged Nu_D by 17%.

Figure 6.30 indicates the effect of varying jet diameter on the area averaged Nu_D level for all channel walls. Note that for the target plate, the level of experimental uncertainties is introduced with error-bars for each configuration indicating the accuracy of the measurements. Obviously, the uncertainty level was similar for the rest of configurations. At a given Z/D , as expected from Figure 6.29, higher Nusselt numbers are obtained for the target plate compared to the other channel walls. In particular, the target plate for $Z/D=1.5$ is about 45% and 65%, and for $Z/D=3$ about 60% and 80%, higher compared to sidewalls and jet plate, respectively. This means that the overall heat transfer rate for the sidewalls and impingement plate is considerably affected by Z/D . The effect of varying jet diameter shows a negligible effect for the target plate for both Z/D where the differences are within the experimental uncertainties, and therefore, it is difficult to conclude a general trend. This is attributed to the fact that the lower Nu_D of the upstream channel regions obtained using a 10%-increasing jet size pattern, is compensated by the increased heat transfer values on the high crossflow dominated region. Similar trends are observed for the sidewalls. For the impingement plate, on the other hand, Nu_D is 10% and 7% higher over the full range of examined Reynolds numbers for both channel heights in case a 10%-increasing jet pattern size is used. This indicates that varying jet diameters could have a beneficial effect on the area averaged heat Nusselt number on the jet plate.

6.9 Thermal Performance

Despite of the achievable heat transfer level, another important parameter of turbine blade cooling architectures is the pressure loss of the cooling system which has a direct influence on the cycle efficiency of the gas turbine. Given that a desirable impingement cooling system requires high heat transfer at low pressure drop expense, the thermal performances of the impingement channels were also evaluated. Generally, the thermal performance balances the change in heat

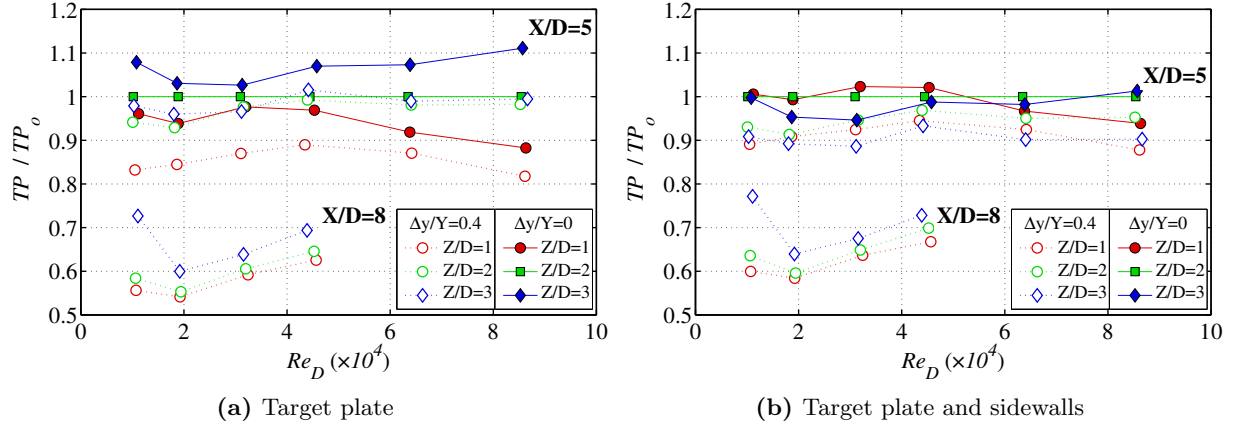


Figure 6.31: Thermal performance comparison of different impingement cooling scenarios

transfer coefficient with the change in pressure losses and allows a fair comparison of different cooling geometries. For the definition of thermal performance, a parameter was chosen similar to what is used to quantify other convective cooling applications, e.g. flow over ripped or dimpled surfaces. The same approach was also applied for impingement cooling geometries by [Gritsch et al. \(2006\)](#). The thermal performance in this study is defined as:

$$TP = \frac{Nu_D}{Nu_{D,o}} \left(\frac{\Delta p_{ch}}{\Delta p_{ch,o}} \right)^{1/3} \quad (6.2)$$

where Nu_D is the area averaged heat transfer coefficient on the exposed surfaces and Δp_{ch} is the pressure drop through the impingement channel. The reference case, $Nu_{D,o}$, $\Delta p_{ch,o}$ was arbitrary chosen as the inline pattern ($\Delta y/y=0$) of $Z/D=2$. The thermal performance of several examined geometries is shown in Figure 6.31. Generally, the overall impingement cooling performance remains at the same level as the Reynolds number is increased similar to [Gritsch et al. \(2006\)](#).

Figure 6.31(a) shows the thermal performance when only the target plate is considered. Higher values of TP are obtained at higher Z/D . Although, impingement channels with low separation distance generate slightly higher heat transfer coefficients the much lower pressure drop at wider channels outweighs the little reduced heat transfer levels resulting in higher overall thermal performance. Increasing the axial jet-to-jet spacing from $X/D=5$ to 8 reduces the thermal performance about 45%. This is attributed to the decreased heat transfer level due to the increased wall-jet regions in the channel as well as to the slightly increased pressure drop due to the higher length of the channel. Hole staggering is observed to reduce the overall thermal performance due to the negligible effect on pressure drop discussed in Section 5.2 and the degradation of heat transfer presented in Section 6.5. Note also that the reduction of TP with increasing $\Delta y/Y$ is higher at low channel heights due to the more direct influence of the generated crossflow.

Figure 6.31(b), on the other hand, indicates the thermal performance when considering also the sidewalls on the achievable area averaged heat transfer coefficients. The main trend remains, with similar values of TP at higher Reynolds numbers for the aforementioned reasons. However, the effect of channel cross-sectional area is less significant at $X/D=5$ and the thermal performance values are situated on the same level. This is attributed to the increased area averaged heat transfer coefficients on the sidewalls at narrower channels (reduced Y/D and/or

Z/D) which compensate the lower pressure drop at wider channels resulting in similar level of thermal performance. For $X/D=8$, TP is about 35% lower compared to $X/D=5$ over the full range of flow conditions while the overall trends observed in Figure 6.31(a) are maintained, although less pronounced, indicating the less significant effect of other geometrical factors as X/D is increased.

6.10 Assessment of the Results

Detailed heat transfer distributions of narrow impingement channels have been experimentally evaluated in the course of this thesis. The narrow impingement channel test models consist of a single row of five impingement jets investigated over a range of engine representative Reynolds numbers. Effects of axial jet-to-jet spacing (X/D), channel width (Y/D) and height (Z/D), impingement jet pattern ($\Delta y/Y$) and varying jet diameter (ΔD) were independently examined composing a test matrix of 30 different large-scale geometries. Full surface heat transfer coefficient distributions for all internal surfaces of channels were evaluated with great spatial resolution using the transient liquid crystal measurement technique.

Regarding the pattern of convection coefficients, the findings of this investigation for the target plate indicated that the heat transfer distribution is progressively converted from a circular to a horseshoe vortex shape distribution towards the exit of the channel, where the overall evolution of the phenomenon is significantly more pronounced, in terms of jet deflection and heat transfer degradation, at channels with lower cross-sectional area due to the increased crossflow momentums (at a given Reynolds number). For the sidewalls of the channels, the distributions indicated higher heat transfer levels closer to the target plate ($z=0$) as the wall jet flow impinges out the sidewalls while the peaks of heat transfer level are also deflected in the axial direction. Heat transfer coefficients on the jet plate are highly affected as the channel sidewalls interfere with the wall jet flow causing a post impingement flow on the top plate. The up-lift moving of the flow causes therefore high local heat transfer levels close to the sidewalls of the channel.

The heat transfer results have been analysed by various post-processing procedures and conclude that for the target plate different separation distances (Z/D) mainly affect the flow domain inside the channel and the local distributions of convection coefficients, i.e. secondary peaks and horseshoe vortex for $Z/D=1$, rather than the level of heat transfer where very low dependence on the spanwise and area averaged Nu_D was observed between $Z/D=1$ and 3. For the sidewalls of the channel, the peak heat transfer region is the same in level and size for low and high channel heights as a direct consequence of the similar thickness of the developed wall jet flow caused by the impingement of the jet. Therefore, the main effect of Z/D is the addition of a region with low interaction with the wall jet flow resulting in reduced spanwise and area averaged heat transfer coefficients. Contrary to the other walls, the interaction between the post-impingement flow and the top plate is highly affected by Z/D and therefore, low channel heights provide increased heat transfer capabilities for the impingement plate. In particular, the spanwise averaged Nu_D distributions for $Z/D=1$ are about 20% higher compared to $Z/D=3$.

Variation of channel width (Y/D) affects the open area of the impingement configuration (A_f) as well as the momentum of the generated crossflow. Generally, the effect of Y/D on the target plate and the sidewalls is similar. For the target plate, in the absence of crossflow (relatively upstream positions), narrower channels provide better cooling capabilities due to the increased channel open area. This holds also for the sidewalls where for low values of Y/D they

are placed closer to the stagnation point regions on the target plate, and hence, experience a more aggressive collision with the wall jet flow. For the downstream regions, on the other hand, lower values of Y/D may significantly increase the momentum of crossflow which prevents the impact of the jet with the target plate as well as the impact of the wall jet flow with the sidewalls. Therefore, high values of Y/D are required for downstream channel positions to compensate the generated crossflow.

Additionally, for all examined cases, the inline jet pattern ($\Delta y/Y=0$) provides a better coverage of the target plate surface by the impinging jets, and thus, higher heat transfer coefficients than the jet staggered arrangements ($\Delta y/Y=0.4$ and 0.76), where the heat transfer degradation is increased with increasing $\Delta y/Y$ and the generated crossflow in the channel. Therefore, hole staggering effects are more pronounced at the downstream positions of channels with smaller cross-sectional area ($Y/D \times Z/D$). A similar effect was also observed for the jet plate. However, for the sidewalls of the channel, heat transfer can be significantly increased at high values of $\Delta y/Y$ since the jets are placed very close to the sidewalls. However, this reduces significantly the heat transfer of the same row for the opposite wall. Therefore, hole staggering effects on the sidewalls is a kind of controversial issue.

The only geometrical parameter which affected reasonably the achievable heat transfer level on the target plate is the axial jet-to-jet spacing (X/D). Higher values of X/D increase the wall jet region and hence decrease the achievable Nu_D in terms of streamwise and area averaged results. In particular, streamwise averaged Nu_D for $X/D=8$ is about 40% lower compared to $X/D=5$ where the stagnation point regions are closer between them. For the sidewalls of the channel, similar trends were observed, however, the reduction was in the order of 30% close to the target plate, where the peak heat transfer takes place, and 15% close to the jet plate, where a low heat transfer region predominates.

By using varying jet diameters (ΔD), the heat transfer rate is mainly affected on the low and the high crossflow dominated regions, while in the middle of the channel the results are very similar for both channel heights. For all channel walls, decreasing jet size patterns are beneficial for the upstream channel positions due to the increased local open areas ($A_{f,j}$), however, they induce more crossflow which attenuates the heat transfer of the downstream jets. Increasing jet size patterns, on the other hand, show the opposite behaviour with reduced heat transfer values at upstream channel positions.

Regarding the area averaged heat transfer level, Nu_D was compared with various literature sources and it was found to be comparable to multi-array impingement cooling systems. However, the level of Nu_D for the target plate was about 20-25% lower compared to existing correlations which are used as industrial design tools, i.e. [Florschuetz et al. \(1981\)](#). Sidewalls and impingement plate area averaged Nu_D are about 45% and 65% lower compared to the target plate heat transfer for $Z/D=1$, and about 60% and 80% lower for $Z/D=3$, respectively.

The experimental results of this thesis can be used for the development of integrally cast turbine blade thermal designs since they contain detailed information for all internal impingement surfaces. Different geometrical factors, although showed no detrimental differences on the level of heat transfer, they could play an important role on the level and distribution of convection coefficients, and hence, on the homogeneity of blade metal temperatures.

HEAT TRANSFER CORRELATION

Given that there are several arrangements possible with impingement cooling jets and different aspects need to be considered before optimising a thermal design, the heat transfer results of the present study are correlated providing the first empirical equation for narrow impingement channels. This chapter demonstrates the overall correlation procedure for the row-by-row area averaged heat transfer model developed for the target plate and the sidewalls of the channels.

7.1 Introduction

Convection transport processes are very difficult to be evaluated analytically or numerically. Therefore, experimental work is preferably carried out under controlled laboratory conditions correlating the heat transfer rate in dimensionless parameters. These parameters are usually described by the following algebraic expression:

$$\frac{Nu_x}{Pr^n} \simeq C Re_x^m \quad (7.1)$$

where coefficient C and exponents m and n vary with the nature of the fluid and the surface geometry. For laboratory test cases, where air is usually the working fluid, exponent n equals 0.33 or 0.4 for heating and cooling conditions, respectively. A convective heat transfer correlation is then obtained by multiple measurements over a range of geometrical factors and flow conditions.

Such empirical models are extensively employed as an industrial design tool allowing turbine blade metal temperature predictions, and therefore, make necessary the existence of reliable and valid correlations for engine representative cooling geometries. One of the first empirical models for multi-array impingement cooling systems with a single exit design (maximum crossflow orientation) was developed by [Florschuetz et al. \(1981\)](#), who correlated the local area averaged Nu_D in the streamwise direction considering also crossflow effects. Despite the relatively poor heat transfer resolution on the examined surfaces (due to the limited amount of embedded thermocouples on the heated walls) the model is quite precise and it is still used in industry during the design phase of impingement cooling systems. Note also that Florschuetz's empirical model was also confirmed later by [Bailey and Bunker \(2002\)](#) using high resolution heat transfer measurements carried out with liquid crystals.

As shown in Section 6.8, the full channel length area averaged Nu_D obtained of narrow

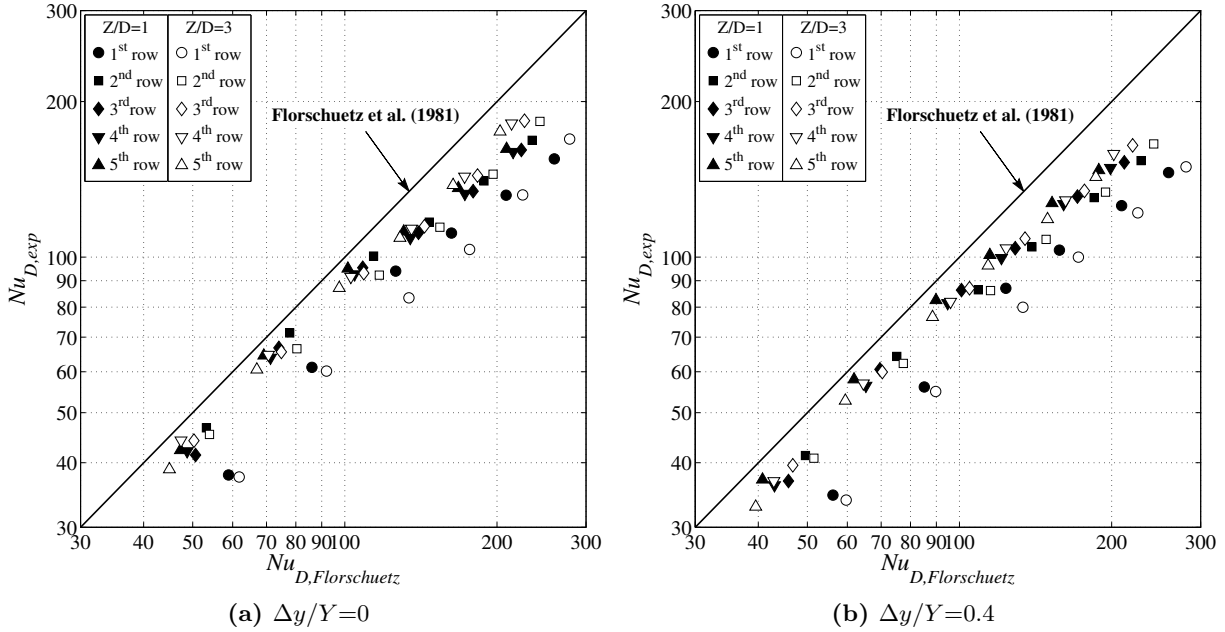


Figure 7.1: Experimental data compared with the empirical model of [Florschuetz et al. \(1981\)](#)

impingement channels are about 20% lower compared to Florschuetz’s correlation. Therefore, direct application of Florschuetz’s empirical model on narrow impingement channels is rather difficult and it requires a regulative coefficient that should be multiplied with the model at a given channel geometry. A direct comparison of the experimentally obtained row-by-row area averaged Nu_D with Florschuetz’s model is illustrated in [Figure 7.1](#) for two different impingement jet patterns. An inline and a low-staggered arrangement. For both patterns, the Nu_D level obtained experimentally is considerably lower compared to Florschuetz’s model and the variation depends on the number of row. Maximum and minimum differences are about 38% and 7%, and they are observed for the row 1 and 5, respectively. This could be attributed to the crossflow effects which are of great importance in narrow impingement channels where the spent air of the jets interferes with the other walls of the channel (sidewalls and jet plate) providing complex flow structures that can be very different compared to single jet-to-crossflow interactions or periodic multi-jet arrangements.

Contrary to periodic multi-array impingement cooling systems, where a number of available correlations are summarised in the review of [Weigand and Spring \(2011\)](#), no correlations are currently available in the open literature for narrow impingement channels. Therefore, the objective of this chapter is to correlate the heat transfer results of the narrow impingement channels including also hole staggering effects in one single equation.

7.2 Regression Analysis

7.2.1 General

The optimisation of a narrow impingement channel at a given cooling scheme scenario requires a mathematical model that should be used as an objective function during the optimisation process. For the development of the empirical correlation several geometries have been tested composing a matrix of 22 different models summarised in [Table 7.1](#). The geometrical discrete variables that have been comprised in the correlation include the streamwise jet-to-jet spacing

Table 7.1: Summary of investigated narrow impingement channel geometries

Test No.	X/D	Y/D	Z/D	$\Delta y/D$	$\Delta y/Y$	Re_D
1	5	3	1.5	1.2	0.40	10,900–45,850
2	5	4	1.5	1.6	0.40	10,900–45,850
3	5	5	1.0	0.0	0.00	10,900–85,900
4	5	5	1.0	2.0	0.40	10,900–85,900
5	5	5	1.0	3.8	0.76	10,900–85,900
6	5	5	1.5	0.0	0.00	10,900–85,900
7	5	5	1.5	2.0	0.40	10,900–85,900
8	5	5	1.5	3.8	0.76	10,900–85,900
9	5	5	2.0	0.0	0.00	10,900–85,900
10	5	5	2.0	2.0	0.40	10,900–85,900
11	5	5	2.0	3.8	0.76	10,900–85,900
12	5	5	3.0	0.0	0.00	10,900–85,900
13	5	5	3.0	2.0	0.40	10,900–85,900
14	5	5	3.0	3.8	0.76	10,900–85,900
15	5	6	1.5	2.4	0.40	10,900–45,850
16	8	3	1.5	1.2	0.40	10,900–45,850
17	8	4	1.5	1.6	0.40	10,900–45,850
18	8	5	1.0	2.0	0.40	10,900–45,850
19	8	5	1.5	2.0	0.40	10,900–45,850
20	8	5	2.0	2.0	0.40	10,900–45,850
21	8	5	3.0	2.0	0.40	10,900–45,850
22	8	6	1.5	2.4	0.40	10,900–45,850

(X/D), the channel width (Y/D), the channel height (Z/D) and the impingement hole offset position from the channel centerline ($\Delta y/Y$). The experiments were carried out at realistic engine flow conditions with a Reynolds number (continuous variable) varying between 10,900 and 85,900. The most appropriate empirical model was selected by compromising model accuracy and physical representation of the results.

A regression analysis was carried out in order to investigate the relation between the geometrical factors of the narrow impingement channels and their effect on the row-by-row area averaged heat transfer coefficient. At a first step, an evaluation of the coefficient C and exponent m of Equation 7.1 was performed in order to provide an estimation of their overall range and levels. The most often used tool in the literature for the evaluation of these regression coefficients is the linearisation of Equation 7.1 by taking *logs* on both sides. A straight line is then implied when Nu_D is plotted against Re_D on a doubly logarithmic diagram where the slope of the line signifies the value of exponent m . The straightness of the line is a necessary, but not sufficient, condition for the data following a power-law and this method may result in significant biases if a small number of experiments is carried out. Therefore, heat transfer correlations for all channel geometries were determined using the *Levenberg-Marquardt* algorithm (LMA) providing the optimised coefficients for the minimisation of the function defined by the sum of squares of the following deviations:

$$\min_{m,C} \sum_{i=1}^k \left(\frac{Nu_{D,i}}{Pr_i^{1/3}} - C Re_{D,j,i}^m \right)^2 \quad (7.2)$$

where k is the number of investigated Reynolds numbers for a given geometry and $Re_{D,j}$ is the local jet Reynolds number predetermined by the experimentally validated (see Chapter 5, Section

Table 7.2: Exponent m and coefficient C statistics

	mean	median	σ	min	max
m	0.704	0.698	0.038	0.608	0.795
C	0.086	0.082	0.040	0.024	0.201

Table 7.3: Exponent m values reported in the literature

Authros	Exponent m	Open area A_f
Kercher and Tabakoff (1970)	0.65-0.95	0.00464-0.0876
Chance (1974)	0.7-0.81	0.012-0.077
Martin (1977)	0.66	0.004-0.04
Hollworth and Berry (1978)	0.8	0.00125-0.00785
Florschuetz et al. (1981)	0.727	0.00654-0.0392
Huang et al. (1998)	0.76	0.049
Van Treuren et al. (1994)	0.506	stagnation regions

5.4) Florschuetz's one-dimensional model. Totally, 112 experiments were conducted resulting in 560 data points (112×5 rows of a single jet). Table 7.2 summarises some basic statistical characteristics for the calculated exponent m and coefficient C for the 112 experiments.

7.2.2 Determination of exponent m

In the majority of heat transfer correlations, exponent m is varied between 0.5 and 0.8 for boundary layers with laminar and turbulent textures. For impingement jet arrays, which include stagnation point and wall jet regions, the area averaged exponent m varies between the above margins depending on the geometrical characteristics of the jet perforated plate. Table 7.3 summarises typical m values from various literature sources indicating also the open area of the impingement configuration. [Kercher and Tabakoff \(1970\)](#) and [Chance \(1974\)](#) indicated that exponent m slightly increases with the jet plate open area (A_f) and the separation distance (Z/D). On the other hand, due to the small size of geometry variations [Martin \(1977\)](#); [Hollworth and Berry \(1978\)](#); [Florschuetz et al. \(1981\)](#) and [Huang et al. \(1998\)](#) reported a single slope value of 0.66, 0.8, 0.727 and 0.76, respectively, while [Van Treuren et al. \(1994\)](#) obtained a value of 0.506 for the stagnation point regions.

As shown in Table 7.2, exponent m in the present study was varied from about 0.6 to 0.8, with a tendency to increase with Z/D and A_f , which is in agreement with the literature. However, 73% of the exponent values fall within one standard deviation and 95% within a range of two standard deviations which is not very far from the normal distribution. Therefore, a single value of m is considered for satisfying all the investigated impingement channels and this value is $m=0.7\pm 0.05$. Possible deviations due to exponent m variation are neglected at this step and they are transferred to the other geometrical parameters within the experimental uncertainties.

7.2.3 Correlation for coefficient C

All measured data points are then divided by the corresponding local Reynolds number to the power of 0.7 and a new dataset for the regression coefficient C is generated. Coefficient C is therefore an unknown function of the geometrical characteristics of the narrow impingement channels. An accurate determination of the achievable heat transfer coefficient at a given Re_D

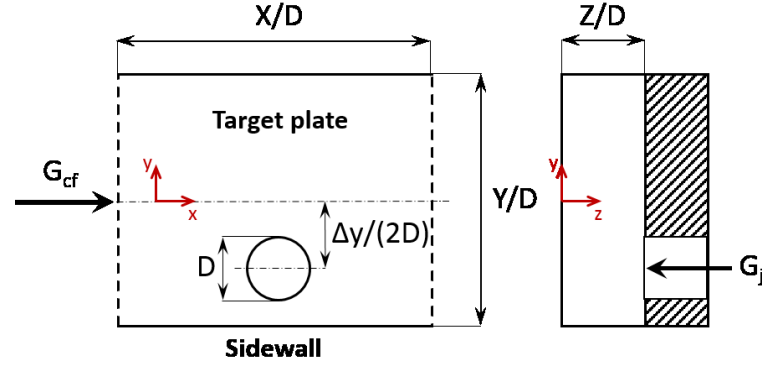


Figure 7.2: Schematic representation of the correlation flow domain

is therefore based on the most appropriate function representing the following relation:

$$\frac{Nu_D}{Re_D^{0.7} Pr^{0.33}} = C = f\left(\frac{X}{D}, \frac{Y}{D}, \frac{Z}{D}, \frac{\Delta y}{D}, \frac{G_{cf}}{G_j}\right) \quad (7.3)$$

Five independent variables (regressors) were used for the prediction of Nu_D at a given Re_D or coefficient C (response variable). A schematic representation of the correlated surfaces is illustrated in Figure 7.2.

A non-linear model approach is selected for the prediction of the Nusselt number at a given Reynolds number for the following reason: Generally, the Reynolds number is based on one reference velocity and one reference length scale. If someone would like to address local changes in heat transfer due to changes in local flow velocities, which are due to change in geometries, and therefore, length scales ($X/D, Y/D, Z/D, \Delta y/D$), the local ‘mean velocity’ will change according to the ‘new length scale’. As a power law is used for the relation of Nusselt number and the Reynolds number, a power law should be also used for the channel length scale (channel geometry variation) in order to approximate the effect of mean local flow situation in relation to the overall flow situation. The non-linear model is selected balancing model accuracy and physical representation of the results. Selecting a non-linear model of the right form to fit a set of data requires the use of empirical evidence in the data, knowledge of the process and several trial-and-error experimentation.

The most suitable form for the regression model was selected after many attempts resulting in the following equation:

$$\frac{Nu_D}{Nu_{D,o}} = \left[1 - B \left(\frac{G_{cf}}{G_j}\right)^{\beta_0} \left(\frac{X}{D}\right)^{\beta_1} \left(\frac{Y}{D}\right)^{\beta_2} \left(\frac{Z}{D}\right)^{\beta_3} \right] \quad (7.4)$$

with

$$\frac{Nu_{D,o}}{Re_{D,j}^{0.7} Pr^{1/3}} = An^{a_0} \left(\frac{X}{D}\right)^{a_1} \left(\frac{Y}{D}\right)^{a_2} \left(\frac{Z}{D}\right)^{a_3} \times f \quad (7.5)$$

where n is the number of row which is empirically evaluated and f is the hole staggering factor given by the following relation:

$$f = 1 - \left(\frac{\Delta y}{D}\right)^{c_0} \left(\frac{Y}{D}\right)^{c_1} \left(\frac{Z}{D}\right)^{c_2} \left(1 - \frac{G_{cf}}{G_j}\right)^{c_3} \quad (7.6)$$

This indicates that the heat transfer degradation observed at a given staggered configuration

Table 7.4: Basic correlation coefficients

Surface	A	a_0	a_1	a_2	a_3	B	β_0	β_1	β_2	β_3
Target	0.413	0.260	-0.872	-0.183	-0.112	0.369	1.000	0.104	0.368	0.705
Sidewalls	0.418	0.347	-0.768	-0.433	-0.341	0.430	0.832	0.126	0.362	0.473
Channel	0.486	0.298	-0.803	-0.423	-0.151	0.432	0.906	0.112	0.296	0.598

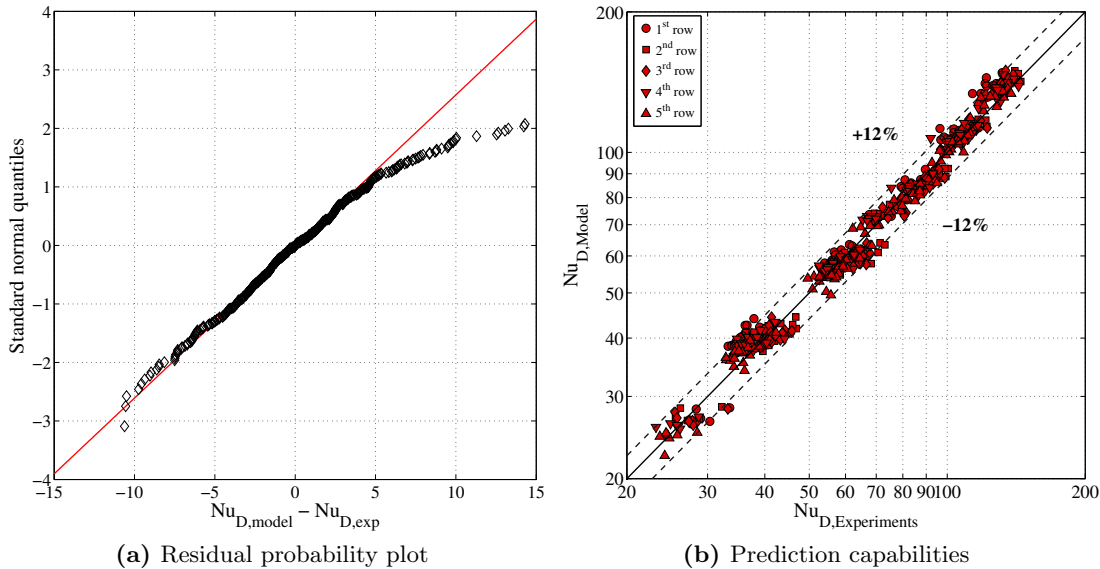
Table 7.5: Hole offset position coefficients

Surface	c_0	c_1	c_2	c_3
Target	1.433	-1.711	-1.051	0
Sidewalls	1	-0.726	-0.733	1.751
Channel	0.299	-2.747	-2.086	0

is more pronounced at smaller channel areas (higher crossflow momentum). Note also that a negative hole offset position should be used in the case where the jet approaches the predicted sidewall, which results in a beneficial effect of the staggered factor. In case an inline pattern is used, f is simply unity for all channel walls. The main difference to Florschuetz's correlation, apart from the different configuration, is that the hole staggering effects are included in a single equation and that the overall correlation is based on the local $Re_{D,j}$ and not on the average one.

The regression analysis was performed for the target plate, the sidewalls and a combination of the two surfaces (referred to as *channel*) considering weighted averaged data for the available heat transfer area on both surfaces. The coefficients for the basic correlation and the hole staggering factor are summarised in Tables 7.4 and 7.5, respectively.

The predictive capabilities of the non-linear model are evaluated based on the distribution of the residuals, $Nu_{D,model} - Nu_{D,exp}$. An example for the target plate heat transfer data is illustrated in Figure 7.3. The left side plot indicates a probability plot where the sorted data (residuals) are plotted against quantiles from a standard normal distribution ($\mu=0$ and $\sigma=1$). In case the residuals are normally distributed, there is a presumption that they proceed from a random process and then that they are caused by experimental noise. The residuals fit relatively

**Figure 7.3:** Evaluation of heat transfer correlation for the target plate

well the normal line, and hence, they are normally distributed which means that their values are randomly caused. The suggested correlation is thus good in terms of standard error which was also within the experimental uncertainties. In particular, for the target plate, the sidewalls and the complete channel (target plate and sidewalls), 65.7%, 46.2% and 70.6% of the data points are predicted within 5% accuracy. Apparently, more calculated data points are predicted with very low deviation from the measured values for the complete channel. This could be attributed to the fact that effects of various geometrical factors, i.e. Z/D , are more pronounced on the sidewalls resulting in more clear trends. Prediction of the sidewall heat transfer was found to be relatively difficult, although the final results are statistically accepted. An additional example of the model predictive capabilities for the target plate is shown in Figure 7.3(b). The measured and predicted values are compared for all the rows of all examined geometries and over the full range of flow conditions. Good agreement is observed over the full range of Nu_D since 94% of the data points are predicted within the experimental uncertainties. The model is therefore considered valid for channels up to five impingement jets and over a range of Reynolds numbers (10,000-85,000), under the following geometrical constraints:

$$5 \leq X/D \leq 8 \quad (7.7a)$$

$$3 \leq Y/D \leq 6 \quad (7.7b)$$

$$1 \leq Z/D \leq 3 \quad (7.7c)$$

$$0 \leq \Delta y/D \leq 3.8 \quad (7.7d)$$

7.3 Concluding Remarks

The resulted Nusselt numbers were correlated in an empirical model for the majority of investigated narrow impingement channel geometries, and this chapter demonstrated the overall correlation procedure. The non-dimensional heat transfer coefficients resolved for one stream-wise jet spacing for the target plate, the sidewalls and the complete channel, can be therefore calculated from Equation 7.4 in case the crossflow and the jet mass velocities are known at the row of interest. The suggested correlation is fairly accurate in terms of standard error with 96% of the data points predicted within the experimental uncertainties ($\pm 12\%$).

CONCLUSIONS AND RECOMMENDATIONS

This chapter summarises the findings of the present thesis highlighting the conclusions of the obtained experimental data in a short overall discussion. The chapter contains also recommendations as to where further research should be focusing on considering also the capabilities of the present measurement equipment.

8.1 Summary

In this thesis, an experimental study about the heat transfer performance of narrow impingement channels has been performed. In modern turbine airfoils, narrow impingement cooling channels of relatively low crossflow can be integrally cast within the external wall of turbine airfoil. Therefore, the coolant is injected in the form of impingement flow inside the cavity, and hence, impingement cooling is obtained within the wall rather than the hollow of the turbine airfoil increasing dramatically the heat exchange capabilities due to the thinner external airfoil wall. An extensive literature survey carried out in the preliminarily phase of this thesis demonstrated that a detailed physical assessment of the heat transfer behaviour of this *double-wall* cooling configurations is not adequately known with limited information published in the open literature. Therefore, the main contribution of this thesis is the:

Experimental evaluation and the detailed analyses of the local heat transfer distributions for all internal surfaces of narrow impingement channels consisting of a single row of five holes, investigating effects of various channel geometrical factors and correlating the data in an empirical model valid over a wide range of engine representative Reynolds numbers.

The present study has used relatively large scale models of an idealised narrow impingement passage to provide an understanding of the convection transport processes in a real part of a turbine blade. Note that the heat transfer experiments were carried out at engine representative Reynolds numbers varying between 10,900 and 85,900 so that the resulted Nusselt numbers are directly applicable to the engine cooling channels.

Effects of various geometrical factors, such as axial jet-to-jet spacing (X/D), channel width (Y/D) and height (Z/D), hole offset position from the channel centerline line ($\Delta y/Y$) and varying jet diameters towards the channel exit (ΔD) have been parametrically composing a

test matrix of 30 different channel models. For the evaluation of heat transfer coefficients, the transient liquid crystal measurement technique has been used providing high spatial resolution on the exposed heat transfer surfaces. Given that different aspects need to be considered before optimising a heat transfer design, the heat transfer results of the present study were correlated providing the first empirical equation for this kind of application.

8.2 Conclusions

This thesis has been the first phase of the development of a new experimental facility for the study of double-wall cooling configurations. In the course of this study, detailed heat transfer distributions in all internal surfaces of narrow impingement cooling channels have been evaluated using high resolved heat transfer measurements. The results concluded similarities with the heat transfer patterns obtained for multi-array impingement configurations, however, the level of area averaged Nusselt numbers was about 20% lower compared to existing correlations used as industrial design tools. This could be attributed to the development of the crossflow in a fully confined, compact and narrow passage. Crossflow effects are therefore of great importance in narrow impingement channels where the spent air of the jets interferes with the other walls of the channel (sidewalls and jet plate) providing complex flow structures that can be very different compared to single jet-to-crossflow interactions or periodic multi-jet arrangements. This is more significant in turbine blade cooling applications where the large applicability of maximum crossflow orientations (single exit designs) reduces the heat transfer capabilities of the downstream regions.

The experimental results of this thesis indicated that the main effect of the various examined geometrical factors are:

1. to significantly affect the distribution patterns of convection coefficients, and hence, they could play an important role on the homogeneity of blade metal temperatures.
2. to directly affect the momentum of the generated crossflow, which is the main source of heat transfer degradation for this kind of application.

The main findings of this investigation regarding the local heat transfer coefficient distributions for all internal surfaces of the channels, have been summarised at the end of Chapter 6. Therefore, no need to be repeated here. On the other hand, a reliable design of an impingement cooling channel for turbine blade cooling applications, requires increased values of convective cooling efficiency through the complete length of the impingement channel. As a result, the impact of generated crossflow on the heat transfer level, connected with the effect of the various channel geometrical factors, are selected to be the main conclusions of the present thesis. Crossflow effects are discussed in brief and separately for the different channel walls as follows:

Target plate

For all examined cases, the highest heat transfer coefficients are observed for the target plate of the channels which experiences the stagnation zones. In particular, the area averaged Nu_D numbers for $Z/D=1.5$ are about 45% and 65%, and for $Z/D=3$ about 60% and 80%, higher compared to sidewalls and jet plate, respectively, over the full range of investigated Reynolds numbers. However, within the examined range of $1 \leq Z/D \leq 3$, no detrimental effects of Z/D on the level of Nu_D were observed for the target plate itself since the the lower stagnation

point heat transfer of the upstream jets 1 and 2 is compensated by a better lateral coverage of the wall jet region, which is attenuated by the crossflow at jets 4 and 5, resulting in similar heat transfer levels in terms of spanwise averaged data for all examined Z/D . Therefore, the streamwise heat transfer level at upstream channel positions can be significantly enhanced with increased values of open area (A_f) due to a better coverage of the target surface. This can be achieved by reducing Y/D or by using a reducing jet size pattern towards the channel exit placing the largest jet diameter at the position of jet 1. In particular, the spanwise averaged Nu_D numbers are about 20% higher for $Y/D=3$ and 4 compared to $Y/D=5$ and 6 at jets 1 and 2. On the other hand, for the high crossflow dominated regions (jets 4 and 5), low values of Y/D , i.e. $Y/D=3$, may significantly increase the momentum of the crossflow which prevents the impact of the downstream jets with the target surface destructing the stagnation point heat transfer. Therefore, the momentum of the crossflow needs to be reduced, and hence, lower values of A_f at a given Reynolds number are required for downstream channel positions. This can be obviously achieved by increasing Y/D or by using an increasing jet size pattern reducing also the massflow added from the upstream jets. The effect of hole offset position ($\Delta y/Y$) on the generated crossflow is not so straightforward. Although, there is not a direct influence on the momentum of the crossflow, the impingement jets at staggered patterns are directly exposed to the mainflow, contrary to the inline pattern where the jets are somehow protected from the upstream jet(s). Therefore, a hole offset position makes the crossflow effects more pronounced. In particular, for $\Delta y/Y=0.76$, the spanwise averaged Nu_D numbers in the stagnation point regions are about 30% and 10% lower compared to the inline pattern for $Z/D=1$ and 3, respectively. The variation of the axial jet-to-jet spacing (X/D) was found to significantly affect the heat transfer level on the target plate but not the generated crossflow. For example, it was observed in terms of complete channel area averaged that the maximum Nu_D are obtained for channels with a cross-sectional area of $4D^2$ for both $X/D=5$ and 8. However, the achievable heat transfer level for $X/D=8$ are about 40% lower compared to $X/D=5$ due to an inadequate coverage of the target surface since the jets are placed farther between them.

Sidewalls

For all cases, the heat transfer distribution indicated higher Nu_D closer to the target plate ($z=0$) as the wall jet impinges out the sidewalls generating peaks of heat transfer. Similar to the target plate, these peaks are also shifted in the direction of the flow due to the development of the crossflow which attenuates downstream heat transfer. For upstream channel positions low values of Y/D , are desirable since the sidewalls are placed closer to the stagnation zones on the target plate experiencing a more aggressive impact with the wall jet flow. On the other hand, if the open area is relatively large, the high momentum of crossflow may prevent the impact of the wall jet flow with the sidewalls for downstream channel positions reducing locally the heat transfer coefficients. Hole staggering effects for the sidewalls is a complicated issue. Although, the overall crossflow effects become more intense when a jet staggered pattern is used, the placement of the jets closer to the sidewall increases and reduces locally the heat transfer at the closest sidewall and the furthest sidewall, respectively. However, combining both sidewalls, $\Delta y/Y$ is beneficial for the heat transfer despite the more pronounced crossflow effects. X/D effects for the sidewalls were similar to the target plate, however, the reduction of Nu_D when X/D is increased from 5 to 8, was in the order of 30% close to the target plate, where the peak heat transfer takes place, and 15% close to the jet plate, where a low heat transfer region predominates.

Impingement plate

The heat transfer coefficients on the target plate are highly affected as the wall jet flow interferes with the sidewalls of the channel causing a post-impingement flow on the jet plate. Therefore, higher heat transfer values are observed close to the sidewalls where the level of Nu_D is strongly depends on Z/D . Obviously, low values of Z/D increase the heat transfer capabilities on the jet plate which experiences a more aggressive post-impingement flow. In particular, the spanwise averaged Nu_D for $Z/D=1$ is about 15% and 35% higher, compared to $Z/D=3$, at the low and high crossflow dominated regions, respectively. Additionally, for both Z/D there is a tendency of increasing Nu_D towards the channel exit which actually means that, contrary to the other walls of the channel, crossflow can be beneficial for the cooling of the jet plate. This is attributed to the continuously increased heat transfer at the wake of each individual jet which act as pedestal to the flow promoting the turbulence at the wake of its potential core.

8.3 Recommendations For Future Work

Crossflow is one of the most important design factors when designing an impingement cooling channel for turbine blade cooling applications. Therefore, it is evident that further research and modifications of the existing test models should focus on the reduction of this quantity in order to ensure increased heat transfer capabilities for downstream channel positions and sustain increased values of convective cooling efficiency through the complete length of the narrow impingement channel. Given that high values of open area are required for upstream channel positions and low crossflow momentums are desirable for the downstream regions, an attempt to minimise the downstream crossflow should be performed. This can be achieved by channel geometry variations, jet shape/design variations, extended guiding areas for both target and jet plate, anti-crossflow arrangements etc.

First of all, varying channel widths (Y/D) and/or heights (Z/D) in a divergent arrangement can be used by increasing constantly the cross-sectional area towards the channel exit. Note also that constant local Y/D_j , Z/D_j values could be achieved by utilising an increasing jet size pattern which will further increase downstream heat transfer. Secondly, different impingement jet shapes/designs, as for example the use of convergent, divergent, elliptical or even inclined jets, may increase the penetration capabilities at the high crossflow dominated regions improving further the heat transfer capabilities. A useful input can be obtained from single impingement jet configurations, as for example, [Colucci and Viskanta \(1996\)](#); [Brignoni and Garimella \(2000\)](#); [Koseoglu and Baskaya \(2010\)](#). In addition, area enhancers, such as pins/fins, vortex generators and ribs of variable dimensions can be used as turbulent promoters at various channel positions increasing the mixing, and hence make the overall convection transport process more intense. Combination of periodic multi-jet impingement arrangements and rib-roughened target surfaces can be found in the studies of [Andrews et al. \(2006\)](#); [Caliskan and Baskaya \(2012\)](#); [Spring et al. \(2012\)](#); [Xing et al. \(2011\)](#). Furthermore, simple extended areas from the target or even the jet plate could be used as impingement jet protectors guiding the generated crossflow close to the sidewalls of the channel eliminating the interaction with the stagnation zones. An example of an anti-crossflow configuration can be found in [Chi et al. \(2013\)](#). Finally, complete turbine blade cooling configurations could be also tested by using the impingement air for film cooling extraction combining all the different means of cooling process in a single passage, i.e. internal convective cooling, impingement cooling and film cooling.

BIBLIOGRAPHY

- Al-Agal, O. (2003). *Heat Transfer Distributions on the Walls of a Narrow Channel With Jet Impingement and Cross Flow*. PhD thesis, University of Pittsburgh.
- Andrews, G. E., Durance, J., Hussain, C. I., and Ojobor, S. N. (1987). Full Coverage Impingement Heat Transfer: Influence of the Number of Holes. *Journal of Turbomachinery*, 109(4):557–563.
- Andrews, G. E., Hussain, R. A. A. A., and Mkpadi, M. C. (2006). Enhanced Impingement Heat Transfer: The Influence of Impingement X/D for Interrupted Rib Obstacles (Rectangular Pin Fins). *Journal of Turbomachinery*, 128(2):321–331.
- Angioletti, M., Di Tommaso, R. M., Nino, E., and Ruocco, G. (2003). Simultaneous visualization of flow field and evaluation of local heat transfer by transitional impinging jets. *International Journal of Heat and Mass Transfer*, 46(10):1703–1713.
- Bailey, J. C. and Bunker, R. S. (2002). Local Heat Transfer and Flow Distributions for Impinging Jet Arrays of Dense and Sparse Extent. In *ASME Turbo Expo 2002: Power for Land, Sea, and Air*, pages 855–864. ASME.
- Ballantyne, A. and Moss, J. B. (1977). Fine Wire Thermocouple Measurements of Fluctuating Temperature. *Combustion Science and Technology*, 17(1-2):63–72.
- Baughn, J. W. (1995). Liquid crystal methods for studying turbulent heat transfer. *International Journal of Heat and Fluid Flow*, 16(5):365–375.
- Baughn, J. W. and Shimizu, S. (1989). Heat Transfer Measurements From a Surface With Uniform Heat Flux and an Impinging Jet. *Journal of Heat Transfer*, 111(4):1096–1098.
- Baydar, E. and Ozmen, Y. (2006). An experimental investigation on flow structures of confined and unconfined impinging air jets. *Heat Mass Research*, 42(4):338–346.
- Beckman, P., Roy, R. P., Whitfield, K., and Hasan, A. (1993). A fast-response microthermocouple. *Review of Scientific Instruments*, 64(10):2947.
- Bell, J. H. and Mehta, R. D. (1988). Contraction Design for Small Low-Speed Wind tunnels. Technical Report NASA-CR-182747.

- Bell, J. H. and Mehta, R. D. (1989). Boundary-Layer Predictions for Small Low-Speed Contractions. *AIAA Journal*, 27:372–373.
- Bouchez, J. P. and Goldstein, R. J. (1975). Impingement cooling from a circular jet in a cross flow. *International Journal of Heat and Mass Transfer*, 18(6):719–730.
- Brignoni, L. A. and Garimella, S. V. (2000). Effects of nozzle-inlet chamfering on pressure drop and heat transfer in confined air jet impingement. *International Journal of Heat and Mass Transfer*, 43(7):1133–1139.
- Bunker, R. S. (2007). Gas Turbine Heat Transfer: Ten Remaining Hot Gas Path Challenges. *Journal of Turbomachinery*, 129(2):193–201.
- Bunker, R. S., Bailey, J. C., Lee, C.-P., and Stevens, C. W. (2004). In-Wall Network (Mesh) Cooling Augmentation of Gas Turbine Airfoils. In *ASME Turbo Expo 2004: Power for Land, Sea, and Air*, pages 1007–1018. ASME.
- Caggese, O., Gnaegi, G., Hannema, G., Terzis, A., and Ott, P. (2013). Experimental and numerical investigation of a fully confined impingement round jet. *International Journal of Heat and Mass Transfer*, 65:873–882.
- Caliskan, S. and Baskaya, S. (2012). Experimental investigation of impinging jet array heat transfer from a surface with V-shaped and convergent-divergent ribs. *International Journal of Thermal Sciences*, 59(0):234–246.
- Chambers, A. C., Gillespie, D. R. H., Ireland, P. T., and Dailey, G. M. (2005). The Effect of Initial Cross Flow on the Cooling Performance of a Narrow Impingement Channel. *Journal of Heat Transfer*, 127(4):358–365.
- Chambers, A. C., Gillespie, D. R. H., Ireland, P. T., and Kingston, R. (2010). Enhancement of Impingement Cooling in a High Cross Flow Channel Using Shaped Impingement Cooling Holes. *Journal of Turbomachinery*, 132(2):021001.
- Chance, L. J. (1974). Experimental Investigation of air Impingement Heat Transfer Under an Array of Round Jets. *TAPPI*, 57(6):108–112.
- Chi, Z., Kan, R., Ren, J., and Jiang, H. (2013). Experimental and numerical study of the anti-crossflows impingement cooling structure. *International Journal of Heat and Mass Transfer*, 64:567–580.
- Chyu, M. K. and Alvin, M. A. (2010). Turbine Airfoil Aerothermal Characteristics in Future Coal–Gas-Based Power Generation Systems. *Heat Transfer Research*, 41(7):737–752.
- Colucci, D. W. and Viskanta, R. (1996). Effect of nozzle geometry on local convective heat transfer to a confined impinging air jet. *Experimental Thermal and Fluid Science*, 13(1):71–80.
- Dailey, G. M., Evans, P. A., and McCall, R. A. B. (2001). Cooled aerofoil for a gas turbine engine. US Patent.

- El-Gabry, L. A. and Kaminski, D. A. (2005). Experimental Investigation of Local Heat Transfer Distribution on Smooth and Roughened Surfaces Under an Array of Angled Impinging Jets. *Journal of Turbomachinery*, 127(3):532–544.
- Esposito, E. I., Ekkad, S. V., Kim, Y., and Dutta, P. (2009). Novel Jet Impingement Cooling Geometry for Combustor Liner Backside Cooling. *Journal of Thermal Science and Engineering Applications*, 1(2):021001.
- Falcoz, C., Weigand, B., and Ott, P. (2006). Experimental investigations on showerhead cooling on a blunt body. *International Journal of Heat and Mass Transfer*, 49(7-8):1287–1298.
- Farahmand, K. and Kaufman, J. W. (2001). Experimental measurement of fine thermocouple response time in air. *Experimental Heat Transfer*, 14(2):107–118.
- Fechter, S. (2011). Numerical Investigation of Narrow Impingement Channels. Master’s thesis, University of Stuttgart, Germany.
- Fechter, S., Terzis, A., Ott, P., Weigand, B., von Wolfersdorf, J., and Cochet, M. (2013). Experimental and numerical investigation of narrow impingement cooling channels. *International Journal of Heat and Mass Transfer*, 67:1208–1219.
- Fisher, E. M. and Eibeck, P. A. (1990). The Influence of a Horseshoe Vortex on Local Convective Heat Transfer. *Journal of Heat Transfer*, 112(2):329–335.
- Florschuetz, L. W., Berry, R. A., and Metzger, D. E. (1980). Periodic Streamwise Variations of Heat Transfer Coefficients for Inline and Staggered Arrays of Circular Jets with Crossflow of Spent Air. *Journal of Heat Transfer*, 102(1):132–137.
- Florschuetz, L. W. and Isoda, Y. (1983). Flow Distributions and Discharge Coefficient Effects for Jet Array Impingement With Initial Crossflow. *Journal of Engineering for Power*, 105(2):296.
- Florschuetz, L. W., Metzger, D. E., and Su, C. C. (1984). Heat Transfer Characteristics for Jet Array Impingement With Initial Crossflow. *Journal of Heat Transfer*, 106(1):34–41.
- Florschuetz, L. W. and Su, C. C. (1987). Effects of Crossflow Temperature on Heat Transfer Within an Array of Impinging Jets. *Journal of Heat Transfer*, 109(1):74–82.
- Florschuetz, L. W., Truman, C. R., and Metzger, D. E. (1981). Streamwise Flow and Heat Transfer Distributions for Jet Array Impingement with Crossflow. *Journal of Heat Transfer*, 103(2):337–342.
- Gao, N., Sun, H., and Ewing, D. (2003). Heat transfer to impinging round jets with triangular tabs. *International Journal of Heat and Mass Transfer*, 46(14):2557–2569.
- Gillespie, D. R. H., Wang, Z., and Ireland, P. T. (1995). Heating Element. British Patent Application.
- Gillespie, D. R. H., Wang, Z., Ireland, P. T., and Kohler, S. T. (1998). Full Surface Local Heat Transfer Coefficient Measurements in a Model of an Integrally Cast Impingement Cooling Geometry. *Journal of Turbomachinery*, 120(1):92–99.

- Goldstein, R. J. and Behbahani, A. I. (1982). Impingement of a circular jet with and without cross flow. *International Journal of Heat and Mass Transfer*, 25(9):1377–1382.
- Goldstein, R. J., Behbahani, A. I., and Heppelmann, K. K. (1986). Streamwise distribution of the recovery factor and the local heat transfer coefficient to an impinging circular air jet. *International Journal of Heat and Mass Transfer*, 29(8):1227–1235.
- Goodro, M., Park, J., Ligrani, P., Fox, M., and Moon, H.-K. (2008). Effects of hole spacing on spatially-resolved jet array impingement heat transfer. *International Journal of Heat and Mass Transfer*, 51(25–26):6243–6253.
- Gorin, A. V. (2008). Turbulent Separated Flows: Near-Wall Behavior and Heat and Mass Transfer. *Journal of Applied Fluid Mechanics*, 1(1):71–77.
- Gorin, A. V. (2011). On Asymptotic Laws and Transfer Processes Enhancement in Complex Turbulent Flows. *World Academy of Science, Engineering and Technology*, pages 700–106.
- Gritsch, M., Schonwalder, D., and Estaun-Echavarren, C. (2006). Thermal Performance of Enhanced Combustor Liner Impingement Cooling Systems. In *ISROMAC-11*, Honolulu, Hawaii, USA.
- Han, J.-C. (2013). Fundamental Gas Turbine Heat Transfer. *Journal of Thermal Science and Engineering Applications*, 5(2):021007–021007–15.
- Hartsel, J. (1972). Prediction of effects of mass-transfer cooling on the blade-row efficiency of turbine airfoils. In *10th Aerospace Sciences Meeting*, Reston, Virginia. American Institute of Aeronautics and Astronautics.
- Hoefer, F., Schueren, S., von Wolfersdorf, J., and Naik, S. (2012). Heat Transfer Characteristics of an Oblique Jet Impingement Configuration in a Passage With Ribbed Surfaces. *Journal of Turbomachinery*, 134(3):031022.
- Hollworth, B. R. and Berry, R. D. (1978). Heat Transfer From Arrays of Impinging Jets with Large Jet-to-Jet Spacing. *Journal of Heat Transfer*, 100(2):352–357.
- Horlock, J. H. and Torbidoni, L. (2008). Calculations of Cooled Turbine Efficiency. *Journal of Engineering for Gas Turbines and Power*, 130(1):011703.
- Huang, L. and El-Genk, M. S. (1994). Heat transfer of an impinging jet on a flat surface. *International Journal of Heat and Mass Transfer*, 37(13):1915–1923.
- Huang, Y., Ekkad, S. V., and Han, J.-C. (1998). Detailed Heat Transfer Distributions Under an Array of Orthogonal Impinging Jets. *Journal of Thermophysics and Heat Transfer*, 12(1):73–79.
- Huber, A. M. and Viskanta, R. (1994). Convective Heat Transfer to a Confined Impinging Array of Air Jets With Spent Air Exits. *Journal of Heat Transfer*, 116(3):570–576.
- Hüning, M. (2010). Comparison of Discharge Coefficient Measurements and Correlations for Orifices With Cross-Flow and Rotation. *Journal of Turbomachinery*, 132(3):031017.

- Hunt, R. J. (2011). *The History of the Industrial Gas Turbine (Part 1 The First Fifty Years 1940-1990)*. Institution of Diesel and Gas Turbine Engines (idgtE).
- Ieronymidis, I., Gillespie, D. R. H., Ireland, P. T., and Kingston, R. (2010). Detailed Heat Transfer Measurements in a Model of an Integrally Cast Cooling Passage. *Journal of Turbomachinery*, 132(2):021002.
- Incropera, F. P., DeWitt, D. P., Bergman, T. L., and Lavine, A. S. (2007). *Fundamentals of Heat and Mass Transfer*. John Wiley and Sons, 6 edition.
- Ireland, P. T. and Jones, T. V. (2000). Liquid crystal measurements of heat transfer and surface shear stress. *Measurement Science and Technology*, 11(7):969–986.
- Ireland, P. T., Neely, A. J., Gillespie, D. R. H., and Robertson, A. J. (1999). Turbulent heat transfer measurements using liquid crystals. *International Journal of Heat and Fluid Flow*, 20(4):355–367.
- Jambunathan, K., Lai, E., Moss, M. A., and Button, B. L. (1992). A review of heat transfer data for single circular jet impingement. *International Journal of Heat and Fluid Flow*, 13(2):106–115.
- Kasagi, N., Moffat, R. J., and Hirrata, M. (1989). Liquid Crystals. In Yang, W. J., editor, *Handbook of Flow Visualization*. Hemisphere, New York.
- Kataoka, K. (1985). Optimal nozzle-to-plate spacing for convective heat transfer in nonisothermal, variable-density impinging jets. *Drying Technology*, 3(2):235–254.
- Katti, V. and Prabhu, S. V. (2008a). Experimental study and theoretical analysis of local heat transfer distribution between smooth flat surface and impinging air jet from a circular straight pipe nozzle. *International Journal of Heat and Mass Transfer*, 51(17-18):4480–4495.
- Katti, V. and Prabhu, S. V. (2008b). Heat transfer enhancement on a flat surface with axisymmetric detached ribs by normal impingement of circular air jet. *International Journal of Heat and Fluid Flow*, 29(5):1279–1294.
- Kays, W., Crawford, M., and Weigand, B. (2004). *Convective Heat and Mass Transfer*. mcgraw-hill.co.uk, 4th edition.
- Kee, R. J., O'Reilly, P. G., Fleck, R., and McEntee, P. T. (1998). Measurement of Exhaust Gas Temperatures in a High Performance Two-Stroke Engine. Technical report, Warrendale, PA.
- Kercher, D. M. and Tabakoff, W. (1970). Heat Transfer by a Square Array of Round Air Jets Impinging Perpendicular to a Flat Surface Including the Effect of Spent Air. *Journal of Engineering for Power*, 92(1):73–82.
- Kleine, S. D. (1968). Liquid Crystals in Aerodynamic Testing. *Astronautics and Aeronautics*, 6:70–73.
- Kobayashi, S., Moriyoshi, Y., and Enomoto, Y. (2008). Development of Local Gas Temperature Measurement Technique inside a Combustion Chamber Using Two-Wire Thermocouple. *Journal of Thermal Science and Technology*, 3(3):486–498.

- Koff, B. L. (2004). Gas Turbine Technology Evolution: A Designers Perspective. *Journal of Propulsion and Power*, 20(4):577–595.
- Koseoglu, M. F. and Baskaya, S. (2010). The role of jet inlet geometry in impinging jet heat transfer, modeling and experiments. *International Journal of Thermal Sciences*, 49(8):1417–1426.
- Kwak, J. S. (2008). Comparison of Analytical and Superposition Solutions of the Transient Liquid Crystal Technique. *Journal of Thermophysics and Heat Transfer*, 22(2):290–295.
- Lamont, J. A., Ekkad, S. V., and Alvin, M. A. (2012). Effects of Rotation on Heat Transfer for a Single Row Jet Impingement Array With Crossflow. *Journal of Heat Transfer*, 134(8):082202–082202–12.
- Lee, C.-P. and Bunker, R. S. (2006). Thermal shield turbine airfoil. United States Patent.
- Lee, D. H., Song, J., and Chan, J. M. (2004). The Effects of Nozzle Diameter on Impinging Jet Heat Transfer and Fluid Flow. *Journal of Heat Transfer*, 126(4):554–557.
- Lee, J. and Lee, S.-J. (2000). The effect of nozzle configuration on stagnation region heat transfer enhancement of axisymmetric jet impingement. *International Journal of Heat and Mass Transfer*, 43(18):3497–3509.
- Liang, G. (2013). Turbine stator vane with near wall integrated micro cooling channels. United States Patent.
- Lichtarowicz, A., Duggins, R. K., and Markland, E. (1963). Discharge coefficients for incompressible noncavitating flow through long orifices. *Journal of Mechanical Engineering Science*, 7(2):210–219.
- Ligrani, P. (2013). Heat Transfer Augmentation Technologies for Internal Cooling of Turbine Components of Gas Turbine Engines. *International Journal of Rotating Machinery*, 2013(3):1–32.
- Liu, X., Gabour, L. A., and Lienhard, J. H. (1993). Stagnation-Point Heat Transfer During Impingement of Laminar Liquid Jets: Analysis Including Surface Tension. *Journal of Heat Transfer*, 115(1):99–105.
- Livsey, D. J. and Hamblet, M. (1996). Air cooled gas turbine airfoil. United States Patents.
- Lutum, E., Semmler, K., and von Wolfersdorf, J. (2002). Cooled Blade for a Gas Turbine. United States Patent.
- Lytle, D. and Webb, B. W. (1994). Air jet impingement heat transfer at low nozzle-plate spacings. *International Journal of Heat and Mass Transfer*, 37(12):1687–1697.
- Mansour, M., Chokani, N., Kalfas, A. I., and Abhari, R. S. (2008). Time-resolved entropy measurements using a fast response entropy probe. *Measurement Science and Technology*, 19(11):115401.
- Martin, H. (1977). Heat and mass transfer between impinging gas jets and solid surfaces. *Advances in Heat Transfer*, 13:1–60.

- Mayer, A. (1941). Schaufel mit Einrichtung zur Bildung einer gegen hohe Temperaturen schützenden Grenzschicht und Verfahren zur Herstellung dieser schaufel. Patentschrift.
- McKenzie, A. B. (1966). An Investigation for Flare Dimensions for Standard and Annular Air Meters. Technical Report Rolls-Royce, Compressor Dept. Report, RCR-90067.
- Meetham, G. W. (1981). *The Development of Gas Turbine Materials*. Applied Science Publishers Ltd, 1st eddition edition.
- Mehta, R. D. and Bradshaw, P. (1979). Desing Rules for Small Low Speed Wind Tunnels. *Aeronautical Journal*, 83:443–449.
- Melvin, A. (2002). The transient behaviour of small thermocouples in static gas environments. *Journal of Physics D: Applied Physics*, 2(9):1339–1343.
- Metzger, D. E., Florschuetz, L. W., Takeuchi, D. I., Behee, R. D., and Berry, R. A. (1979). Heat Transfer Characteristics for Inline and Staggered Arrays of Circular Jets with Crossflow of Spent Air. *Journal of Heat Transfer*, 101(3):526–531.
- Metzger, D. E. and Korstad, R. J. (1972). Effects of Crossflow on Impingement Heat Transfer. *Journal of Engineering for Power*, 94(1):35–41.
- Miles, P. and Gouldin, F. C. (1993). Determination of the Time Constant of Fine-Wire Thermocouples for Compensated Temperature Measurements in Premixed Turbulent Flames. *Combustion Science and Technology*, 89(1-4):181–199.
- Miller, N., Siw, S. C., Chyu, M. K., and Alvin, M. A. (2013). Effects of Jet Diameter and Surface Roughness on Internal Cooling with Single Array of Jets. In *ASME Turbo Expo 2013: Power for Land, Sea, and Air*, page 9 pages, San Antonio.
- Moffat, R. J. (1988). Describing the uncertainties in experimental results. *Experimental Thermal and Fluid Science*, 1(1):3–17.
- Mohanty, A. K. and Tawfek, A. A. (1993). Heat transfer due to a round jet impinging normal to a flat surface. *International Journal of Heat and Mass Transfer*, 36(6):1639–1647.
- Moore, R. P. (1997). Cooled airfoils for a gas turbine engine. United States Patent.
- Murdock, J. W., Foltz, C. J., and Gregory, C. (1963). A Practical Method of Determining Response Time of Thermometers in Liquid Baths. *Journal of Engineering for Power*, 85(1):27.
- Obot, N. T. and Trabold, T. A. (1987). Impingement Heat Transfer Within Arrays of Circular Jets: Part 1—Effects of Minimum, Intermediate, and Complete Crossflow for Small and Large Spacings. *Journal of Heat Transfer*, 109(4):872–879.
- O'Donovan, T. S. and Murray, D. B. (2007). Jet impingement heat transfer – Part II: A temporal investigation of heat transfer and local fluid velocities. *International Journal of Heat and Mass Transfer*, 50(17-18):3302–3314.
- Owen, J. M., Newton, P. J., and Lock, G. D. (2003). Transient heat transfer measurements using thermochromic liquid crystal. Part 2: Experimental uncertainties. *International Journal of Heat and Fluid Flow*, 24(1):23–28.

- Park, J., Goodro, M., Ligrani, P., Fox, M., and Moon, H.-K. (2007). Separate Effects of Mach Number and Reynolds Number on Jet Array Impingement Heat Transfer. *Journal of Turbomachinery*, 129(2):269–280.
- Park, S. J. and Ro, S. T. (1996). A new method for measuring time constants of a thermocouple wire in varying flow states. *Experiments in Fluids*, 21(5):380–386.
- Parsley, M. (1991). The use of thermochromic liquid crystals in research applications, thermal mapping and non-destructive testing. In *Seventh IEEE Semiconductor Thermal Measurement and Management Symposium*, pages 53–58. IEEE.
- Petit, C., Gajan, P., Lecordier, J. C., and Paranthoen, P. (2000). Frequency response of fine wire thermocouple. *Journal of Physics E: Scientific Instruments*, 15(7):760–770.
- Popiel, C. O. and Trass, O. (1991). Visualization of a free and impinging round jet. *Experimental Thermal and Fluid Science*, 4(3):253–264.
- Poser, R., Ferguson, J. R., and von Wolfersdorf, J. (2011). Temporal Signal Processing and Evaluation of Thermochromic Liquid Crystal Indications in Transient Heat Transfer Experiments. In *8th European Conference on Turbomachinery Fluid Dynamics and Thermodynamics (ETC8)*, pages 785–795.
- Poser, R. and von Wolfersdorf, J. (2011). Liquid Crystal Thermography for Transient Heat Transfer Measurements in Complex Internal Cooling Systems. *Heat Transfer Research*, 42(2):181–197.
- Poser, R., von Wolfersdorf, J., and Lutum, E. (2007). Advanced evaluation of transient heat transfer experiments using thermochromic liquid crystals. *Proceedings of the Institution of Mechanical Engineers, Part A: Journal of Power and Energy*, 221(6):793–801.
- Praisner, T. J. and Smith, C. R. (2006a). The Dynamics of the Horseshoe Vortex and Associated Endwall Heat Transfer—Part I: Temporal Behavior. *Journal of Turbomachinery*, 128(4):747.
- Praisner, T. J. and Smith, C. R. (2006b). The Dynamics of the Horseshoe Vortex and Associated Endwall Heat Transfer—Part II: Time-Mean Results. *Journal of Turbomachinery*, 128(4):755.
- Pugh, P. (2001). *The Magic of a Name. The Rolls-Royce Story II: The Power Behind the Jets*. Icon Books Ltd.
- Rao, Y. and Xu, Y. (2012). Liquid Crystal Thermography Measurement Uncertainty Analysis and Its Application to Turbulent Heat Transfer Measurements. *Advances in Condensed Matter Physics*, 2012(4):1–8.
- Richardson, P. D. (1963). Heat and mass transfer in turbulent separated flows. *Chemical Engineering Science*, 18(3):149–155.
- Ricklick, M. and Kapat, J. S. (2011). Determination of a Local Bulk Temperature Based Heat Transfer Coefficient for the Wetted Surfaces in a Single Inline Row Impingement Channel. *Journal of Turbomachinery*, 133(3):031008.

- Ricklick, M., Kapat, J. S., and Heidmann, J. (2010). Sidewall Effects on Heat Transfer Coefficient in a Narrow Impingement Channel. *Journal of Thermophysics and Heat Transfer*, 24(1):123–132.
- Schuere, S., Hoefler, F., von Wolfersdorf, J., and Naik, S. (2013). Heat Transfer in an Oblique Jet Impingement Configuration With Varying Jet Geometries. *Journal of Turbomachinery*, 135(2):021011.
- Son, C., Gillespie, D. R. H., Ireland, P. T., and Dailey, G. M. (2001). Heat Transfer and Flow Characteristics of an Engine Representative Impingement Cooling System. *Journal of Turbomachinery*, 123(1):154–160.
- Spring, S., Lauffer, D., Weigand, B., and Hase, M. (2010). Experimental and Numerical Investigation of Impingement Cooling in a Combustor Liner Heat Shield. *Journal of Turbomachinery*, 132(1):011003.
- Spring, S., Xing, Y., and Weigand, B. (2012). An Experimental and Numerical Study of Heat Transfer From Arrays of Impinging Jets With Surface Ribs. *Journal of Heat Transfer*, 134(8):082201.
- Stasiek, J. and Kowalewski, T. A. (2002). Thermochromic liquid crystals applied for heat transfer research. *Opto-Electronics Review*, 10:1–10.
- Stoakes, P. and Ekkad, S. V. (2011). Optimized Impingement Configurations for Double Wall Cooling Applications. In *Proceedings of ASME Turbo Expo 2011*, pages 1535–1543. ASME.
- Strahle, W. C. and Muthukrishnan, M. (1976). Thermocouple time constant measurement by cross power spectra. *AIAA Journal*, 14(11):1642–1644.
- Tagawa, M., Kaifuku, K., Houra, T., Yamagami, Y., and Kato, K. (2011). Response compensation of fine-wire thermocouples and its application to multidimensional measurement of a fluctuating temperature field. *Heat Transfer-Asian Research*, 40(5):404–418.
- Tagawa, M., Shimoji, T., and Ohta, Y. (1998). A two-thermocouple probe technique for estimating thermocouple time constants in flows with combustion: In situ parameter identification of a first-order lag system. *Review of Scientific Instruments*, 69(9):3370–3378.
- Terzis, A., von Wolfersdorf, J., Wagner, G., Weigand, B., and Ott, P. (2012a). Influence of thermocouple time constant on impingement heat transfer experiments using transient techniques. In *XXI Biannual Symp. Meas. Techniques in Turbomachinery*, Valencia, Spain.
- Terzis, A., von Wolfersdorf, J., Weigand, B., and Ott, P. (2012b). Thermocouple thermal inertia effects on impingement heat transfer experiments using the transient liquid crystal technique. *Measurement Science and Technology*, 23(11):115303.
- Terzis, A., Wagner, G., and Ott, P. (2012c). Hole Staggering Effect on the Cooling Performance of Narrow Impingement Channels. In *ASME Turbo Expo 2012: Turbine Technical Conference and Exposition*, pages 127–138. ASME.

- Terzis, A., Wagner, G., von Wolfersdorf, J., Ott, P., and Weigand, B. (2014). Effect of Hole Staggering on The Cooling Performance of Narrow Impingement Channels Using The Transient Liquid Crystal Technique. *Journal of Heat Transfer*, 136(7):071701.
- Uysal, U., Li, P. W., Chyu, M. K., and Cunha, F. J. (2006). Heat Transfer on Internal Surfaces of a Duct Subjected to Impingement of a Jet Array with Varying Jet Hole-Size and Spacing. *Journal of Turbomachinery*, 128(1):158–165.
- Van Der Meer, T. H. (1991). Stagnation point heat transfer from turbulent low reynolds number jets and flame jets. *Experimental Thermal and Fluid Science*, 4(1):115–126.
- Van Treuren, K. W., Wang, Z., Ireland, P. T., and Jones, T. V. (1994). Detailed Measurements of Local Heat Transfer Coefficient and Adiabatic Wall Temperature Beneath an Array of Impinging Jets. *Journal of Turbomachinery*, 116(3):369–374.
- Viskanta, R. (1993). Heat transfer to impinging isothermal gas and flame jets. *International Journal of Heat and Mass Transfer*, 6(2):111–134.
- Vogel, G. and Boelcs, A. (2000). A Novel Digital Image Processing System for the Transient Liquid Crystal Technique applied for Heat Transfer and Film Cooling Measurements. *Annals of the New York Academy of Sciences*, 934(1):297–304.
- Vogel, G. and Weigand, B. (2001). A new evaluation method for transient liquid crystal experiments. In *Proceedings of ASME NHTC01 35th National Heat Transfer Conference*, Anaheim, California.
- Wagner, G., Schneider, E., von Wolfersdorf, J., Ott, P., and Weigand, B. (2007). Method for analysis of showerhead film cooling experiments on highly curved surfaces. *Experimental Thermal and Fluid Science*, 31(4):381–389.
- Weigand, B. and Spring, S. (2011). Multiple Jet Impingement - A Review. *Heat Transfer Research*, 42(2):101–142.
- Wilcock, R. C., Young, J. B., and Horlock, J. H. (2005). The Effect of Turbine Blade Cooling on the Cycle Efficiency of Gas Turbine Power Cycles. *Journal of Engineering for Gas Turbines and Power*, 127(1):109–120.
- Xing, Y., Spring, S., and Weigand, B. (2010). Experimental and Numerical Investigation of Heat Transfer Characteristics of Inline and Staggered Arrays of Impinging Jets. *Journal of Heat Transfer*, 132(9):092201.
- Xing, Y., Spring, S., and Weigand, B. (2011). Experimental and numerical investigation of impingement heat transfer on a flat and micro-rib roughened plate with different crossflow schemes. *International Journal of Thermal Sciences*, 50(7):1293–1307.
- Yan, Y. and Owen, J. M. (2002). Uncertainties in transient heat transfer measurements with liquid crystal. *International Journal of Heat and Fluid Flow*, 23(1):29–35.
- Zhou, D. W. and Ma, C. F. (2006). Radial heat transfer behavior of impinging submerged circular jets. *International Journal of Heat and Mass Transfer*, 49(9-10):1719–1722.

EXAMPLE OF TECHNICAL DRAWINGS

This Appendix section presents some basic technical drawings produced during the design phase of the impingement cooling test rig, in the beginning of 2010. As discussed in Chapter 3, the general arrangement comprises an open circuit small-scale wind tunnel operated in suction mode. The wind tunnel consists of an inlet flare, a straight section of square ducting that contains an air heater and the large-scale narrow impingement channel test models at the top of the test rig. Example of drawings are included for the heater mesh configuration and the large-scale narrow impingement channel test models, which were the most innovative parts designed. The basic drawings of these test rig components can be found in the following pages. A size scale of the impingement cooling test rig is illustrated in Figure A.1.

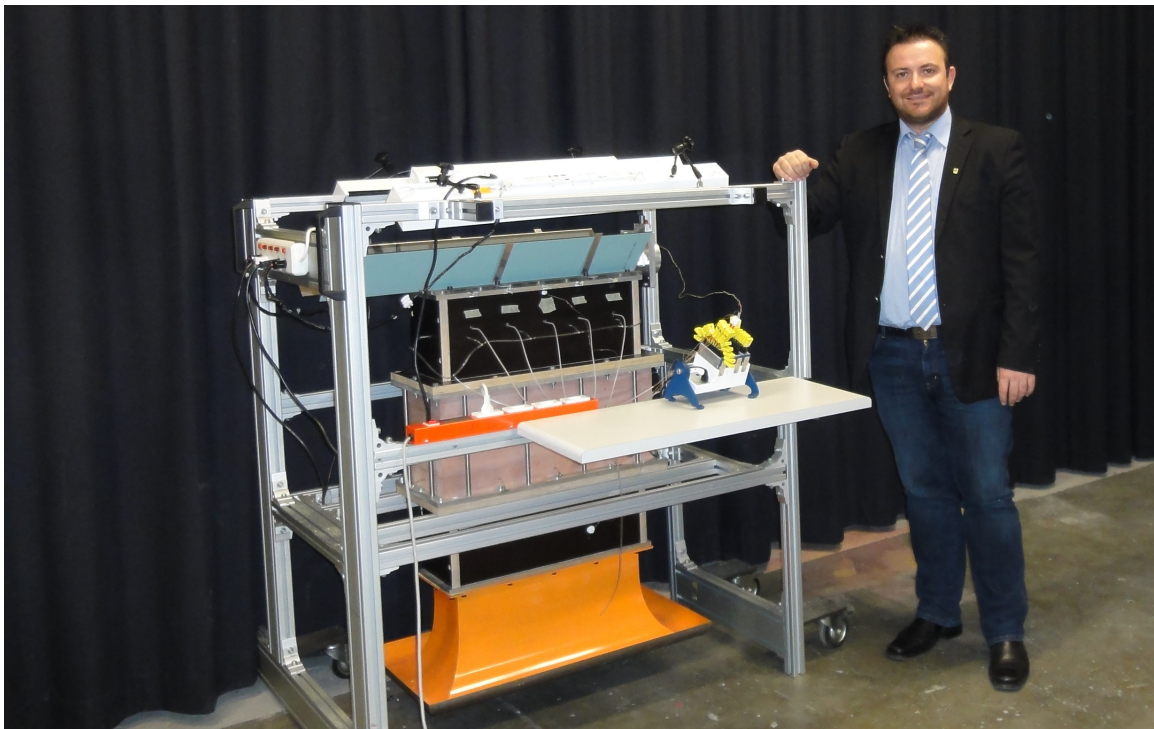


Figure A.1: The impingement cooling test rig of EPFL-GTT, photo taken by *Sounas*

A. Example of Technical Drawings

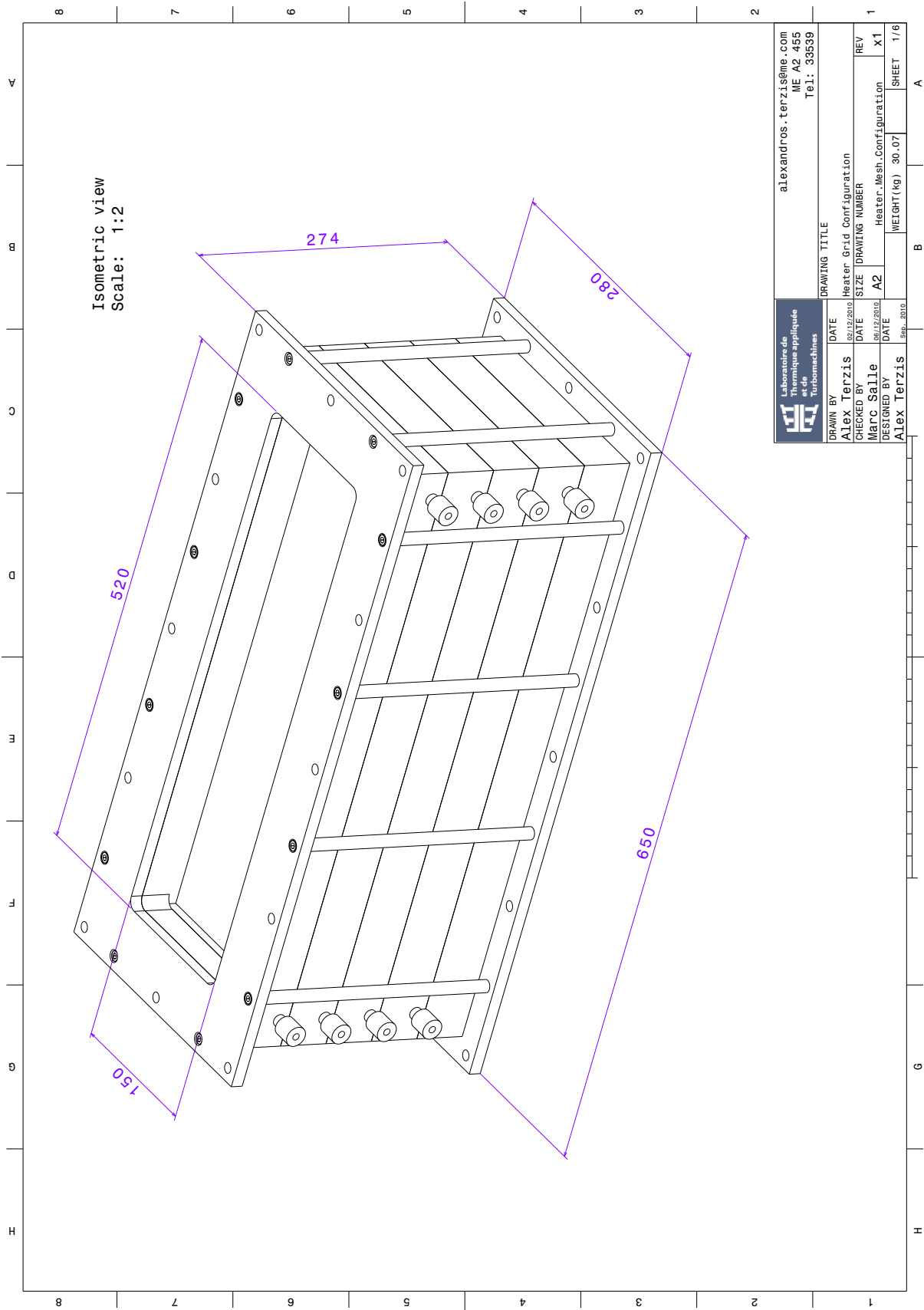


Figure A.2: Isometric view of the heater grid consisting of four individual mesh layers

A. Example of Technical Drawings

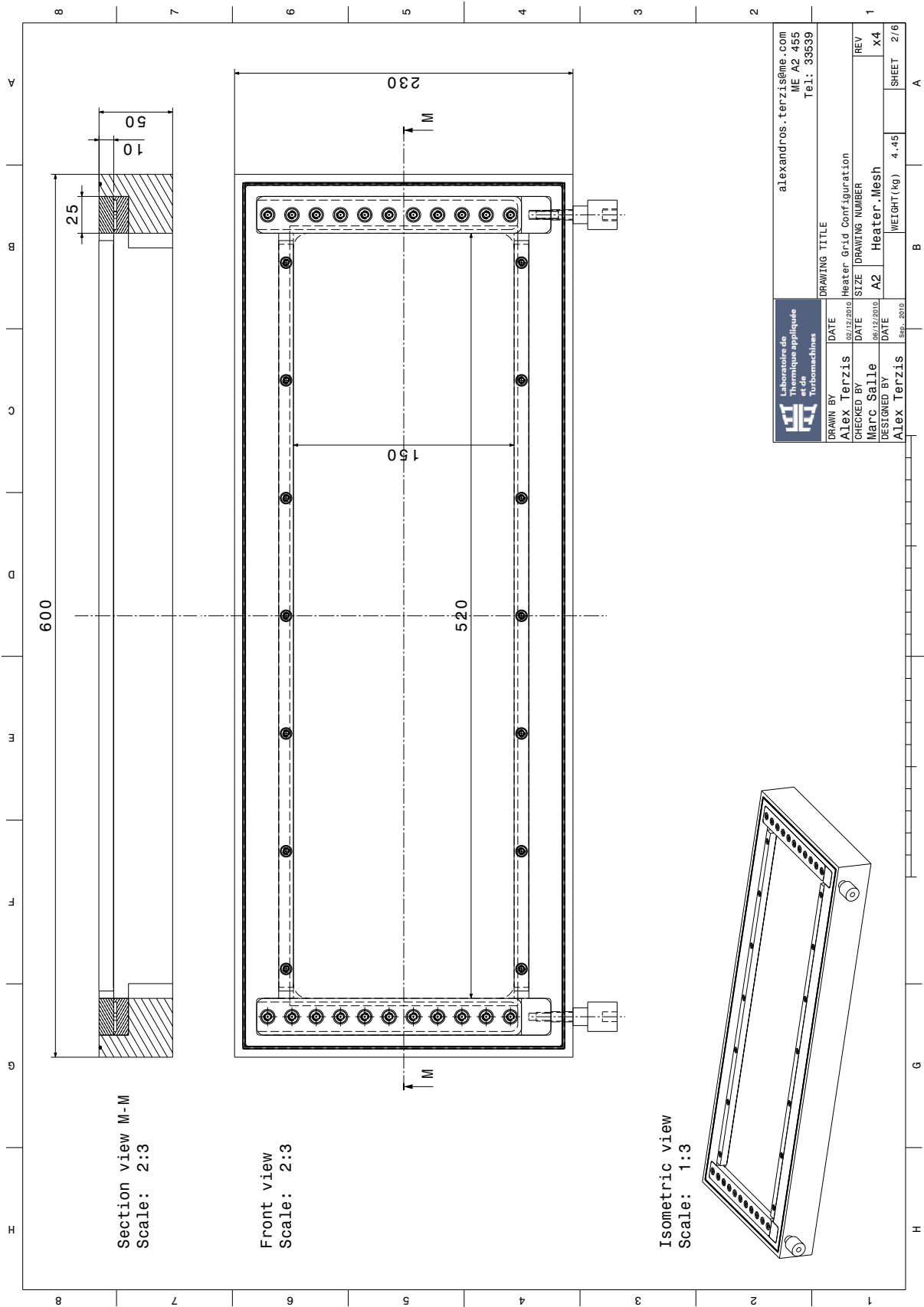


Figure A.3: A single heater mesh layer

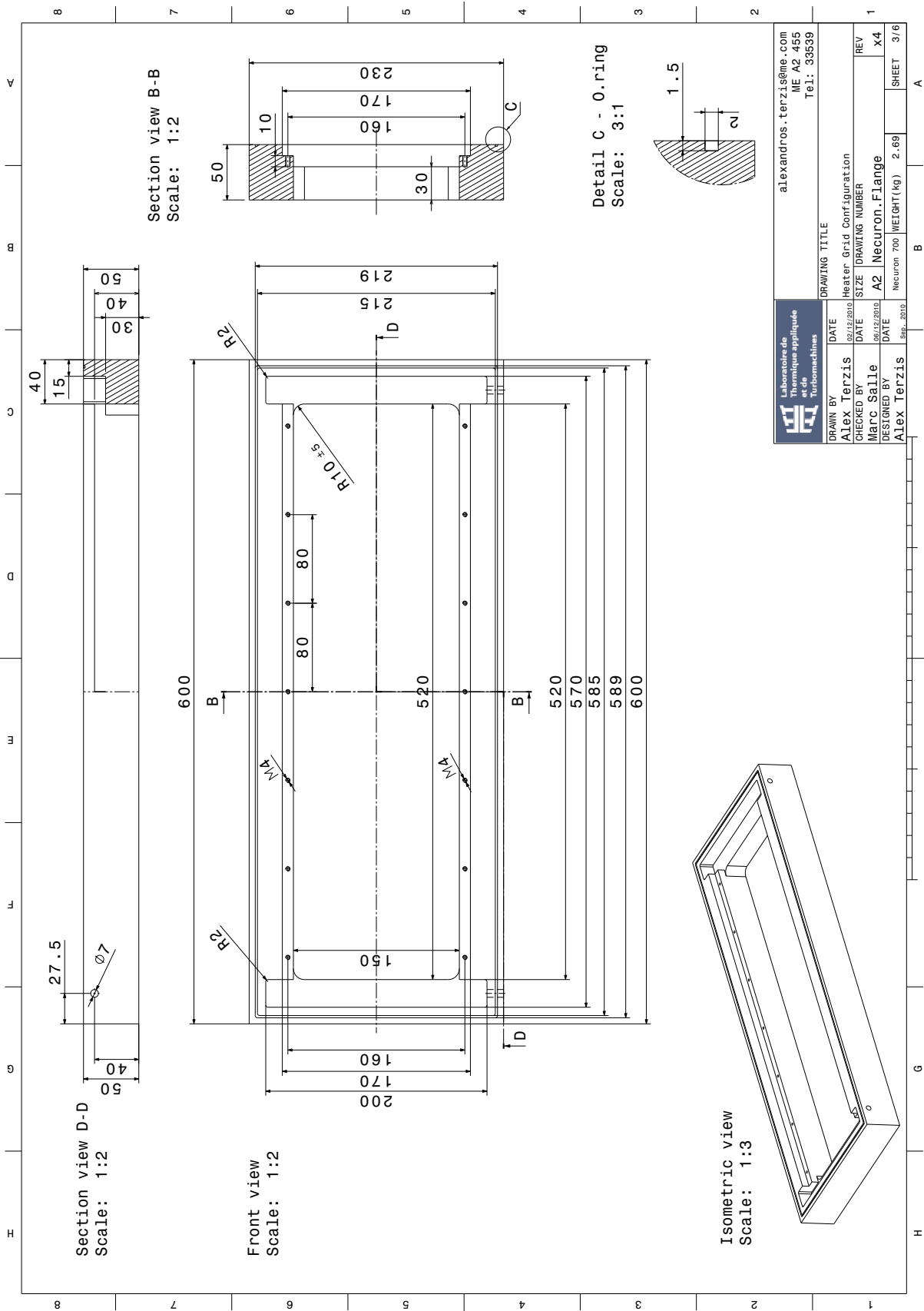


Figure A.4: Neuron 700 flange

A. Example of Technical Drawings

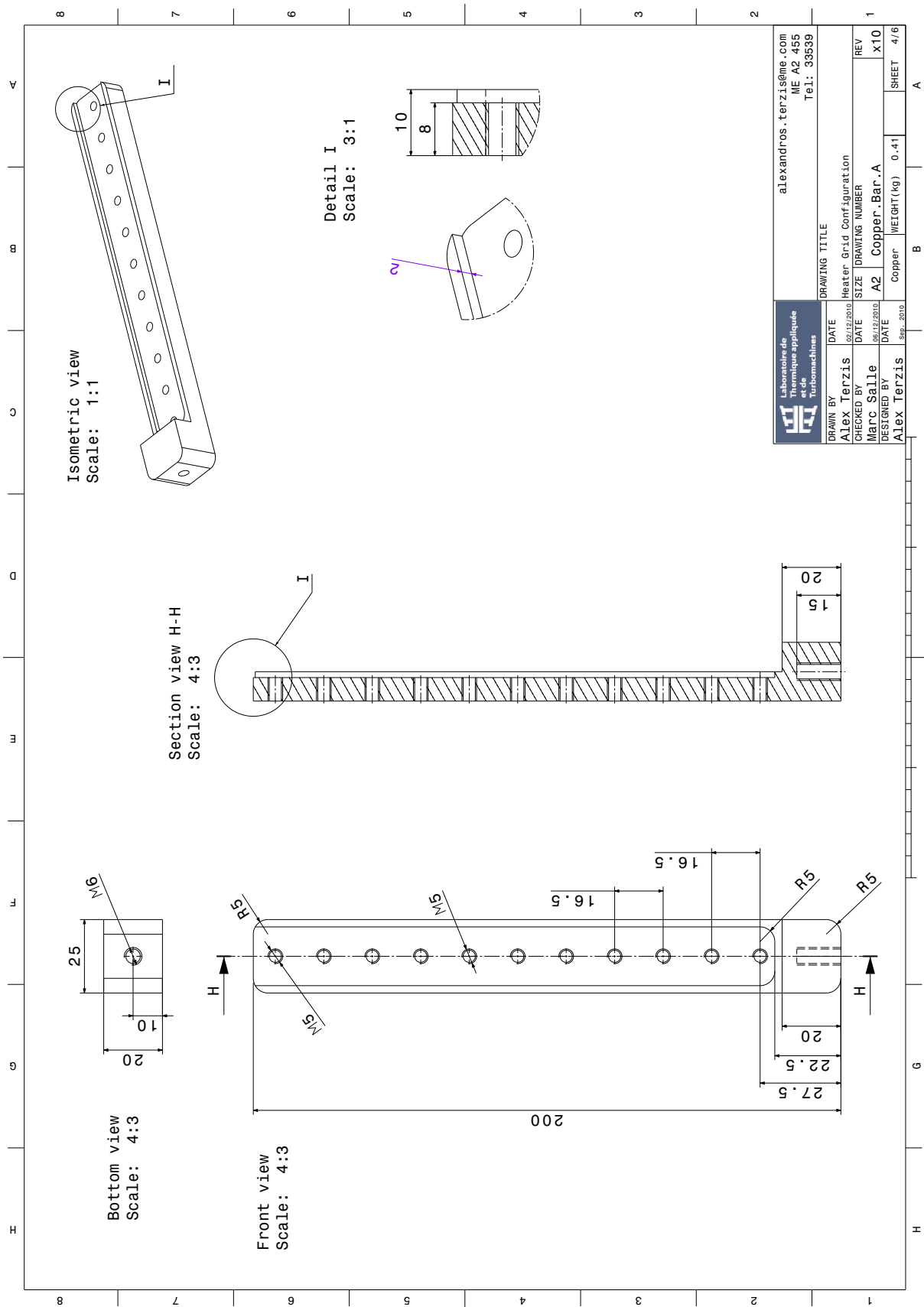


Figure A.5: 1st copper bar electrode for electrical power supply

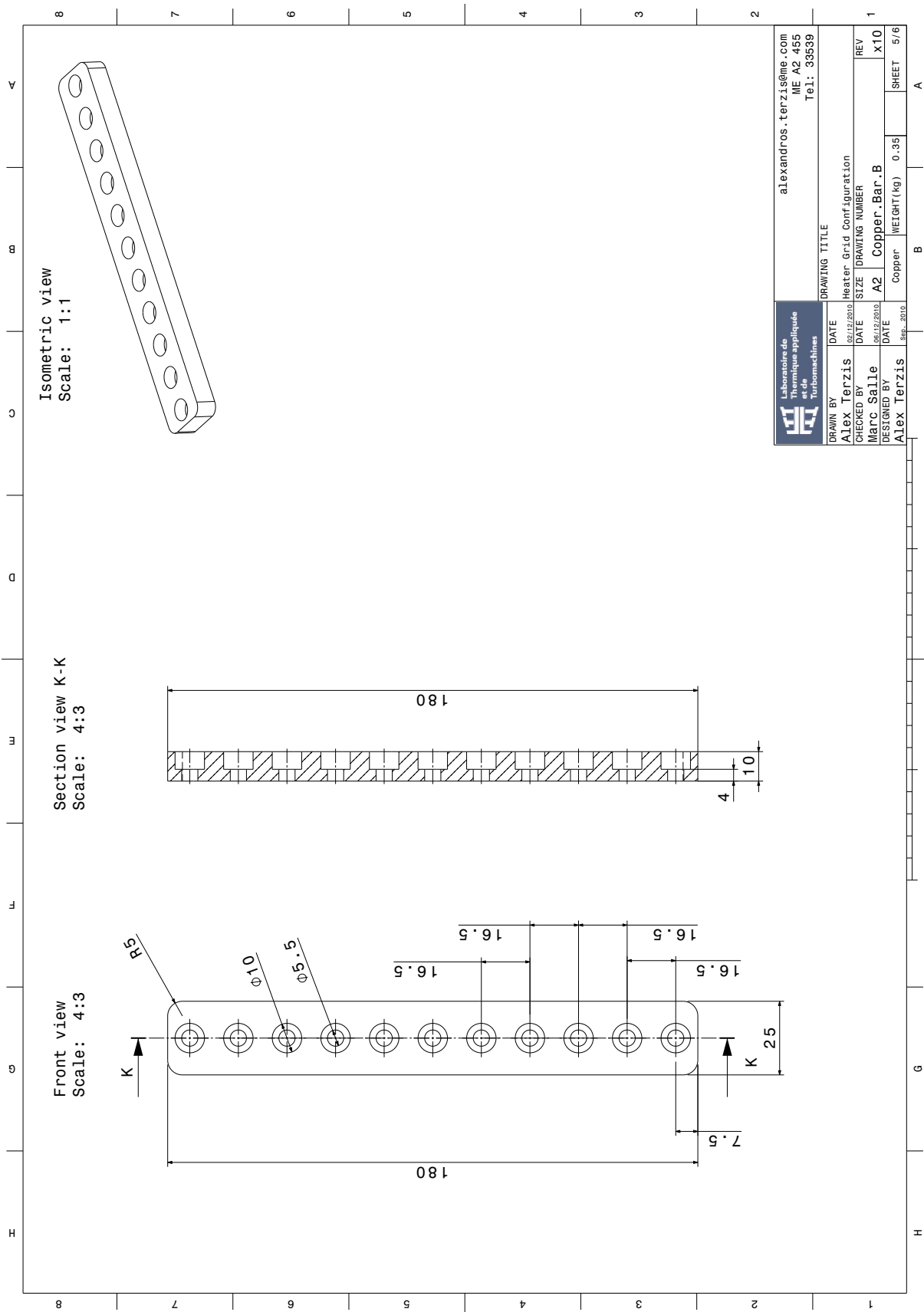


Figure A.6: 2nd copper bar electrode for electrical power supply

A. Example of Technical Drawings

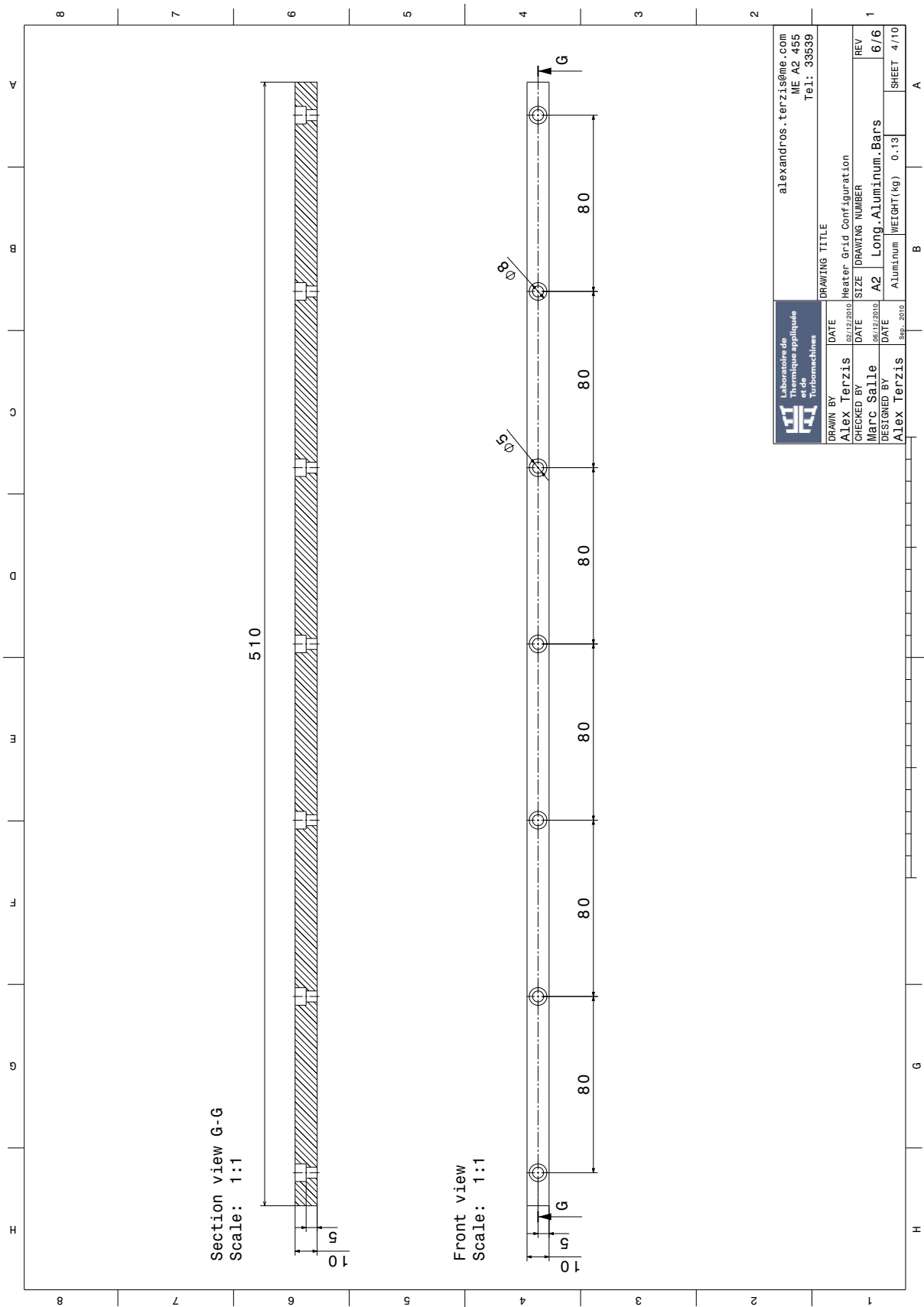


Figure A.7: Aluminium bars used to sandwich the heater along the complete flow path

A. Example of Technical Drawings

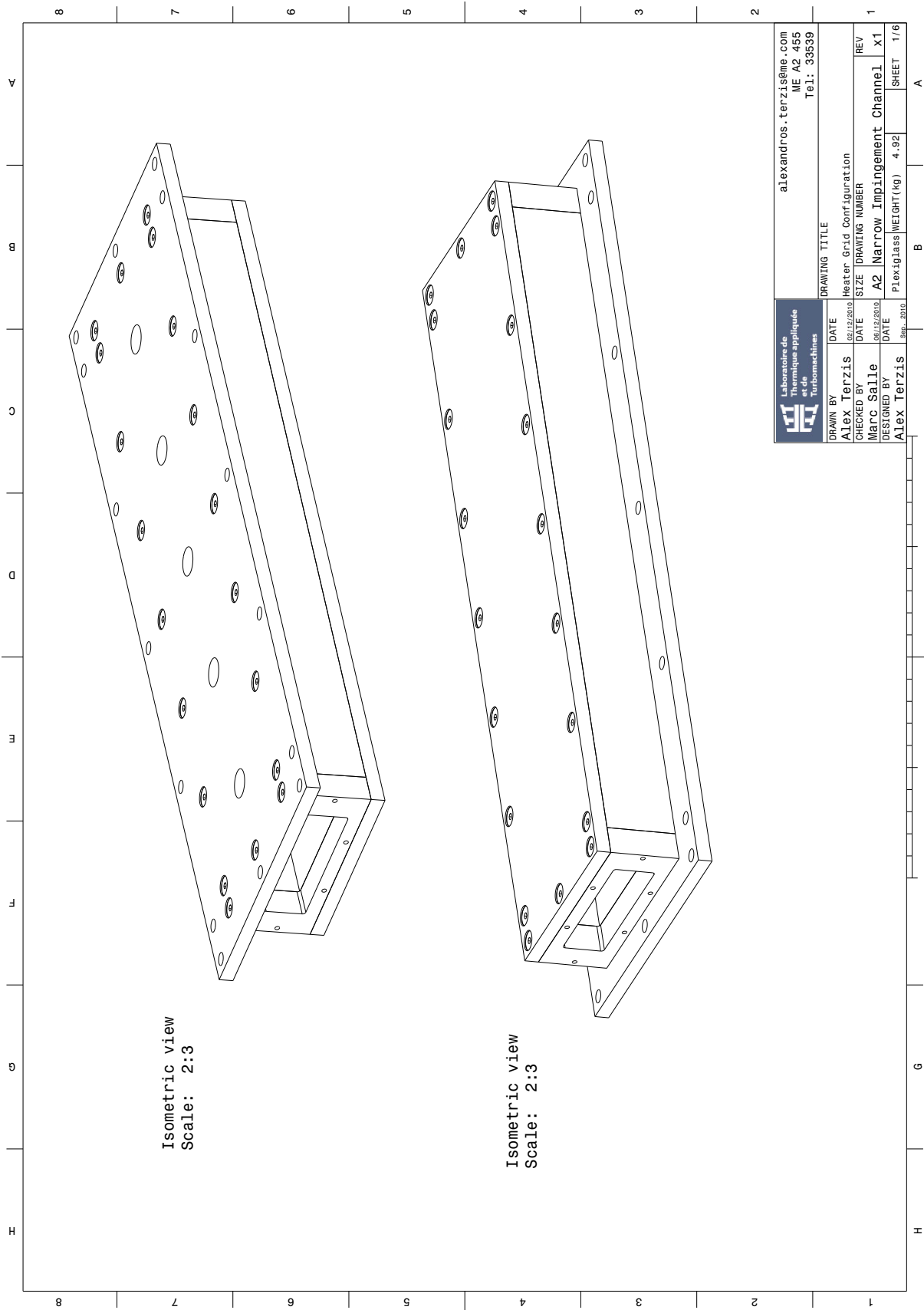


Figure A.8: Isometric view of the narrow impingement channel at $X/D=Y/D=5$, $Z/D=1.5$

A. Example of Technical Drawings

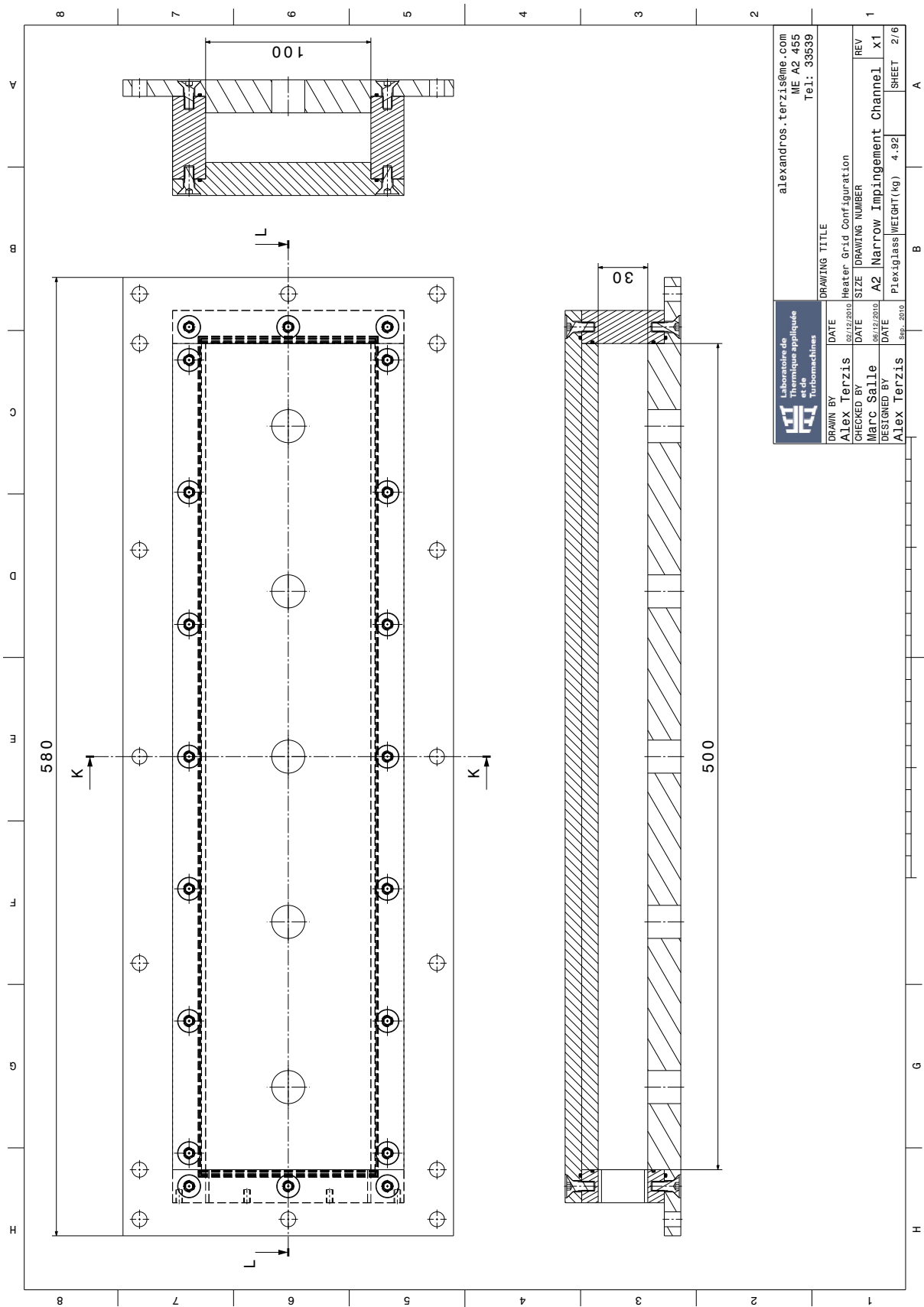


Figure A.9: Narrow impingement channel at $X/D=Y/D=5$, $Z/D=1.5$

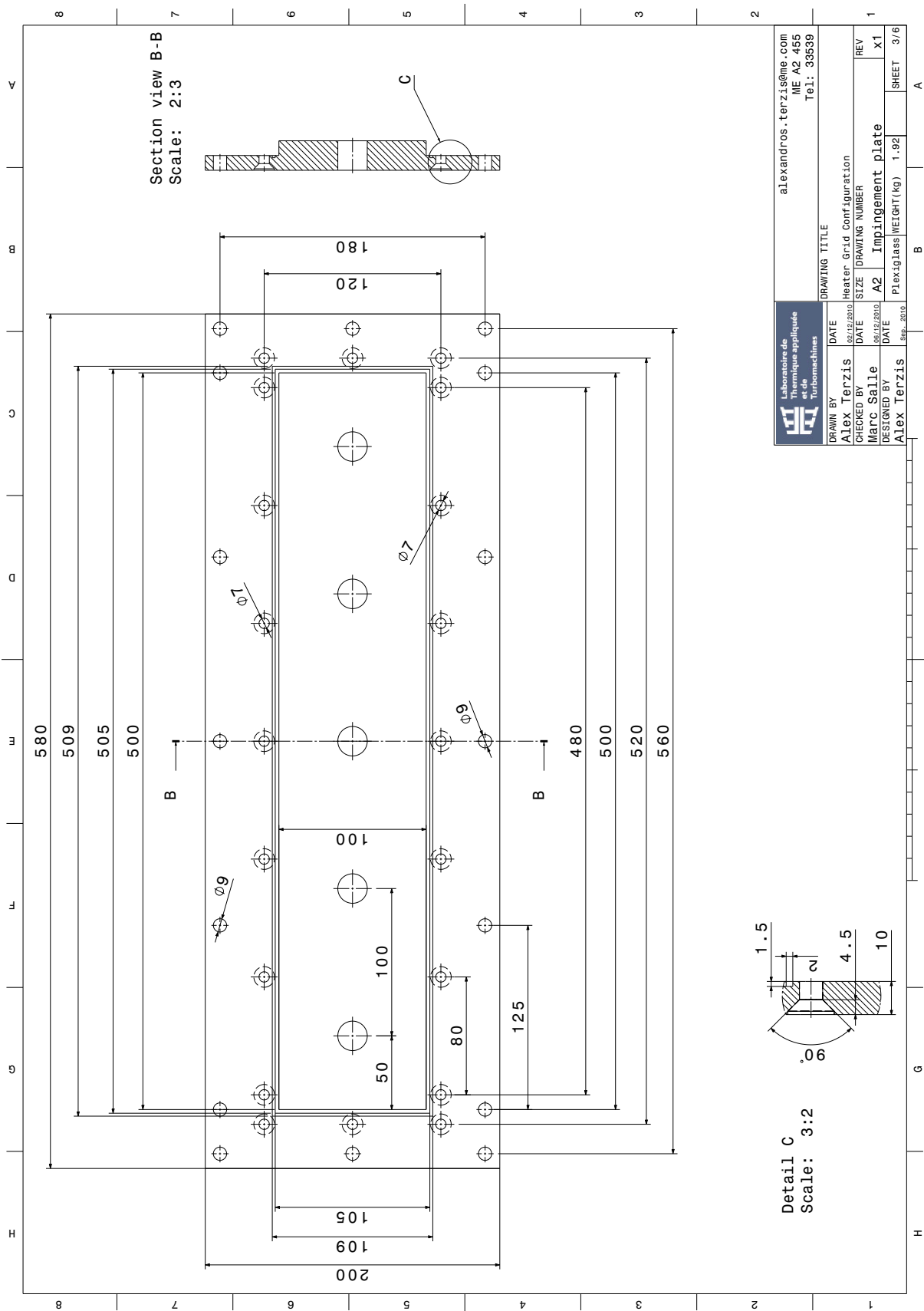


Figure A.10: Impingement plate for $X/D=Y/D=5$, $\Delta y/Y=0$

A. Example of Technical Drawings

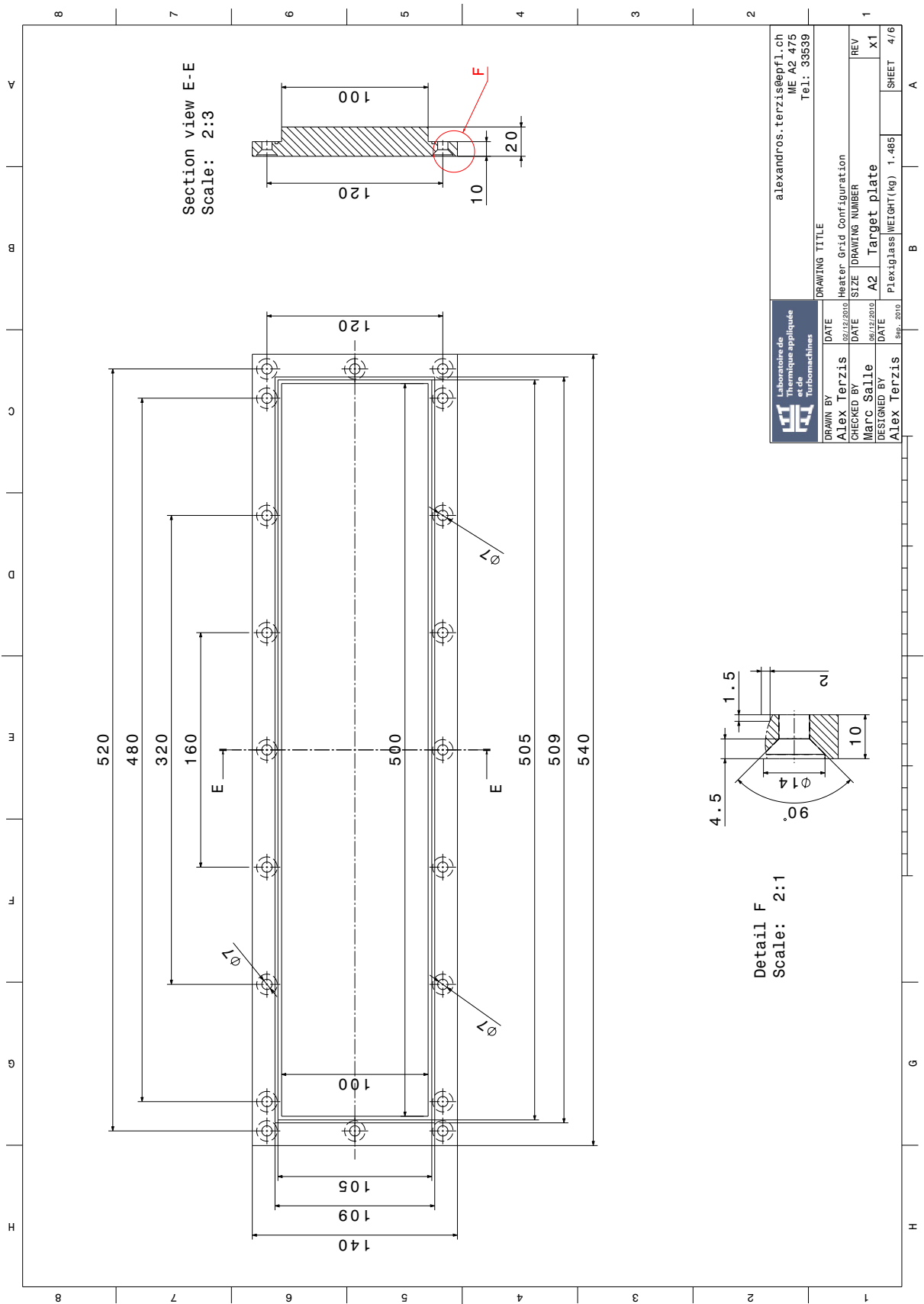


Figure A.11: Target plate for $X/D=Y/D=5$, $\Delta y/Y=0$

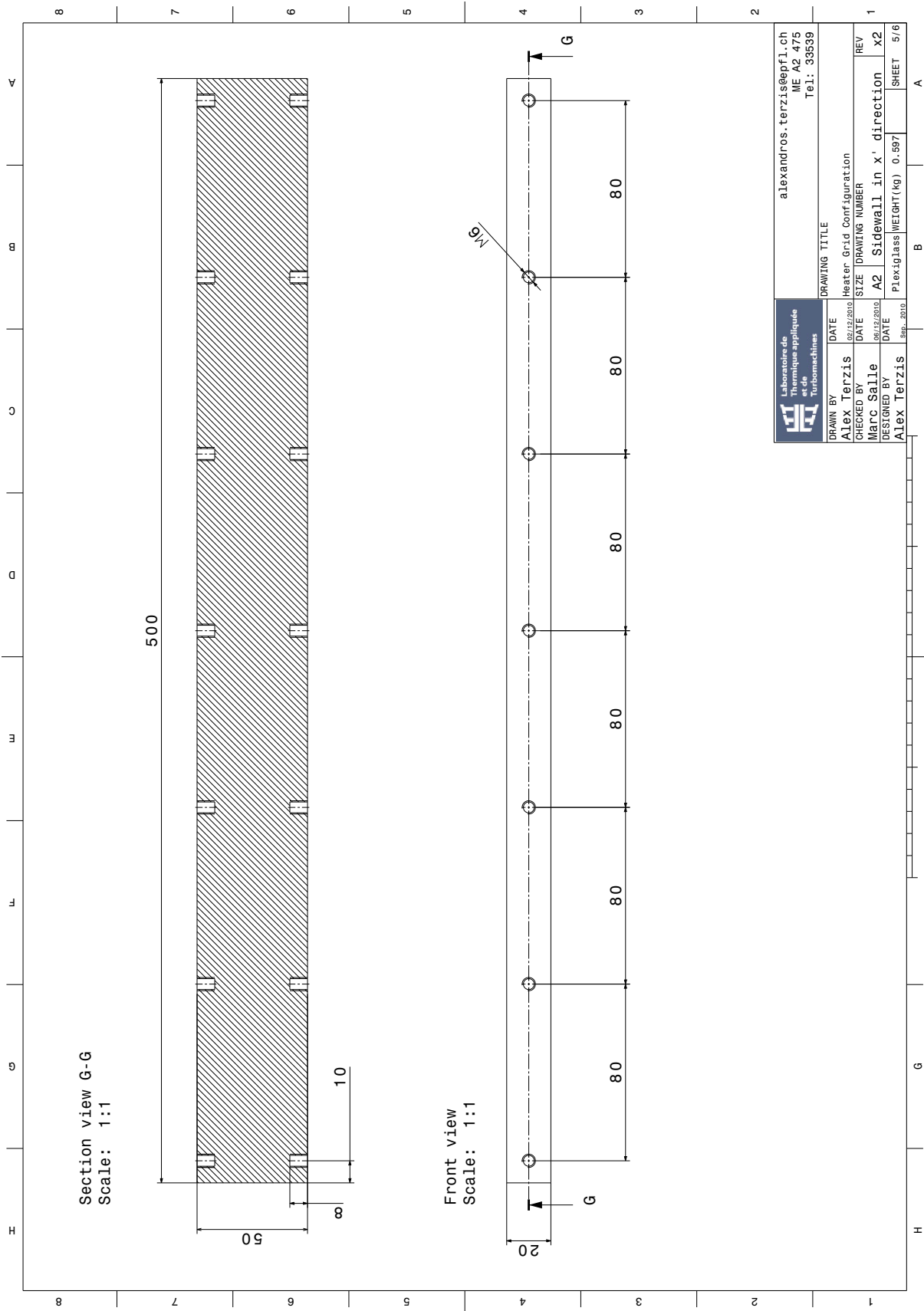


Figure A.12: Sidewall in the streamwise direction for $X/D_5, Z/D=1.5$

A. Example of Technical Drawings

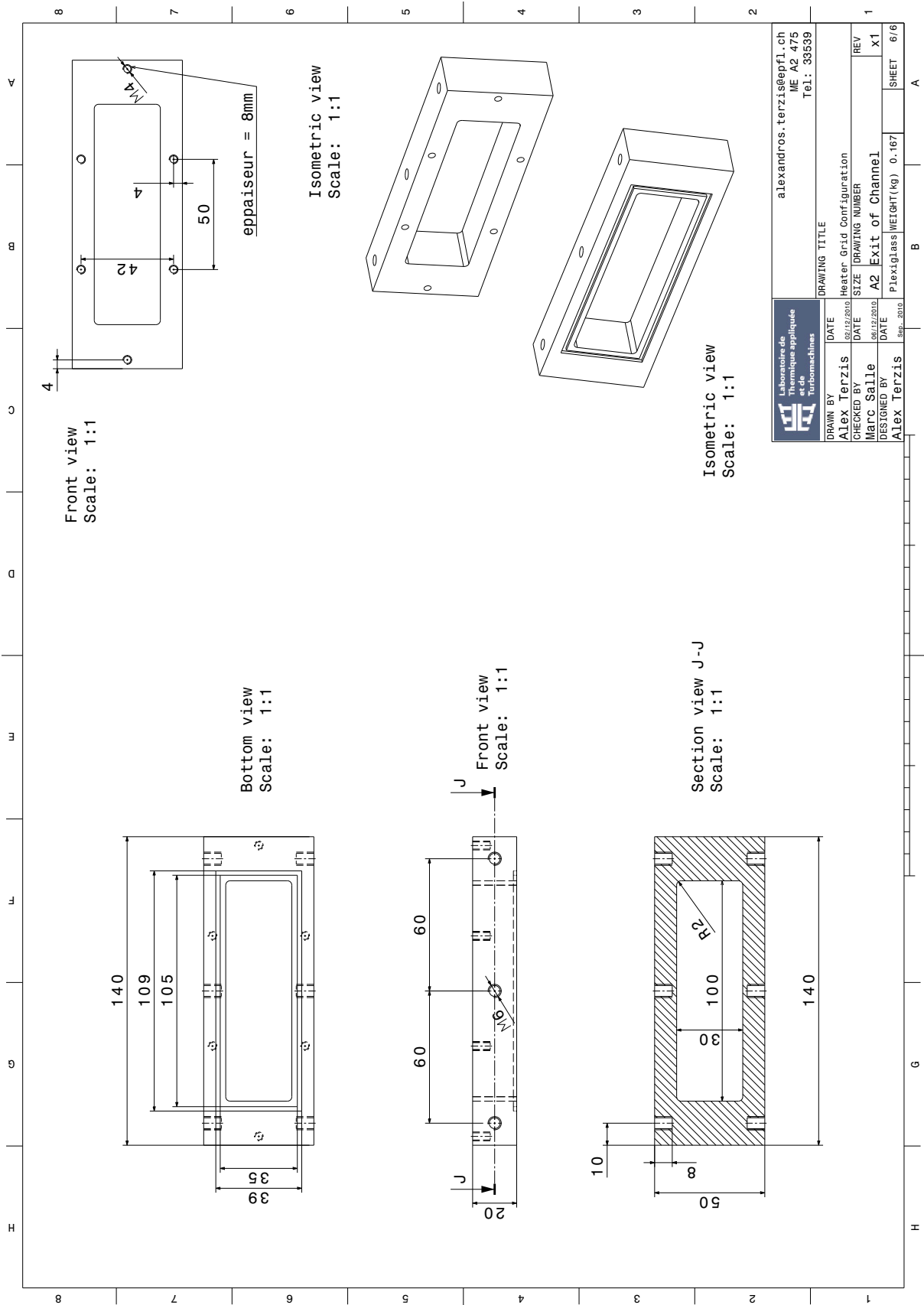


Figure A.13: Sidewall in the spanwise direction for $Y/D5$, $Z/D=1.5$

DIGITAL IMAGE PROCESSING TOOL

This Appendix section describes the image processing system that has been used for the evaluation of the heat transfer coefficients, as well as a comparison between the two different liquid crystal calibration methods. All the videos were acquired in a standard RGB mode with a CCD camera, model AVT Pike-310C. For the post-processing, a new digital image processing tool has been developed in MATLAB based on the previous works of [Vogel and Boelcs \(2000\)](#) and [Poser et al. \(2011\)](#). Note that the video length was cropped with a commercial software package (VirtualDub), and only the area of interest was loaded for post-processing.

First of all, a noise reduction filter was applied. In order to eliminate shadows, reflections, in-homogeneities, a difference operation function is applied between all the images of the video sequence and a reference image (usually the first image of the video) that does not contain any liquid crystal signal information. The best result is obtained by performing the difference in the RGB mode so that the hue information of liquid crystal is not altered in case the hue values are considered for the evaluation of the heat transfer coefficients. This video cleaning process will therefore eliminate all the undesired zones and only the useful information, which is liquid crystal evolution, will remain on the video sequence. An example of such a subtraction for one image of a sequence is shown in Figure B.1.

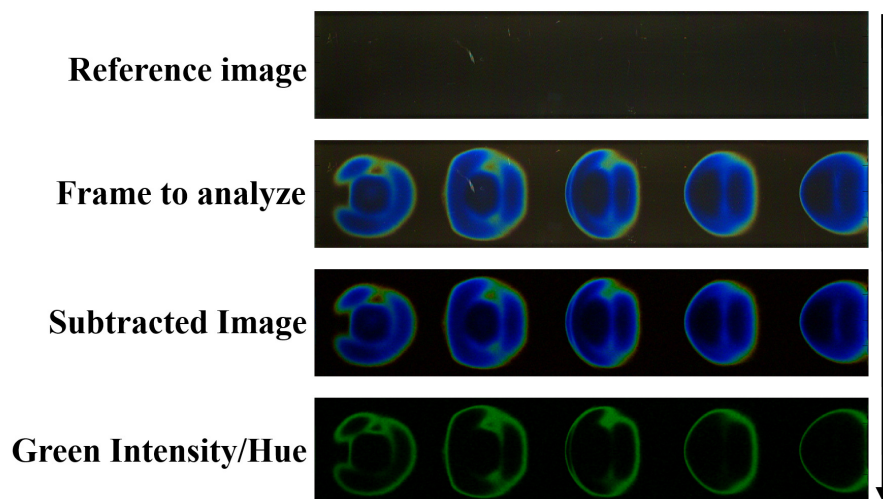


Figure B.1: Subtraction operation for one image of the video and green colour determination

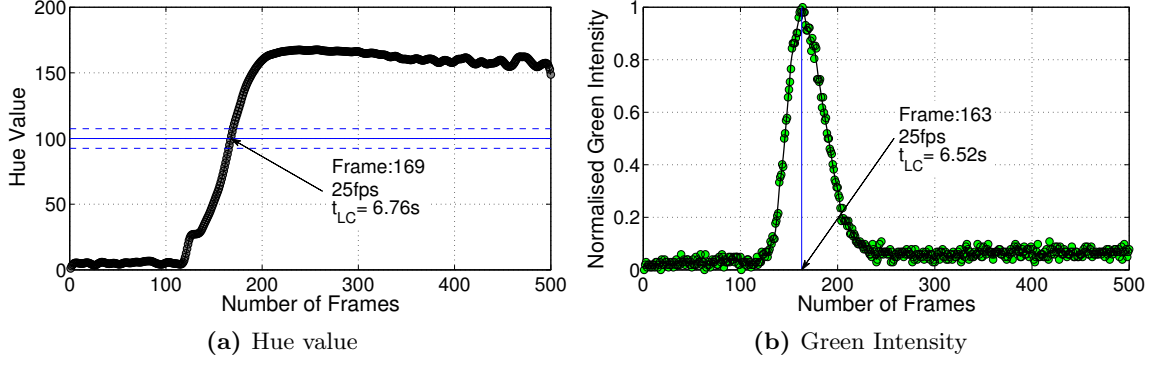


Figure B.2: Hue and green intensity evolution for a given pixel during the transient experiment

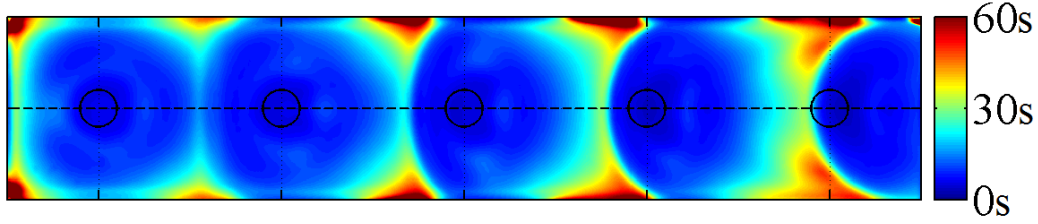


Figure B.3: Detection time of liquid crystal at a pixel size level. $X/D=Y/D=5$, $Z/D=1.5$

By using steady state calibration a specific hue value can be related to a specific temperature level. Therefore, knowing the detection time of liquid crystals for each pixel location, the local heat transfer coefficient can be calculated from Equation 4.2 given that all other quantities are accurately known. Typically, the green colour signal is considered due to the higher inclination of the calibration line, and thus, lower uncertainty compared to other colours (see calibration curves in Figure 4.3). The green hue value of around 100 (on a scale of 0 to 255) and a margin of ± 7.5 was taken into account. This gives an accuracy of the surface temperature of about $\pm 0.15^\circ\text{C}$. On the other hand, for the maximum green intensity method, an adaptive intensity normalisation of the filtered RGB signals is first performed in order to enhance signal stability and comparability. In the present work, base levels were determined by temporally averaging the signal and calculating the mode of all those values below the average, similar to Poser et al. (2011). It was shown that the green intensity peaks for each pixel could be sufficiently determined by the absolute maxima of the normalised signals. At this point, a noise filtering of the transient TLC indication intensity histories with a discrete Wavelet filter (WLF) is performed. Therefore, the position of the global intensity maximum can be determined precisely based on the filtered signal.

Once the sequence contains only events of the chosen hue or intensity filtered colours (and hence of a specific temperature level), the time lap between the start of the transient experiment and a local event appearance needs to be extracted. If the filtered images of the video sequence are of good quality, time event detection can be performed for each pixel position leading to relatively high spatial resolution. For this series of experiments, a resolution of approximately 6 pixels/(mm)² was obtained, which is translated to approximately 1735 pixels per impingement hole area. The detection time of liquid crystals (t_{LC}) at a given pixel location was then simply calculated by dividing the number of the analysed frame with the frame rate of the camera ($\sim 25\text{Hz}$). An example of the hue and green intensity evolution at a particular pixel is indicated in Figure B.2.

B. Digital Image Processing Tool

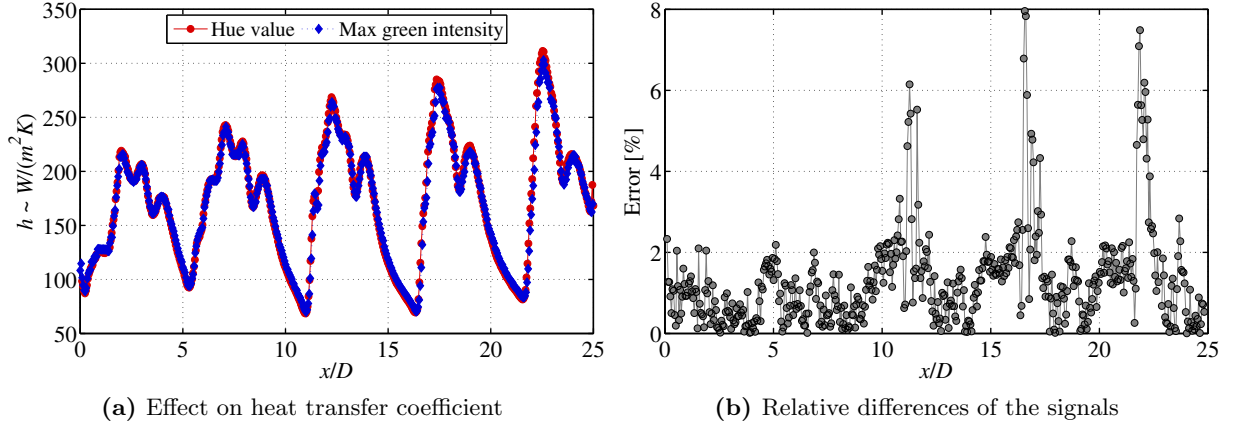


Figure B.4: Comparison between the hue and the maximum green intensity method for the evaluation of local heat transfer coefficients. $X/D=Y/D=5$, $Z/D=1$, $Re_D=32,900$

The same procedure is repeated for all the pixels of the area of interest resulting in a 2D contour map which contains information for the appearance time of liquid crystals. An example is illustrated in Figure B.3. Note that the liquid crystal detection times are maximised in the stagnation point regions where heat transfer coefficients are relatively high. Therefore, Equation 4.2 can be solved numerically for each pixel location providing the level of convective heat transfer coefficients.

Additionally, the two different calibration methods that can be used for the evaluation of heat transfer coefficients are compared in Figure B.4(a). Excellent agreement is observed between the evaluated local heat transfer coefficients in the channel centerline ($y=0$), with some visible difference at the stagnation point of jets 4 and 5. The relative difference between the heat transfer coefficients calculated from the wavelet filtered TLC signals (max green intensity) and the raw TLC signals (hue value) as a reference is given in Figure B.4(b). For the presented geometry the relative differences for the local heat transfer coefficients are generally below 4% which is in agreement with the values reported by Poser et al. (2011) and Poser and von Wolfersdorf (2011).

THERMOCOUPLE TIME CONSTANT EFFECTS ON HEAT TRANSFER LEVEL

This Appendix section discusses thermocouple thermal inertia effects on the evaluated heat transfer coefficients. In this series of experiments, thermocouples with a wire diameter of 0.13mm are used, and the data were evaluated with three different hot gas temperature approaches: 1–Ideal temperature step in the flow, 2–Duhamel’s superposition theorem applied directly on the thermocouple outputs, 3–Correction for thermocouple thermal inertia prior to Duhamel’s superposition theorem.

Figure C.1 illustrates the full surface heat transfer coefficient contours (h/h_{ref}) normalised with the maximum value appeared in the data evaluated with an ideal step assumption, which was $218\text{W}/(\text{m}^2\text{K})$ and $338\text{W}/(\text{m}^2\text{K})$ for $Re_D=19,450$ and $46,530$, respectively. Although the general flow patterns are similar for the three different gas temperature approaches, the level of heat transfer coefficient differs significantly, especially in the stagnation point regions of the jets

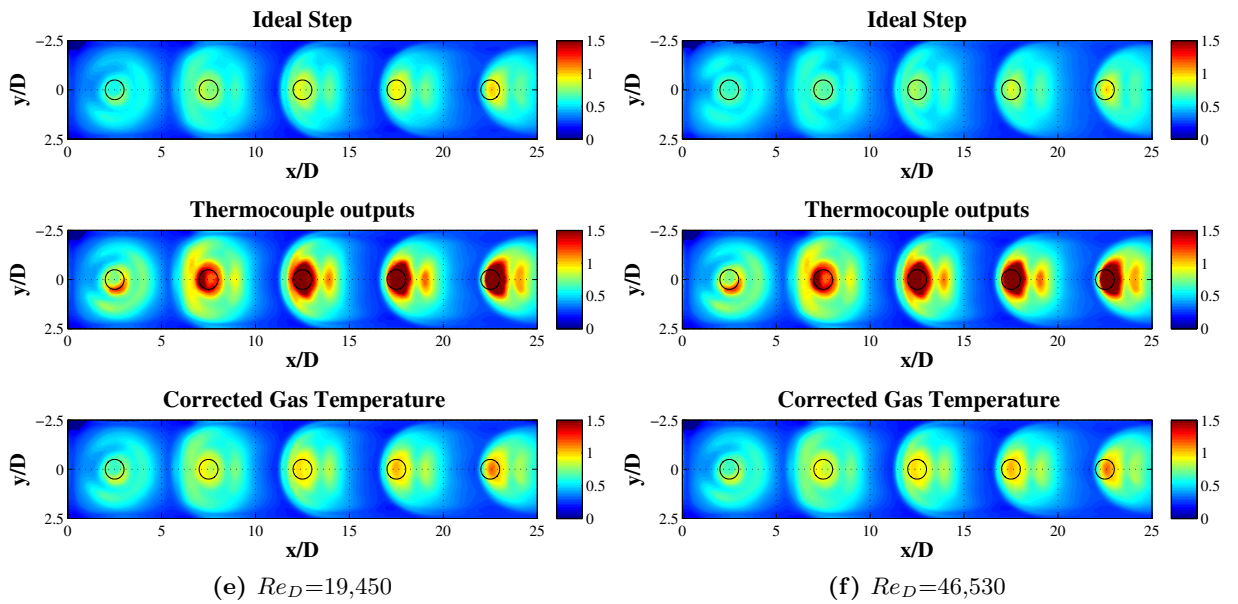


Figure C.1: Heat transfer coefficient surface contours (h/h_{ref}). $X/D=Y/D=5$, $Z/D=1$

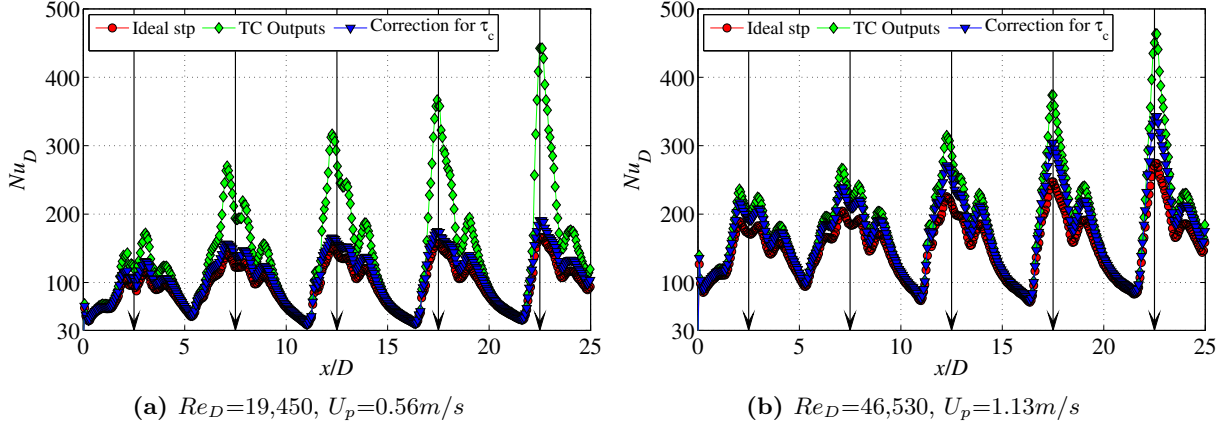


Figure C.2: Thermocouple time constant effect on the spanwise averaged Nu_D distributions. $X/D=Y/D=5$, $Z/D=1.5$

where the detection time of liquid crystals is shorter than the time needed for the thermocouples to reach steady state conditions. Therefore, a relatively lower $T_g(t)$ is considered in the solution of Equation 4.2 and an overestimation of the heat transfer level is unavoidable and far above 50% in case Duhamel's theorem is applied directly on the thermocouple outputs. On the other hand, an ideal temperature step approach results in an underestimation of the stagnation point heat transfer because a step change in the power settings does not cause a pure temperature step in the flow nor is the temperature overshoot considered. As a result, a correction based on thermocouple thermal inertia is required. If the plenum temperature is corrected according to Equation 4.4, the level of heat transfer coefficient lies between the above cases but it is closer to the ideal step assumption. This is not very far from reality since the DC-Power supply needs less than 0.1s to reach steady-state conditions. Note also that lower values of convective coefficients agree better as TLC indications appear later in time, and therefore, the fluid temperature history has a smaller influence on the evaluated data.

It is also noticeable that the differences between the evaluated data are smaller at higher Reynolds numbers which is attributed to the smaller thermocouple time constants caused by the higher plenum velocities. This is more evident in the local heat Nu_D distributions in Figure C.2. For both Re_D an overestimation of the local heat transfer level is observed in the stagnation point regions when Duhamel's superposition theorem is directly applied on thermocouple outputs. In particular, for low Reynolds, and thus plenum velocities of about 0.5m/s, Nu_D can be more than double overestimated compared to the ideal temperature step approach. For example, the stagnation point heat transfer of jet 5 (shortest TLC detection time) is situated on the same order of magnitude for $Re_D=19,450$ and 46,530, which of course represents a non-realistic situation. The differences between the three mainstream approaches are reduced with increasing Re_D , and hence thermocouple time constants, since the heat transfer coefficients for $Re_D=46,530$ are apparently closer between them. However, the Nu_D overestimation compared to the data evaluated with an ideal step approach is still 25% for the stagnation point of jet 1 and approximately 70% for jet 5. When $T_g(t)$ is corrected for thermocouple thermal inertia, the obtained heat transfer coefficients lie between the above cases. Note again, that in the wall jet regions the temperature level is nearly independent of the mainstream temperature due to the larger liquid crystal detection times.

CROSSFLOW MODEL

This Appendix section summarises the one-dimensional model presented by [Florschuetz et al. \(1981\)](#) which calculates the developed crossflow in a multi-jet impingement configuration with a single exit design (maximum crossflow orientation).

At a first step, the discrete hole array is considered as a surface over which the injection of the impingement flow through the different jets is continuously distributed, as shown in [Figure D.1](#). The jet velocity G_j , is related to the continuously distributed injection velocity G_j^* through the open area as, $G_j^* = G_j A_f$. Therefore, assuming incompressible flow the distributed injection velocity can be written in terms of the discrete hole discharge coefficient as follows:

$$G_j^* = C_D A_f \sqrt{2\rho(p_o - p)} \quad (\text{D.1})$$

where the streamwise pressure gradient is assumed to be primarily due to the acceleration of the flow caused by the continuously injected flow. Accordingly, a force momentum balance on the control volume in the left part of [Figure D.1](#) results to:

$$dp = -\frac{2G_{cf}dG_{cf}}{\rho} \quad (\text{D.2})$$

A mass balance leads to:

$$G_j^* = Z \frac{dG_{cf}}{dx} \quad (\text{D.3})$$

For constant C_D and p_o , the elimination of G_j^* and p from [Equations D.1, D.2 and D.3](#) in

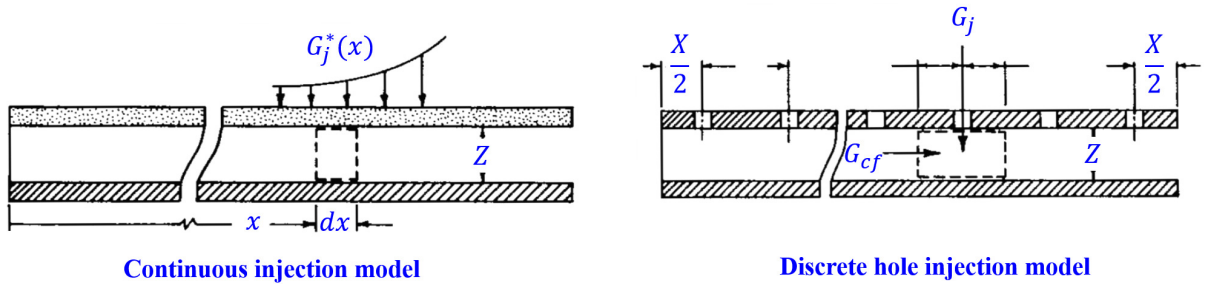


Figure D.1: Continuous injection (left) and discrete hole injection (right) models. Figure adopted from [Florschuetz et al. \(1981\)](#)

favour of G_{cf} yields to:

$$\frac{d^2 G_{cf}}{dx^2} - M G_{cf} = 0 \quad (D.4)$$

where $M = \sqrt{2} A_f C_D / Z$. The upstream boundary condition is $G_{cf} = 0$ at $x = 0$. A second boundary condition results from an overall mass balance for a channel of length L written in terms of an overall mean injection velocity, i.e. $G_{cf} = \bar{G}_j^* Z L$ at $x = L$. Integration of Equation D.4 then gives for the crossflow distribution:

$$\frac{G_{cf}}{\bar{G}_j^*} = \frac{L \sinh(Mx)}{Z \sinh(ML)} \quad (D.5)$$

The corresponding injected flow distribution obtained from Equation D.3 with the aid of D.5 is given by:

$$\frac{G_j^*}{\bar{G}_j^*} = \frac{ML \cosh(Mx)}{\sinh(ML)} \quad (D.6)$$

The discrete hole array jet velocity distribution is determined from Equation D.6 by assuming that the value G_j for a given spanwise row of holes is that corresponding to $G_j^*(x)$ with x evaluated in the centerline of the row. For uniform arrays, $A_f = (\pi/4) / [X/D \ Y/D]$, $L = XN$ and the first row is at $x = X/2$. Noting again that $G_j^* = G_j A_f$, the jet velocity distribution based on Equation D.6 can be written as:

$$\boxed{\frac{G_j}{\bar{G}_j} = \frac{\beta N \cosh(\beta(x/x_j))}{\sinh(\beta N)}} \quad (D.7)$$

where

$$\beta = \sqrt{2} C_D \frac{\pi D}{4 Y Z}, \quad x = x_j(i - 1/2), \quad i = 1, 2, 3 \dots N.$$

Besides the jet array velocity distribution given by Equation D.7, an additional flow parameter relevant with the correlation of the streamwise resolved heat transfer coefficients is the ratio of the crossflow velocity immediately upstream of a given spanwise row to the jet velocity of that row. This may be satisfactorily approximated utilising G_{cf} from Equation D.5 evaluated one-half a hole spacing upstream of the given row (see right part of Figure D.1), divided by G_j from Equation D.7. This results in:

$$\boxed{\frac{G_{cf}}{G_j} = \frac{1}{\sqrt{2} C_D} \frac{\sinh(\beta(x/x_j - 1/2))}{\cosh(\beta(x/x_n))}} \quad (D.8)$$

where the spanwise hole row locations are the same as previously indicated following Equation D.7. The model leads to the result that the flow distribution is independent of the streamwise hole spacing and impingement hole pattern, depending, for a given discharge coefficient and number of rows, only on the channel flow area.

LOCAL VARIATION OF EXPONENT m

It is well established empirical correlations since early 60' (Richardson, 1963), that Nusselt numbers are increased with increasing Reynolds numbers following a power law relation in the form: $Nu_x \sim Re_x^m$, where exponent m is 0.5 and 0.8 for boundary layers with laminar and turbulent textures, respectively. Apparently, exponent m is somehow related to the flow characteristics close to the wall and/or the state of the boundary layer.

The local variation of exponent m , shown in Figure E.1, is discussed in the present Appendix section. Given that the structure of the boundary layer is characterised by the value of exponent m , Figure E.1 shows actually a kind of flow visualisation pictures obtained directly from the heat transfer experiments. For all examined geometries, exponent m is about 0.5 at the stagnation point regions as a direct consequence of the laminar state of the boundary layer. On the other hand, m is increased in the wall jet regions and the downstream positions of the jets approaching values of $2/3$ or even larger. According to Gorin (2008, 2011), the “two-third” power law is valid for turbulent separated flows. For the horseshoe vortices exponent m is close to 0.8 indicating fully turbulent flow. The dynamics and the role of horseshoe vortex on convective heat transfer mechanisms have been addressed by Fisher and Eibeck (1990); Praisner and Smith (2006a) and

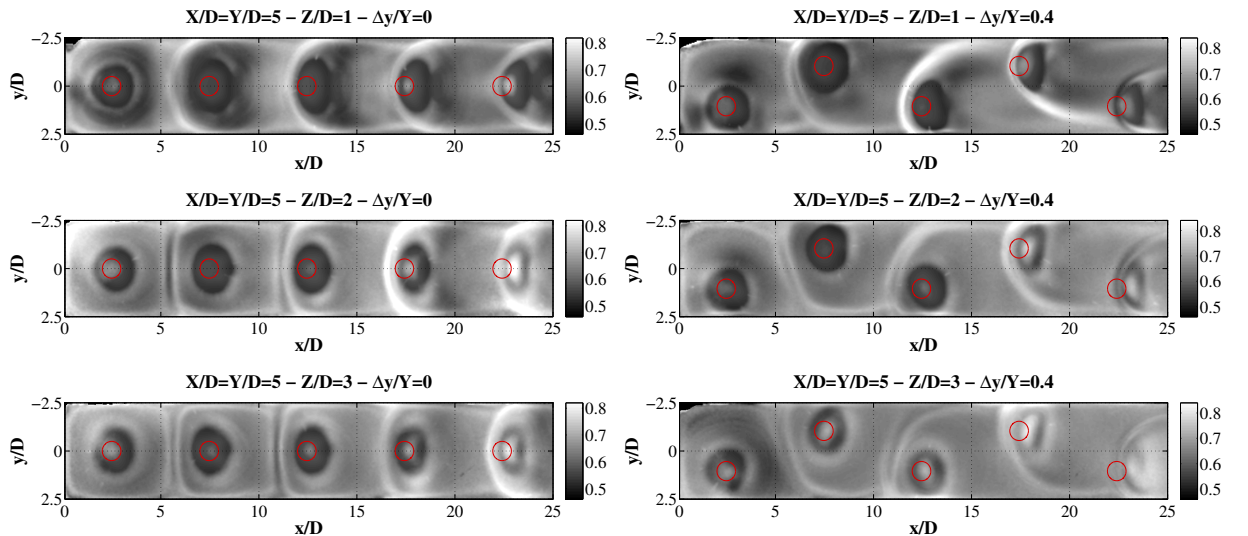


Figure E.1: Local variation of exponent m for various impingement channel geometries

[Praisner and Smith \(2006b\)](#).

The flow pattern is clearly observed as the flow accelerates towards the exit of the channel and the effect of crossflow generated by the upstream jet(s) becomes visible. Similar to the heat transfer pattern, the jet traces are progressively converted from a circular distribution (jet 1) to a horseshoe vortex shape distribution (jet 5) for all Z/D . Note that the secondary peak ring for $Z/D=1$, is better observed in the exponent m contours rather than the heat transfer coefficient patterns presented in Figure 6.6. However, the overall vortical structures of the flow domain, as for example the deflection of the jets and the curvature of the horseshoe vortices of the downstream jets, are significantly more pronounced at $Z/D=1$ due to the more intense jet and crossflow interactions. For the staggered patterns ($\Delta y/Y=0.4$), it is interesting to notice the attempt of the main flow to overcome the blockage of the area from the forthcoming jets, especially at jet 4.

The main outcome of this Appendix section is that locally resolved heat transfer experiments can be used for visualisation of relatively complex flow patterns since the various potential flow structures are better distinguishable compared to the heat transfer data.

ADDITIONAL HEAT TRANSFER RESULTS

This Appendix section presents additional heat transfer results which were not presented in the main part of this thesis. Heat transfer coefficient surface contours and spanwise averaged Nusselt number distributions are presented for the majority of the examined geometries over the full range of investigated Reynolds numbers.

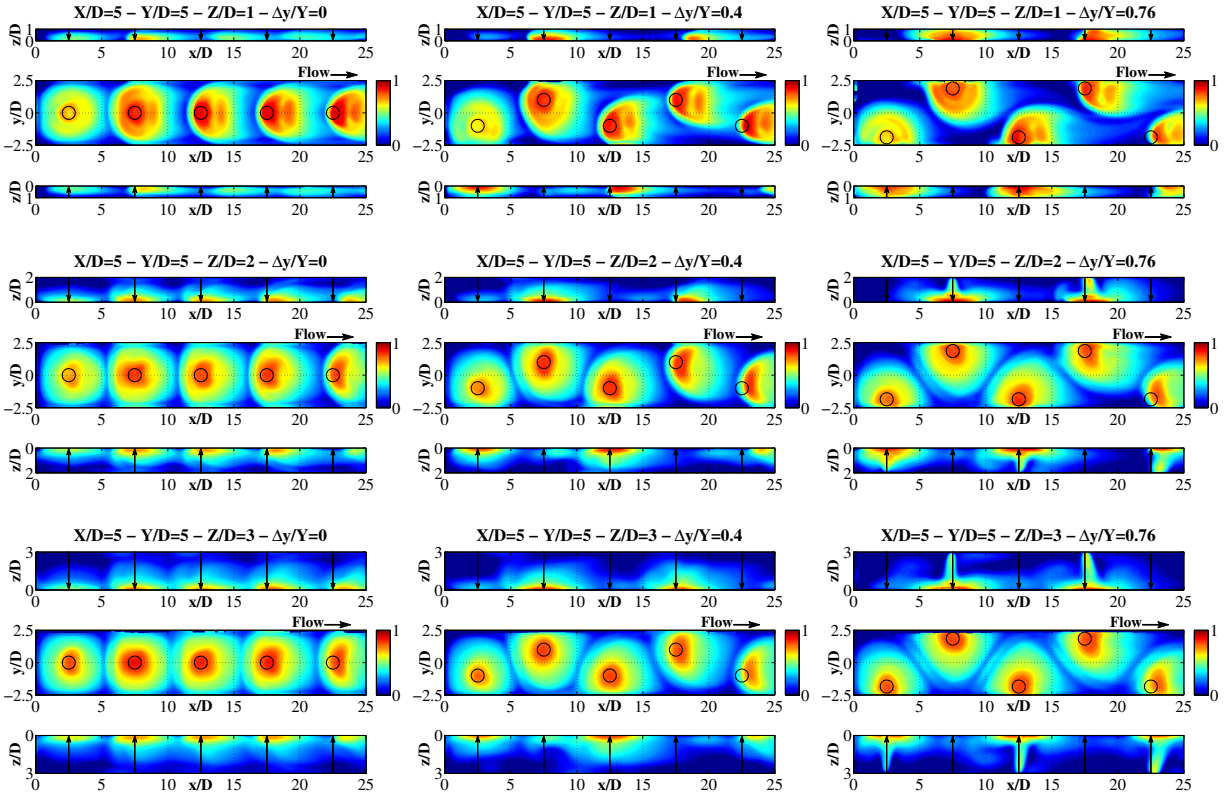


Figure F.1: Surface contours of h/h_{ref} at $Re_D=10,900$. $h_{ref}=139W/(m^2K)$

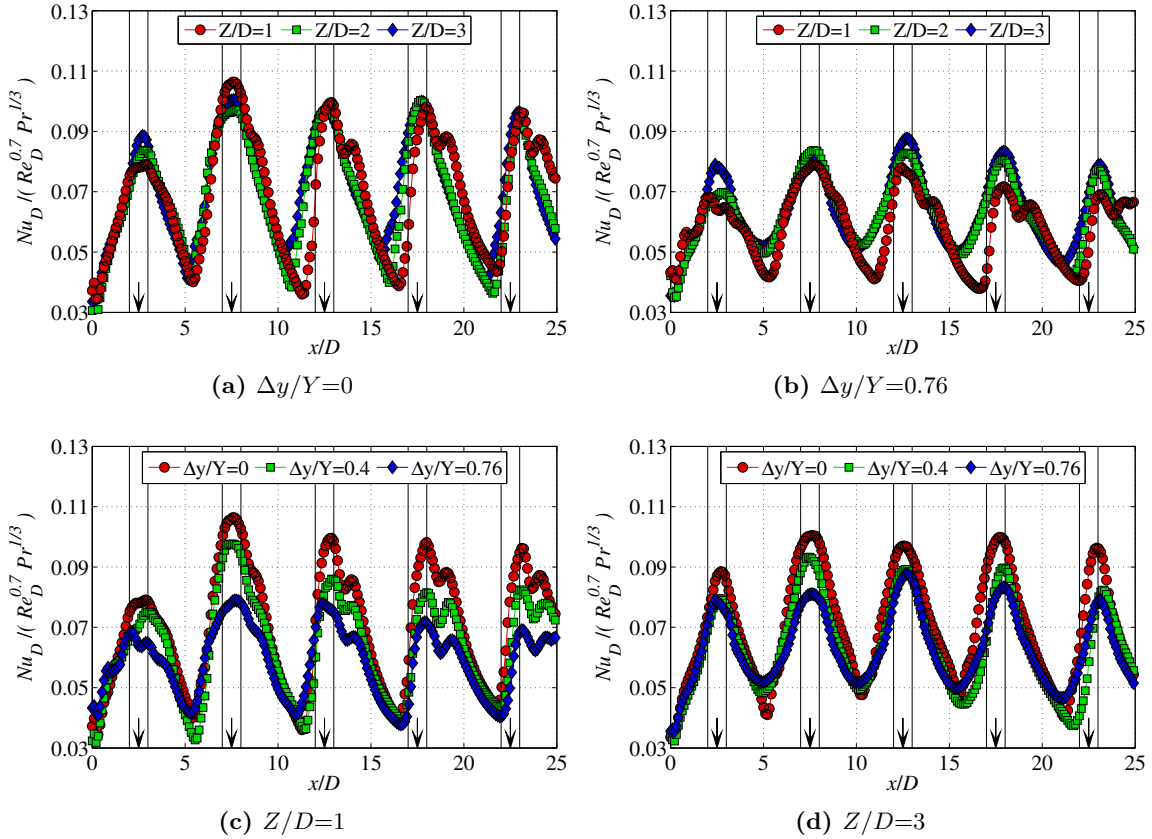


Figure F.2: Spanwise averaged $Nu_D/(Re_D^{0.7} Pr^{1/3})$ distributions at $Re_D=10,900$

F. Additional Heat Transfer Results

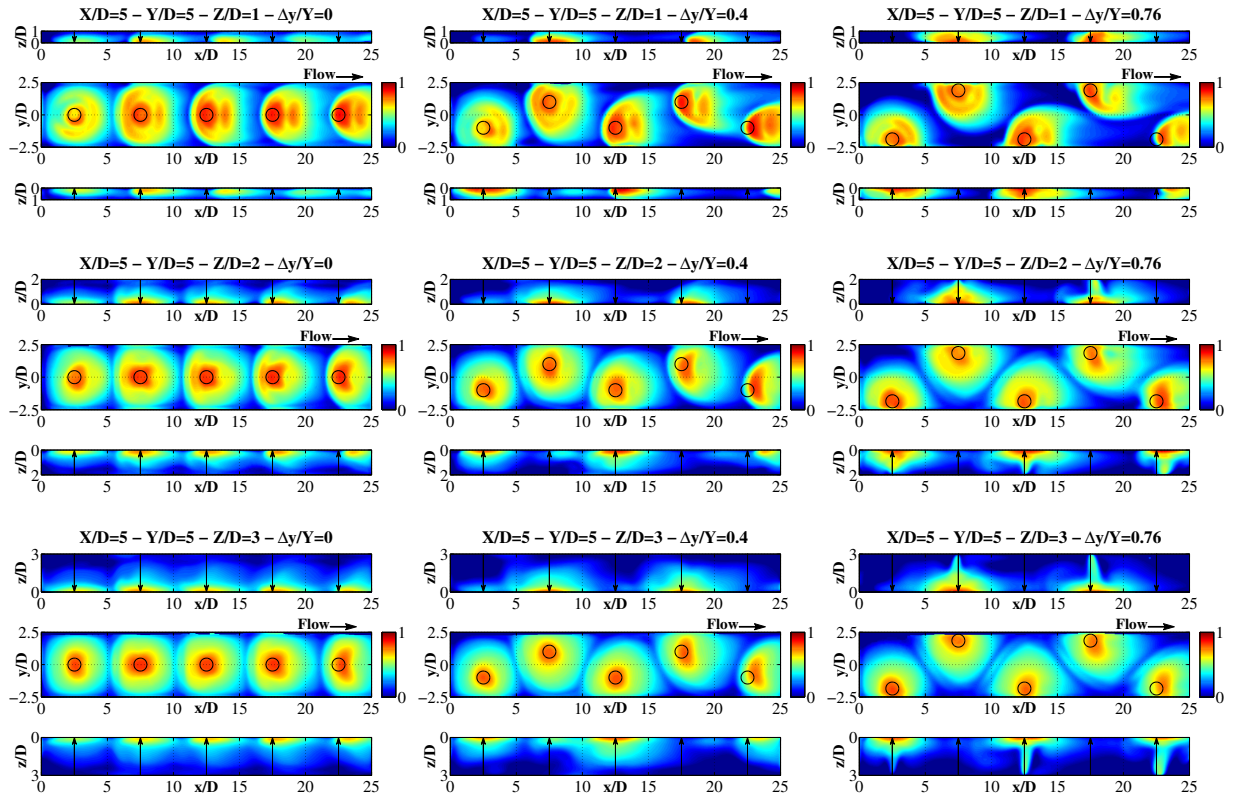


Figure F.3: Surface contours of h/h_{ref} at $Re_D=19,200$. $h_{ref}=207W/(m^2K)$

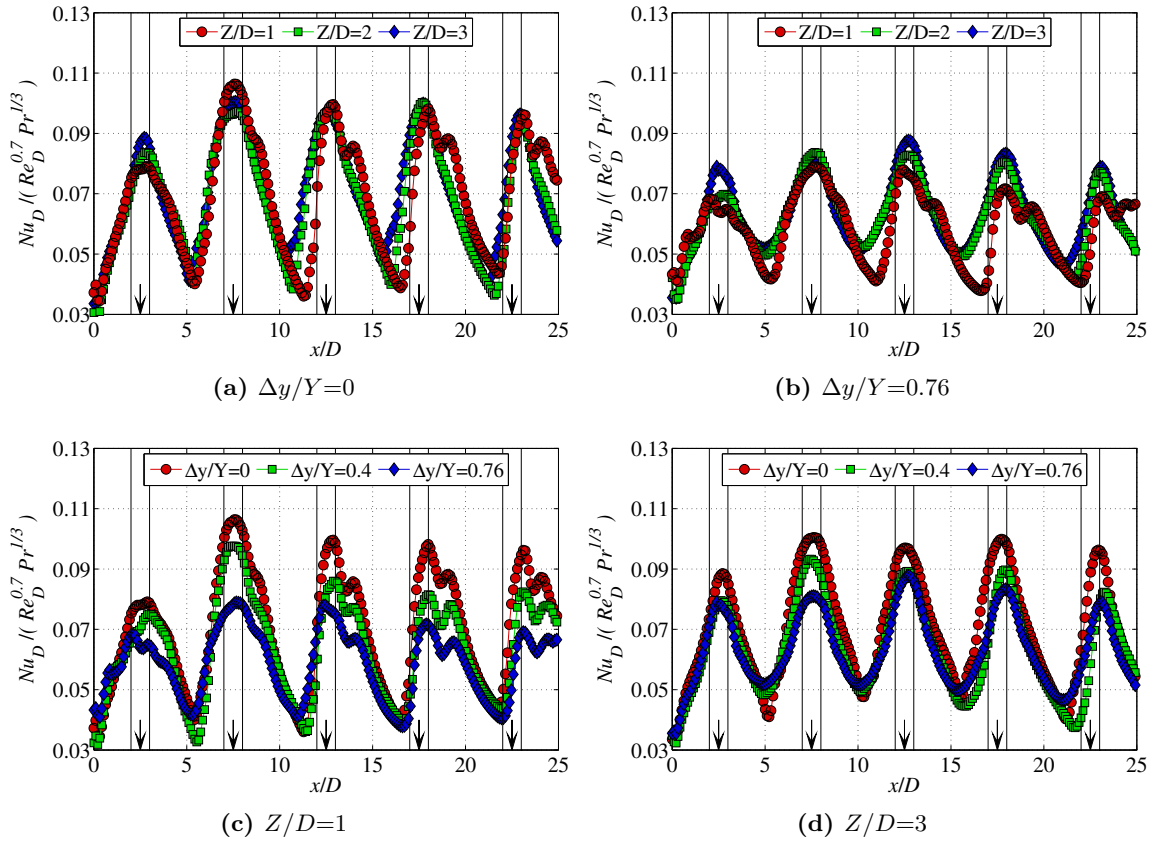


Figure F.4: Spanwise averaged $Nu_D/(Re_D^{0.7} Pr^{1/3})$ distributions at $Re_D=19,200$

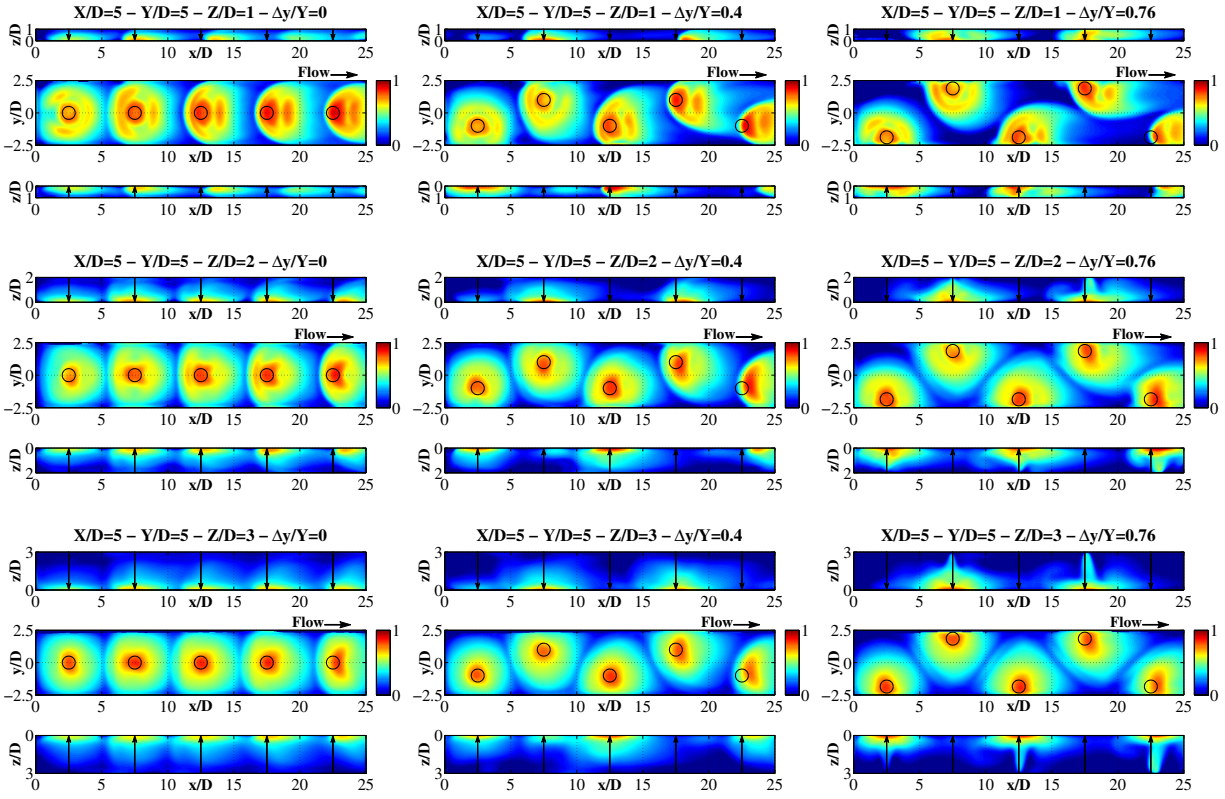


Figure F.5: Surface contours of h/h_{ref} at $Re_D=32,400$. $h_{ref}=395W/(m^2K)$

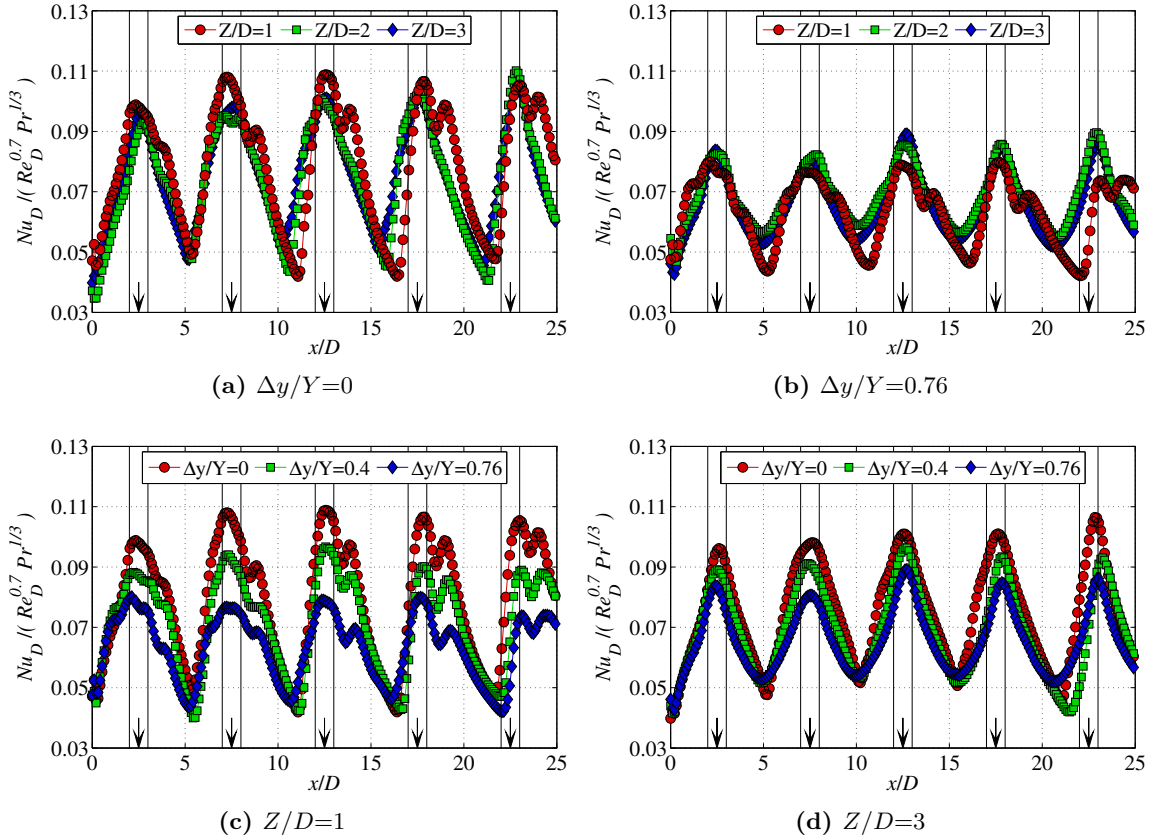


Figure F.6: Spanwise averaged $Nu_D/(Re_D^{0.7} Pr^{1/3})$ distributions at $Re_D=32,400$

F. Additional Heat Transfer Results

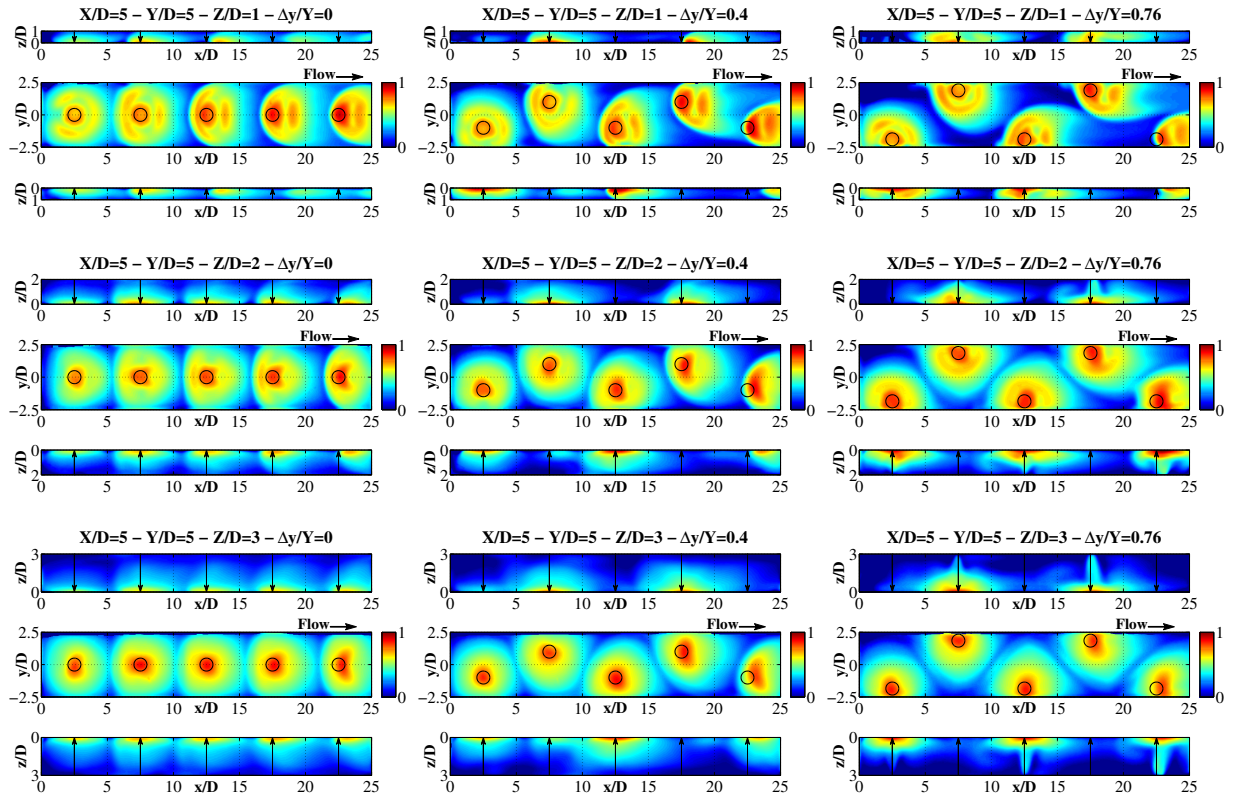


Figure F.7: Surface contours of h/h_{ref} at $Re_D=45,850$. $h_{ref}=100W/(m^2K)$

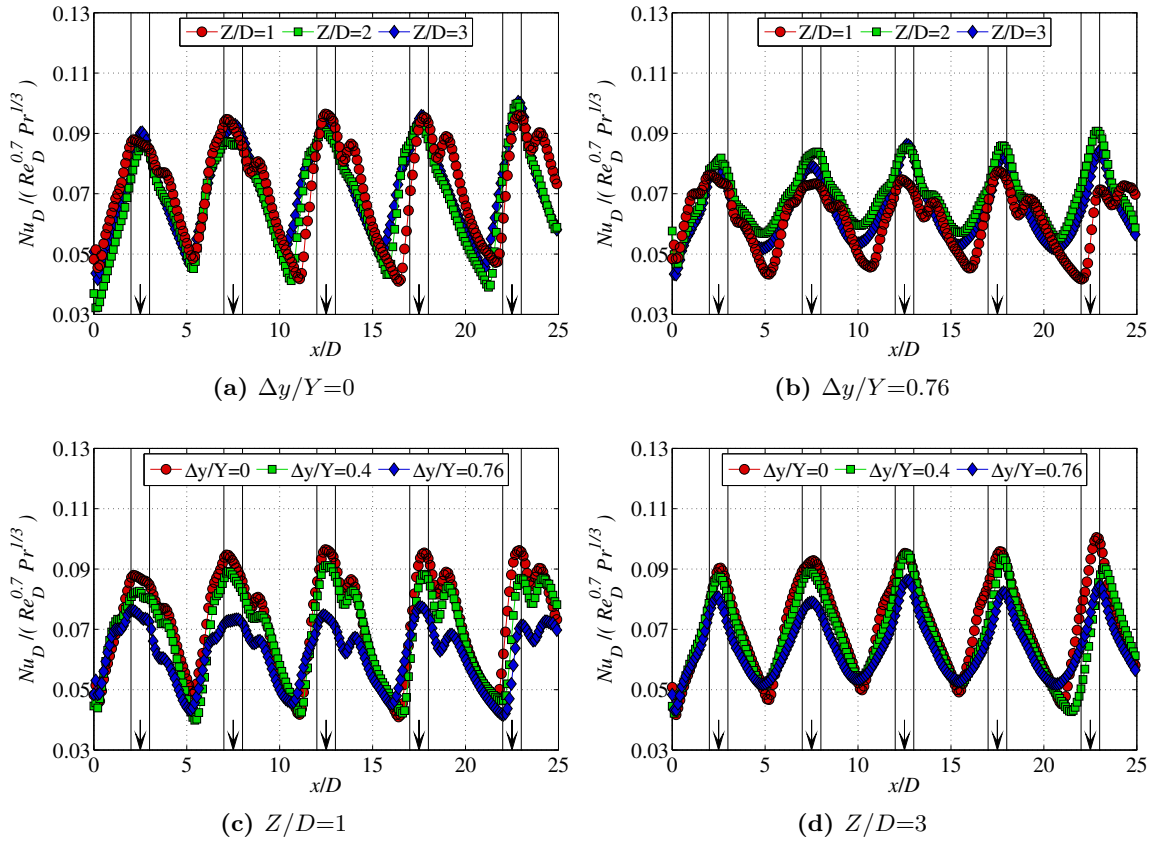


Figure F.8: Spanwise averaged $Nu_D/(Re_D^{0.7} Pr^{1/3})$ distributions at $Re_D=45,850$

F. Additional Heat Transfer Results

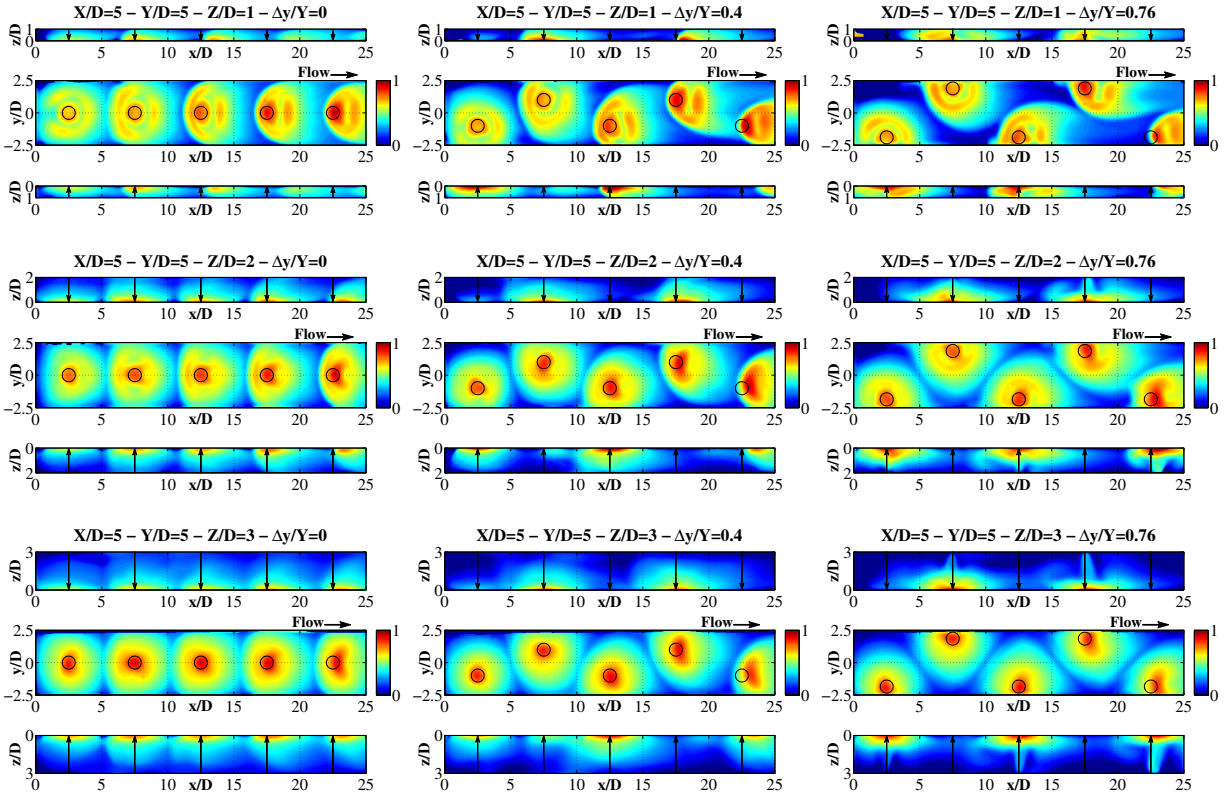


Figure F.9: Surface contours of h/h_{ref} at $Re_D=63,850$. $h_{ref}=477W/(m^2K)$

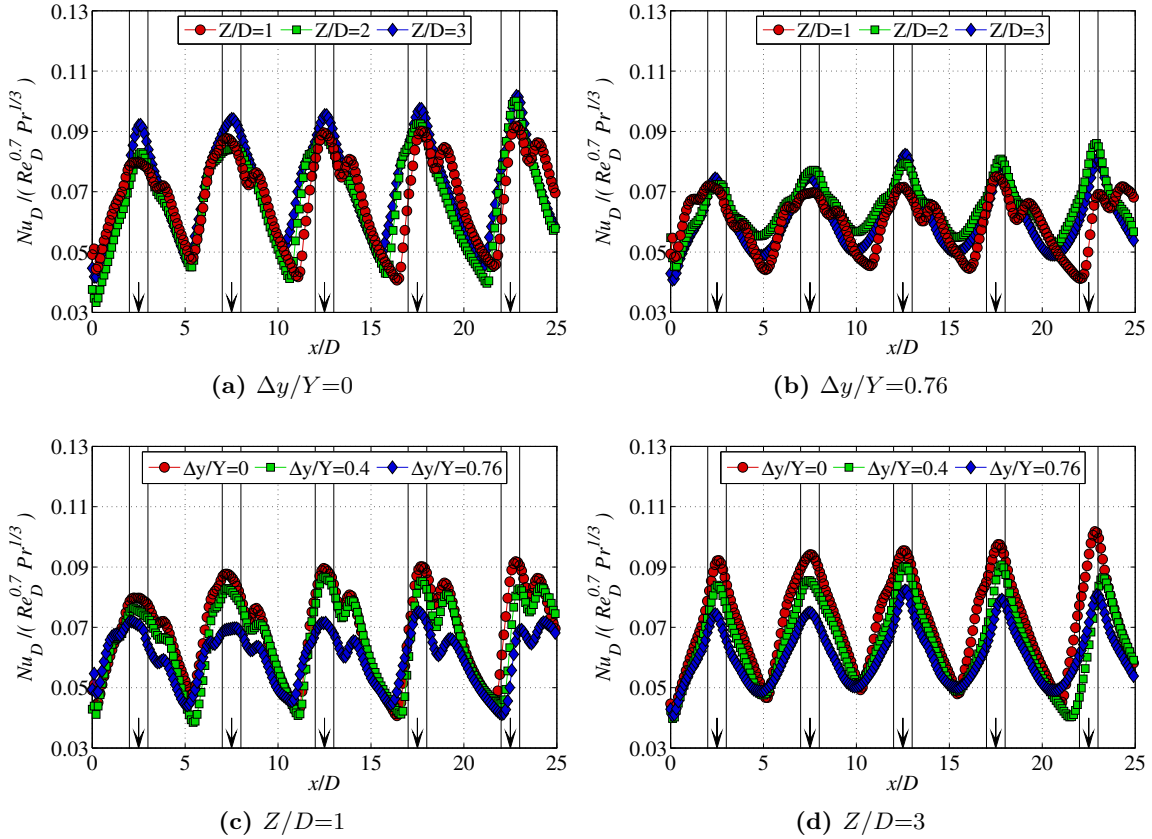


Figure F.10: Spanwise averaged $Nu_D/(Re_D^{0.7} Pr^{1/3})$ distributions at $Re_D=63,850$

F. Additional Heat Transfer Results

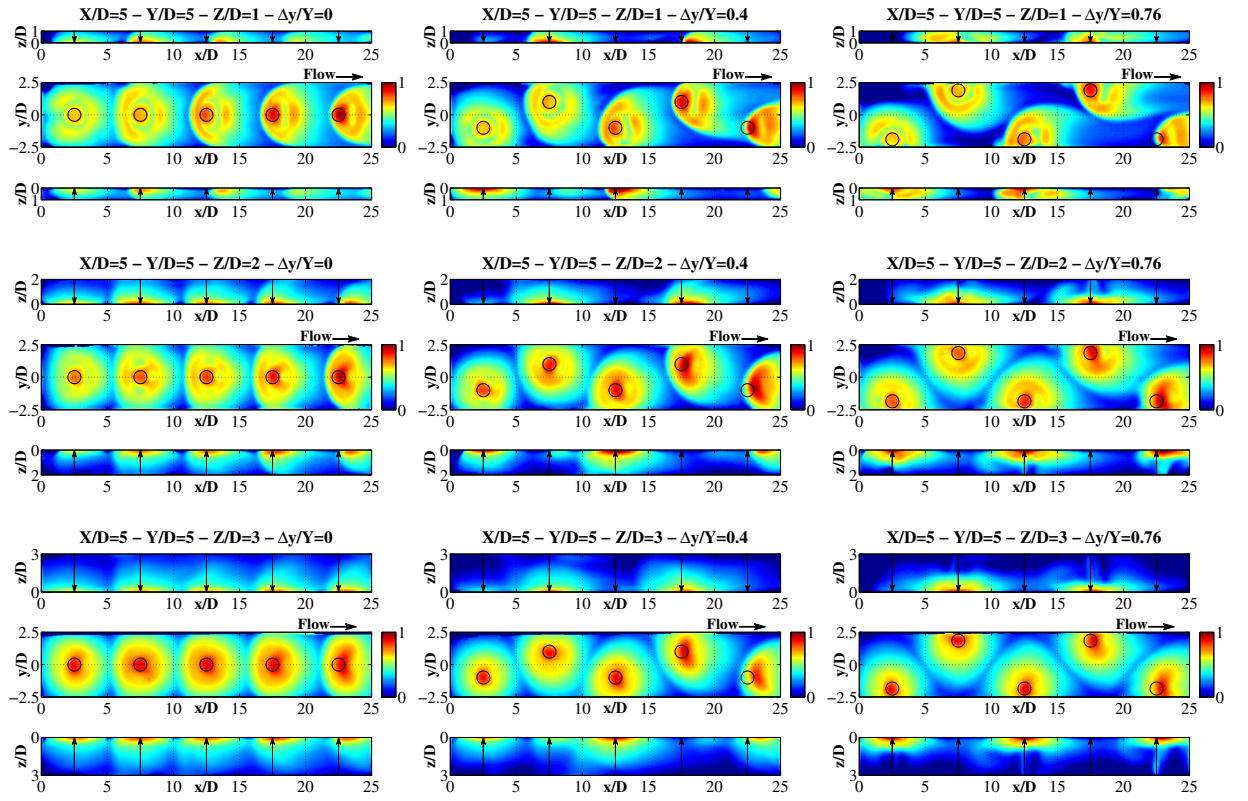


Figure F.11: Surface contours of h/h_{ref} at $Re_D=85,900$. $h_{ref}=616W/(m^2K)$

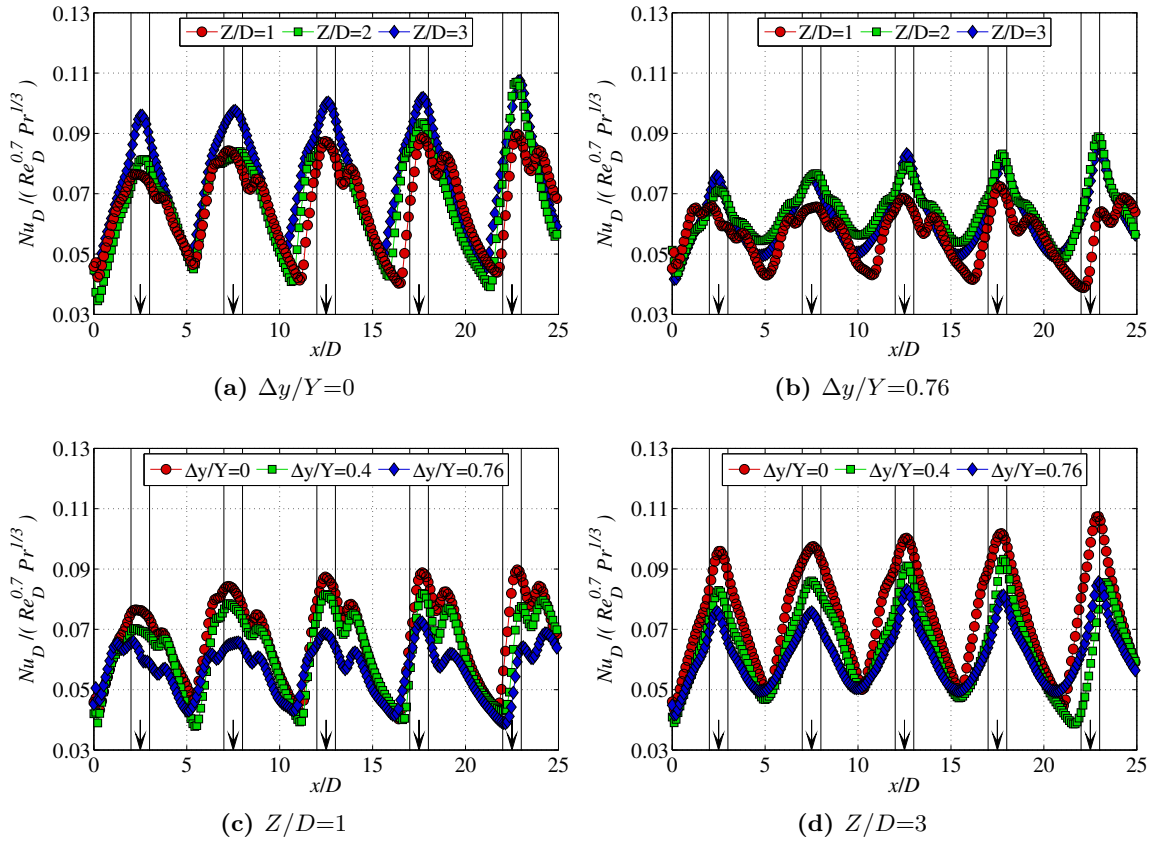


Figure F.12: Spanwise averaged $Nu_D/(Re_D^{0.7} Pr^{1/3})$ distributions at $Re_D=85,900$

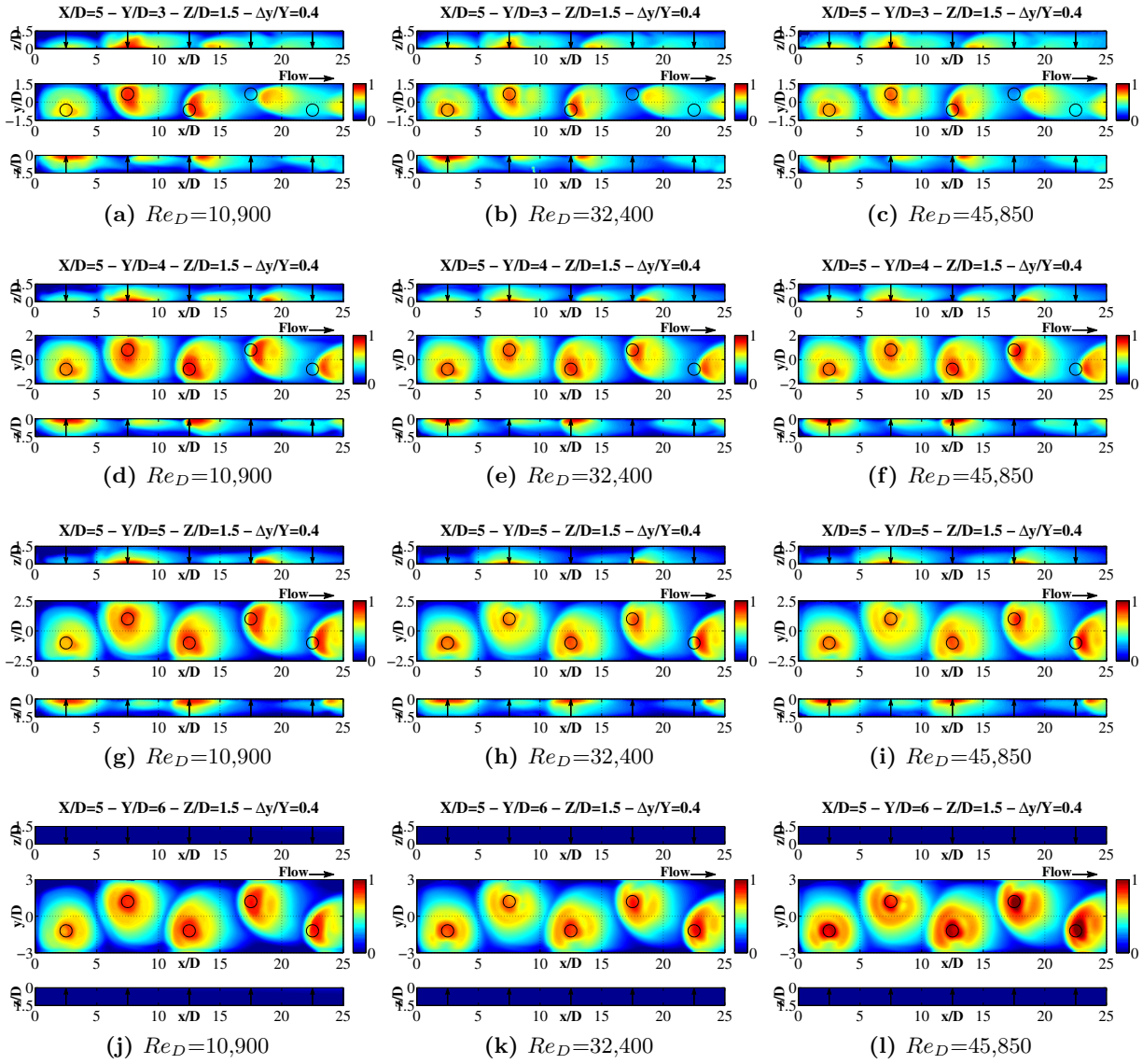


Figure F.13: Surface contours of h/h_{ref} various Reynolds numbers. $h_{ref}=132, 197$ and $386W/(m^2K)$ for $Re_D=10,900, 32,400$ and $45,850$ respectively.

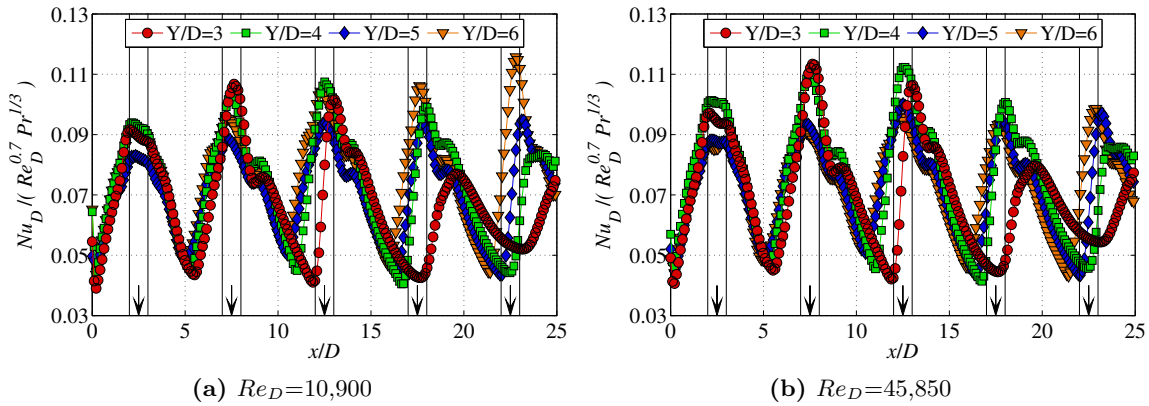


Figure F.14: Spanwise averaged $Nu_D/(Re_D^{0.7} Pr^{1/3})$ distributions

ALEXANDROS TERZIS

Chemin du Salève 16, CH-1004 Lausanne, Switzerland ◊ +41 (0) 78 917 29 77

Istrou 11, GR-65404, Kavala, Greece ◊ +30 (0) 693 616 8482

alexandros.terzis@me.com ◊ alexandros.terzis@epfl.ch

PERSONAL DETAILS

Date of birth 14 September 1984
Nationality Greek

EDUCATION

École Polytechnique Fédérale de Lausanne, Switzerland 11/2009 - 03/2014

PhD in Gas Turbine Heat Transfer

Experimental heat transfer for turbine blade cooling applications

Thesis: *Detailed heat transfer distributions of narrow impingement channels for integrally cast turbine airfoils*

Cranfield University, Bedfordshire, UK 10/2008 - 09/2009

MSc in Gas Turbine Technology

Master Thesis Mark: 86% (joint 1st)

Overall Mark: 81% (4th overall)

Thesis: *Experimental evaluation of impact ice fracture toughness and preliminary design of a shear test rig for use in an icing tunnel*

Aristotle University of Thessaloniki, Greece 10/2002 - 06/2008

Dipl.Ing. in Mechanical Engineering

Diploma Thesis Mark: 10/10

Overall Mark: 7.16/10 (top 25%)

Thesis: *Flow visualisation and performance of small axial cooling fans in crossflow*

WORKING EXPERIENCE

École Polytechnique Fédérale de Lausanne 02/2011 - 03/2014

Teaching assistant

EPFL, Switzerland

- Exercises in the course of thermal turbomachinery for gas turbine performance
- Measurement techniques, student laboratory for thermochromic liquid crystals

Turbomachinery and Icing Group

05/2008 - 09/2008

Researcher for aero-engine icing

Cranfield University, UK

- Experimental evaluation of the atmospheric ice fracture toughness - Temperature effects

SHORT COURSES

École Polytechnique Fédérale de Lausanne, Switzerland 11/06/2012 - 15/06/2012

Microscale Heat Transfer: Boiling, Condensation, Single- and Two-Phase Flows

Von Karman Institute for Fluid Dynamics, Belgium

03/05/2010 - 06/05/2010

Internal Cooling of Turbomachinery Blades

Cranfield University, UK

29/06/2009 - 03/07/2009

Gas Turbine Combustion

Cranfield University, UK

02/06/2008 - 06/06/2008

Gas Turbine Performance

AWARDS

Baxter Memorial Prize
Cranfield University, UK

11/06/2010

MEMBERSHIPS

Technical Chamber of Greece
American Society of Mechanical Engineers (ASME)
American Association for the Advancement of Science (AAAS)

SKILLS

Software Matlab, Labview, CATIA, Fluent
Languages English (Fluent), French (Beginner), Greek (Native)

PUBLICATIONS

Journal papers

- **A. Terzis**, M. Cochet, J. von Wolfersdorf, B. Weigand and P. Ott (201X) “Detailed heat transfer distributions of narrow impingement channels with varying jet diameters”, *ASME Journal of Turbomachinery*, Accepted through TurboExpo 2014
- **A. Terzis**, M. Cochet, J. von Wolfersdorf, B. Weigand and P. Ott (201X) “Detailed heat transfer distributions of narrow impingement channels for cast-in turbine airfoils”, *ASME Journal of Turbomachinery*, Accepted
- **A. Terzis**, G. Wagner, J. von Wolfersdorf, B. Weigand and P. Ott (2014) “Hole staggering effects on the cooling performance of narrow impingement channels using the transient liquid crystal technique”, *ASME Journal of Heat Transfer*, Vol.136(7), 071701 (9 pages) ↓
- R. Wyssmann, D. Ullmer, **A. Terzis** and P. Ott (2014) “A Comparative study of the local heat transfer distributions around various surface mounted obstacles”, *Journal of Thermal Science*, Vol.23(2), pp.162-171 ↓
- S. Fechter, **A. Terzis**, B. Weigand, J. von Wolfersdorf and P. Ott (2013) “Experimental and numerical investigation of narrow impingement cooling channels”, *Int. Journal of Heat and Mass Transfer*, Vol.67, pp.1208–1219 ↓
- O. Caggese, G. Gnaegi, G. Hannema, **A. Terzis** and P. Ott (2013) “Experimental and numerical investigation of a fully confined impingement round jet”, *Int. Journal of Heat and Mass Transfer*, Vol.65, pp.873–882 ↓
- **A. Terzis**, J. von Wolfersdorf, B. Weigand and P. Ott (2012) “Thermocouple Thermal Inertia Effects on Impingement Heat Transfer Experiments Using the Transient Liquid Crystal Technique”, *Measurement Science and Technology*, Vol.23, p. 115303 (13 pages) ↓
- **A. Terzis**, I. Stylianou, A. Kalfas and P. Ott (2012) “Heat Transfer and Performance Characteristics of Axial Cooling Fans with Downstream Guide Vanes”, *Journal of Thermal Science*, Vol.21(2), pp.162-171 ↓
- **A. Terzis**, P. Zachos, B. Charnley, V. Pachidis and A. Kalfas (2011) “On the Applicability of Oil and Dye Technique During the Design Phase and Operation of Experimental Rigs”, *Journal of Flow Visualization and Image Processing*, Vol.18(3), pp.199-214 ↓
- **A. Terzis**, C. Kazakos, N. Papadopoulos, A. Kalfas and P. K. Zachos and P. Pilidis (2011) “Effects of Swirl Velocities From Fan Assemblies Mounted on Lifting Surfaces”, *ASME Journal Of Engineering For Gas Turbines And Power*, Vol.133(3), 031702 (9 pages) ↓

Conferences Proceedings

- **A. Terzis**, M. Cochet, J. von Wolfersdorf, B. Weigand and P. Ott (201X) “Detailed heat transfer distributions of narrow impingement channels for cast-in turbine airfoils”, ASME TurboExpo, GT2014-25910, 16–20 June, Düsseldorf, Germany
- **A. Terzis**, J. von Wolfersdorf, B. Weigand and P. Ott (2014) “Local heat transfer distributions of small impingement configurations: A detailed experimental procedure using transient heat transfer methods”, ISROMAC-15, Paper No.172, 24-28 February, Honolulu, Hawaii, USA
- **A. Terzis**, G. Wagner and P. Ott (2012) “Hole staggering effect on the cooling performance of narrow impingement channels”, ASME TurboExpo, GT2012–68323, 11–15 June, Copenhagen, Denmark
- **A. Terzis**, J. von Wolfersdorf, G. Wagner, B. Weigand and P. Ott, (2012) “Influence of thermocouple thermal inertia in impingement heat transfer experiments using transient techniques”, XXI Biannual Symp. on Meas. Techniques in Turbomachinery, 22–23 Mar., Valencia, Spain
- **A. Terzis**, K. Pervier and D.W. Hammond (2011) “Temperature effect on fracture toughness of atmospheric ice accreted on a typical fan blade material”, 20th Int. Symp. Air Breathing Engines, ISABE-2011-1611, Gothenburg, Sweden
- **A. Terzis**, I. Stylianou, A.I. Kalfas and Peter Ott (2011) “Effect of stators on the performance and the thermal capabilities of small axial cooling fans”, 10th Int. Symp. on Aerothermodynamics of Internal Flows (ISAIF), 4-7 Jul., Brussels, Belgium
- **A. Terzis**, Kazakos C., P.K. Zachos A.I. Kalfas and Peter Ott (2011) “Swirl jet and crossflow interaction at low velocity ratios and incompressible flows”, 9th European Turbomachinery Conference (ETC), Vol.I, pp.133–144, 21–25 Mar., Istanbul, Turkey
- C. Rülke, **A. Terzis**, P.K. Zachos and V. Pachidis and R. Singh (2010) “Experimental and numerical evaluation of the pressure loss through a compressor cascade operating at highly negative incidence”, XX Biannual Symp. on Meas. Techniques in Turbomachinery, 23-24 Sep., Milan, Italy
- **A. Terzis**, P.K. Zachos, B.A. Charnley and A.I. Kalfas, (2010) “Application of oil and dye flow visualization in incompressible turbomachinery flows”, XX Biannual Symp. on Meas. Techniques in Turbomachinery, 23-24 Sep., Milan, Italy
- **A. Terzis**, C. Kazakos, N. Papadopoulos, A.I. Kalfas, P.K. Zachos and P. Pilidis (2010) “Effects of the swirl velocity of a jet in crossflow from fan assemblies mounted on lifting surfaces”, ASME TurboExpo, GT2010–23357, 14-18 June, Glasgow, Scotland, UK
- **A. Terzis**, K. Kyprianidis, P. Pilidis and A.I. Kalfas (2009) “Comparative performance evaluation of a multi-stage axial fan assembly”, 9th Int. Conf. on Industrial Ventilation, 18-21 Oct, Zurich, Switzerland
- **A. Terzis**, K. Kyprianidis, P. Pilidis and A.I. Kalfas (2009) “Experimental performance evaluation of axial ventilators”, 19th Int. Symp. Air Breathing Engines, ISABE-2009-1187, Montreal, Canada

Invited Talks/Seminars

- 11/03/2014: Massachusetts Institute of Technology (MIT), Cambridge, USA
Seminar at Reacting Gas Dynamics Laboratory, Center for Energy and Propulsion Research
“Detailed heat transfer distributions of narrow impingement channels for integrally cast turbine airfoils”